Molecular Thin Films: Fundamentals and Potential Routes for Spintronic Applications

Julie Ann Gardener

Thesis submitted for the degree of
Doctor of Philosophy

University College London

April 2008

UMI Number: U591572

All rights reserved

INFORMATION TO ALL USERS
The quality of this reproduction is dependent upon the quality of the copy submitted.

In the unlikely event that the author did not send a complete manuscript
and there are missing pages, these will be noted. Also, if material had to be removed,
a note will indicate the deletion.

UMI U591572
Published by ProQuest LLC 2013. Copyright in the Dissertation held by the Author.
Microform Edition © ProQuest LLC.
All rights reserved. This work is protected against
unauthorized copying under Title 17, United States Code.

ProQuest LLC
789 East Eisenhower Parkway
P.O. Box 1346
Ann Arbor, MI 48106-1346

Declaration of Originality

I confirm that, except where specific reference is made to the work of others, this work is both original and my own. This thesis has not been already submitted either wholly or in part to satisfy any degree required at this of any other institution.

J. Gardener

Abstract

Metal phthalocyanine (MPc) thin films are of interest for potential applications in spintronics and quantum computing. Two MPc-based routes towards spintronics devices are assessed here; an organic-based approach and one in which MPc films serve as precursors for inorganic routes. For the all-organic approach, a selection of copper phthalocyanine (CuPc) thin films have been characterised; these comprise molecular stacks (columns) that can be engineered to run parallel or orthogonal to the substrate plane. Electron paramagnetic resonance has been used to study interactions between unpaired electron spins of the CuPc molecules and shows that stronger intra- rather than inter-column interactions exist, implying that coherent spin transport would be most efficient along the column directions. Furthermore, this technique has been developed to assess the molecular structure of the CuPc films. Scanning tunnelling microscopy has been used to study the initial stages of CuPc growth on passivated Si(100) surfaces wherein an arrangement similar to the bulk α-phase is observed. Different growth modes are observed on surfaces passivated with hydrogen or ammonia; this is attributed to differences in chemical interactions between the phthalocyanine ligand and passivating species. For the second route, a new method for introducing metal spins into silicon is presented wherein MPc films are irradiated with 172 nm UV light. The UV photons rupture the organic ligands forming volatile fragments, whilst the metals remain behind to form a metal oxide surface layer and are introduced into the substrate. X-ray absorption and secondary ion mass spectrometry measurements demonstrate that, for the specific example given of manganese phthalocyanine, Mn atoms do not cluster and instead occupy interstitial sites within the Si lattice. This method has the potential to create arrays of spins in silicon, which would be of interest as dilute magnetic semiconductors and for quantum computing applications.

Table of Contents

Declaration of Originality 2

Abstract 3

Acknowledgements 7

Glossary 11

1. INTRODUCTION 11

1.1 Phthalocyanine Molecules 13

1.2 Copper Phthalocyanine Thin Films 15

1.2.1 Bulk CuPc Thin Films 15

1.2.2 Ultra-Thin CuPc Films on Silicon 22

1.3 Applications 29

1.3.1 Inorganic Spintronics 29

1.3.2 Organic Spintronics 33

1.3.3 Quantum Computing 39

1.3.4 Dopants in Silicon 43

2. EXPERIMENTAL 51

2.1 Phthalocyanine Film Growth 51

2.1.1 Substrate Preparation 51

2.1.2 Purification of Raw Material 54

2.1.3 Organic Molecular Beam Deposition 54

2.1.4 Formation of CuPc Crystals 56

2.2 UV Excimer Lamp Processing 56

2.3 Scanning Tunnelling Microscopy 58

2.4 Atomic Force Microscopy 61

2.5 Secondary Ion Mass Spectrometry 63

2.5.1 Sputtering Yields 65

2.5.2 Relative Scattering Factors 66

2.5.3 Depth Profiling....67
2.6 Electronic Absorption Spectroscopy....69
2.7 Raman Spectroscopy....71
2.8 Electron Paramagnetic Resonance....74
2.8.1 Zeeman Splitting....74
2.8.2 Hyperfine Splittings....77
2.8.3 Experimental Conditions....79
2.9 X-ray Absorption Spectroscopy....80
2.9.1 X-rays....80
2.9.2 Synchrotron Radiation....81
2.9.3 X-ray Absorption....82
2.9.4 X-ray Absorption Near-Edge Structures....84
2.9.5 Extended X-ray Absorption Fine Structure....85
2.10 X-ray Photoelectron Spectroscopy....88
2.11 X-ray Diffraction....90
2.11.1 Crystal Structure....91
2.11.2 Bragg's Law....92
2.11.3 Experimental Conditions....93
3. CuPc GROWTH ON PASSIVATED Si(100) SURFACES....94
3.1 Global Morphology: Molecular Island Growth....97
3.1.1 Initial Stages of CuPc Deposition....97
3.1.2 First Layer Island Formation....99
3.1.3 Multilayer Island Formation....101
3.1.4 Comparison of Molecular Coverages....104
3.2 Molecular Arrangement within Columns....107
3.2.1 Texture of Islands: Observation of Molecular Rows....107
3.2.2 Determination of Alignment with respect to Substrate....109
3.2.3 Molecular Resolution....110
3.2.4 Proposed Model and Comparisons with Bulk Films....112
3.3 Conclusions....114

4. SPIN COUPLING IN CuPc FILMS 116

4.1 Copper Phthalocyanine Thin Films 120

4.1.1 Electronic Absorption Spectroscopy 120

4.1.2 Atomic Force Microscopy 121

4.1.3 X-ray Diffraction 123

4.1.4 Electron Paramagnetic Resonance 125

4.2 Templated Copper Phthalocyanine Thin Films 132

4.2.1 Electronic Absorption Spectroscopy 133

4.2.2 X-ray Diffraction 133

4.2.3 Electron Paramagnetic Resonance 136

4.3 Magnetically Diluted Copper Phthalocyanine Thin Films 142

4.3.1 Electronic Absorption Spectroscopy 143

4.3.2 Atomic Force Microscopy 145

4.3.3 X-ray Diffraction 147

4.3.4 Electron Paramagnetic Resonance 155

4.4 Conclusions 165

5. INTRODUCTION OF METAL DOPANTS INTO SI FROM MPc FILMS 168

5.1 Degradation of the Phthalocyanine Ring 170

5.1.1 Raman Spectroscopy 172

5.1.2 Electronic Absorption Spectroscopy 179

5.1.3 Atomic Force Microscopy 182

5.2 Characterisation of the Surface after UV Treatment 185

5.2.1 Secondary Ion Mass Spectrometry 186

5.2.2 X-ray Photoemission Spectroscopy 193

5.2.3 X-ray Absorption Spectroscopy 201

5.3 Examination of the Bulk Substrate after UV Exposure 205

5.3.1 X-ray Photoemission Spectroscopy 205

5.3.2 Secondary Ion Mass Spectrometry 207

5.3.3 X-ray Absorption Spectroscopy 215

5.3.4 Mechanisms for the Introduction of Mn into Si 217

5.4 Conclusions 219

6. CONCLUSIONS 221

6.1 Applications of MPc Films for Organic Spintronics 221

6.2 Applications of MPc films as Precursors for Inorganic Spintronics 224

6.3 Implications for Future Work 225

6.3.1 Future Work 226

6.3.2 MPc Routes to MRAM devices 227

REFERENCES 231

Acknowledgements

I would firstly like to thank my supervisor, Dr. Sandrine Heutz for her kind guidance, support, optimism, patience and encouragement during my PhD. She has ensured that I have had every opportunity to undertake a wide variety of fascinating research, for which I am extremely grateful. I would also like to thank Prof. Marshall Stoneham and Prof. Gabriel Aeppli for providing me with the opportunity to join the LCN QIP team and work on such a diverse and interesting project. I have greatly benefited from their suggestions and encouragement. I also thank the EPSRC for financial support. The advice, guidance and understanding I have received from Prof. Sara Majetich is also greatly appreciated, both during my time at UCL and as a member of her group at CMU.

I have been very fortunate to work with such a wide range of very talented scientists, ranging from undergraduate students to distinguished professors, to all of whom I am very grateful. In particular, I would like to thank the other members of the QIP and Heutz groups for the help and support that they have given me.

Many thanks to Prof. Tim Jones, Prof. Franco Cacialli and their groups for allowing me access to their OMBD chambers. A special thanks to Dr. Paul Sullivan and Dr. Sanggyu Yim for their assistance on the thin film growths and HF etching of Si, and to Soumaya Mauthoor and Hsiang-Han Teng for help with the Pc purification. I also thank Prof. Ian Boyd, Irving Liaw and Sara Lauzurica for their assistance with the excimer UV lamp experiments.

I am very grateful to the IYCS of NIMS for providing me with the opportunity to spend 10 weeks in the laboratory of Miki-san and James Owen, during which the STM measurements in Chapter 3 were performed. I greatly enjoyed my time working in the group and the experience of living in Japan.

I am extremely grateful to the help and support of Prof. Sankar Gopinathan, Prof. Geoff Thornton, Dr. Marcin Sikora and Dr. Steve Fiddy (along with Sandrine and Irving) for their assistance with the XAS measurements during trips to Daresbury and the ESRF. I thank Prof. Ivan Parkin, Dr. Geoff Hyett and Rob Palgrave for their help with the XPS measurements. I am also very grateful to Dr. Chris Kay, Dr. Gavin Morely, Marc Warner and Daniel Klose for teaching me how to use the CW EPR spectrometer and their assistance with the experiments. Many thanks to Richard Chater and Dr. David McPhail for training me and granting me access to their SIMS equipment. I am also extremely grateful to Sandrine, Marshall, Neil, Gavin, Marc, Andy and Nick for their assistance in checking this manuscript.

Lastly I wish to thank my friends and family for their encouragement, generosity and good humour. In particular, I would like to thank my Mum and Dad for the love, support and understanding they have given me. Without such a support network I would not be where I am today!

Glossary

AFM	Atomic Force Microscopy
CuPc	Copper Phthalocyanine
CVD	Chemical Vapour Deposition
CW EPR	Continuous Wave Electron Paramagnetic Resonance
DMS	Dilute Magnetic Semiconductor
EPR	Electron Paramagnetic Resonance
EXAFS	Extended X-ray Absorption Fine Structure
GMR	Giant Magnetoresistance
H_2Pc	Metal-free Phthalocyanine
HOMO	Highest Occupied Molecular Orbital
k-cell	Knudsen Cell
LUMO	Lowest Unoccupied Molecular Orbital
MBE	Molecular Beam Epitaxy
ML	Monolayer
MnPc	Manganese Phthalocyanine
MPc	Metal Phthalocyanine
MRAM	Magnetic Random Access Memory
OMBD	Organic Molecular Beam Deposition
Pc	Phthalocyanine
PTCDA	Perylene-3,4,9,10-tetracarboxylic dianhydride
QCM	Quartz Crystal Microbalance
RSF	Relative Scattering Factor
SIMS	Secondary Ion Mass Spectrometry

STM	Scanning Tunnelling Microscopy
UHV	Ultra-high Vacuum
UV	Ultraviolet
XANES	X-ray Absorption Near-Edge Structures
XAS	X-ray Absorption Spectroscopy
XPS	X-ray Photoelectron Spectroscopy
XRD	X-ray Diffraction

Chapter One: Introduction

The aim of this work is to study the fundamental properties of phthalocyanine thin films with a specific focus on their potential for applications in spintronics.

Phthalocyanines (Pcs) are archetypal organic semiconductors that can contain a single metal ion [1]. If this ion is chosen to be a transition metal species, such as copper, the molecule may contain an unpaired electron (or multiple unpaired electrons); this is of interest for spintronic applications wherein the charge and spin properties of such electrons are combined to create devices [2, 3]. Their semiconducting nature has led to a considerable amount of interest in phthalocyanine thin films for applications in organic electronic devices [4–6] and so many of their electronic properties are already well understood. Therefore, for spintronic applications it remains to characterise their spin-related properties, as will be discussed here. In addition, this class of molecules is readily and cheaply available with a large variety of metal centres [1] and so much of the work described could be easily modified for other applications. In general, organic molecular thin films are advantageous for spintronic applications due to their low cost, versatility, high chemical purity, lack of clustering of spins and potential to fabricate flexible devices [7, 8].

Spintronics is a fast growing area of research which aims to combine conventional electronics with the additional information that can be stored in the spin of an electron. Silicon-based technology has led to increasingly smaller devices, however it is widely accepted that a continuation of this scaling, famously described by Moore's law [9], is not sustainable using current approaches. Instead, a large effort is underway to develop new low power, nano-sized devices which rely on the quantum mechanical property of electron spin to write, manipulate, store and read information. So far the most intense research and progress have been made in this area with inorganic materials [2, 3], but recent developments of organic-based devices have been promising [10, 11]. In this

work, properties and procedures that could lead to the development of inorganic and organic based devices will be discussed.

Two main approaches will be followed. Firstly, in order to capitalise on their inherent semiconducting and magnetic properties, the Pc molecules will be used "as-is" in an organic-based route. Here, the fundamental properties of metal phthalocyanine (MPc) thin films grown by vacuum sublimation will be studied. This will encompass the mechanisms for monolayer formation on silicon substrates (which are of importance for assessing potential device performance) and how the unpaired spins of the metal species interact with each other in thicker films. Since possessing an unpaired spin is a requirement for spintronic applications, the discussions will be based on the specific example of copper phthalocyanine (CuPc) thin films, although these could readily be extended to other paramagnetic metal Pc molecules. This work will involve the characterisation of a selection of CuPc films in terms of their topography, crystallographic order and optical absorption properties, in addition to assessing their spin-spin interactions by electron paramagnetic resonance. The fundamental growth studies will be presented in Chapter 3, whilst the spin interactions will be discussed in Chapter 4.

The second route (Chapter 5) will involve the use of MPc molecules as precursors in the development of a new technique for the introduction of metal species containing unpaired electrons into silicon, for applications in inorganic spintronics and quantum computing. Here, the natural self-assembly of MPc molecules to form ordered thin films on passivated silicon surfaces will be used to control the initial separation of metal atoms, which after being subjected to irradiation from an ultra-violet (UV) excimer lamp will be released from the organic framework and will diffuse into the silicon substrate. This method is particularly advantageous since it could be used to introduce a variety of metal species into silicon with the potential to control their spatial distribution, whilst it could be easily incorporated into current device manufacturing processes.

The remainder of this chapter will comprise an introduction to Pc molecules in Section 1.1 and an overview of the properties and morphology of thin (Section 1.2.1) and ultra-thin (Section 1.2.2) films, in particular those of CuPc films. Following this, a brief

overview of recent developments in inorganic and organic spintronics will be presented in Section 1.3 with a specific emphasis on silicon-based devices and potential applications of Pc films. This section will also include a summary of current methods for introducing dopants into silicon and their diffusional properties therein, which will be of relevance to the work described in Chapter 5.

1.1 PHTHALOCYANINE MOLECULES

The phthalocyanines were first discovered in 1907 when a blue by-product (which is now known as metal-free phthalocyanine, H_2Pc) was reported from a reaction of phthalimide and acetic acid [12]. This was followed by the first accidental synthesis of copper phthalocyanine (CuPc) in 1927, which was remarked upon for its chemical stability [13]. However, it was not until their discovery at Scottish Dyes Ltd (who later became ICI) that phthalocyanines were synthesised for applications as pigments, with CuPc known as Monastral Blue. Since their discovery their range of applications has been dramatically increased beyond that as industrial dyes, as will be discussed shortly.

The chemical structures of the copper and metal-free phthalocyanine molecules (empirical formulae of $C_{32}H_{16}CuN_8$ and $C_{32}H_{18}N_8$ respectively) are shown in Figure 1.1. These molecules comprise four iminoisoindoline units that make up the phthalocyanato ring, commonly abbreviated as Pc^{2-}, and a central cation. The molecules are approximately 1.4 nm in diameter [14], as indicated in the figure. The Pc^{2-} ligand is largely delocalised, owing to the π-orbitals arising from the unsaturated C-C bonds. The central cavity is occupied by either two H^+ ions or a metal ion bound to the innermost N atoms of the Pc ring. In the former case, the two H^+ ions are bound to opposite N atoms (for H_2Pc, Figure 1.1(b)) whilst metal ions are effectively equally bound to all four central N atoms (due to the delocalised nature of the molecule), as shown for CuPc in Figure 1.1(a). This leads to two-fold (D_{2h}) or four-fold (D_{4h}) symmetries respectively. Since the organic ligand is in a 2- oxidation state, it is most common for small cations such as Cu^{2+}, Zn^{2+}, Fe^{2+}, Ni^{2+}, Co^{2+} and Pt^{2+}, or for two H^+ ions (in the case of H_2Pc) to be accommodated into the molecule and these form planar structures. However, MPc

molecules containing larger cations such as Pb^{2+} can also be synthesised; these are not planar and in this case the metal sits just out of the plane of the Pc ligand. In total, over 70 different MPc species have been synthesised with oxidation states of the central metal ranging from 1+ to 5+, which is sometimes facilitated by the addition of axial substituents to the metal (such as Cl) or by sandwiching the metal between two Pc ligands [1].

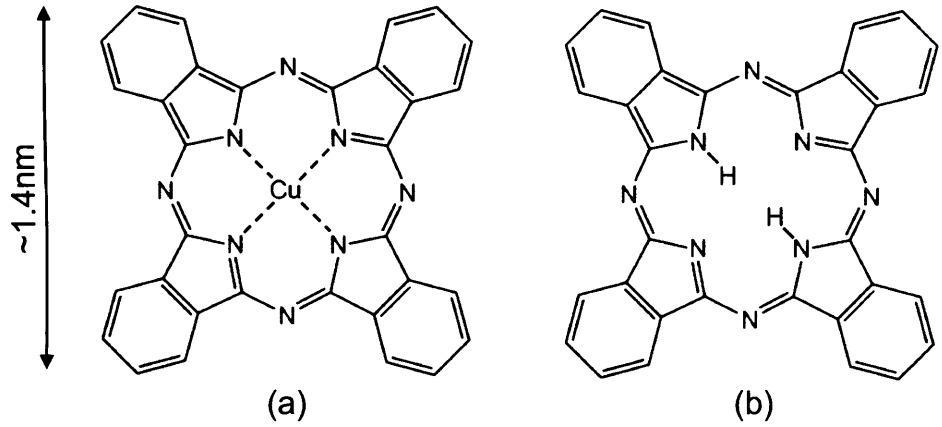

Figure 1.1. *The chemical structures of (a) CuPc and (b) H_2Pc molecules.*

The properties of phthalocyanines can be readily modified through the addition of chemical substituents. For example, replacing the outer hydrogen atoms with Cl shifts the absorption spectrum of CuPc giving rise to a bright green colour. Alternatively, by adding four extra benzene rings to those of the Pc ligand to form naphthalocyanine the optical absorption is redshifted [1]. Further modifications to the Pc ring can also be performed, whilst it is also possible chemically join them to form dimers and higher order oligmers [15–17].

Currently, the widest use of metal phthalocyanines are as industrial dyes and pigments, for example CuPc is used on the £5 note. In addition, Pc films are semiconductors (charge carriers can migrate through the material due to π-π intermolecular interactions) with a band gap of ~1.8 eV [1]. As a result, they are

members of a family of organic molecules that are subject to intense research for use in organic electronics. Although this field is relatively immature in comparison to silicon-based technology, organic devices would be cheaper and offer the possibility for flexible, printable devices [7, 8, 18]. A common application of phthalocyanine thin films is in field-effect transistor based devices [4, 5] which can be used for sensing dangerous gases [19–23]. Other important applications of Pc molecules combine their semiconducting and optical properties for use as solar cells and organic light emitting devices (OLEDs). Here they are often used as donors, for example in CuPc/C_{60} solar cell devices which have been reported to give efficiencies of up to 5% [6, 24], or as hole injecting layers in OLEDs [25, 26].

1.2 COPPER PHTHALOCYANINE THIN FILMS

In the first half of this section (Section 1.2.1) the structural, optical and topographic properties of CuPc thin films will be discussed. Following this, an introduction to the formation of ultra-thin CuPc films will be given (Section 1.2.2) with a specific focus on the initial stages of growth on Si substrates, as will be studied in Chapter 3.

1.2.1 Bulk CuPc Thin Films

Many different polymorphs of CuPc molecules have been discovered. This section will comprise an introduction to the two most common bulk crystallographic phases, namely the α- and β- phases, since these are the phases that are formed as a result of vacuum sublimation and so have been studied here. Following this, an overview of the spectroscopic, vibrational and topographic properties of CuPc films will be given.

Crystal Phases of Pc Films

In the solid state, Pc molecules naturally self-assemble to form crystalline arrays. Owing to their planar structure, they stack in a face-to-face geometry, forming columns. Within the columns, the molecules are weakly bound via both van der Waals forces and π–π

interactions [1], the latter being a non-covalent interaction due to overlapping of neighbouring π-orbitals. Since the intermolecular interactions are relatively weak, multiple molecular arrangements (for example, the tilt angle between the molecules and their stacking direction) are possible for differing growth conditions, and hence different molecular phases can be observed.

In general, it is the molecular tilt angle with respect to the stacking direction and the separation between neighbouring molecules within the column which define the Pc phase, with up to 10 phases of CuPc currently known [27–31]. The two most common crystallographic phases of Pc's are known as the α- and β- phases, in which the molecules are tilted at angles of ~25° and ~45° with respect to their stacking directions respectively, as shown in Figure 1.2 (slight variations in these angles are observed for the different Pc species). For thin films grown at temperatures close to room temperature, the α-phase is formed, whilst for higher temperatures (or after post-deposition annealing) the more thermodynamically stable β-phase is formed [32–35].

Figure 1.2. *The molecular orientation of CuPc in (a) the β-phase projected along the c-axis [36] and the α-phase as predicted by (b) Ashida [27] and (c) Hoshino [28] models, projected down the a-axis.*

The molecular arrangement of β-phase CuPc [36] is shown in Figure 1.2(a). Here, the CuPc molecules are tilted at an angle of 45.9° with a separation of 3.3 Å between neighbouring molecules (the face-to-face distance). In the case of α-phase CuPc, two commonly cited proposed crystallographic orientations can be found; these will be referred to as the Ashida [27] and Hoshino [28] models, as depicted in Figures 1.2(b) and (c) respectively. The unit cell parameters of the α-phase Ashida and Hoshino models are summarised in Table 1.1, along with those for β-phase CuPc. Similar molecular tilt angles are predicted by both models, however the tilt direction of neighbouring columns is different in each case; Ashida *et al.* predict a herringbone arrangement whilst the model of Hoshino *et al.* comprises a brickstone pattern. Since the strongest molecular interactions are anticipated to occur within the molecular chain (rather than between molecules of neighbouring columns) this difference in packing would not have a significant effect on the physical properties of the film (the inter- and intra-column interactions will be discussed in Chapter 4). Significantly, a smaller tilt angle is observed for α-phase CuPc with respect to that of β-phase; this gives rise to different properties, such as their absorption spectra [30], topography [32, 34] and magnetic signature [37].

Polymorph	**β-phase**	**α-phase**	
Model	**Brown *et al.* [36]**	**Ashida *et al.* [27]**	**Hoshino *et al.* [28]**
Cell Type	Monoclinic	Monoclinic	Triclinic
a (Å)	19.4	25.9	12.9
b (Å)	4.79	3.79	3.77
c (Å)	14.6	23.9	12.1
α (°)	90.0	90.0	96.2
β (°)	120	90.4	90.6
γ (°)	90.0	90.0	90.3
Z	2	4	1

Table 1.1. *A summary of the unit cell parameters of α- and β-phase CuPc.*

Optical Properties of CuPc films

As was described in Section 1.1, CuPc has a bright blue colour, owing to its strong optical absorption in the visible region. Therefore, a common method for characterising CuPc films is to study their electronic absorption spectra (also known as UV/vis).

The transitions responsible for the optical properties of CuPc solutions are summarised in Figure 1.3(a). Absorption events arise from excitation of electrons in a π-π^* transition from the highest occupied molecular orbital (HOMO) singlet level (the ground state, S_0) of the Pc ligand to unoccupied singlet levels such as the lowest unoccupied molecular orbital (LUMO, S_1) [1, 38]. This transition, known as Q-band absorption, typically requires energies of ~1.8–2.0 eV and results in the absorption of red photons, giving rise to the famous blue colour of CuPc molecules. Transitions to higher energy unoccupied singlet levels, such as the LUMO+1 (S_2), occur towards the UV and these are known as B-band or Soret absorption events.

Figure 1.3. *(a) The energy levels (including vibrational levels) associated with electronic absorption transitions of CuPc in the visible region. Arrows directed upwards represent absorption events, whilst downwards arrows denote non-radiative (dotted) or emission (solid) paths. The thickness of the solid arrows serves as a guide to the relative intensities of the transitions. (b) A comparison of the Q-band electronic absorption spectra of CuPc in solution (dotted line) and an α-phase CuPc film (solid line) (from [30]).*

In the case of CuPc, emission is dominated by non-radiative decays. The fluorescence (singlet-singlet emission) is quenched by the paramagnetic Cu centre which promotes conversion to the triplet manifold via inter-system crossing. This effect leads to a weak phosphorescent (triplet to singlet) yield of $\sim 10^{-3}$ for CuPc solutions [38, 39]. It should be noted that fluorescence is generally observed for other MPc molecules. For example, H_2Pc has a relatively high fluorescence yield of 0.7 in solution, however it does not phosphoresce [39] (there are no unpaired electron spins to enhance the singlet-to-triplet transition). The quantum yields are reduced in thin films due to enhanced non-radiative decays facilitated by lattice phonons; the fluorescence yield of H_2Pc films decreases to $\sim 2 \times 10^{-4}$ whilst the phosphorescence of CuPc cannot be easily detected [40].

The electronic absorption spectra of CuPc in solution and as an α-phase film are compared in Figure 1.3(b). As seen from the figure, the electronic absorption spectrum of thin CuPc films is noticeably different to that of the solution. A single intense, sharp absorption maximum is observed for dilute CuPc solutions at ~690 nm and this is accompanied by lower intensity peaks due to vibronic transitions. The film spectra are much broader due to scattering of phonons in the lattice and interactions between neighbouring molecules [30]. In addition, the Q-band is observed to split into two peaks; several interpretations of this splitting have been offered. Firstly, whilst the peak at higher wavelengths is slightly shifted from that of the monomer (solution) spectrum, it can still be attributed to single-molecule behaviour [41]. However, that at shorter wavelengths is observed when molecular aggregates (such as dimers) are formed [42]. When a Pc molecule absorbs a photon, an electron is excited to a higher energy level and so an electron-hole pair (exciton) is created. Therefore, an alternative explanation is that the splitting and shifting of the absorption spectrum with respect to that observed in solution is due to exciton splitting of the LUMO level (Davydov splitting [43]) [30, 44]. In addition, other interpretations such as the higher energy (shorter wavelength) peak being a vibrational mode of the 695 nm peak have been proposed [45].

The observed shifts and relative intensities of the peaks are dependent on the molecular packing within the phthalocyanine film, and so the absorption spectra can be

used to distinguish between different crystallographic phases [30]. As has already been described, the two most common arrangements of CuPc are the α- and β- phases; the α-phase is known to absorb at ~695 nm and ~623 nm, whilst the β-phase absorbs at ~719 nm and ~645 nm, with different relative intensities of the two peaks for the two crystallographic phases [30, 46].

In addition to the main optical absorption bands, important information about the MPc molecules can also be gained from their vibrational spectra, which will be studied here by Raman spectroscopy. An example of the Raman signature of an α-phase CuPc film is shown in Figure 1.4(a). As will be discussed in Section 2.7, Raman signals arise from optical excitation to 'virtual' energy levels, leading to emission lines that are slightly shifted in energy with respect to the excitation source. The energy difference is known as the Raman Shift and is equivalent to the energy of a vibrational mode. Owing to its four-fold symmetry, CuPc has many vibrational modes that are symmetric about the molecular plane. The main vibrational peaks observed between ~600 cm^{-1} and 1700 cm^{-1} are due to the breathing modes of CuPc, whilst those at higher energies arise from the stretching of sub-groups within the Pc molecule (for example C-H) [47]. As an example, a vector diagram of the molecular breathing mode responsible for the 1530 cm^{-1} peak is shown in Figure 1.4(b).

Figure 1.4. *(a) Raman spectrum of α-phase CuPc (λ_{exc}=514.5 nm). (b) The molecular stretching mode responsible for the 1530 cm^{-1} vibration (both adapted from [48]).*

Morphology of CuPc Thin Films

Different morphologies are observed for the various CuPc phases, with films, crystallites or nanowires formed [1, 49]. The topographies of bulk α- and β-phase CuPc films, as measured by atomic force microscopy, are shown in Figure 1.5. Small, spherical crystallites are formed in the α-phase, whilst long needle-like structures are observed for β-phase CuPc. The morphology of the films is highly dependent on the crystallographic phase and therefore on the temperature at which the film was grown at (or annealed to post-deposition) [32–34].

Figure 1.5. *The morphology of (a) α-phase and (b) β-phase CuPc films (adapted from [37]). Small spherical crystallites are observed for the α-phase, whilst the β-phase film shows long, narrow features.*

Each crystallite consists of a single crystallographic domain. Calculations performed by Iwatsu have shown that the α-phase is more thermodynamically stable for small crystallites, whilst for larger domain sizes the β-phase is more stable [29]. These authors suggest that the α- to β-phase transition occurs when the mean potential energy per molecule of the two crystallites are equal; simulations suggest a critical size of ~2 x 10^4 molecules which for a spherical α-phase crystallite would correspond to a diameter of ~28 nm.

1.2.2 Ultra-Thin CuPc Films on Silicon

The study of thin and ultra-thin films of CuPc on Si surfaces is of great importance for many applications, since the properties of any devices which incorporate neighbouring layers of CuPc and Si will be affected by the interface region. Of particular significance is the orientation of the molecules with respect to the substrate plane, as will be discussed in this section.

Many studies have been performed on the growth of ultra-thin layers of CuPc on a variety of substrates, with different morphologies observed. In general, the molecular orientation is governed by the relative strengths of the interactions between the molecule and substrate, and that between the molecules with each other [50]. For strong molecule-substrate interactions CuPc molecules are observed to lie parallel to the substrate, whereas if this interaction is weak, the molecules preferentially form stacks in which each molecule is aligned perpendicular to the substrate plane. These two scenarios are summarised in Figure 1.6.

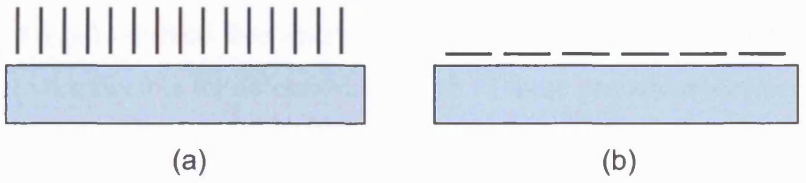

Figure 1.6. *The relative orientations of CuPc molecular monolayers (shown side-on as black lines) upon (a) weakly (b) strongly interacting substrates.*

When CuPc is deposited onto very strongly interacting substrates, such as clean Si surfaces, the molecules are oriented with their molecular planes parallel to the substrate [14, 51–53]. However, since the molecules are often pinned at or close to the point where they first contact the surface and are not free to migrate across it, these layers are often disordered, as will be discussed in further detail shortly. For moderately interacting substrates, highly ordered arrays of flat-lying CuPc molecules are formed (Figure 1.6(b)).

Such arrangements are observed on Au(111) [54–56], Cu(100) [57], III-V semiconductors such as InAs and InSb [58], highly oriented pyrolytic graphite (HOPG) [59, 60] and MoS_2 [59]. In addition, studies have shown that two different species of MPc molecules (for example CuPc and CoPc) can be co-deposited onto Au(111) to form ordered mixtures of the two species [55, 56]. For weakly interacting substrates, such as those in which an inert passivating layer is inserted between the substrate and CuPc molecules (as will be described shortly), or rough and/or amorphous substrates, the molecules are observed to align perpendicular to the substrate (Figure 1.6(a)). This has been attributed to stronger intermolecular rather than molecule-substrate interactions [50, 61].

Types of growth mode

Commonly, when adsorbates (such as CuPc) are deposited to form ultra-thin films, the morphology will be characterised by one of three different growth modes, namely Volmer-Weber, Stranski-Krastanov or Frank-van-der-Merwe [62]. These three growth modes are summarised in Figure 1.7. The relative strengths of the surface free energy of the molecule (γ_{CuPc}), surface free energy of the substrate (γ_{sub}) and the interface free energy (γ_{int}) are responsible for determining which of these growth modes occur.

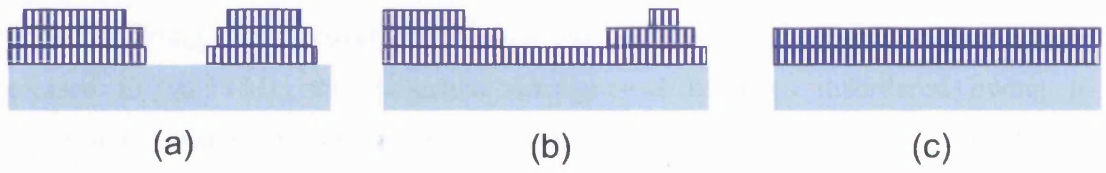

Figure 1.7. *Common growth modes for low coverages of adsorbates. (a) Volmer-Weber, (b) Stranski-Krastanov and (c) Frank-van-der-Merwe.*

If $\gamma_{sub} < \gamma_{CuPc} + \gamma_{int}$, then it is energetically favourable for the contact area between the molecular layer and substrate to be a minimum, and so three dimensional islands are observed. This is known as a Volmer-Weber growth mode, as depicted in Figure 1.7(a). Alternatively, if $\gamma_{sub} \geq \gamma_{CuPc} + \gamma_{int}$, a layer-by-layer growth is preferable and is referred to as a Frank-van-der-Merwe type growth (Figure 1.7(c)). However, in some cases the free energy of the molecule (γ_{CuPc}) can increase as a function of film thickness due to strain effects arising from a lattice mismatch; in this case $\gamma_{sub} \geq \gamma_{CuPc} + \gamma_{int}$ for the first few layers, but for higher order layers $\gamma_{sub} < \gamma_{CuPc} + \gamma_{int}$. As a result, the first few layers grow in a homogeneous manner, but for higher order layers, island growth occurs. This is known as a Stranski-Krastanov growth mode, as shown in Figure 1.7(b).

CuPc Growth on Si(111)

The first studies of CuPc growth on clean (i.e. unpassivated) Si(111) were performed by Kanai *et al.* [53]. Here, at very low molecular coverages, CuPc lie flat on the clean Si(111) surface. This is similar to what is observed for other MPc molecules on this substrate [51]. Interestingly an unusual sample bias dependence of the images was reported, wherein the molecules appear bright above 2.0 V and below –0.6 V, whilst at intermediate bias voltages the molecules are dark or transparent. This cannot be explained by the bias dependence of the substrate and instead has been attributed to a strong interaction between the Si(111) and CuPc molecules, as observed for other small organic molecules on clean Si surfaces [63]. A similar molecular orientation has been reported by Wang *et al.* at coverages of ~0.33 ML, however, as the molecular coverage is increased to ~0.93 ML the molecular arrangement becomes disordered owing to competition between flat-lying and upright-standing orientations [64]. At higher molecular coverages these authors observed that the system re-established order, with the molecules aligned perpendicular to the substrate, as observed for thicker films [50, 65, 66]. These observations were explained in terms of the relative substrate-molecule versus molecule-molecule interactions, as outlined previously.

Whilst highly ordered, close-packed monolayers of CoPc can be grown on Ag terminated Si(111) surfaces [67], similar reports for CuPc on passivated Si(111) surfaces

have not been found. A flat-lying molecular orientation of CuPc on atomically flat H passivated Si(111) (Si(111):H) has been reported by Nakamura *et al.*, although this configuration is not uniform across the surface [68]. In this work, large, isolated single crystals were formed at elevated substrate temperatures (>140°C) that were up to 100 nm in height and comprised molecules lying parallel to the substrate, in contrast to the growth reported beyond monolayer coverage on clean Si(111). These authors noted that a low roughness of the initial substrate is crucial to the molecular orientation, with an upright standing molecular geometry observed on rough surfaces.

In other studies of CuPc on Si(111):H, a molecular rotation as a function of thickness has been observed within the first 15 nm [69]. However, these findings were assessed using spectroscopic rather than topographic techniques, and cannot be directly compared to the result of Nakamura *et al.*, since the initial surface roughness is not known (it should be noted that in these studies the substrates were prepared by HF treatment, which is known to result in an increased surface roughness). In addition, a preferential one-dimensional growth direction of CuPc on Si(111):H can be obtained on vicinal surfaces (cut at a slight offset from the natural cleavage plane resulting in a high density of terraces) [70]. Here, features are observed to run parallel to the step edges, although it is not clear whether the molecules are aligned parallel or perpendicular to the substrate.

Si(100) Surface Reconstruction

Some clean surfaces, including silicon, germanium, gold and platinum undergo a surface reconstruction [71]. In an infinite lattice the atomic arrangements are defined by the bulk lattice parameters. However, for the surface layer, dangling bonds are present since there are no other Si atoms above to bind to. This leads to a different arrangement from the bulk, although a two-dimensional array is still formed. Surfaces are characterised most frequently by relating the surface Bravais lattice to that of the bulk substrate. This is usually achieved by either comparing the primitive translation vectors of the substrate and surface (a method proposed by Park and Madden in 1968), or by using the ratios of the lengths of the two meshes along with the angle of rotation between them (as was

proposed by Wood in 1964). The latter is the most commonly used notation and so this will be followed here, with the structure denoted as outlined in Equation 1.1.

$$X\{hkl\}(p \times q)R\phi° - A \qquad [1.1]$$

In this notation, X represents the substrate material, $\{hkl\}$ denotes the surface plane, Φ is the angle of rotation between the surface and bulk crystal meshes and A is the surface material (if not the same as the bulk substrate), for example an absorbate. The values of p and q are calculated from $|\vec{a}'| = p|\vec{a}|$ and $|\vec{b}'| = q|\vec{b}|$ where $\vec{a}$ and $\vec{b}$ are primitive translation vectors of the unreconstructed substrate and $\vec{a}'$ and $\vec{b}'$ are those of the surface.

The reconstruction of the silicon surface depends on the direction through which the wafer is cleaved, for example the Si(100) surface gives a (2 x 1) reconstruction whilst Si(111) has a (7 x 7) reconstruction. The arrangement of the bulk and surface atoms of the Si(100) surface are shown in Figure 1.8, where the surface atoms (orange) are seen to form pairs, known as dimer rows, that run along the [0 $\bar{1}$ 1] direction. The dimer rows are 0.23 nm wide, with a separation of 0.76 nm between neighbouring rows, whilst the atomic spacing along the direction of the dimer rows is 0.38 nm [72].

Figure 1.8. *Reconstruction of the Si(100) surface leading to a (2 x 1) pattern comprising dimer rows (surface atoms shown in orange) from [73].*

CuPc Growth on clean Si(100)

The deposition of very low coverages of CuPc onto clean Si(100) results in a random distribution of molecular features across the surface, where in all cases the isolated molecules are observed to lie parallel to the substrate surface [14, 52, 53]. Three different molecular orientations with respect to the Si dimer rows are observed, the most common of which is when the centre of the CuPc molecule is directly above the Si dimer rows and the four lobes of the molecules are readily resolved [52]. In this arrangement a strong interaction is anticipated between the central Cu atom and the Si surface via the dimer row dangling bonds, as has also been observed for $CuF_{16}Pc$ (hexadecafluoroCuPc) on this surface [74]. For the other two possible orientations of CuPc on Si(100) the centre is positioned between Si dimer rows, with the molecules forming two different angles with respect to the [011] directions [52]. In these cases, the molecules interact with the Si substrate via the Pc ligand.

As the molecular coverage is increased to multilayers, the molecules rotate to form an upright geometry [14, 75], in a similar manner to that described for the clean Si(111) surface. Studies of 40 nm thick CuPc films performed by Nonaka *et al.* show a similar behaviour to bulk α-phase films, although preferential growth is observed along the [011] directions [75]. This suggests that the substrate plays a role in the growth morphology even for thicker films. Here, the authors used EPR to measure the molecular tilt angle with respect to the substrate directions and found this to be $21 \pm 3°$, which is comparable to that observed in the bulk CuPc phases (Figure 1.2).

CuPc Growth on passivated Si(100)

Studies of 20 nm thick CuPc film on Si(100):H performed by Nakamura *et al.* have shown that the CuPc molecules align perpendicular to the substrate, stacking to form linear structures that run along the [011] directions of the Si lattice [76, 77]. The height of each CuPc layer was determined to be 11.8 ± 0.1 Å, with a separation of $\sim 13.5 \pm 0.5$ Å between neighbouring molecular columns. Within the columns, the authors suggest that

the molecules are slightly rotated about their axes such that one benzene ring of each molecule protrudes from the top of the film, giving rise to a textured column topography [76]. These studies have led to the proposal of a model of the orientation of the CuPc molecules with respect to the Si substrate, wherein the molecules stack at an angle of 17° with respect to the [011] direction. It should be noted that the work that will be discussed in Chapter 3 contains the first studies of (sub-) monolayer coverage of CuPc on passivated Si(100) surfaces, and offers a more detailed discussion of the molecular arrangement with respect to this substrate [72].

Since Si dangling bonds provide highly reactive sites, as demonstrated by the relative molecular orientations on the clean versus passivated Si surface, these can be used to control molecular adsorption and to generate patterns [78]. Hersam *et al.* have used in-situ feedback-controlled lithography to selectively remove H atoms from a Si(100):H surface, exposing Si dangling bonds [79, 80], onto which very low coverages of CuPc are deposited. The authors report that CuPc molecules preferentially bond to the pre-patterned sites, where they are pinned by the exposed silicon dangling bonds with their molecular planes parallel to the substrate. Two different molecular appearances are reported; the most frequent arrangement is when the molecules are pinned via their central Cu atom, resulting in circular features of ~16 Å diameter. However, larger (~40 Å) diameter features are also observed and these have been interpreted as molecules that are bound via an outer benzene ring; these molecules rotate in-plane about this point, giving rise to their larger apparent diameter. These studies are of a similar nature to those observed on the clean Si(100) surface and demonstrate that a much stronger interaction occurs between the CuPc molecules and Si dangling bonds, whilst interactions with the passivated surface are weak. This will be important for the discussion presented in Section 3.1.1.

1.3 APPLICATIONS

This section will summarise some recent developments in the fields of inorganic and organic spintronics (Sections 1.3.1 and 1.3.2 respectively), along with providing an introduction to quantum computing in Section 1.3.3. In particular, the discussions will be focussed on those developments most relevant to the work that will be described in Chapters 3–5, namely silicon-based inorganic spintronics/quantum computing and potential applications of Pc films in organic spintronics. Following this, an overview of doping techniques and the diffusion of dopants in silicon will be presented in Section 1.3.4, which is of relevance to the content of Chapter 5.

1.3.1 Inorganic Spintronics

Conventional electronic devices have progressively decreased in size, as predicted by Moore's law, which states that the number of transistors placed on an integrated circuit is expected to double every two years [9]. However, it is widely accepted that this reduction in device dimensions is not sustainable using current silicon technologies and that new routes must be sought [81]. Traditionally, the charge of the electron is used to transfer information in conventional electronic devices, whilst the spins of ferromagnetic domains are used to store information in magnetic recording media. Spintronics ("spin transport electronics") is a fast-growing field which combines these properties by utilising the magnetic moment of an electron, i.e. its spin, for device applications. Spintronic devices offer the potential for non-volatility (the ability to store information when the power is switched off) and increased data processing speed, combined with decreased dimensions and power consumption [2, 3, 82–84].

Overview of Spintronic Devices

Although the phenomenon of magnetism has been used for centuries, and the quantum mechanical property of spin has been known for over 50 years, it wasn't until the

discovery of giant magnetoresistance (GMR) in the late 1980's* [85, 86] that it was realised that these two properties could be combined for device applications. GMR devices comprise alternating layers of ferromagnetic and non-magnetic material, whilst their electronic transport resistance is dependent on the relative magnetic moments of the ferromagnetic layers (this is higher when successive layers are of opposite magnetisation direction). The simplest type of GMR structure is the spin valve, as shown in Figure 1.9, which consists of two ferromagnetic layers sandwiching a non-magnetic metallic layer. The magnetisation direction of one of the ferromagnetic layers is pinned, often through placing an antiferromagnetic layer next to it (as shown in the figure), whilst the other is of a relatively low coercivity and so can be changed by applying a small in-plane magnetic field to the device.

Figure 1.9. *(a) A schematic of an inorganic spin valve device (adapted from [2]). (b) The path of electrons through a spin valve, which is highly dependent on their spin orientation with respect to the ferromagnetic layers (adapted from [84]).*

The mean free path of electrons with their spin aligned parallel to the magnetisation direction of the ferromagnetic layer will be considerably greater than that

* The 2007 Nobel Prize for Physics was awarded to Fert and Grunberg for the discovery of GMR.

of electrons with antiparallel spin [2, 11]. If the thickness of the ferromagnetic layers is intermediate between the mean free paths of these two electron spins, then electrons which have their spin direction aligned parallel to the magnetisation direction will pass through easily, whilst those of opposite spin will be significantly scattered. The relative directions of the two magnetic layers have a large effect on the paths of the electrons, and therefore on the resistance of the device, as shown in Figure 1.9(b). Specifically, when the magnetic layers are aligned antiparallel to each other, both electrons will undergo multiple collisions in one of the layers. However, for two parallel magnetisation directions the electrons whose spin are aligned parallel to the ferromagnetic layers will pass through the device with negligible scattering, whilst those of opposite spin will undergo many collisions [84]. A large resistance will be detected when the layers are antialigned due to the high number of scattering events. In contrast, when the magnetisation directions are the same, those electrons of parallel spin can easily pass through the device giving rise to a low resistance (note that those of opposite spin alignment will be scattered). GMR devices based on this principle are used commercially as magnetic read heads for hard drives [2].

Another important device in spintronics is the magnetic tunnel junction. This device is very similar to the spin valve but with the non-magnetic spacer layer replaced by a non-magnetic insulator. This forces the electrons to tunnel between the magnetic layers, which is only possible if the magnetisation directions of the two ferromagnetic layers are aligned. Early magnetic tunnel junctions, developed in the mid 1990's, often used an amorphous Al_2O_3 insulating layer [87, 88]. However, the efficiencies of these devices have subsequently been improved though the use of a single-crystal MgO barrier [89]. The main advantages of these devices is that they generally require smaller magnetic fields than that needed for spin valves and display larger changes in resistance [2].

The development of the magnetic tunnel junction opened up the possibility of storing data within the orientation of the magnetization direction of the non-pinned ferromagnetic layer to provide magnetic random access memory (MRAM) [90]. Here, a cross-network of pinned and non-pinned layers are used to store information at the cross-over points which form magnetic tunnel junctions, producing a two-dimensional array of

binary 1's and 0's (defined by the relative magnetisations of the layers). MRAM is non-volatile, has faster write times than conventional silicon-based read only memory, and in theory can be re-written an infinite number of times [2, 84].

Integration with Silicon Technology

Although there have been many breakthroughs in the field of spintronics, one of the major hurdles remaining in the goal to succeed current electronic data storage is to integrate spintronic functionalities with silicon. Significant progress has been made in injecting, transporting and manipulating spin into III-V semiconductors such as GaAs [91–93], along with the development of detectors such as the spin-LED [94, 95]. One of the main reasons for this success was the discovery in the late 1990's of high temperature ferromagnetism in GaMnAs containing only ~5% of Mn [96], an early dilute magnetic semiconductor (DMS). More recently, it has been shown that ordered Mn arrays in GaAs produce an even higher Curie temperature [97]. However, it is highly desirable to incorporate spintronics with silicon-based devices; not only will this take advantage of the advanced status of silicon technologies, but it has also been predicted that in silicon spin polarisation will be long-lived and have a larger spin transport length than that found in compound semiconductors [3].

More specifically, one of the major obstacles in silicon-based spintronics is the difficulty in injecting a spin-polarised current into silicon. Although the current can be readily spin-polarised after passing through a ferromagnetic metal, when placed in contact with a semiconductor there will be a large voltage drop (due to the significantly lower resistance in the semiconductor). This leads to the formation of a Schottky barrier [98], and so the spin polarisation will be lost; this is known as the conductivity mismatch problem [99]. Recently though, significant progress in overcoming this problem has been made through the injection of "hot" electrons across the device through undoped Si [100]. An alternative approach is to insert an Al_2O_3 layer between the ferromagnetic metal and silicon. This provides a spin-dependent tunnel barrier with tuneable resistance to reduce the size of the Schottky barrier [101, 102], permitting the spin-polarised current to be injected into silicon [103].

Another approach to overcome this mismatch is to replace the ferromagnetic metal with a ferromagnetic silicon layer, in a similar method to that described for Mn-doped III-V dilute magnetic semiconductors. The report of Bolduc *et al.* of room temperature ferromagnetism in ion-implanted Mn in silicon [104] has sparked much interest in this area [105, 106]. Theoretical calculations have shown that substitutional Mn is responsible for the ferromagnetism [107, 108]. Recent reports also suggest that interstitial Mn in Si, which requires less energy to form than substitutional, may also lead to magnetic order, although each Mn is of slightly lower magnetic moment (2.46 μ_B for interstitial compared to 3.14 μ_B for substitutional) [109, 110]. However, it is well known that ion-implantation induces damage into the silicon, creating defects (as will be discussed in Section 1.3.4). In addition, it has been shown that the magnetism arises largely from Mn atoms not trapped at these defect sites [111], suggesting that other methods for the introduction of Mn into silicon, such as that described in Chapter 5, may lead to further advances in this field.

1.3.2 Organic Spintronics

Following the recent development of inorganic spintronics, a fast-emerging field is that of organic spintronics, which utilises the electronic and magnetic properties of small organic molecules and polymers [10, 112]. As has already been mentioned, some of the major advantages of organics for device applications are that they are cheap, that molecules are easily adapted to tailor their properties and that they could produce flexible devices [7]. In addition, they possess weak spin-orbit and hyperfine interactions, which should lead to the electron spin polarisation direction being long-lived (i.e. long spin-coherence times due to low coupling) [10], whilst interactions could be switched optically [113].

Many organic-based routes are currently being explored, with magnetoresistance discovered in a range of organic molecules [114, 115]. Bulk organic systems such as graphene have shown that spin polarisation can be maintained over lengths of up to 1.5 μm [116], however spin relaxation times in these systems are generally short [10]. Perhaps the most extensive research to date has been focussed on the preparation of

organic spin-valve devices [117, 118] (an overview of these will be given shortly). An important breakthrough was made by the formation of molecular bridges between inorganic quantum dots, for which a spin transfer efficiency of ~20% was observed through conjugated molecules via their π orbitals [119]. In an approach based on the inorganic tunnel junction (Section 1.3.1), organic (as opposed to inorganic) spacer layers have been grown between two nickel layers; these permit spin-polarised transport resulting in magnetoresistance values of ~16% [120]. In addition, recent work has also been performed on the use of single magnetic organic molecules for spintronic applications, as will be described shortly.

Organic Spin Valves

Since the field of organic spintronics is so new, much of the work so far has been to demonstrate that organic materials can conserve spin polarisation. For this, the most common approach has been to focus on devices analogous to the spin valves described in Section 1.3.1. In these structures, an organic layer is sandwiched between two ferromagnetic metals, commonly with different coercive fields so that they can be aligned parallel or antiparallel depending on the applied magnetic field (generally, neither of the magnetisation directions are fixed, in contrast to the case of the inorganic spin valve) [10, 11]. Theoretical calculations have shown that such devices can give large magnetoresistance ratios and that by tailoring the nature of organic species the spin-polarised current will tunnel or flow through molecules [121].

The first experimental demonstration of an organic spin valve was in 2002 by Dediu *et al.*. These authors demonstrated that devices made from sexithienyl, when placed between two colossal magnetoresistance manganite layers ($La_{0.7}Sr_{0.3}MnO_3$, LSMO), show a magnetoresistance of up to 30% and spin polarisation retention over distances of up to 200 nm within the organic layer at room temperature [117]. Following this, devices containing amorphous layers of trishydroxyquinoline aluminium (Alq_3) between LSMO and Co electrodes were shown to have a low temperature magnetoresistance of 40% at low temperatures [118], whilst those containing a poly-3-hexylthiophene layer show magnetoresistance of ~80% at 5 K [122]. Recently, the Alq_3

based devices have been shown to posses the ability to store charge whilst the voltage is off and survive numerous write-read-erase cycles (up to 600 over more than 6000 s) opening up new possibilities for non-volatile data storage [123]. However, it has also been reported that ultra-thin layers of Alq_3 placed between these electrodes (with an additional Al_2O_3 layer between the organic and cobalt) transmit spin-polarised current through a tunnelling mechanism [124], whilst other authors were unable to detect any magnetoresistance [125]. It is apparent that further studies on the Alq_3 based devices and the role of interfaces are required. In addition, although the spin transport through thicker films is thought to rely on diffusion, the exact mechanism for this is not currently understood [10, 11].

Single Molecule Magnets

Of recent interest is the use of single molecule magnets to create molecular spin transistors and molecular spin valves [113, 126]. Typically, these are molecules containing one or more transition metal atoms that are bound to inorganic source and drain electrodes via their organic ligand. For example, molecules containing clusters of Mn atoms (typically 6-12 Mn) have shown blocking temperatures of up to ~4.5 K and spin retention up to temperatures of 86 K [127, 128]. In an analogous manner to the spin valve, when placed between two ferromagnetic contacts, these molecules form devices that show enhanced electrical conductance when the molecular magnetisation is aligned parallel to the ferromagnetic electrodes, and this is drastically reduced when not aligned [113, 129]. This suggests that only spin aligned parallel to the molecular magnetisation can pass through the device, leading to "giant" spin amplification and permitting the magnetisation direction of the molecule to be read out [130].

In addition, single molecule studies of molecules closely related to metal phthalocyanines, in particular a Fe porphyrin, have shown coupling between the molecular spin and magnetic substrates [131]. Specifically, the spin of the Fe ion was shown to align parallel to the magnetisation of Co (which was in the plane of the substrate) or Ni (out of plane) through indirect exchange via N atoms of the organic ligand with the two substrates. Similarly, the transition metal ion of a Mn porphyrin has

been observed to couple magnetically to Co substrates [132]. This highlights the potential to use such molecules for single molecule spin-polarised devices [131, 133].

Applications of Phthalocyanine Films in Spintronics

One of the key requirements for organic spintronic devices is the ability to controllably switch the interactions between the molecules. Liljeroth *et al.* have recently demonstrated that the position of H atoms bonded in the central cavity of naphthalocyanine molecules (see Section 1.1 for structural information) can be manipulated by an STM tip [134]. In their low temperature STM studies of flat-lying naphthalocyanine molecules, they observed that by imaging at a tip bias in resonance with the LUMO level the location of the H atoms bound to central N atoms of the Pc ring could be determined. Through subsequently increasing the bias to higher voltages and then returning to that of the LUMO level, the positions of the H atoms had been swapped, equivalent to a molecular rotation by 90° (a physical molecular rotation was ruled out since this effect was observed in close-packed arrays). No such switching was observed at an applied bias corresponding to the LUMO level (or at lower voltages), ruling out a spontaneous swapping of the H atoms, whilst the switching rate was observed to be proportional to the tunnelling current. In this paper, the authors have also shown that three naphthalocyanine molecules can be coupled together if positioned sufficiently close to each other, wherein they observed that they could switch one molecule by current injection through one of its neighbours.

Although no spintronic devices have been constructed from MPc films to date, these molecules have been shown to possess intriguing magnetic properties, owing to the unpaired electron spin of the metal ion in transition metal phthalocyanines. This renders them good candidates for spintronic applications. In particular, studies have focussed on varying their magnetic properties by either introducing dopants into the films [135, 136] or by varying their crystal structure [37].

The introduction of electron donating dopants, such as potassium, into metal phthalocyanine films during deposition is known to modulate their electronic conductivity by varying the oxidation state of the organic molecule [137]. Different

properties are observed depending on whether additional electrons occupy the orbitals of the organic ligand or central metal. In a similar manner, Taguchi *et al.* have shown that the addition of Li to MnPc crystallites changes the magnetic ordering; the undoped material is weakly ferromagnetic, but upon increasing doping with Li the crystallites become antiferromagnetic [136]. This was attributed to a strong interaction between the Li atoms and Pc ring, leading to structural changes to the film, in addition to a change of spin of the Mn^{2+} ions from 3/2 to 5/2. In contrast, Sharoyan *et al.* found that doping CuPc with Na (also a group I metal) gives rise to ferromagnetic behaviour with a Curie temperature higher than 77 K [135].

The magnetic properties of CuPc films and crystallites have been investigated by Heutz *et al.*, where we have specifically focussed on the interactions present in different polymorphs [37]. As has already been described in Section 1.2.1, the two most common crystallographic phases of CuPc films are the α and β-phases, the main difference between these polymorphs being the molecular tilt angle with respect to the stacking direction (see Figure 1.2). We have observed that α-phase CuPc is weakly antiferromagnetic whilst the β-phase is paramagnetic. Theoretical calculations have shown that this change can be attributed to an indirect exchange mechanism between the unpaired Cu electrons, and that this is dependent on the orbital overlap between neighbouring CuPc molecules (this in turn is dependent on their crystallographic orientation). In addition, we have found that β-phase MnPc films are ferromagnetic, in agreement with the reports of Taguchi *et al.* performed on crystallites, whilst α-phase MnPc is antiferromagnetic. The fact that the magnetic interactions of MPc films can be controlled through their structure, and that they are inherently magnetic suggests that such systems have a large potential to create thin film spintronic devices.

Electron Paramagnetic Resonance studies of bulk CuPc crystallites

In order to make successful MPc thin film spintronic devices, it is important to understand how the unpaired electron spins interact. EPR provides a useful tool for probing this since it is only sensitive to unpaired electrons, whilst the degree of coupling can be assessed by the extent of hyperfine splitting (see Section 2.8.2 for more details)

and measuring the spin lifetimes. Although no detailed EPR literature reports of MPc films are known, the properties of CuPc crystallites have been studied using this technique and form a good basis for the thin film studies that will be presented in Chapter 4.

Continuous wave (CW) EPR measurements on bulk α- and β-phase CuPc crystallites have been performed since the 1960's [30, 138–145]. These materials are EPR active since the Cu^{2+} ion has an unpaired *d* electron, mostly localised in the $d_{x^2-y^2}$ orbital, which leads to a Zeeman splitting of the energy levels when placed in a magnetic field. Transitions between energy levels, which are accessible with microwave photons, can be measured as a function of the applied magnetic field (as will be described in Section 2.8). Furthermore, fine structure is observed due to interactions between the electron spin and nearby nuclei (known as hyperfine coupling), and the anisotropy of CuPc in a magnetic field.

For concentrated CuPc crystallites, this fine structure is not observed and instead a broad spectrum is detected, as shown in Figure 1.10(a) (bottom spectrum) for α-phase CuPc [142]. This is due to dipolar interactions between nearby Cu ions which suppress and average out any hyperfine couplings. However, upon dilution, the appearance of fine structure can be seen, as depicted in the figure. Four peaks arise from hyperfine coupling between the unpaired Cu electron and spins of the Cu nucleus ($I_{Cu} = 3/2$), whilst the sharper lines superimposed on these peaks (most visible at high fields) are due to interactions with the nuclear spins of the innermost N atoms of the Pc ligand ($I_N = 1$).

In the case of pure CuPc crystallites, a difference in the CW EPR spectra is seen for the α- and β-phases. A shaper spectrum is observed in the latter case which has been attributed to a stronger molecular coupling in the β-phase [30, 142] (this interpretation will be commented upon in Section 4.1.4). However, upon dilution in a H_2Pc lattice there is not expected to be a difference between α- and β-phase crystallites, since a more single-molecule like behaviour is observed [141]. EPR spectra of very dilute CuPc β-phase crystallites display well-defined hyperfine structure, for example as shown in Figure 1.10(b) [145]. This demonstrates that the degree of coupling between CuPc molecules can be controlled through spatial separation in a non-magnetic lattice.

Figure 1.10. *Continuous wave EPR spectra of CuPc crystallites as a function of dilution in H_2Pc. (a) Experimental spectra of 100% CuPc, 1:1 and 1:4 CuPc:H_2Pc α-phase crystallites (adapted from [142]). (b) Experimental and theoretical spectra of 1:500 CuPc:H_2Pc β-phase crystallites (from [145]).*

1.3.3 Quantum Computing

Quantum computing is a rapidly growing field in which data is manipulated and stored capitalising on quantum mechanical phenomena. Although development is at an early stage, it is believed that quantum computers will have the capacity to solve certain complex mathematical problems exponentially faster than classical computers. For example, an important demonstration of the power of quantum computers is the application of Grover's algorithm to a database search for which N possible answers are known to a problem, each must be selected and checked in turn until the correct one is found. A classical computer will take a time proportional to $\frac{N+1}{2}$ however, using Grover's algorithm the quantum computer will take a time proportional to $\sqrt{N}$.

Whilst current computers rely on operations of classical bits of value zero or one to store information, quantum computers rely on quantum mechanical *qubits* which can have values of zero, one or a superposition in which the zero and one states co-exist. For spin–1/2 particles this can be represented by a wavefunction ($|\psi\rangle$) as shown in Equation 1.2, in which $|0\rangle$ and $|1\rangle$ represent spin "up" and spin "down" states respectively, whilst α, β, γ and δ are complex coefficients.

$$|\psi\rangle = \alpha|00\rangle + \beta|01\rangle + \gamma|10\rangle + \delta|11\rangle \qquad [1.2]$$

The probability of each state is given by multiplication of the relevant coefficient with its complex conjugate. For example, the probability of the $|00\rangle$ state (i.e. both particles being "spin up") is given by $\alpha^*\alpha$.

For a quantum computer, a series of quantum gates (making up an algorithm) are generally required to manipulate the data stored in qubits. These are unitary transformations that operate in a similar manner to conventional logic gates (such as NOT, AND etc), although they become more complex as the number of qubits are increased. In addition, the final result must be accurately measured; since measurement destroys the system, this is performed statistically via a probability distribution.

Requirements for Practical Quantum Computers

In order for quantum computers to be practical, data must be stored in the qubits for a reasonable length of time. The loss of information over time is known as quantum decoherence; this generally occurs due to the interaction of the qubit with the local environment (for example spin-lattice relaxation). The requirements for a practical quantum computer have been outlined in the DiVicenzo checklist [146]. This states that qubits must be read out easily, that quantum operations must be performed faster than the decoherence time, that it must be possible to initialise the qubits to arbitrary values and

that the system must be physically scalable to increase the number of qubits. The latter point is an important challenge for quantum computing since more than 100 qubits are needed to perform a useful calculation, but the system changes as the number of qubits is increased.

Overview of Other Experimental Routes

Although traditionally research in this area has been mainly theoretical, recently important progress in the development of experiments that demonstrate quantum computation has been made. Currently, one of the most promising routes to build a quantum computer involves the use of trapped ions, for which the entanglement of up to eight Ca^+ ions has been demonstrated [147]. Superconducting circuits present a more readily scalable alternative wherein Cooper pairs are used as qubits, for which two-qubit entanglement has already been shown [148–150]. Other promising experimental routes include the use of quantum dots [151], electrons in helium [152] and fullerenes [153, 154].

The Stoneham-Fisher-Greenland Proposal

One of the potential applications of the work that will be described in Chapter 5 is the fabrication of systems that could be used in a quantum computation scheme proposed by Stoneham *et al.* [155]. Here, the two qubits can be individual atoms or molecules. Their interaction is manipulated through an intermediary *control* species (also an atom or molecule), which can be optically excited to induce interactions between the qubits. The two qubits (A and B) and one control species (C) are spatially separated by a distance of the order of a few nanometres, although this value is highly dependent on the choice of qubit and control species. This separation is chosen such that when all species are in their ground states, there is almost no overlap between the respective wavefunctions, and so interactions between the spins are negligible. However, due to the careful selection of the qubit and control species, once the control is optically excited there is significant wavefunction overlap and so the qubits interact (performing a *quantum dance*), as is

shown in Figure 1.11. The qubit-qubit interactions can then be switched off by stimulated de-excitation of the control and so in this manner the spins of the qubits can be manipulated by the excitation and de-excitation pulses. Once in the off state, the spins of the qubits should be retained; the quantum information is stored.

Figure 1.11. *The scheme proposed for the manipulation of quantum information by Stoneham et al. between qubits A and B via optical excitation of the control species (C) (adapted from [155]). The wavefunctions of each state are shown in blue. When the control is in its excited state (red) there is a considerable wavefunction overlap with the qubits permitting them to interact, whilst when in the ground state this overlap is negligible (the off state).*

One of the main advantages to this approach is that the energy scales involved are generally large, thus potentially permitting operation at liquid nitrogen temperatures or possibly even at room temperature. Also, since this scheme relies on electronic excitations, there is no need for electrodes and by design, exact positioning of the species

is not required. The only condition is that the separation must be small enough to allow overlap of the wavefunctions when the control is in its excited state and large enough to avoid interaction of qubits in the ground state. Of course, it is important to choose suitable candidates for the qubits and the control. The excited state wavefunction of the control atom must have significantly larger spatial dimensions than its ground state. In addition, the lifetimes of the spins must be acceptable for computation purposes (each operation is anticipated to last 3–100 ns [155]). It is also preferable that the final system is compatible with existing silicon technology.

1.3.4 Dopants into Silicon

The inclusion of dopants into silicon to form electron rich (n-type) and hole rich (p-type) regions is crucial to the silicon industry. Dopants such as P, As and B are commonly used to control the electrical properties of Si wafers. These are responsible for creating p-n junctions, which underpin important components such as transistors, from which many modern electronic devices are constructed. In addition, doped silicon has a wide range of other applications; for example, rare-earth doped silicon is used for light emitting devices [156] and in the telecommunications industry [157], whilst superconductivity has been observed in boron doped silicon [158]. Of high interest in the context of this work are the applications for inorganic spintronic and quantum computing (as outlined in Sections 1.3.1 and 1.3.3).

Methods for Doping Silicon

It is highly desirable to have control over the concentration, uniformity and purity of the dopants within bulk silicon. In addition, in order to be commercially viable, the dopant species should be introduced at low cost and over large areas. For certain applications, high control and spatial resolution of the doped region, and the ability to introduce a range of dopants (either randomly or in controlled heterostructures) is crucial. Specifically, for spintronics and quantum computing, the formation of dopant-rich clusters should be avoided, whilst it is desirable to have control over the individual

dopant separations within the silicon lattice. During manufacture, a silicon chip will undergo almost 100 processing steps and it is important that these are performed in the correct order. In particular, any procedures that involve thermal annealing will cause the migration of dopants introduced at earlier stages to undesirable sites. Therefore, low temperature and rapid processes are preferable (this is often referred to as the "low thermal budget" problem) [159].

One of the most commonly employed methods of introducing dopants into silicon is ion implantation. In this technique, ions of the element to be implanted are accelerated to energies between 10–500 keV onto the silicon target, with the amount of material implanted determined by the beam current (typically microamperes) and exposure duration. The energy of the ions, ion species and angle at which they impinge on the silicon target determine the depth profile of the implanted species. Typical ion ranges (defined as the average penetration depth) of 10 nm to 1 μm are commonly created, as can be modelled using Monte-Carlo simulation packages (such as the SRIM package that will be used in Chapter 5). Higher energy ions reach greater depths and lead to broader dopant distributions, whilst ultra-low energy techniques have been developed to create more precise, near-surface dopant distributions [160].

The main disadvantage of the ion implantation technique is the creation of numerous point defects inside the silicon lattice, such as vacancies. This leads to a mixture of types of dopant (such as substitutional and interstitial, as will be discussed in the following section) and leads to variations in electrical properties. Some of the damage induced by the ion beam can be repaired with a high temperature anneal but this treatment can further broaden the dopant distribution and be detrimental to device efficiency [161]. In the case of high energy beams, the Si lattice can be destroyed irreparably and annealing has no effect. In addition, ion implantation requires specialist facilities (which can be expensive) and does not allow control over the lateral separation between individual dopants.

Epitaxial growth techniques such as molecular beam epitaxy (MBE) and chemical vapour deposition (CVD) can be used to give a much greater control of the dopant distribution in silicon since, in both cases, the sample is grown in a layer-by-layer

manner. In MBE, the dopants are usually deposited from a Knudsen cell (k-cell) whilst Si is deposited from electron beam deposition onto the target in UHV conditions at a very slow rate. This allows a high precision of the separation of dopants in addition to the production of a very crystalline substrate and the ability to create abrupt interfaces between layers [162]. However, the range of dopants is limited since they must be deposited by sublimation; common dopants in the silicon industry, such as B, sublime at temperatures too high for MBE, whilst As and P sublime too quickly to permit control over their fluxes [163]. Instead, n-type layers are generally grown from Sb [164], whilst Ga or Al is often used to grow p-type layers [165].

Alternatively, CVD can be used to grow doped silicon layers at a faster rate and lower cost than MBE. Furthermore, since CVD does not require UHV conditions it lends itself more readily to industrial applications. Here, the target is exposed to volatile precursors which react at the surface with the products forming the film layer. Si is often deposited from SiH_4, SiH_2Cl_2 or Si_2H_6, whilst p-type layers are grown from B_2H_6 [166, 167] and n-type layers from PH_3 or AsH_3 [168–170] (however, it should be noted that these compounds are generally toxic). This leads to homogeneous, layer-by-layer growth on substrates of up to 300 mm in diameter [171]. Both of these techniques are successfully used for the growth of high quality thin films of doped silicon. However, these have limited appeal for mass production of bulk doped wafers since the layer-by-layer growth is generally slow and can be expensive (especially in the case of MBE).

In addition to conventional growth techniques, new methods for doping silicon are being developed using small molecules as precursors that remain intact upon adsorption to the surface (as opposed to CVD). This has the advantage that molecular self-assembly can be used to produce greater control over the lateral distribution of the dopant species. Recently, Ho *et al.* proposed a method in which a self-assembled monolayer of P or B containing organic molecules is deposited onto a Si(100):H surface, subsequently capped with a 50 nm SiO_2 layer and finally subjected to an rapid thermal annealing process [172]. These authors have shown through SIMS and resistance measurements that the dopant depth profile can be controlled by the temperature of the annealing step and that this procedure can be used to create nano-structured devices. However, this process relies

on chemisorption which limits the range of possible molecular species and therefore dopants that can be introduced. In addition, since this method requires of thermal annealing it is not possible to control the distribution profile of fast diffusing species (such as transition metals, which are of significance for DMS), as will be discussed in the following section.

Diffusion of Dopants in Silicon

Diffusion is the migration of low concentration impurity species from regions of high concentration to regions of lower concentration. There are two main forms of dopants in semiconductor, namely substitutional and interstitial. Substitutional dopants occupy positions in the host lattice and migrate by interchanging positions with vacancies (as shown in Figure 1.12(a)). Alternatively, dopant atoms can exist at interstitial positions (between the atoms of the Si lattice) and these can move around without occupying a lattice site (Figure 1.12(b)). As a result, interstitial dopant diffusion is generally much faster than subsitutional (the latter process is reliant on the density of lattice vacancies).

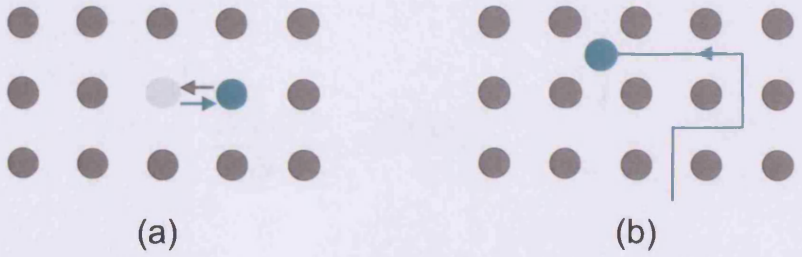

Figure 1.12. *The motion of dopant atoms (green) within a host silicon matrix (dark grey) for (a) substitutional and (b) interstitial diffusion. Arrows represent the direction of motion whilst a silicon vacancy is shown in light grey.*

A theoretical model for diffusion was proposed by Fick in 1855 [173], in which the flux of dopant species passing through a unit area per unit time (F) is proportional to the concentration gradient (with respect to distance), as shown in Equation 1.3. Here, C is

the dopant concentration per unit volume, x is the direction of flow and D is the diffusion coefficient (measured in cm^2/s).

$$F = -D\frac{\partial C(x,t)}{\partial x} \qquad [1.3]$$

Due to conservation of matter, the change in concentration must be equal to the decrease in flux as a function of distance (assuming that no material is formed or consumed by the host), as expressed in Equation 1.4.

$$\frac{\partial C(x,t)}{\partial t} = -\frac{\partial F(x,t)}{\partial x} \qquad [1.4]$$

The diffusion coefficient can be approximated as being constant at low concentrations, and so substitution of Equation 1.3 into 1.4 leads to the following relationship, commonly known as Fick's diffusion equation.

$$\frac{\partial C(x,t)}{\partial t} = D\frac{\partial^2 C(x,t)}{\partial x^2} \qquad [1.5]$$

For the case of a layer of dopant instantaneously deposited onto a silicon surface at time $t = 0$, with a total number of dopant atoms per unit area (S), the initial and boundary conditions are given by Equations 1.6–1.8.

$$C(x,0) = 0 \qquad [1.6]$$

$$\int_0^\infty C(x,t)dx = S \qquad [1.7]$$

$$C(\infty,t) = 0 \qquad [1.8]$$

The solution of Equation 1.5 for this case is a Gaussian distribution, as given in Equation 1.9 [98].

$$C(x,t) = \frac{S}{\sqrt{\pi Dt}} \exp\left[\frac{-x^2}{4Dt}\right] \qquad [1.9]$$

From this, it is apparent that the concentration at the surface $C(0,t)$ decreases as a function of $\frac{1}{\sqrt{t}}$, whilst the concentration profile within the bulk as a function of depth is highly dependent on the diffusion length (approximated by $\sqrt{Dt}$).

The motion of dopant species is highly temperature dependent, with a higher rate of diffusion at higher temperatures. This can be expressed as shown in Equation 1.10, where D_0 (measured in cm^2/s) is the value of the diffusion coefficient at an infinite temperature, E_A is the activation energy (eV), k_B is the Boltzmann constant and T is the temperature.

$$D = D_0 \exp\left[-\frac{E_A}{k_B T}\right] \qquad [1.10]$$

A plot of the diffusion coefficient of as a function of inverse temperature is shown in Figure 1.13 for a selection of dopants. As can be seen from the figure, the diffusion coefficient varies widely across the periodic table, with lower values of E_A for faster

diffusing species. Typically systems in which the dopants diffuse interstitially have activation energies between 0.6 eV and 1.2 eV, whilst for substitutional diffusion this value is higher (greater than 2 eV). Table 1.2 summarises the diffusion properties of a selection of species in silicon. Copper is a very fast diffuser in silicon, whilst Bi diffusion is a far slower.

Figure 1.13. *The diffusion coefficients of a range of dopants in Si as a function of temperature (from [98]).*

Dopant	D_0 (cm^2/s)	E_A(eV)	D_{300K} (cm^2/s)	Reference
Cu	4.5×10^{-3}	0.39	1.3×10^{-9}	[174]
Mn	2.4×10^{-3}	0.72	2.8×10^{-15}	[175]
Fe	6.2×10^{-3}	0.86	2.2×10^{-17}	[176]
Bi	1.0×10^{3}	4.63	1.8×10^{-75}	[177]

Table 1.2. *The diffusion coefficients and activation energies of a selection of dopants in Si. The diffusion coefficients at room temperature were calculated using Equation 1.10.*

Chapter Two: Experimental

This chapter will introduce the experimental techniques and procedures that will be used in Chapters 3, 4 and 5. The growth of thin Pc films will be described in Section 2.1, whilst an overview of the UV lamps used in Chapter 5 will be presented in Section 2.2. Following this, a review of each of the techniques used will be given, along with specific details regarding the experimental conditions. These will be presented in the following order: topographic characterisation (STM and AFM), depth profiling (SIMS), optical spectroscopy (electronic absorption and Raman), EPR, and then x-ray techniques (XAS, XPS and XRD).

2.1 PHTHALOCYANINE FILM GROWTH

This section will outline the methods used for the growth of thin Pc films. The preparation of the substrates to be used will be discussed in Section 2.1.1, whilst the Pc purification and subsequent deposition via organic molecular beam deposition will be discussed in Sections 2.1.2 and 2.1.3 respectively. A brief description of the growth of bulk CuPc crystallites (for use in Chapter 4) will be given in Section 2.1.4.

2.1.1 Substrate Preparation

As noted in Section 1.2.2, the interaction between the substrate and Pc layer plays an important role in the determination of the molecular crystallographic structure. It is therefore necessary to deposit the Pc films onto surfaces that are free of contaminants (such as grease or dust) so that the true characteristics of the film-substrate interface can be determined. In addition, since many of the characterisation techniques that will be used have been specifically chosen for their surface sensitivity, it is desirable that all

contaminants are removed prior to film growth to avoid spurious signals in the post-deposition analyses.

In-situ Preparation of Passivated Si(100) Surfaces

For the experiments that will be described in Chapter 3, all sample preparation was performed in-situ. A rectangular segment from a Si(100) wafer (0.01 Ωcm, B-doped) was mounted onto a specially designed holder that allowed current to be passed along the substrate's length. The substrate was loaded into the ultra-high vacuum (UHV) chamber and outgassed overnight (this involved a gentle heating in UHV conditions to desorb surface water). Following this, repeated flashing cycles were performed during which a current of 3.2 A was applied quickly to the sample for 30 seconds (raising the temperature to ~1150°C), which was then allowed to rest at a lower temperature. This process was repeated several times until the native SiO_2 layer had been removed, as monitored by the pressure rise upon flashing (the substrate was deemed to be oxide free once the pressure no longer increased significantly upon flashing). Following the final flashing sequence, the substrate was cooled slowly in an attempt to minimise the number of step edges (i.e. to maximise the size of the terraces and reduce surface roughness).

Two passivating species were employed to terminate the dangling bonds of the clean Si(100) surface; ammonia and hydrogen. The ammonia passivated surface was achieved by exposing 9 L (3×10^{-6} Pa for 4 minutes) NH_3 gas whilst the clean substrate was held at room temperature. In the case of the H terminated surface, the sample was held at 300°C (a directly applied current of 1.0 A) whilst exposed to atomic hydrogen produced by a filament (10 V, 0.18 A) at a pressure of 5×10^{-5} Pa for 30 minutes. In both cases, the substrates were allowed to cool and/or settle for at least one hour before STM imaging and CuPc deposition.

For some studies in Chapter 3, Bi nanolines were grown on the clean Si(100) surface prior to passivation. The creation of the nanolines are not the main focus of this work, and so only a brief description of the method used to create them is given here since a well-established procedure was followed [178]. After flashing, the sample was cooled to approximately 570°C, at which point Bi was deposited from a Knudsen cell (k-

cell) at a temperature of 470°C for 10 minutes. The sample was then annealed at the same temperature and monitored by STM whilst Bi islands desorbed, until only the Bi nanolines remained. It was subsequently cooled to room temperature and passivated with NH_3, as described previously.

Ex-situ Preparation of Si(100):H

In industry, the most common method for the removal of the native oxide layer of Si is to submerse the substrate in HF [179], as will be used for the substrates described in Chapter 5. Here, the oxide layer is etched away by the HF acid, creating a clean Si surface which is terminated with H atoms [180]. However, it should be noted that this process produces a rougher surface than that created by the in-situ flashing technique, and that the Si dangling bonds are passivated with up to three hydrogen atoms [181] (the in-situ hydrogen gas passivation method leads to a monohydride terminated surface).

The preparation of these substrates was performed in a cleanroom. The wafers were held in a Teflon dipper and immersed in HF (VWR, 50%, VLSI selectipur grade) for 30 seconds and then rinsed in high purity de-ionised water for one minute. After treatment, the wafers were observed to be hydrophobic, as expected for a H-terminated surface [179], with any excess water (in particular from the back of the wafer) removed by drying in a nitrogen gas stream. The samples were immediately transferred to the UHV growth chamber to minimise any oxide re-growth.

Preparation of Non-crystalline Substrates

Amorphous substrates, namely glass and kapton, were used for the studies that will be described in Chapter 4. Glass substrates were chosen due to their optical transparency and flatness, whilst kapton has little magnetic (EPR) signal, is flexible and easily cut, rendering it a good material for the demonstration of the potential of Pc thin films for spintronic applications. The substrates were de-greased prior to film growth. For glass substrates this was performed by sonicating in acetone and then isopropanol, each for ~10 minutes, followed by drying in a nitrogen stream. The kapton substrates are less

robust and so these were cleaned by washing in isopropanol and then drying between filter paper. The kapton substrates were 25 μm thick and were cut using a ceramic knife to avoid contamination of magnetic particles (such as Fe).

2.1.2 Purification of Raw Material

CuPc, H_2Pc and MnPc were purchased from Sigma-Aldrich (purity ~97%) in powder form. These were then purified by two cycles of gradient sublimation*. Several grams of the raw material were loaded into the sealed end of a quartz tube. The open end was connected to a rotary and turbo pump (with glass wool placed at the open end of the tube to prevent volatile impurities entering the pumping set-up) and the tube was evacuated. The sealed end was placed in a tube furnace and heated until the sublimation temperature was reached (typically 350-450°C). Due to the well-defined temperature gradient within the chamber, purified Pc crystallites were formed at a localised region of the walls of the tube, whilst impurities condensed elsewhere. The purified crystals were then removed and subjected to another cycle of gradient sublimation.

2.1.3 Organic Molecular Beam Deposition

Organic molecular beam deposition (OMBD) is a standard technique used for the growth of high purity films of small organic molecules. For the work described in Chapter 3, CuPc was deposited in-situ from a k-cell attached to the preparation chamber of the STM, whilst the films described in Chapters 4 and 5 were grown in two chambers specially designed for organic molecular film growth (both supplied by Kurt Lesker Ltd). In all cases, the purified Pc material was loaded into a ceramic crucible and placed in a k-cell. Briefly, a k-cell comprises a set of heating coils that surround a ceramic crucible containing the organic material. The coils resistively heat the cell, with the temperature monitored by an in-situ thermocouple.

For the films deposited in the OMBD chambers, the substrates were positioned upside down, behind a shutter ~50–100 cm away from the k-cell so that they were in a

* The purification was performed with Soumaya Mauthoor and Hsiang-Han Tseng.

uniform region of the molecular beam. In this work, all substrates remained at room temperature during film deposition. The chamber was then evacuated to pressures of ~2–4 x 10^{-6} mbar. Once evacuated, the temperature of the k-cell was gradually increased, as monitored via the in-situ thermocouple. The flux of sublimed molecules was monitored by two quartz crystal microbalances (QCMs), one placed in the vicinity of the k-cell and the other near the substrates (neither were blocking the path between the k-cell and substrate). Once the temperature had reached the point of sublimation (typically 320-400°C) and a stable molecular flux of 0.2 Å/s to 2.0 Å/s had been established, with faster growth rates chosen for thicker films, as determined by the temperature of the k-cell, the shutter shielding the substrates was opened. At this point the molecular flux was carefully monitored and the shutter not replaced until the desired thickness had been reached, after which the k-cells were cooled and the samples removed. In the case of the co-deposited Pc films (as will be described in Section 4.3), two k-cells containing different Pc crystallites were simultaneously heated to provide a mixed beam composition ratio controlled by the k-cell temperatures. Care was taken that the ratio of the two Pc species was kept constant throughout deposition, as monitored by the QCM readings from close to the organic sources.

In the case of the ultra-thin film studies in Chapter 3, a similar procedure was followed wherein the purified CuPc crystallites were deposited from a k-cell at a temperature of 272 ± 3°C in UHV conditions (~10^{-9} mbar). Film deposition was performed in the sample preparation chamber, which was connected via a gate valve to the main STM chamber, permitting the in-situ analysis of the films. Here, the deposition rate was not measured in-situ and instead was calculated post-deposition from the STM images. The rate was defined in terms of upright standing CuPc monolayers (ML) and was typically ~8 x 10^{-5} ML/s.

2.1.4. Formation of CuPc crystals

Powder α-phase crystallites, for comparison with the α-phase CuPc films in Chapter 4, were synthesised using the acid paste method*. Briefly, these were created by diluting 10 mg pure CuPc crystallites (the result of two gradient sublimation cycles as outlined in Section 2.1.2) in 0.5 ml H_2SO_4. The solution was subsequently mixed with 2.5 ml deionised H_2O, then filtered to collect the crystallites which were dried using a rotary pump and acetone (to remove any excess water).

The β-phase crystallites studied in Section 4.1 are those obtained after two cycles of gradient sublimation, as described in Section 2.1.2.

2.2 UV EXCIMER LAMP PROCESSING

UV excimer lamps generate monochromatic, high power radiation, uniformly over a large coverage area [182, 183]. This is both a cheap and clean processing technique that operates at temperatures close to room temperature. UV photons are produced by the radiative decomposition of excimer states in gases. The excimers are created by applying a high voltage (typically 7-10 kV) at high frequency (100-500 kHz), causing a barrier discharge between the electrodes (see Figure 2.1). Various exchange gases can be sealed into the lamps, flooding the space between the electrodes, in order to produce the desired emission wavelength. Common exchange gasses include Xe, KrF, ArF and Ar and these produce emission at 172 nm, 248 nm, 192 nm and 126 nm respectively. In all cases, the widths of the emission spectra produced by excimer lamps are generally in the range 10-20 nm [182]. Common applications of VUV lamps include materials coatings [184], modification of polymers [185], surface cleaning [186] and water purification [187].

* The preparation of the crystallites was performed with Soumaya Mauthoor.

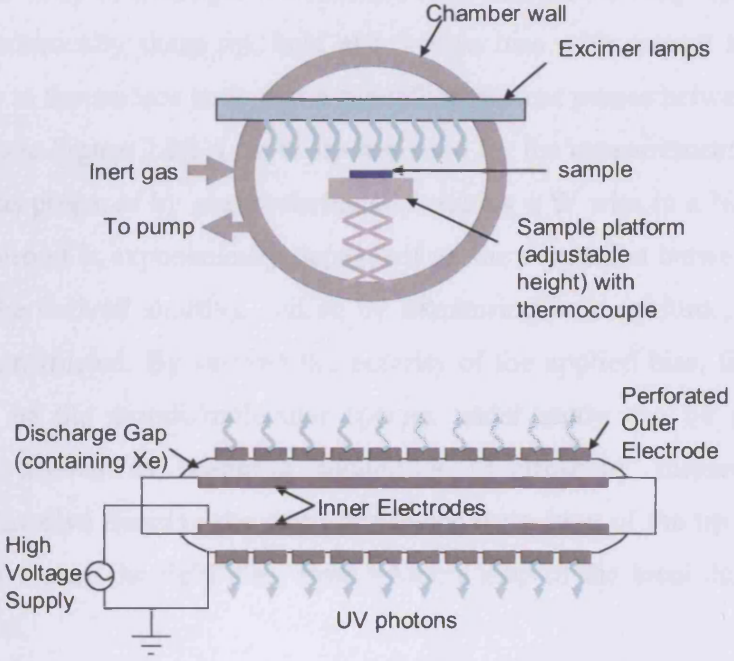

Figure 2.1. *Schematic views of the experimental set-up of the UV excimer lamp chamber (top) and one of the 172 nm UV lamps (bottom).*

A home-built UV chamber containing four parallel Xe (172 nm emission) lamps was used for the experiments described in Chapter 5, a schematic of which is shown in Figure 2.1. The samples were positioned film-side-up, at a distance of 8 cm directly below the four-lamp array. The chamber was evacuated to a pressure of 0.3 mbar and then backfilled with nitrogen gas to 3.0 mbar, at which point the lamps were turned on (applied power of 750 W). The temperature of the samples was monitored by an in-situ thermocouple and observed to remain between 25°C and 60°C at all times.

2.3 SCANNING TUNNELLING MICROSCOPY

Scanning tunnelling microscopy (STM) is a technique that can provide images of the surface electron density of a sample with atomic resolution [188, 189]. This is achieved by scanning an atomically sharp tip, held at a known bias with respect to the sample, sufficiently close to the surface such that a tunnelling current passes between the tip and sample (as shown in Figure 2.2(a)). A W tip was used for the measurements described in Chapter 3 and was prepared by electrochemically etching a W wire in a NaOH solution. The tunnelling current is exponentially dependent on the separation between the tip and surface (as will be derived shortly), and so by monitoring its magnitude, a map of the surface can be constructed. By varying the polarity of the applied bias, filled or empty electronic states of the atomic/molecular species under study can be probed. More detailed studies known as scanning tunnelling spectroscopy measurements (not performed here) involve freezing the three dimensional position of the tip above a point of interest and sweeping the field bias, from which a map of the local density of states can be constructed.

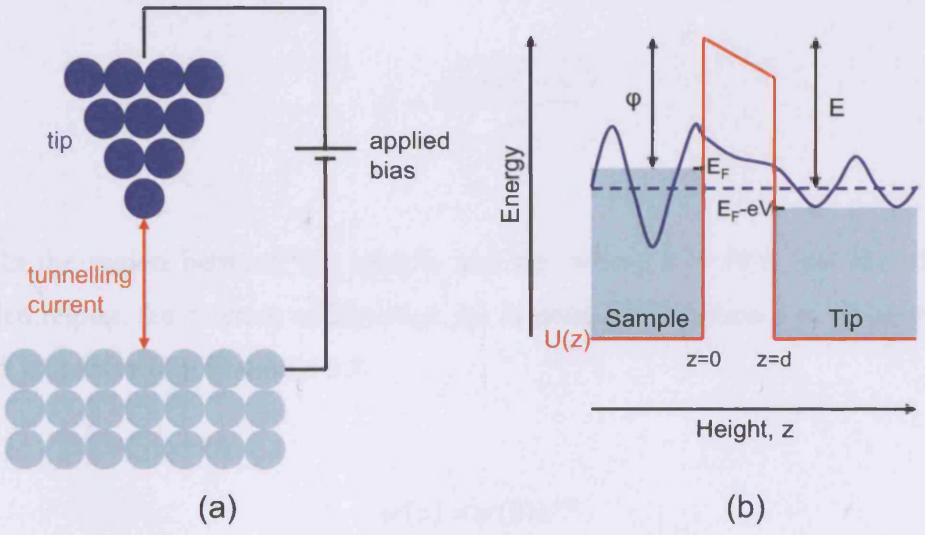

Figure 2.2. *(a) A schematic view of the experimental set-up of STM. (b) A model of a 1D tunnel barrier between a tip and sample for an applied bias V.*

A time independent wavefunction (ψ) can be used to describe the motion of an electron in a one dimensional tunnel barrier represented by a potential $U(z)$ (as shown in red in Figure 2.2(b)). This is described by Schrödinger's equation (Equation 2.1), where $\hbar$ is Planck's constant, z is the co-ordinate of position, m is the mass of an electron and E is the energy of the electron.

$$-\frac{\hbar^2}{2m}\frac{\partial^2\psi(z)}{\partial z^2}+U(z)\psi(z)=E\psi(z) \qquad [2.1]$$

If $E > U(z)$, i.e. in the region of the tip or sample (as shown in Figure 2.2(b)), where classically the electron is permitted to be, Equation 2.1 has two solutions as given by Equation 2.2. The wavevector k is defined in Equation 2.3.

$$\psi(z)=\psi(0)e^{\pm ikz} \qquad [2.2]$$

$$k=\frac{\sqrt{2m(E-U)}}{\hbar} \qquad [2.3]$$

In the region between the sample and tip, where $E < U(z)$, i.e. the classically forbidden region, the solution of Equation 2.1 is given by Equation 2.4, where the decay constant κ is defined in Equation 2.5.

$$\psi(z)=\psi(0)e^{-\kappa z} \qquad [2.4]$$

$$\kappa=\frac{\sqrt{2m(U-E)}}{\hbar} \qquad [2.5]$$

The work function (φ) of a metal surface is defined as the minimum energy required to remove an electron to the vacuum level, whilst the electrons occupy energy levels up to the Fermi energy (E_F). If a bias (V) is applied between the sample and tip, as shown in Figure 2.2(b), this results in tunnelling of electrons of energy between E_F and $E_F - eV$ across the barrier, in the case shown from the sample to the tip. For small applied bias values, only electrons from close to the Fermi level can tunnel, with $E \approx -\varphi$. The probability of an electron tunnelling across a barrier of width d is given by the modulus squared of the wavefunction (i.e. the square of Equation 2.4) and so can be described by Equation 2.6, where the decay constant κ is expressed in Equation 2.7.

$$P \propto |\psi(0)|^2 e^{-2\kappa d} \qquad [2.6]$$

$$\kappa = \frac{\sqrt{2m\varphi}}{\hbar} \qquad [2.7]$$

The tunnelling current (I) is proportional to the sum of the probabilities of the electrons tunnelling through the barrier from all energy levels between $E_F - eV$ and E_F, as given by Equation 2.8.

$$I \propto \sum_{E_n = E_F - eV}^{E_F} |\psi_n(0)|^2 e^{-2\kappa d} \qquad [2.8]$$

Therefore, for a fixed bias, the tunnelling current decays exponentially as a function of the tip-sample separation.

There are two commonly used modes of operation of STM, known as constant current and constant height modes. In the former, the tip height is adjusted as it scans the

surface in order to maintain a constant tunnelling current. In constant height mode, the height of the tip is fixed and the tunnelling current varies with x-y position (this mode can only be performed on reasonably flat surfaces otherwise the tip might crash into the surface). The height of the tip is controlled by a piezoelectric crystal connected to a feedback circuit, permitting sensitive control of the sample-tip distance. For constant current mode, the height of the tip is adjusted by varying the voltage applied to the piezoelectric element, via the feedback loop, in order to retain the set tunnelling current, whereas in constant height mode the feedback loop is effectively turned off.

The images described in Chapter 3 were obtained in constant height mode using a JEOL 4500XT high temperature UHV-STM at room temperature.

2.4 ATOMIC FORCE MICROSCOPY

Atomic force microscopy (AFM) is another of a number of scanning probe techniques that is commonly used to provide detailed information about the topography of a surface. One of the major advantages that AFM has over STM is that it does not require the sample to be electrically conductive and so a wider range of surfaces can be studied, however, in general STM offers higher resolution.

The general principle of AFM operation is outlined in Figure 2.3. A sharp tip is mounted on a cantilever of known stiffness and is swept across the sample surface. The interaction between the tip and surface is monitored as a function of position, and is used to construct a map of the sample topography. Since the tip is very close to the surface it is subject to a force which may bend the cantilever. A laser beam is aligned so that it is incident upon the back of the cantilever which reflects the beam onto a split photo-diode detector; the detector monitors the location of the reflected light, allowing information about the degree of bending of the cantilever to be gained. The deflection is small enough that Hooke's law can then be applied to determine the force between the tip and sample. The force experienced by the tip is highly dependent on its separation from the surface; when the separation is small, the tip experiences a repulsive force, but as the separation is

increased the tip becomes attracted towards the sample. If the separation is increased further, the tip-surface interaction becomes negligible and results in no deflection of the laser beam.

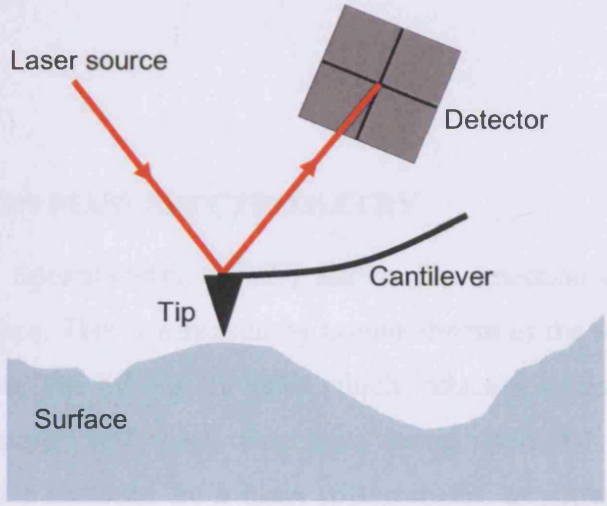

Figure 2.3. *A schematic of the experimental set-up of AFM. A tip is mounted onto the end of a cantilever. The tip interacts with the surface causing the cantilever to bend; the degree of bending is monitored by the deflection of a laser beam reflected off the back of the cantilever.*

The two most commonly used methods for AFM measurement are contact and tapping modes. Contact mode is the simplest, and involves the tip maintaining the same deflection and therefore the same distance from the sample by means of a feedback loop control, as it scans the surface. However, this can damage soft samples (such as Pc films) when used in air, as a significant force must be applied in order to overcome the effects of surface moisture and other contaminants. Alternatively, tapping mode can be used. This involves an oscillating tip at a frequency close to its resonant frequency, and then scanning over the surface (as in contact mode). Due to the oscillatory motion of the tip, it

is only in contact with the surface for a short time and so this drastically limits the damage to the surface. The image produced is a map of the force between the sample and tip, translated as surface topography.

The AFM measurements that will be described in Chapters 4 and 5 were performed in tapping mode, using a Veeco Dimension 3100 AFM, at room temperature and ambient conditions.

2.5 SECONDARY ION MASS SPECTROMETRY

Secondary Ion Mass Spectrometry (SIMS) allows the detection of elemental species present at a solid surface. This is achieved by bombardment of the surface with energetic ions (typically between 100 eV and 10 keV) which induce a series of collisions. These collisions result in atoms and small fragments being sputtered from the surface, a proportion of which are analysed by a mass spectrometer, as shown in Figure 2.4. The angle created between the profiling beam and normal to the sample is defined as the tilt angle (θ), which is varied by rotating the sample about its central point (the ion gun remains fixed). It is desirable for samples to be electrically conducting, since otherwise collisions would lead to surface charging; prolonged bombardment of insulating materials would cause the surface potential to rise, and this would lead to variations in the detected yields of ions from the surface as a function of charging (the kinetic energy of the emitted ions would deviate from the detectable range). Analysis of such samples must be carried out in the presence of an electron beam, which compensates for the surface charging. However, since the samples in Chapter 5 originate from silicon substrates, the use of an electron beam is not necessary here.

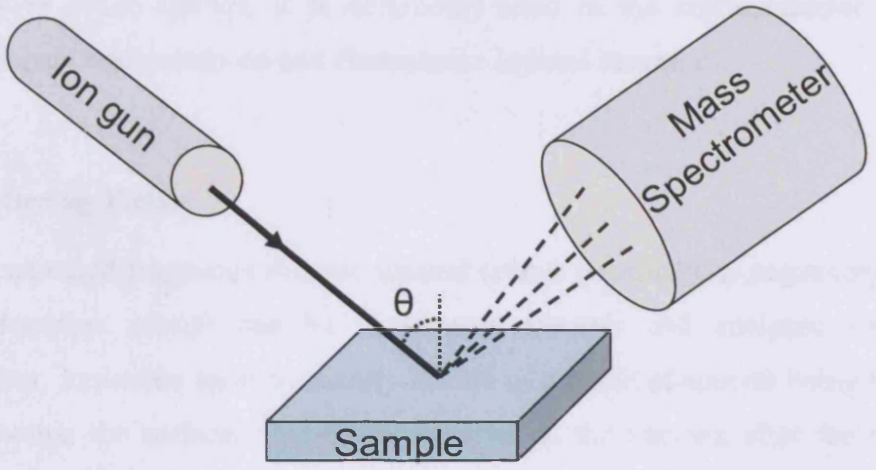

Figure 2.4. *A schematic of the set-up of a SIMS experiment. Energetic ions are incident on the sample, which result in the sputtering of surface species that are collected and analysed by the mass spectrometer.*

The SIMS process is initiated when an incident energetic particle from the profiling beam collides with near-surface species, transferring its kinetic energy to the surface. This induces a series of surface atom recoils, knock-on collisions and cascades within approximately 30 Å of the initial point of impact, and these cause substantial local damage. The cascades can be modelled using Monte-Carlo simulations; packages such as SRIM (Stopping and Range of Ions in Matter) calculate parameters such as elemental mixing, ion energy loss and defect distributions as a function of beam energy, angle, species and target material composition. This software will be used in the interpretation of the experimental profiles in Chapter 5. Many of the cascades return to the surface and result in the ejection of species from the uppermost two layers with typical energies of less than 20 eV [190]. These ejected (sputtered) particles not only allow the chemical characterisation of the surface, but also result in erosion of the surface and as a result, a depth profile can be obtained. There are three main variations on the SIMS technique; namely static (in which sputtering is minimal and so only the surface is probed), time-of-

flight (which uses a pulsed beam to analyse the surface) and dynamic SIMS. Dynamic SIMS was used in Chapter 5 since it permits detailed depth profiling and has a high sensitivity to dilute species; it is commonly used in the semiconductor industry to measure dopant concentrations and characterise layered structures.

2.5.1 Sputtering Yields

Only the sputtered fragments that are ionised (either positively or negatively depending on the detection set-up) can be accelerated towards and analysed by the mass spectrometer. Ionisation most frequently occurs as a result of species being forced close together within the surface, or due to ionisation in the vacuum after the atom/cluster leaves the surface region. Only a small fraction of the total sputtered yield is ionised [190], however, this is generally sufficient to permit a true analysis of the surface composition. Different mass spectra are obtained when collecting either positive or negative ions from a given surface (some species preferentially form cations whilst others more readily form anions), whilst larger fragments have lower yields.

The sputtered yield is heavily dependent on the surface binding energy, electronic state, local chemical environment, topography and crystallinity of the sample. Figure 2.5 shows how the measured yields vary by several orders of magnitude across the different elements of the periodic table, in addition to the effect of varying the beam species and collection mode. The presence of readily ionising species such as oxygen enhances the measured yield of some species. For example, the yield of Si^+ increases by over an order of magnitude as the ambient oxygen pressure is increased by a factor of four [191]. This is due to the incorporation of oxygen into the uppermost layers; since oxygen is highly electronegative, the breaking of Si-O bonds leads to an efficient Si^+ production. Therefore, oxygen is commonly used as a profiling beam for studies of dilute species, however does not give a true representation of the surface.

Figure 2.5. *The variation of (a) positive ion yields from an O^- beam and (b) negative ions from a Cs^+ beam as a function of atomic number (from [192]).*

2.5.2 Relative Scattering Factors

Although the detected sputtering yield is highly dependent on the local chemical composition of a surface, this does not vary significantly for dilute concentrations of dopants (less than 10^{20} atoms/cm^3) in the same host material [190]. In fact, a relationship between the dopant species concentration (ρ_{dopant}, measured in atoms/cm^3) and the ratio of the detected yields of dilute species (I_{dopant}) with respect to that of the host matrix (I_{host}) has been established for common systems (such as metal dopants in silicon). This is described by Equation 2.9, where the relative scattering factor (*RSF*) is a known constant for that particular system.

$$\rho_{dopant} = \left(\frac{I_{dopant}}{I_{host}} \right) RSF \qquad [2.9]$$

The RSF values for a selection of metal dopants in silicon have been determined experimentally, as shown in Figure 2.6. These vary greatly as a function of dopant species and are dependent on the profiling beam species used [193, 194]. However, they are often used to determine the concentrations of dopants in silicon; the analyses in Section 5.3.2 will be performed in this manner.

Figure 2.6. *A plot of the RSF values of different atomic species in silicon. In general, these are dependent on the quantity of O present (from [193]). The specific example of Mn is highlighted since these values will be used in Chapter 5.*

2.5.3 Depth Profiling

As was mentioned earlier, continuous sputtering of a surface results in its erosion and this permits depth profiling of a sample, provided that material is removed in a uniform manner within the profiled region. This can be achieved by rastering the ion beam across a surface, creating a crater of uniform depth, whilst also providing information on the spatial distribution of species within the crater. However, the data must be gated to avoid the detection of sputtered ions from the edge of the crater (near the walls) and so obtain a profile that is a true function of depth. Different chemical species are sputtered at different rates. Initially, an enhanced concentration of species that have a high sputter rate

will be detected, resulting in a reduction in the concentration of these species at the surface. However, equilibrium will become established as the number of low sputter rate atoms/clusters at the surface increases, leading to a steady-state yield that more accurately represents the chemical composition of the sample. For this reason, the first few data points of a SIMS depth profile are difficult to interpret.

The experimental set-up, including the incident beam energy and angle with respect to surface, plays an important role in both the sputtered yield and interface depths. For example, the sputtering yield is proportional to $\frac{1}{\cos\theta}$, where θ is the tilt angle (as defined in Figure 2.4) [195]. It should be noted that this relationship is only valid for tilt angles of up to 60°, since at greater angles the beam imparts less energy to the surface and so the sputtering rate drastically drops off. In addition, the depths of the collision cascades are proportional to the beam energy; at lower energies less mixing of the species from different layers occurs. When profiling abrupt changes in composition, beam-induced mixing can result in a smeared interface, with further perturbation due to instrumental effects and/or a large surface roughness [196]. The best depth resolution is obtained with lower incident beam energies and for layers near the surface (due to less mixing and a reduction in beam-induced roughness).

The SIMS depth profiles shown in Chapter 5 were obtained using an Atomika 6500 instrument, with a typical base pressure of ~10^{-8} mbar. Argon was selected as the profiling beam (incident energy of 1.25 keV) in order to minimise perturbation to the depth profiles due to chemical interaction between the beam species and surface (as would be expected for oxygen). A relatively low sample current of 30 nA was used, which resulted in a low sputter rate that permitted reasonable resolution of the thin Pc films studied. The samples were oriented such that the beam was incident at grazing a large tilt angle of $\theta = 45°$ in an effort to increase the sputtering yield and depth resolution. Craters of ~0.5 mm x ~1 mm were created (again, large dimensions were chosen to decrease the sputter rate). The crater depths were measured using an optical interferometer (Zygo), with an etch rate of typically 2.4 nm/min in bulk Si measured for the experimental conditions described here.

2.6 ELECTRONIC ABSORPTION SPECTROSCOPY

Electronic absorption spectroscopy, commonly referred to as UV-vis absorption, is a non-destructive technique for characterising samples that absorb in the visible and ultra-violet regions, typically of wavelengths between 200 nm and 900 nm. Traditionally, this method is applied to solutions and thin films of molecular species containing transition metal ions or conjugated organic molecules, since for these species electronic transitions occur within the aforementioned wavelength range [197, 198]. For inorganic compounds, absorption events can arise from transitions within the partially filled *d* or *f* orbitals, or from charge-transfer transitions. In the case of organic complexes, such as those that will be studied here, electronic excitation can occur between bonding and anti-bonding states (such as $\sigma^* \leftarrow \sigma$ and $\pi^* \leftarrow \pi$) or non-bonding and anti-bonding levels ($\sigma^* \leftarrow$ n and $\pi^* \leftarrow$n). In general, transitions to the σ^* levels occur at wavelengths of less than ~200 nm and so are often not detected by electronic absorption spectroscopy. Instead, the $\pi^* \leftarrow \pi$ transitions are most attractive to study using this technique since they correspond to observable wavelengths and are up to ~1000 times more intense than $\pi^* \leftarrow$n transitions (although these also occur in this region) [198]. In aromatic molecules, such transitions occur from the highest occupied molecular orbital (HOMO) to low-lying empty electronic levels, such as the lowest unoccupied molecular orbital (LUMO). Further structure in the absorption spectrum is often observed due to molecular vibrational modes, which is seen as additional peaks or shoulders close to the main absorption electronic absorption peaks, as was shown in the solution spectrum of CuPc in Figure 1.3.

The spectrometer compares the intensity of the incident and transmitted light after passing through the sample. Light in the visible region is provided by a tungsten lamp, whilst hydrogen or deuterium lamps generally provide UV light. The light is filtered and passed through a monochromator, which produces light of a single wavelength. For dual beam spectrometers, such as that used here, the beam is split and follows two routes of the same path-length; one optical path is directed through the sample and the other through a reference (typically the solvent or a blank substrate). The intensities of the two beams are then measured by a photomultiplier tube.

The absorbance of a material is calculated from the ratio of the intensities of the transmitted light (I_T) to incident light (I_0), known as the transmittance (T), as defined in Equation 2.10.

$$T = \frac{I_T}{I_0} \qquad [2.10]$$

The absorbance (A) can then be expressed in terms of the transmittance or percentage transmittance (%T), as outlined in Equation 2.11.

$$A = \log_{10}\left(\frac{1}{T}\right) = 2 - \log_{10} \%T \qquad [2.11]$$

Therefore, if all light passes through the sample without any absorption, $A = 0$ and $\%T = 100\%$, whereas if all light is absorbed, $A = 2$ and $\%T = 0$.

The Beer-Lambert law is commonly used to relate the absorbance of a material to the molar absorptivity (ε), which is a fundamental property of the absorbing species (it is independent of sample concentration). This is described in Equation 2.12, where b is the path-length of the solution and c is the concentration.

$$A = \varepsilon bc \qquad [2.12]$$

The Beer-Lambert law can be adapted for application to thin films, assuming that the absorbance does not saturate (i.e. remains below 2). This is achieved by relating it to the absorptivity via the density of the material (ρ), film thickness (l) and molecular weight (M_W), or to the absorption coefficient (a) as shown in Equation 2.13.

$$A = \frac{\varepsilon l \rho}{M_W} = al \qquad [2.13]$$

The electronic absorption spectra in Chapters 4 and 5 were collected using a Perkins-Elmer Lambda 950 UV/VIS spectrometer. After the background had been measured, the film samples were each mounted in turn, perpendicular to the beam, positioned beyond a mask (the mask ensured that each spectrum was measured over the same total area and in the same position within the beam, normalising intensities). The absorption was recorded as a function of incident wavelength with 1 nm resolution between 200 nm and 1000 nm. The spectra of the substrate and background were both subtracted from the raw data.

2.7 RAMAN SPECTROSCOPY

Raman spectroscopy provides information about the vibrational modes of a molecule. Vibrations generally arise from the stretching or bending of molecular bonds [197, 198], although more exotic features, such as those arising from breathing modes of conjugated organic molecules, can arise (this is the case for CuPc, as described in Section 1.2.1).

The sample is irradiated with a monochromatic light source in the visible region; most of the light passes through the sample unperturbed, however, approximately 1 in 10^5 photons interact with the molecules of the sample and are scattered [198]. The scattered photons are detected and their energies analysed by a monochromator and photomultiplier tube, with the vast majority (~99%) of the scattered photons of the same energy as the excitation source. Such scattering events give rise to an intense emission line, known as Rayleigh scattering, as shown in Figure 2.7(a). These can be thought of as either an elastic collision between the photon and molecule or as the creation of an instantaneous virtual state (the energy of which is the combination of those of the photon and ground state molecule), from which the photon is re-emitted without change to its wavelength [197]. Such a process is depicted in Figure 2.7(b).

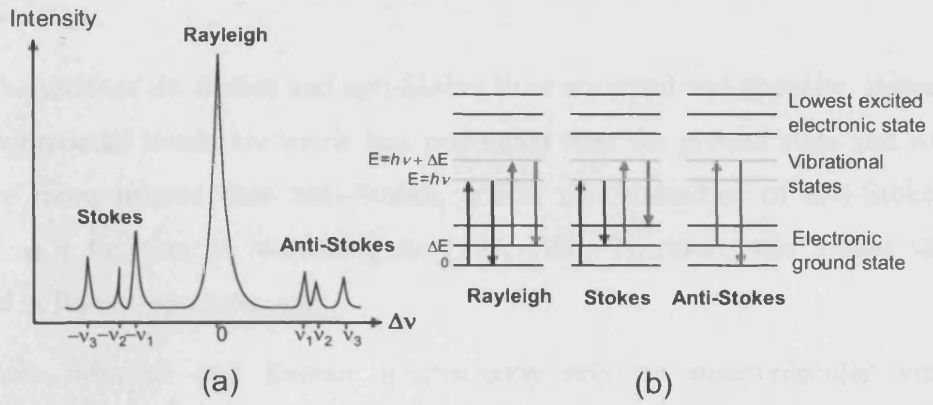

Figure 2.7. *(a) The relative intensities of Rayleigh, Stokes and anti-Stokes shifts observed when monochromatic light is incident upon a sample. (b) The electronic levels responsible for Rayleigh, Stokes and anti-Stokes shifts. Black arrows represent more intense transitions than those drawn in grey.*

Occasionally, the energy of the scattered photon is shifted from that incident upon the sample. This can be thought of as an inelastic collision and is due to a change in vibrational state of the molecule. These shifts can also be explained using the concept of virtual states, as shown in Figure 2.7(b). If the molecule is initially in its ground state and absorbs a photon to form a virtual state, it may relax to an excited vibrational level (rather than back to its original state). This results in a lower energy photon being emitted and is known as a Stokes shift. More rarely, the photon may interact with a molecule that is already in an excited vibrational state, whilst upon re-emission the molecule may return to the ground state and so the photon will have an increased energy. The latter process is known as an anti-Stokes shift. The observed shifts ($\Delta\upsilon$) are measured from comparing the incident and scattered wavelengths (denoted $\lambda_{incident}$ and $\lambda_{scattered}$ respectively), as indicated in Equation 2.14.

$$\nu = \frac{1}{\lambda_{incident}} - \frac{1}{\lambda_{scattered}} \qquad [2.14]$$

The shifts of the Stokes and anti-Stokes lines are equal and opposite. However, the excited vibrational levels are much less populated than the ground state and so Stokes shifts are more intense than anti-Stokes, whilst the intensities of anti-Stokes shifts decrease as a function of increasing $\Delta\upsilon$ [197, 198]. Therefore, the Stokes shifts are measured in Raman spectroscopy.

Both infra-red and Raman spectroscopy rely on intermolecular vibrational transitions, and so as a result often yield very similar spectra. However, there are large differences between the mechanisms responsible for the two techniques and so in general they measure different vibrational modes. Infrared spectroscopy requires a change in molecular dipole moment upon absorption of a photon [197, 198]. However, this is not necessary for Raman spectroscopy, where instead the electric field of the incident photon distorts the molecule, producing a temporary dipole moment. This requires that the polarizability of the molecule is changed by the vibration. The induced dipole moment (P) is proportional to the external electric field that induces the distortion (E), as is shown in Equation 2.15, where α (a tensor) is the polarizability of the molecule.

$$\vec{P} = \alpha \vec{E} \qquad [2.15]$$

In general, the excitation source is chosen such that the energy of the incident photons does not coincide with the electronic absorption of the sample. However, if the laser wavelength is chosen to correspond to a region where the sample is absorbing, this will lead to an enhanced yield. In particular, vibrations arising due to the chromophore will have a selectively increased relative yield with respect to those from the rest of the molecule.

A Renishaw Raman Spectrometer was used to collect the data described in Section 5.1, using a green laser ($\lambda = 514.5$ nm, between electronic absorption bands) with a typical power of 0.97 mW. A cover was placed over the spectrometer to prevent spurious signal from the ambient lights.

2.8 ELECTRON PARAMAGNETIC RESONANCE

Electron paramagnetic resonance (EPR), also commonly known as electron spin resonance (ESR) and electron magnetic resonance (EMR), is a technique that allows the study of paramagnetic species, such as transition metal ions and free radicals, through the detection of unpaired electron spins [199]. The general principle of measurement is very similar to that of nuclear magnetic resonance (NMR), but in EPR it is the electron spins (rather than nuclear spins) that are excited. Although the requirement in EPR for unpaired electron spins renders many systems undetectable, this can be advantageous since signal only arises from the species of interest (solvents and substrates are often invisible). It is a non-destructive technique that has a wide range of applications, from the identification of paramagnetic species and subsequent characterisation of their electronic and geometric structures in Chemistry and Biology, to single-spin detection (which is of interest for spintronics and quantum computing applications).

2.8.1 Zeeman Splitting

The first experimental evidence that electrons possess an intrinsic angular momentum (spin) was achieved by the Stern-Gerlach experiment (1922), in which a directional beam of silver atoms was passed through an inhomogeneous magnetic field and seen to split into two discrete peaks. This demonstrated that the spin of electrons is quantized, with only two possible values, known as "spin up" and "spin down". Each electron possesses a spin of $S = ½$, with magnetic moments $m_s = \pm ½$. In a magnetic field, the spin of the electron aligns either parallel or antiparallel to the field direction, causing a split in energy levels, known as the Zeeman effect. In order for this effect to be observed, it is

necessary that at least a component of the spin is parallel to the magnetic field direction. As shown in Figure 2.8, the size of the splitting is proportional to the magnitude of the applied magnetic field (of magnitude B_z, applied in the z-direction), as summarised in Equation 2.16 in which g is the g-factor (for the case of the free electron, this is known as the Landé g-factor with a value of 2.0023) and μ_B is the Bohr magneton.

$$\Delta E = g\mu_B B_Z \qquad [2.16]$$

The case shown in Figure 2.8 is for a $S = ½$ system in which there are two levels in a magnetic field. In general, the Zeeman splitting leads to $(2S+1)$ levels, which correspond to values of $m_s = -S, -S+1, \ldots, S-1, S$.

Figure 2.8. *The Zeeman splitting of electrons due to their spin when placed in a magnetic field (adapted from [197]).*

The populations of two non-degenerate energy levels for a statistical ensemble of electrons spins are determined by the Maxwell-Boltzmann distribution. This is summarised in Equation 2.17, in which $N_{+½}$ corresponds to the number of electrons

aligned antiparallel to the magnetic field (the upper level in Figure 2.8, $m_s = +½$) whilst $N_{-½}$ is the number of electrons aligned parallel to the field (the lower level, $m_s = -½$).

$$\frac{N_{+1/2}}{N_{-1/2}} = e^{-\Delta E/k_B T} \qquad [2.17]$$

At room temperature and for the typical magnetic fields applied in EPR (typical fields of 250 mT – 400 mT have been used here), the lower level is significantly more populated. This means that when photons (in this case microwaves) of energy $h\nu = \Delta E$ are introduced to the sample region, they are absorbed (they excite an electron from the lower to upper level) and this absorption event is detected by the spectrometer. A sharp absorption line is therefore observed if the resonance condition given in Equation 2.18 is met.

$$h\nu = g\mu_B B_Z \qquad [2.18]$$

In principle, the EPR signal (absorption of microwaves) could be measured by either keeping the magnetic field constant whilst varying the microwave frequency, or by sweeping the magnetic field and holding the microwave frequency fixed; in general, it is the latter case which is employed. In order to increase the sensitivity of the measurement, a small a.c. magnetic field is superimposed onto the main applied magnetic field, and this permits the detection of the first derivative of the absorption spectra. This is known as continuous wave (CW) EPR (this method will be used in Chapter 4 and so is described in the following) for which the spectra are presented as the first derivative of the absorption profile. An example of the absorption profile of a free electron and its first derivative are shown in Figure 2.9.

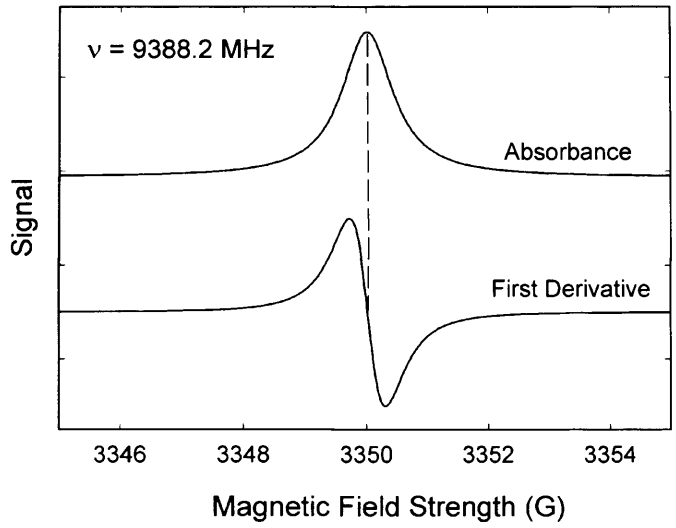

Figure 2.9. *The absorbance of microwaves due to Zeeman splitting of a free electron (top spectrum), along with the signal as measured in continuous wave EPR (first derivative, bottom spectrum).*

2.8.2 Hyperfine Splittings

For real systems, unpaired electrons not only experience the applied magnetic field but are also sensitive to any local magnetic fields due to nearby atoms or molecules, which cause them to gain or lose angular momentum through spin-orbit coupling. When a measurement is performed, this is reflected in the magnetic field at which resonance occurs and is interpreted as a change in the value of the *g*-factor. In the majority of cases, the value of *g* is very close to the Landé *g*-factor, however, larger deviations from this value are observed for transition metal ions.

In addition to the spin of an electron, the atomic nuclei also possess their own nuclear spin (*I*). The value of the nuclear spin can vary for different elements and isotopes; for example for H, $I = 1$, for Cu^{63} and Cu^{65}, $I = 3/2$, whilst $I = 1$ for N^{14} but $I = 1/2$ for N^{15}. The nuclear spin leads to a further non-degeneracy when in an applied

magnetic field that is analogous to that of electron spin with $(2I+1)$ levels, in this case known as the nuclear Zeeman effect. Electrons possess significantly larger magnetic moments than nuclei due to the large difference in their respective masses, and so the nuclear Zeeman effect produces a smaller energy shift than the electron Zeeman effect.

The unpaired electrons can also interact with local (neighbouring) nuclear spins, known as hyperfine coupling, wherein the local magnetic field that the electron experiences is modified by the magnetic moment of n nearby nuclei of spin I, giving rise to $(2nI+1)$ additional EPR lines. The relative intensities of the hyperfine splittings are given by the binomial expansion coefficients. For example, interaction with a Cu nucleus gives rise to 4 lines (intensity ratios 1:3:3:1) whilst interaction with four N^{14} nuclei leads to 9 hyperfine lines (Cu and N hyperfine splittings are important for the work presented in Chapter 4). The spacing of these lines indicates the degree of interaction, with the magnitude of the hyperfine splitting given by Equation 2.19, where $\boldsymbol{A}$ is the hyperfine coupling tensor, and $\boldsymbol{S}$ and $\boldsymbol{I}$ are the electron and nuclear spin vectors respectively.

$$E = \boldsymbol{I}.\boldsymbol{A}.\boldsymbol{S} \qquad [2.19]$$

The effect of nuclear Zeeman splitting and hyperfine coupling on a system containing one electron and one proton is summarised in Figure 2.10. Absorption transitions must satisfy the selection rules of $\Delta m_s = \pm 1$, $\Delta m_I = 0$, with those allowed denoted by arrows in the figure. Both the g-factor and hyperfine interactions can be anisotropic and can lead to detailed information about the physical and electronic structure of the species studied. In addition, if the concentration of unpaired electron spins is sufficiently high, they can interact with each other via dipole-dipole interactions which induces a broadening of the EPR lineshape. The dipolar coupling is expressed in Equation 2.20, where g_N and β_N are the nuclear g-factor and nuclear magneton respectively, and r is the separation between the electron spins. It should be noted that the degree of interaction decreases with r^3.

$$H = g\mu_B g_N \beta_N \left[\frac{I.S}{r^3} - \frac{3(I.r)(S.r)}{r^5} \right] \qquad [2.20]$$

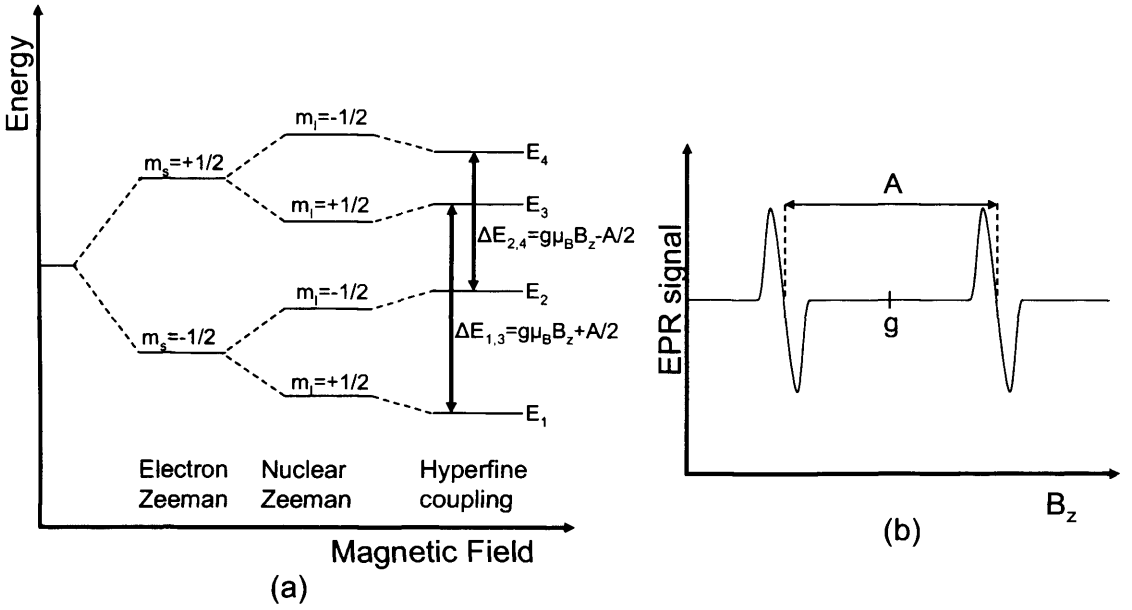

Figure 2.10. *(a) Schematic of the energy level splittings due to the electron Zeeman, nuclear Zeeman and hyperfine coupling for a one electron, one proton system, and (b) the resulting CW EPR signal.*

2.8.3 Experimental Conditions

A Bruker ESP300 spectrometer was used to measure the EPR spectra of the samples studied in Chapter 4. These were placed into a quartz tube (containing no unpaired electrons) which was loaded into the resonator cavity and cryogenically cooled to temperatures between 10 K and 15 K. Care was taken to align the thin films with respect to each other, with their orientation within the magnetic field also noted. Microwaves of frequency 9.37 GHz (so called "X-band" measurements) were used to irradiate the sample, with their absorption measured by the spectrometer. The microwave cavity was

situated between two superconducting magnets, with the magnetic field swept between 260 mT and 360 mT. Variations in microwave absorbance were then measured (in derivative mode) as a function of the applied magnetic field.

2.9 X-RAY ABSORPTION SPECTROSCOPY

X-ray absorption spectroscopy (XAS) is a technique that is sensitive to the nature and local chemical environment of atomic species. Here, x-rays are absorbed by atoms and lead to the excitation of core electrons to the continuum [190, 200]. Detailed information can be gained from monitoring the x-ray absorption profile as a function of energy, close to the onset of absorption (there exists a threshold below which x-rays are not absorbed, as will be described in further detail shortly). In this region, the structure of the absorption profile is dependent on the oxidation state, co-ordination number and chemical species of neighbouring atoms (see Section 2.9.4). In addition, small oscillations are observed just beyond the absorption threshold due to the interference of outgoing photoelectrons that are reflected by neighbouring atoms, and these can be used to determine the bond lengths of the absorbing species (as will be described in Section 2.9.5).

2.9.1 X-rays

X-rays provide a non-destructive tool for probing the structure and atomic arrangement of a sample [200]. Measurements can be performed on any material (solid, liquid, gas, crystalline, amorphous etc), whilst the sample can be subjected to non-ambient temperatures or pressures during measurement. Typical energies of x-rays are between 100 eV and 10^6 eV which corresponds to wavelengths of 0.01 Å to 100 Å. X-rays are usually generated by a sudden deceleration of fast moving electrons at a target material, which transfer their kinetic energy to the target atoms, knocking electrons out of the inner atomic orbitals and so creating vacancies in the core shell. Electrons from the outer levels fill the holes, with the energy released either as ejected electrons (known as an Auger

process) or as emitted x-ray photons. Typically, the x-ray spectrum created in this manner consists of a broad continuum (bremsstrahlung) superimposed with characteristic sharp lines. The lines are of well defined energy and correspond to electronic transitions (as will be discussed shortly); these will be used in the techniques described in Sections 2.10 and 2.11. However, the XAS measurements in Chapter 5 were performed with synchrotron radiation, since this provides a higher intensity beam.

2.9.2 Synchrotron Radiation

Synchrotron radiation is generated from accelerating electrons to relativistic speeds in a magnetic field, at which point energetic photons are emitted [190]. The photons are of high density, with brilliances of up to 10^{16} photons s^{-1} mm^{-2} $mrad^{-2}$, which is six orders of magnitude more intense than the sun. In addition, the radiation is plane polarised, is tuneable between ~0.1 eV to ~1 MeV and is pulsed (~0.1 ns pulses separated by a few ns). Originally, synchrotron experiments were performed at particle accelerators (synchrotron radiation is a by-product at these facilities), however more recently, specialist synchrotron facilities have been developed.

To produce the synchrotron radiation, electrons are accelerated to high speeds in several stages, until their energies are of the order of a few MeV. The electron beam is injected into a small booster synchrotron in bunches wherein the electrons are further accelerated to energies of ~500 MeV, at which point they are tangentially injected into the main storage ring. In the storage and booster rings, strong magnetic fields are applied to guide the electrons around a circular path (in ultra high vacuum conditions) whilst being further accelerated by RF radiation; they reach energies of ~2 GeV in the main storage ring. At such energies they are travelling close to the speed of light and so emit radiation from the infra-red to hard x-rays [190]. A new beam is generally injected every 12 to 48 hours to compensate for energy losses that arise from collisions between the electrons and particles in the vacuum. In order to perform x-ray absorption experiments, the energy of the photons must be selected. This is performed in an optics hutch where monochromators (for example two single crystals of Si(111), as used for the experiments described in Chapter 5) to select the required energies (in this case 2–30 keV). The

samples are mounted in the experimental hutch and are positioned in the x-ray beam, whilst the experiments are controlled from a separate cabin. The measurements described in Chapter 5 were performed at Station ID26 at the European Synchrotron Radiation Facility (ESRF), Grenoble.

2.9.3 X-ray Absorption

As has already been described, transitions between electronic levels can give rise to either the absorption or emission of x-ray photons. Examples of such transitions are shown in Figure 2.11(a). Absorption events arise when electrons from the electronic levels K, L, M, N... (i.e. of principle quantum numbers n = 1, 2, 3, 4...) are excited to the continuum by an x-ray photon with sufficient energy. In the case of *K*-edge absorption only one line is observed, whereas for the L level up to three absorption events will occur from the 2s, $2p_{1/2}$ and $2p_{3/2}$ orbitals (these are known as L_I, L_{II} and L_{III} absorptions respectively). The XAS experiments described in Chapter 5 were performed at the Mn *K*-edge. Alternatively, transitions can occur between different electronic shells, and these must in general obey the selection rule of $\Delta l = \pm 1$. For example, two emission lines are observed between the K and L shells corresponding to transitions between the 1s and 2p orbitals; in the case of emission (as depicted by blue arrows in the figure), these give rise to the characteristic K_α lines.

Generally, absorption is monitored by measuring the incident and transmitted intensity (I_0 and I respectively) of the x-ray beam that passes through the sample using ion gas chambers. From such measurements, the linear absorption coefficient (μ) of a sample of thickness x can be calculated from Equation 2.21.

$$\mu x = \ln\left(\frac{I_0}{I}\right) \qquad [2.21]$$

Figure 2.11. *(a) An energy level diagram showing examples of electronic transitions which either arise from x-ray absorption (red) or result in x-ray emission (blue) (adapted from [200]). (b) A typical x-ray absorption spectrum, showing the positions of the pre-edge, absorption edge, EXAFS oscillations and XANES (red box) (adapted from [201]).*

However, since the samples to be studied in Chapter 5 are very dilute and are concentrated towards the surface, the absorption was measured by fluorescence mode detection. As has already been described, *K*-edge absorption results in the creation of a hole in the 1*s* level. Such a state is unstable and so the atoms relax by demotion of an outer electron to fill the hole; the excess energy can be emitted as a fluorescent x-ray. The intensity of the fluorescent x-rays (F) was measured as a function of incident x-ray energy using a 13-element Ge fluorescence detector positioned close to the sample, with the absorption coefficient calculated from Equation 2.22.

$$\mu x = \frac{F}{I_0} \qquad [2.22]$$

Plotting the measured absorption coefficient as a function of incident x-ray energy produces an absorption profile, an example of which is shown in Figure 2.11(b). As seen in the figure, a sharp rise in the absorption spectrum occurs at a well-defined energy; at energies above this the sample absorbs x-rays, whereas below this energy x-rays are not generally absorbed (although sometimes small peaks are observed, as will be described shortly). The energy that this sharp rise occurs at is known as the absorption edge, and is generally defined as the maximum of the first derivative of the absorption spectrum. This energy corresponds to the point at which core level electrons are excited to the continuum. Sometimes, small peaks are observed just below the absorption edge; these are known as pre-edge features and are due to the promotion of core electrons to levels below the continuum (these are often forbidden transitions, as will be described in Section 2.9.4). At higher energies, oscillations are observed in the absorption coefficient, known as extended x-ray absorption fine structure (EXAFS). Such oscillations will be discussed in Section 2.9.5.

2.9.4 X-ray Absorption Near-Edge Structures

X-ray absorption near-edge structures (XANES) can be used to gain information about the oxidation state and co-ordination number of the absorbing species. As is shown in Figure 2.12, the position of the Mn edge is highly dependent on oxidation state, with the spectra of higher oxidation states increasingly shifted to higher energies. Therefore, the oxidation state of a sample can be determined by comparing the edge position to that of known reference compounds. In addition, the pre-edge features can give information about the local chemical environment and binding geometry of the species. For the example of Mn, a small peak arises due to electronic promotion from the 1s to 3d levels; this should be forbidden (due to the $\Delta l = \pm 1$ selection rule), however for certain nearest neighbours (for example oxygen) the d-orbital takes on p-like character and so this orbital-mixing leads to some 1s to 3d transitions [202]. This effect is particularly apparent for tetrahedral complexes (such as MnO [203]) and can therefore be used to assign this particular environment.

Figure 2.12. *The x-ray absorption spectra of a series of manganese oxides (adapted from [204]).*

2.9.5 Extended X-ray Absorption Fine Structure

More detailed information on the local chemical environment of the absorbing species can be obtained from analysis of the EXAFS oscillations. Upon x-ray absorption, a photoelectron is emitted; this can be treated as a spherical wave propagating radially outwards from the absorbing atom. As is shown in Figure 2.13(a), this wave is reflected by neighbouring atoms which leads to an interference effect. Shells can be defined as groups of atoms of the same chemical species, all of which are the same distance from the absorbing atom. The interference is dependent on the distance between the absorbing atom and its neighbours (the bond length), in addition to the chemical species of the surrounding atoms, whilst its intensity is dependent on the co-ordination number (the number of atoms in each shell). Frequently, the measured oscillations occur from the innermost three or four shells, and so one of the most effective methods for analysing the data is to perform a Fourier transform to determine the frequencies (and therefore distances) responsible for the oscillations.

Figure 2.13. *(a) A schematic of the interference of photoelectrons due to scattering from neighbouring atoms that is responsible for EXAFS oscillations (from [190]). (b) Normalisation of raw fluorescence mode EXAFS data by fitting to μ_0 (adapted from [201]).*

A series of steps are required to analyse EXAFS data, after which the data can be theoretically modelled to determine the co-ordination numbers and bond distances for the innermost shells. As seen in Figure 2.13(b), at high energies the absorption tail is not constant; this is due to the sample spectrum being different to that of a single atom (for which an absorption coefficient of μ_0 would be expected). Since the spectrum of μ_0(E) cannot be determined experimentally, this is approximated through a linear extension of the smooth part of $\mu(E)$ at higher energies, as shown in Figure 2.13(b). The data can then be normalised, with the change in absorption coefficient ($\Delta\mu(E)$) calculated, as defined by Equation 2.23 and shown in the figure. From this, an expression for the interference function ($\chi(E)$) can be determined, as outlined in Equation 2.24.

$$\Delta\mu(E) = \mu(E) - \mu_0(E) \qquad [2.23]$$

$$\chi(E) = \frac{\Delta\mu}{\mu_0} \qquad [2.24]$$

In order to fit the data, it is easier if the interference function is converted to be a function of the photoelectron wavevector (k) rather than energy. These quantities are related via the mass of an electron (m), Planck's constant ($\hbar$) and the absorption edge position (E_0), as given in Equation 2.25.

$$k = \sqrt{\frac{2m}{\hbar^2}(E - E_0)} \qquad [2.25]$$

Although comparison of the processed data with that of known reference samples can be used to determine the chemical composition, it is more common to theoretically model the data and compare with that determined experimentally. This is achieved by using the EXAFS equation (Equation 2.26), where N is the number of neighbouring atoms, R is the distance to the neighbouring atom, σ^2 is the disorder in the neighbour distance, $f(k)$ and $\delta(k)$ are scattering properties of the atoms in each shell. The interference function $\chi(k)$ is summed over each of the j shells.

$$\chi(k) = \sum_j \frac{N_j f_j(k) e^{-2k^2\sigma_j^2}}{kR_j^{\,2}} \sin[2kR_j\delta_j(k)] \qquad [2.26]$$

The theoretical modelling is generally performed by iterative fitting (using initial estimates of the fitting parameters) and comparing to the experimental spectrum of $\chi(k)$ and its Fourier transform.

2.10 X-RAY PHOTOELECTRON SPECTROSCOPY

X-ray photoelectron spectroscopy (XPS), also known as electron spectroscopy for chemical analysis (ESCA), can be used to determine the elemental composition and local chemical environment of a surface [190]. X-ray photons are directed onto a surface, resulting in the emission of photoelectrons, whose kinetic energies are measured and related to the binding energies (which will be defined shortly) of the species present. Since the photoelectrons quickly lose energy as a result of inelastic scattering, only those emitted by atoms from within approximately 10 nm of the surface are detected, rendering XPS a highly surface sensitive technique. The chemical composition of the illuminated region (for all elements except H and He) is determined from the measured electron binding energies, whilst the respective intensities provide information about the relative elemental abundances. High resolution spectra yield information about the local chemical and electronic states of the species present. In addition, the chemical composition in terms of surface position or depth can be obtained (these are outside the scope of this work).

In this technique, monochromatic x-ray photons are incident upon the surface atoms; the x-rays can either pass straight through the atoms, be scattered (either elastically or inelastically) or transfer their energy to core-level electrons. If the latter process occurs, a core electron can be emitted (provided the energy of the incident photon is greater than a threshold, known as the binding energy) and a core hole is created. The binding energy (E_B) is the energy required to excite an electron from the core shell to the continuum and is dependent on the atomic species, electronic level excited and any bonding to neighbouring atoms (bound atoms alter the local electron distribution). In XPS, the kinetic energy (E_K) of the emitted photoelectrons is measured. This is related to the binding energy, as expressed in Equation 2.27, in which the work function of the spectrometer (φ) is the additional energy required to remove an electron from the surface (for conductive samples) and $h\nu$ is the energy of the incident x-ray.

$$E_B = h\nu - E_K - \phi \qquad [2.27]$$

If the other electrons of the atom do not re-arrange themselves upon emission of the photoelectron, then the binding energy is equal and opposite of the orbital energy for the ejected photoelectron (ε), as expressed by Koopman's theorem (Equation 2.28).

$$E_B \approx -\varepsilon \qquad [2.28]$$

However, this approximation is not valid since the remaining electrons do re-arrange themselves, in order to minimise the energy of the ionised electron and partially shield the core hole. The reduction in energy caused by this re-arrangement is known as the relaxation energy, E_r. In addition, there are other correction factors due to electron correlation (ε_{corr}) and relativistic effects (ε_{rel}), although these are generally negligible. An expression for the binding energy in terms of these factors is given in Equation 2.29.

$$E_B = -\varepsilon - E_r - \varepsilon_{corr} - \varepsilon_{rel} \qquad [2.29]$$

A typical XPS spectrum contains many sharp lines, and these are due to core electrons being emitted from the various elements present at the sample surface. In addition, less intense (Auger) peaks are detected from outer electrons that are ejected as a result of the rearrangement of core level electrons (to fill the core hole). The width of each spectral line is determined not only by the instrumental resolution, but also by the lifetime of the core hole; holes created in the innermost levels (e.g. 1*s*) have shorter lifetimes and so have wider peaks (due to Heisenberg's uncertainty principle, the line-width is inversely proportional to the hole lifetime). The measured intensities of the peaks vary for different electronic levels and across the periodic table; this is mainly due to variations in the principal (n) and angular momentum (l) quantum numbers. In order to correct for this, the integrated area of each peak must be divided by the known sensitivity factor (for example, as given in [205, 206]).

Shifts in the binding energies of elements can be a result of different oxidation states; the binding energy of a species generally increases with increasing oxidation state. In addition, these shifts can be due to different chemical environments, with local bonding often having a significant effect on the relaxation energy (Equation 2.29). Once a photoelectron has been emitted it can interact with the other electrons and excite a valence electron to an unoccupied state, thus losing some of its energy. This gives rise to additional peaks in the XPS spectra that occur at slightly lower binding energies, known as shake-up satellites. Another important spectral feature is the splitting of the *p*, *d* and *f* orbitals. After the photoemission of an electron from the 3*p* orbital, the remaining electron can be in a spin up or spin down state; a magnetic interaction between this electron and its orbital angular momentum (*j*) gives rise to a splitting of the degenerate states (spin-orbit coupling). For the case of the *p* orbital, this means that the $p_{1/2}$ and $p_{3/2}$ levels are split with an intensity ratio of 1:2 (given by $(2j + 1)$ where $j = (l + s)$, $l = 1$ and $s = \pm 1/2$).

The XPS measurements discussed in Chapter 5 were performed using an Escalab 220i-XL instrument* (typical base pressure of 2×10^{-9} mbar). Al K_α x-rays of 1486.6 eV were incident upon the sample with a spot size of 1 mm x 0.25 mm. The photoelectrons were collected and their kinetic energy measured using a hemispherical electrostatic energy analyzer.

2.11 X-RAY DIFFRACTION

X-ray diffraction (XRD) is used to investigate the crystallographic order within a solid sample. This technique is based on the ability of atoms to diffract x-rays (via their electron cloud); atoms with higher atomic mass act as stronger scattering centres. For an ordered array of atoms or molecules, diffraction peaks will be observed at specific beam-sample angles which are dependent on the crystal structure of the sample (as given by

* Measurements performed with Geoff Hyett and Rob Palgrave.

Bragg's law, which will be described shortly). By measuring the intensity of the diffracted x-rays as a function of angle, a diffraction spectrum can be constructed, from which the crystal structure can be determined. Information about crystallite size and the degree of order within a sample can be obtained from the width of the peaks, as will be discussed in Chapter 4.

2.11.1 Crystal Structure

The unit cell is used to define the crystal structure; this is an arrangement of atoms of the smallest volume from which the crystal lattice can be constructed (when many unit cells are stacked together in a three dimensional manner). The lengths and angles that make up the unit cell are known as the lattice parameters, and are defined as in Figure 2.14(a). There are only seven crystal systems that can be used to construct a three dimensional crystal from the lattice parameters in such a way that each lattice point has an identical environment to that around every other lattice point [207]. These are known as triclinic, monoclinic, orthorhombic, hexagonal, rhombohedral, tetragonal and cubic systems, and in turn make up the 14 Bravais lattices, when combined with the possible lattice centrings (for example, face centred cubic and body centred cubic).

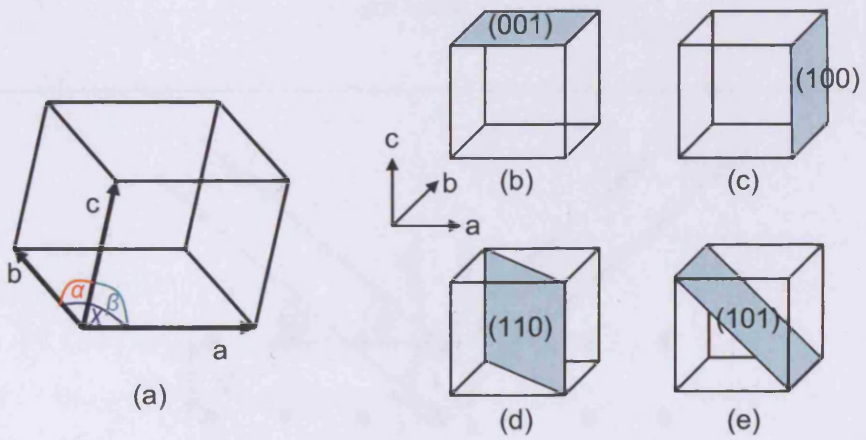

Figure 2.14. *(a) Definition of the angles and lengths that make up a unit cell. (b)-(e) A selection of planes of a cubic unit cell, as denoted by the Miller indices shown.*

The directions and planes within a Bravais lattice are defined by Miller indices. These are written as (*h k l*) to denote planes in the reciprocal lattice where *h*, *k*, and *l* are integers. Examples of a selection of planes with different Miller indices for a cubic lattice are given in Figures 2.14(b)-(e). It should be noted that [*h k l*] denotes a direction in the basis of the direct lattice vectors (rather than the reciprocal lattice), and this notation will be used in Chapter 3. The lattice vectors in reciprocal space are inversely proportional to those in real space.

2.11.2 Bragg's Law

X-ray diffraction measurements are performed using a monochromatic, collimated x-ray beam, which is directed onto the sample forming an angle θ, as shown in Figure 2.15. At specific values of θ there will be constructive interference from beams that are diffracted from successive horizontal lattice planes (separated by a distance of d). This occurs when the extra additional pathlength ($2x$), denoted by the two red arrows in the figure, is equal to an integer multiple of the wavelength (λ), as outlined in Equation 2.30.

$$n\lambda = 2x \qquad [2.30]$$

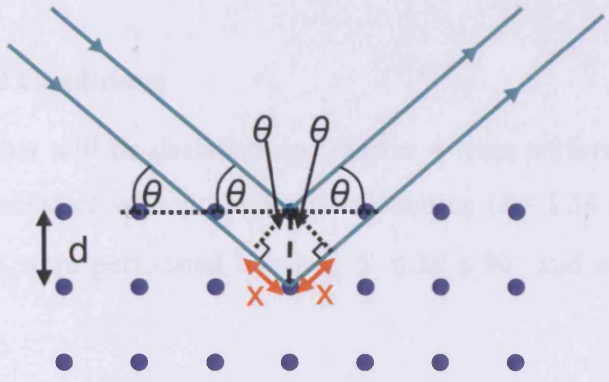

Figure 2.15. *A schematic of the diffraction of x-rays from a crystal lattice in which scattering centres (atoms or molecules) are shown as dark blue spheres whilst the x-ray beam is shown as a mid-blue line.*

From the figure it is apparent that the distance x can be related to the separation between the crystal planes via simple trigonometry, as given by Equation 2.31.

$$x = d \sin \theta \qquad [2.31]$$

This can then be combined with Equation 2.30 to give Bragg's law (Equation 2.32).

$$n\lambda = 2d \sin \theta \qquad [2.32]$$

The x-ray diffraction spectra described in Chapter 4 were acquired in θ-2θ mode, in which the incident x-ray beam is fixed and the sample is rotated in a stepwise manner by and angle of θ, whilst the detector is moved through an angle of 2θ. From an experimental plot of the diffracted x-ray intensity as a function of 2θ, values of d can be calculated, using Bragg's law.

2.11.3 Experimental Conditions

The measurements that will be described in Chapter 4 were performed using a Phillips X'pert x-ray diffractometer with a Cu $K\alpha$ x-ray source ($\lambda = 1.54$ Å) and step size of 0.02°. Typical scans were performed between $5^\circ \leq 2\theta \leq 50^\circ$ and accumulated for 7 to 16 hours.

Chapter Three: CuPc Growth on Passivated Si(100) Surfaces

It is of interest to determine the morphology of ultra-thin CuPc films on technologically important substrates such as silicon. Scanning tunnelling microscopy is used here to study the growth modes of CuPc on three surfaces; Si(100) passivated with either hydrogen or ammonia (Si(100):H or Si(100):NH_3 respectively) and a Si(100) surface containing Bi nanolines also passivated with ammonia (Si(100):NH_3/Bi). Molecular islands are observed on all surfaces. The islands are of a uniform height corresponding to upright standing CuPc molecules and do not preferentially form at step edges, defects or in the vicinity of Bi nanolines. Different global morphologies are observed on the H or NH_3 passivated surfaces, wherein larger, more isolated and ordered molecular islands are formed on Si(100):NH_3. These differences are attributed to an enhanced molecular mobility on this surface arising from a repulsive interaction between the Pc^- ligand and N lone pairs of the Si(100):NH_3 surface. Molecular columns can be resolved and these run across the surfaces, forming an angle of ±64° to [011] directions of the Si substrate, with higher order CuPc layers following the morphology of those below. Detailed images in which individual molecular features can be resolved have allowed a model for molecular orientation with respect to the Si dimer rows to be constructed, in which strong similarities with the bulk α-phase are noted suggesting that the initial stages of formation of this phase are being observed.

This chapter will present studies of the growth of CuPc on a range of passivated Si(100) surfaces. As has already been described in Chapter 1, the relative strengths of the molecule-substrate and intermolecular interactions play an important role in the growth morphology of ultra-thin films. In particular, for CuPc monolayers on strongly interacting substrates the molecules lay flat against the substrate in either a disordered manner, for

example as seen on clean Si(100) surfaces [14, 52, 53], or forming ordered arrays, as seen on metallic surfaces [54–57, 208, 209] and III-V semiconductors [58]. In contrast, on polycrystalline and amorphous substrates where the molecule-substrate interaction is reduced, parallel stacks of molecules are formed wherein the molecular plane is perpendicular to the substrate [50].

One of the aims of this work is to determine the morphology of ultra-thin CuPc films on Si(100) surfaces passivated with either NH_3 or H. These surfaces will be denoted Si(100):NH_3 and Si(100):H respectively, whilst schematics of the two surfaces are shown in Figure 3.1. When an NH_3 molecule is absorbed on a clean Si(100) surface it dissociates into a NH_2 group and H atom which passivate the Si dangling bonds of the dimer row (as shown in the figure), resulting in the presence of N lone pairs at the surface [210]. The NH_2 groups are known to form both linear and zigzag arrangements; the former case is depicted in Figure 3.1, whilst for zigzag patterns the position of the NH_2 and H groups along the alternate dimer rows. Small, localised regions of each of these arrangements are observed across the surface but overall the distribution of the NH_2 groups is close to random [211]. For the case of Si(100):H, all Si dangling bonds are terminated by H atoms, producing a more uniform surface.

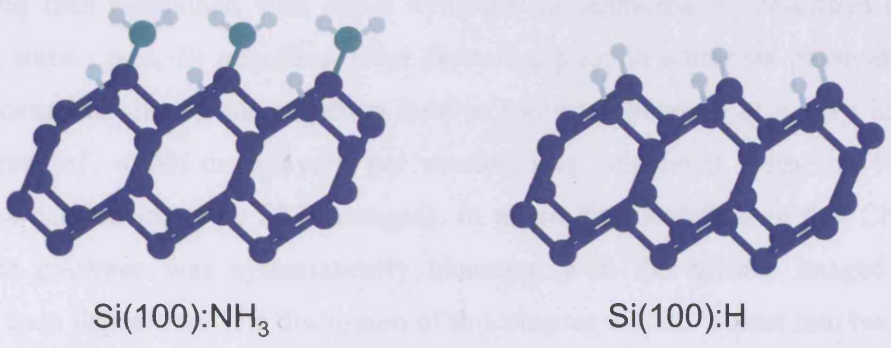

Figure 3.1. *Schematics of the Si(100):NH_3 and Si(100):H surfaces. Si atoms are shown in dark blue, whilst turquoise and light blue spheres represent N and H atoms respectively.*

The other main aim of this chapter is to investigate the possibility of the CuPc molecules templating to Bi nanolines. For this, Bi nanolines were deposited in-situ onto a clean Si(100) wafer which was subsequently passivated with NH_3 to form a Si(100):NH_3/Bi surface. The nanolines self-assemble on the Si(100) surface forming atomically straight pairs of Bi rows that are 1.5 nm wide and run for up to microns in length along the [011] substrate direction. A detailed study of the Bi nanolines is outside the scope of this work and has been reported elsewhere (a review of their properties is presented in [178]). Importantly, metals such as In and Ag have been observed to template to these structures after NH_3 passivation [212, 213], suggesting that they provide more reactive sites than the NH_2 or H groups. In addition, their width is close to the dimensions of the CuPc molecule [14] and so it seems feasible that the molecules would preferentially adsorb onto these structures. It should be noted that since this work was performed, it has been reported that CuPc molecules do not adsorb onto Bi nanolines on clean Si(100) surface (i.e. without passivation) and instead are pinned by Si dangling bonds [214]. This is not surprising as CuPc molecules are known to interact strongly with the Si(100) surface, as has already been described, and does not necessarily imply that molecular templating will not be observed on the Si(100):NH_3/Bi surface since a weaker interaction strength is anticipated between the CuPc and passivating layer.

The surfaces were created in-situ by the preparation of a clean Si(100) surface which was then passivated with either hydrogen or ammonia, as described in Section 2.1.1. In some cases, Bi nanolines were deposited prior to ammonia passivation. CuPc was deposited in-situ on the substrate held at room temperature at a very low flux (a typical rate of ~0.005 monolayers per minute was calculated from the total CuPc coverages derived from the STM images). In all studies described in this Chapter, the molecular coverage was systematically increased with the surface imaged by STM between each deposition. The discussion of this chapter will be broken into two sections; in Section 3.1 the surface morphology will be discussed as a function of increased molecular coverage on the surfaces, whilst Section 3.2 will comprise a more detailed discussion of molecular orientation with respect to the substrate. All lengths quoted are calculated from performing multiple measurements, with the standard error calculated (from the standard deviation) in all cases.

This work was performed during a 10 week internship funded by the International Centre for Young Scientists at the National Institute of Materials Science, Tsukuba, Japan.

3.1 GLOBAL MORPHOLOGY: MOLECULAR ISLAND GROWTH

In this section, studies will focus on the large-scale morphology of the CuPc structures formed on the passivated Si(100) surfaces as a function of increasing molecular coverage (Sections 3.1.1–3.1.3). In Section 3.1.4, observed differences in the morphology as a function of coverage on the Si(100):NH_3 and Si(100):H surfaces will be discussed and explanations for any trends offered.

3.1.1 Initial Stages of CuPc Deposition

Initially, a very low coverage of CuPc was deposited onto the freshly prepared surfaces; the STM images show the appearance of many small features scattered across the surface, as seen in Figure 3.2. Images obtained from each of the passivated Si surfaces show a similar morphology (examples on the Si(100):H and Si(100):NH_3/Bi surfaces are given). The features are distributed in a random and homogeneous manner, with no preferential formation of clusters or nucleation at Si step edges. Upon close inspection, these features are seen to frequently comprise four lobes, as shown in the inset of Figure 3.2(a). In addition, they all appear to be of similar dimensions, typically 1.7 ± 0.2 nm x 1.7 ± 0.2 nm and apparent height of 0.7 ± 0.1 nm. These lateral dimensions are close to that known for CuPc (as shown in Figure 1.1) which, in addition to the observed four-lobed appearance, permits these features to be attributed to CuPc molecules lying parallel to the substrate.

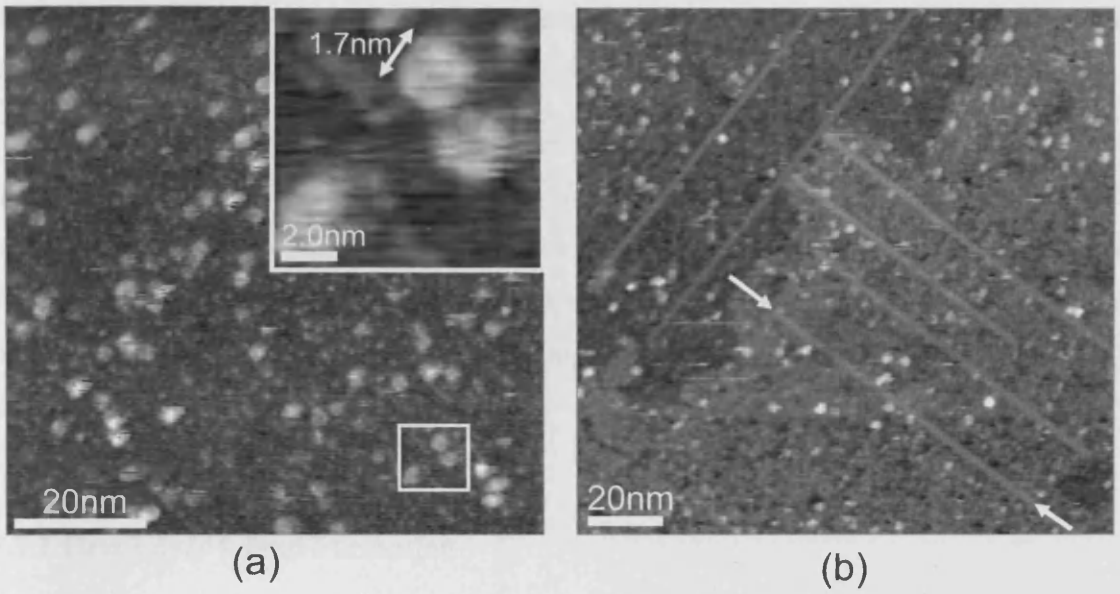

Figure 3.2. *Typical STM images of (a) the Si(100):H and (b) the Si(100):NH_3/Bi surfaces after a short deposition of CuPc (-2.00 V, 0.200 nA). The inset to (a) is taken from the boxed region, whilst the white arrows in (b) highlight a Bi nanoline structure.*

As described in Section 1.2.2, Hersam *et al.* have shown that the deposition of CuPc onto Si(100):H surfaces where H atoms have been selectively removed results in the pinning of CuPc molecules by the exposed Si dangling bonds [79, 80]. These authors demonstrated that CuPc molecules can interact with the dangling bond via the central Cu atom or through the organic ligand, with the former interaction being more probable and leading to the molecules appearing bright when probed with tunnelling conditions similar to those in Figure 3.2. This suggests that the features observed in Figure 3.2 are CuPc molecules that have been trapped by Si dangling bonds resulting from an incomplete passivation layer. Repeated scanning of the same sample region does not show significant changes in the positions of the features, further supporting this assignment. The feature

density is observed to saturate at similar coverages for all surfaces (0.030 ± 0.005 nm^2 and 0.042 ± 0.005 nm^2 for the Si(100):NH_3 and Si(100):H surfaces respectively). These values correlate well with the known defect densities produced by the passivation techniques used here and so these coverages are expected to mark the complete termination of the unpassivated dangling bonds with CuPc.

One of the initial aims of these experiments was to investigate the possibility of molecular templating to the Bi nanoline surface. As can be seen in Figure 3.2(b), no preferential adsorption onto the Bi nanolines was observed. Instead, the molecules were seen to avoid the nanolines; these structures are known to be defect free [178, 215] and do not contain Si dangling bonds, further highlighting the requirement for Si dangling bonds in the pinning of the molecules.

3.1.2 First Layer Island Formation

Once the flat-lying molecules have saturated all defect sites, further deposition leads to the formation of molecular islands. In all cases, the underlying flat CuPc molecules pinned to the substrate can be observed as bright features through the islands with their density remaining at the saturated values given in Section 3.1.1. Typical images of the islands formed on the Si(100):NH_3 surface are shown in Figure 3.3. These features have a kinked outline and are of uniform height, measuring 1.7 ± 0.2 nm in all cases. This height is in close agreement with the lateral dimensions of CuPc and implies that the molecules are aligned in a standing manner, with their molecular plane perpendicular to the substrate. Such an orientation suggests that the intermolecular van der Waals and π-π interactions are stronger than those between the molecules and substrate.

At low coverages (Figure 3.3(a)) the islands are isolated but relatively large, being up to ~1 μm in length, suggesting a high molecular mobility on this surface. They appear to have one or two large-scale net directions giving the appearance of branches or arms running across the surface, and these are generally orthogonal to one other. This behaviour is similar to that observed for 40 nm thick CuPc films on unpassivated Si(100) in which linear features align along the [011] directions [75]. In addition, no preferential nucleation at surface defects or step edges is observed, whilst the islands readily cross Si

terraces without perturbation (Figure 3.3). The long-range directionality suggests that the substrate lattice plays an important role in island morphology, whilst the orthogonal nature of the branches can be explained by the (2 x 1) surface reconstruction of Si(100), as will be returned to in Section 3.2.4. Islands of similar appearance are observed on the Si(100):NH_3/Bi surface, with no preferential nucleation in the vicinity of or away from the Bi nanolines. This indicates that the CuPc-Bi interactions are not strong enough to provide a preferential nucleation site for molecular templating and that the nanolines are effectively invisible to the CuPc molecules.

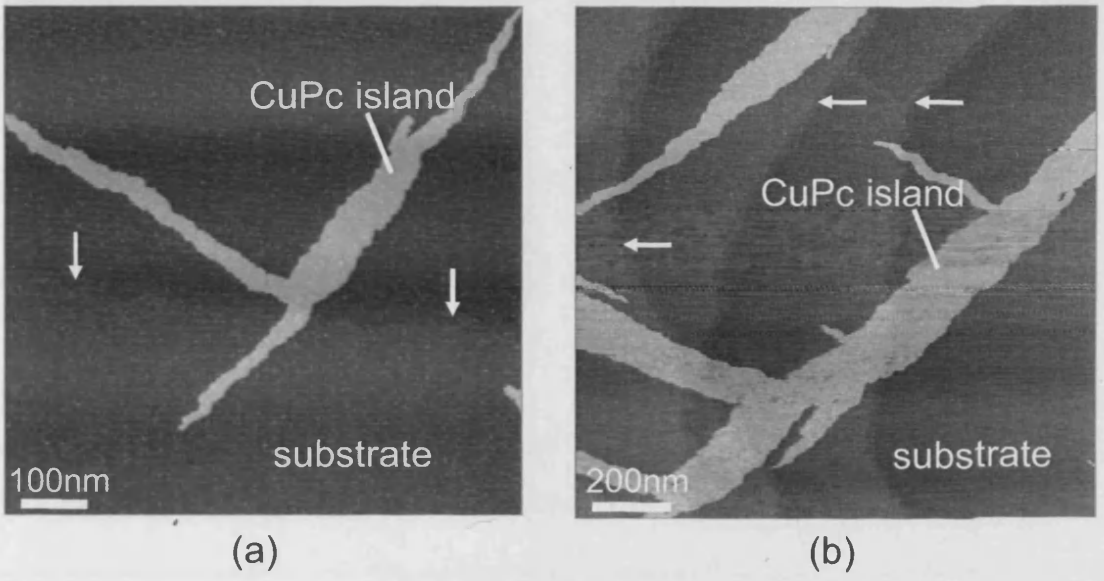

Figure 3.3. *The formation of molecular islands on the Si(100):NH_3 surface at coverages of (a) ~0.047 ML (-2.80 V, 0.120 nA) and (b) ~0.18 ML (-2.80 V, 0.150 nA). White arrows highlight Si step edges. A similar morphology was observed for the Si(100):NH_3/Bi surface.*

Molecular islands are also formed on the Si(100):H surface at similar CuPc coverages, examples of which are shown in Figure 3.4. Again, these are measured to be of uniform height 1.7 ± 0.2 nm, suggesting that they comprise upright standing molecules. A preferential directionality is seen along similar directions to those on the

Si(100):NH_3 surface, however the size and appearance of the features on Si(100):H are notably different; many more islands have nucleated and these are smaller and more fragmented than those in Figure 3.3. This suggests a lower molecular mobility on the Si(100):H surface, a more detailed discussion of which will be presented in Section 3.1.4.

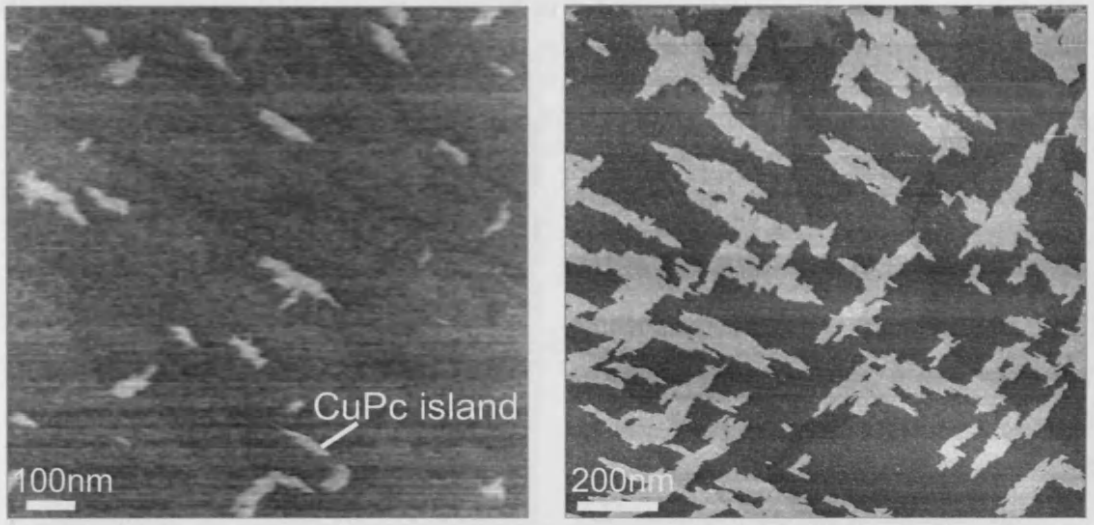

Figure 3.4. *The morphologies of CuPc islands observed on a Si(100):H surface at coverages of (a) ~0.034 ML (-2.00 V, 0.100 nA) and (b) ~0.21 ML (-3.00 V, 0.100 nA).*

3.1.3 Multilayer Island Formation

Multilayer islands are formed upon further CuPc deposition on all surfaces. Typical images of second layer coverage on the Si(100):NH_3 surface are shown in Figure 3.5, where the substrate, first and second layers of CuPc are labelled accordingly. These additional layers are of uniform height, and this is again measured to be 1.7 ± 0.2 nm suggesting that they too comprise molecules aligned perpendicular to the plane of the substrate, in a similar manner to the first layer. The long-range directionality is maintained with the formation of narrow islands that follow the direction of the

underlying monolayer island branch. Note that these higher order structures always follow the directionality of the layer beneath and are never observed to run perpendicular to it, suggesting that the first layer plays a crucial role in the morphology of higher order layers. As seen in Figure 3.5, the second layers are observed to have a kinked outline, as in an analogous manner to the first layer, which could be explained by the formation of well-defined domains (this will be returned to in Section 3.2).

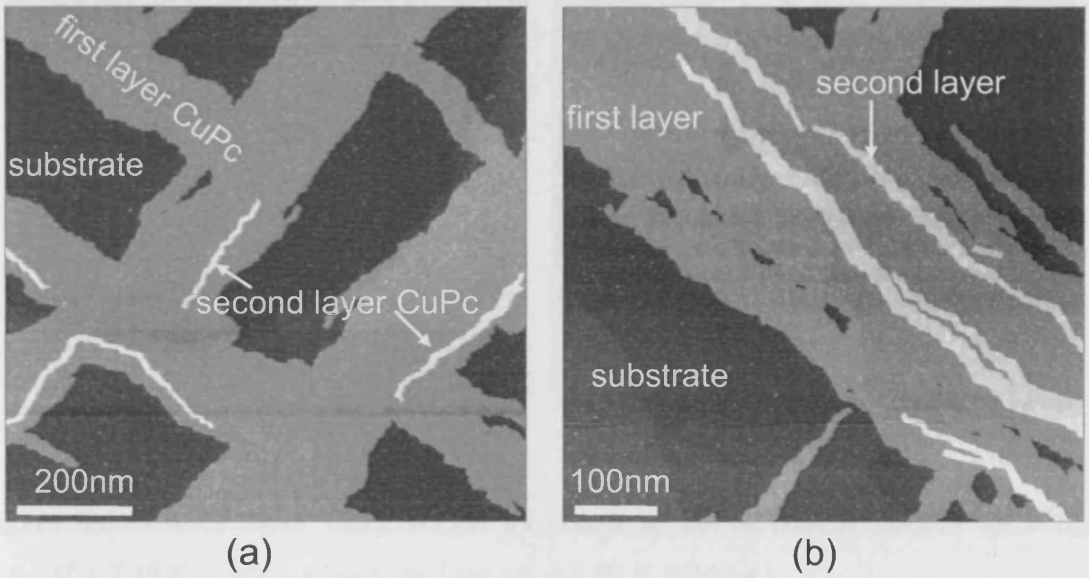

Figure 3.5. *Typical STM images of the formation of a second layer of CuPc on the Si(100):NH_3 surface at molecular coverages of (a) ~0.49 ML (-2.80 V, 0.120 nA) and (b) ~0.59 ML (-3.00 V, 0.100 nA).*

The growth of a second layer CuPc on the Si(100):H surface has also been studied, with two typical images shown in Figure 3.6. Again, the second layer is of a uniform height that corresponds to the molecules standing upright, and the long-range preferential directionality described previously is also maintained. Interestingly, the onset of second layer nucleation occurs when the first layer is approaching completion (it is more than 80% complete) whilst the corresponding first layer coverage at this point on the Si(100):NH_3 surface is less than 50%. As shown in Figure 1.7, the formation of three

dimensional islands is typical of a Volmer Weber growth mode, whilst a more layer-by-layer growth is known as Stranski-Krastanov. The behaviour on Si(100):NH_3 can be attributed to a the former case, whilst that observed on the Si(100):H surface is more similar to a Stranski-Krastonov growth mode.

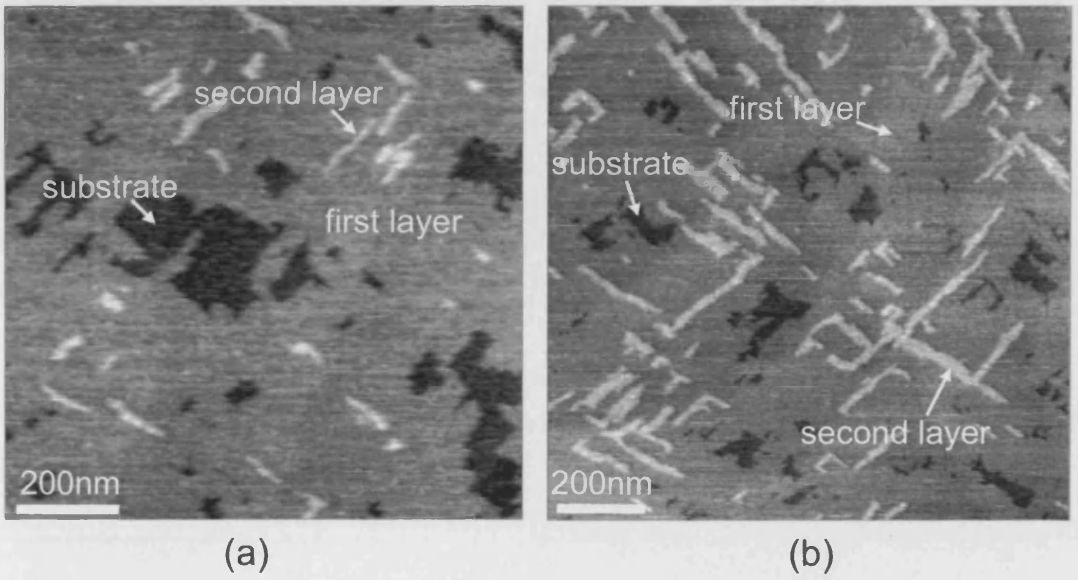

Figure 3.6. *Second layer CuPc island formation of the Si(100):H surface after (a) 0.91 ML (-2.70 V, 0.080 nA) and (b) 1.04 ML (-2.80 V, 0.10 nA).*

Figure 3.7 depicts the onset of third layer growth on the Si(100):NH_3 and Si(100):H surfaces, which have similar properties to the other layers. It is interesting to note that the point of third layer nucleation occurs whilst the second layer islands are relatively small on both surfaces. This suggests a different growth mode to that described for the second layers which is not as dependent on the interaction between the molecule and substrate. However, the higher order layers remain more fragmented on Si(100):H, as was seen for the first layer, demonstrating that the passivating species does play a role in their morphology. It should be noted that studies of layers more than 3 molecules thick were not possible due to difficulties in maintaining a tunnelling current between the tip and substrate.

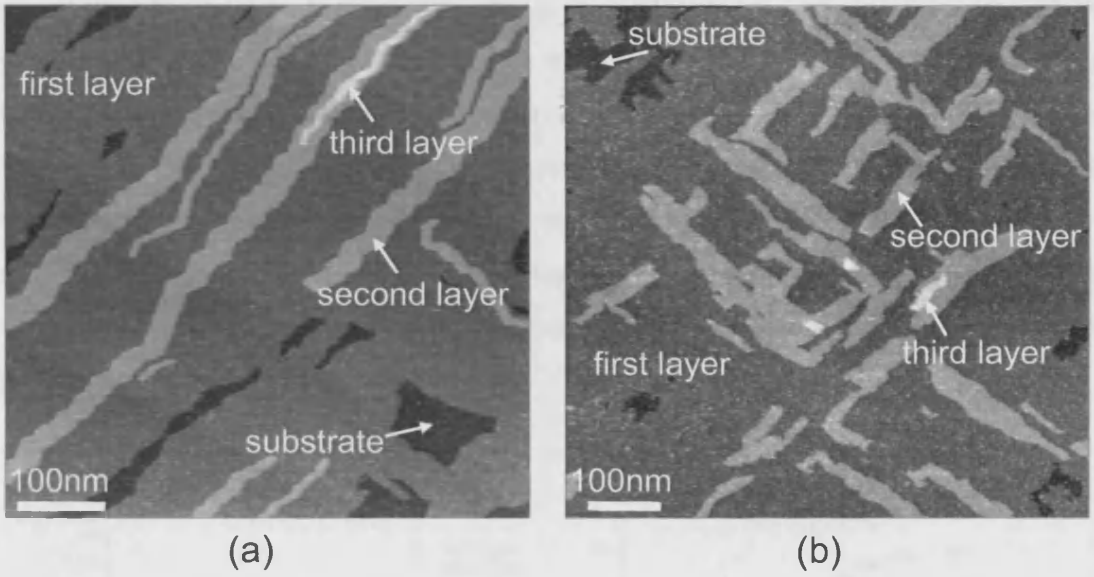

Figure 3.7. *Multilayer CuPc islands on the (a) Si(100):NH_3 surface (-3.00 V, 0.100 nA, 0.68 ML) and (b) Si(100):H surface (-2.70 V, 0.100 nA, 1.34 ML).*

3.1.4 Comparison of Molecular Coverages

As has already been commented upon, the onset of second and higher order growth occurs at different molecular coverages on the ammonia and hydrogen passivated surfaces. These are summarised as a function of total molecular material deposited (defined in terms of complete upright standing monolayers) in Figure 3.8. It should be noted that the coverage values were obtained by averaging the measured area of each layer for a series of large-scale images taken after each period of CuPc deposition.

The most notable difference is that the onset of the second layer CuPc on the Si(100):H surface occurs once the coverage of the first layer starts to plateau, i.e. as the first layer nears completion. In contrast, on the Si(100):NH_3 surface the second layer islands are observed whilst the first layer is less than 50% complete (such a growth mode is analogous to the case of pentacene on oxidised Si(100) [216]). As has already been postulated, it seems likely that multilayer growth, especially that of the second layer, is strongly influenced by the first layer morphology. The first layer islands on Si(100):NH_3

are significantly larger than their Si(100):H counterparts. This is likely, at least in part, to be responsible for the observed differences in total coverage needed for second layer nucleation; when arriving on larger islands there is a higher probability that any incident molecules will encounter others and therefore nucleate the next layer instead of reaching the island edge, diffusing onto the substrate and increasing the expansion of the underlying layer. Interestingly, third layer nucleation occurs before the second layer is even 50% complete in both cases, suggesting that for higher order layers the role of the substrate is reduced and that it is the molecule-molecule interactions which govern the growth morphology of higher order layers.

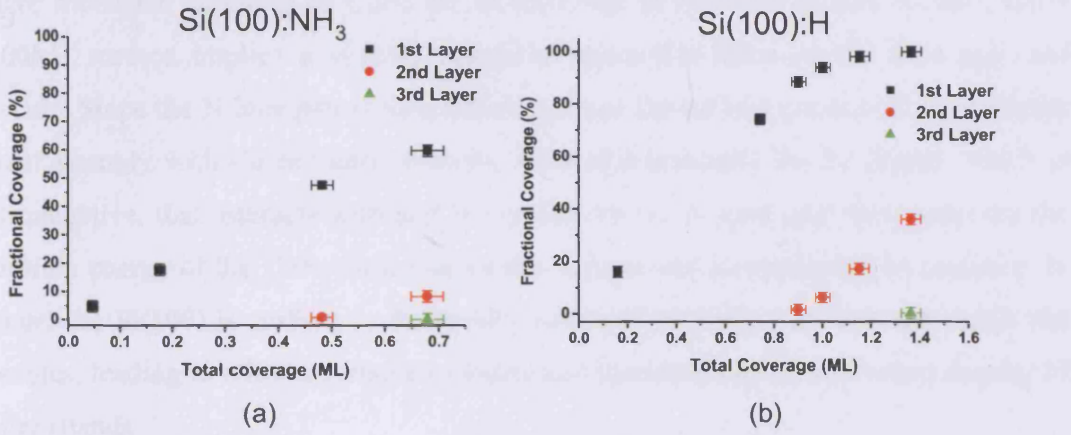

Figure 3.8. *Calculated fractional island coverages as a function of total molecular coverage for the (a) Si(100):NH_3 and (b) Si(100):H surfaces.*

There is clearly a higher molecular mobility on Si(100):NH_3 than on the equivalent H terminated surface, as is seen in the numerous, small, fragmented islands in Figure 3.4 as opposed to large isolated islands in Figure 3.3. Although the H termination was less complete than that of ammonia, as given by the saturation densities of flat lying molecules observed at low coverages, this difference is small (0.030 ± 0.005 nm^2 vs 0.042 ± 0.005 nm^2). Therefore, it is unlikely that the resulting variation in roughness could be solely responsible for these observed differences. Instead, this phenomenon can

be attributed to differences in the interactions between the CuPc molecules and passivating species.

For the Si(100):NH_3 surface, NH_2 and H groups terminate the Si dangling bonds, as shown in Figure 3.1, resulting in the presence of N lone pairs at the surface. Isolated N lone pairs display an attractive interaction with the central metal in MPcs, for example, as seen in gasses or loosely packed monolayers [217] and so this may be expected to occur here. However, an exclusively attractive interaction would result in flat-lying molecules on the Si(100):NH_3 surface, with a similar appearance to those trapped by the unpassivated Si dangling bonds in Figure 3.2, but with a significantly higher saturation coverage; this does not agree with the experimental observations. Instead, the higher relative molecular mobility of CuPc on Si(100):NH_3 as opposed to that on the neutral Si(100):H surface implies a slightly repulsive interaction between the lone pair and molecule. Since the N lone pair is directed away from the surface normal [211], it cannot interact strongly with Cu for steric reasons. Instead it is mainly the Pc ligand, which is electronegative, that interacts with and is repelled by the N lone pair, thus reducing the adsorption energy of the CuPc molecule on this surface and so increasing its mobility. In contrast, the Si(100):H surface is chemically inert and so neither attracts nor repels the molecules, leading to a lower relative mobility and therefore higher nucleation density of smaller islands.

In addition to the aforementioned size differences of the CuPc islands which could themselves be responsible for the lower total molecular coverage required for second layer nucleation on the Si(100):NH_3 surface, the slightly repulsive NH_2-Pc interaction may also have an effect on the formation of the second layer. On this surface, the second layers are often formed in the vicinity of the first layer boundary (as shown in Figure 3.5(a)) and it is feasible that at the point of nucleation they were even closer to the first layer edge. In contrast, the corresponding layer on the H passivated surface forms closer to the centre of the islands (Figure 3.6). These differences may be explained by the lower molecular stability on Si(100):NH_3 (due to the Pc ligand-N lone pair repulsion), which would reduce the rate of diffusion of molecules from on top of the first layer to the passivating layer, acting as a Schwoebel barrier [218].

3.2 MOLECULAR ARRANGEMENT WITHIN COLUMNS

In this section, a more detailed discussion of the structure of the molecular islands will be presented. The images described here will be those obtained for the Si(100):NH_3 surface since these were of the highest resolution and discussion of one surface should lead to a more coherent analysis. It should be noted that images of the molecular islands formed on Si(100):H show a similar structure to those on Si(100):NH_3 but with smaller domain sizes. Detailed images of the texture of the molecular islands will be presented and discussed in Sections 3.2.1–3.2.3. These studies have led to the proposal of a model of the molecular alignment with respect to the surface, which is included along with a discussion of how this correlates to bulk CuPc structures in Section 3.2.4.

3.2.1 Texture of Islands: Observation of Molecular Rows

As has already been noted, the molecular islands are observed to have a kinked outline. This suggests that there exist preferential molecular alignments and that these average out to give the overall directionality of the island branches. More detailed images, such as those in Figure 3.9, show that the islands themselves have a striped texture. Since discrete heights corresponding to the known lateral dimensions of CuPc molecules have been measured, implying that the islands comprise upright standing molecules, this suggests the formation of molecular rows which give rise to this striped appearance. As was described in Section 1.2.1, within the bulk crystallites CuPc molecules stack to form columns due to π-π and van der Waals interaction and so the formation of molecular rows is energetically favourable for bulk systems. Therefore, the observation of molecular columns here is not surprising, especially since this has been observed on other substrates elsewhere [50]. The average lengths of the molecular columns have been determined over a selection of images; these were measured to be 9.7 ± 1.2 nm and 7.3 ± 0.9 nm for the Si(100):NH_3 and Si(100):H surfaces respectively. The larger domain size of the islands on Si(100):NH_3 is in agreement with the earlier observation of an increased molecular mobility (and therefore order) on this surface. It should be noted that the domains were observed to be longer in a direction running perpendicular to the column direction (on

Si(100):NH_3 the domains were frequently up to 30–100 nm wide), which may suggest a degree of strain on the column formation, possibly due to templating to the underlying Si surface, as will be discussed further in Section 3.2.4.

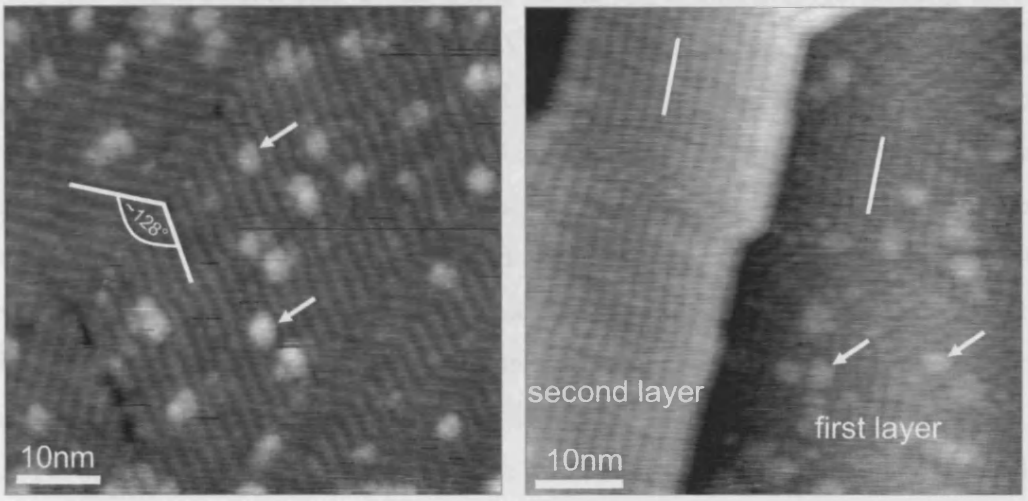

Figure 3.9. *The observation of a striped texture to the molecular islands formed on Si(100):NH_3 for (a) first layer (-3.20V, 0.100 nA, 0.49 ML) and (b) second layer on first layer (-3.00 V, 0.100 nA, 0.68 ML) islands. Examples of molecular column directions and underlying CuPc molecules are indicated by white lines and arrows respectively.*

As highlighted in Figure 3.9, flat underlying molecules are clearly visible through the islands. These do not appear to influence the column growth since neither kinks nor domain boundaries frequently occur in the vicinity of the underlying molecules. In addition, these molecules themselves appear larger than when not covered by islands (2.4 ± 0.3 nm versus 1.7 ± 0.2 nm). This suggests that the rows pass straight over, effectively blurring the true boundaries of the flat-lying underlayer in a blanket-like effect and demonstrates that these features arise from molecules below rather than above the islands.

The columns are arranged in domains, within which the molecular rows are aligned parallel to each other. Significantly, only two column directions are observed within each branch of an island. The columns are therefore responsible for the kinked outline of the islands, averaging out to give the long-range directionality described in Section 3.1, and are separated by an angle of $128 \pm 2°$. The average spacing between rows (perpendicular to the column direction) is measured to be 1.7 ± 0.2 nm, which again agrees well with the lateral dimensions of CuPc and the claim that the stripes comprise molecular rows. Large-scale images show that there is an approximately even distribution of domain directions. From this it can be ascertained that the overall branch direction is determined by an average of the two domain directions. As is seen in Figure 3.9(b), higher order layers also contain domains of columns, the directions of which follow those of the underlying layer, in a molecular templating-like effect. On a larger scale, similar effect has been observed for 190 nm thick H_2Pc films grown at room temperature (i.e. under the conditions that lead to the α-phase) on a β-phase film, wherein the morphology of the underlayer is adopted [219].

3.2.2 Determination of Alignment with respect to the Substrate

As has already been described, the presence of the Bi nanolines has very little effect on the growth of the CuPc layers, with the morphology observed on the Si(100):NH_3/Bi surface being very similar to that on Si(100):NH_3, suggesting that no significant interaction between the CuPc molecules and Bi structures occurs. As seen in Figure 3.10, the Bi nanolines do not coincide with the preferential row directions formed on the Si(100):NH_3 surface and molecular templating to the Bi lines was not achieved. However, one advantage of the Bi structures is that they are well known to align along the [011] directions of the Si(100) surface [178, 215] and so provide markers of the underlying substrate orientation. In addition, the visibility of the nanolines through the molecular overlayer adds further support to the claim that the bright spots seen in Figure 3.9 are indeed due to underlying molecules.

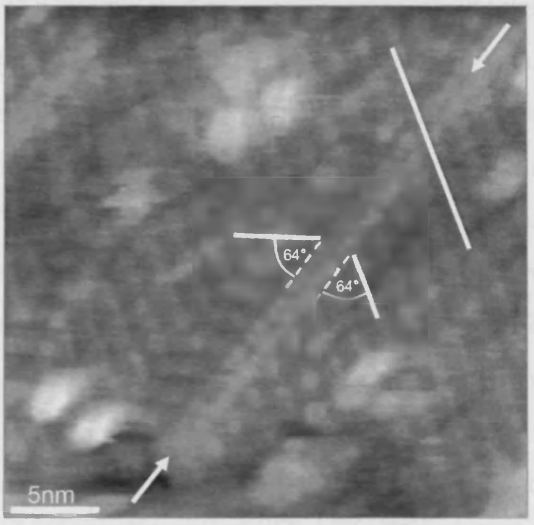

Figure 3.10. *A CuPc layer on Si(100):NH_3/Bi (-2.50 V, 0.100 nA) in which an underlying Bi nanoline (as marked with white arrows) lies underneath molecular columns, the directions of which are highlighted with white lines.*

On rare occasions, for example that shown in Figure 3.10, two domain boundaries are observed to meet at the nanolines (as indicated by two white lines towards the centre of the image). It should be noted that for most cases the molecular columns pass straight over the nanolines as shown in the top left and top right of this figure (the latter of which is marked by a single white line). From this image, the Bi nanoline was observed to bisect the two stripe directions, with the angle between the molecular columns and the [011] directions measured to be $64 \pm 1°$. Since the macroscopic island direction is determined by the average of the column directions, it is therefore perpendicular to the Bi nanoline in this case, i.e. along the $[1\,\bar{1}\,0]$ direction.

3.2.3 Molecular Resolution

The molecular columns seen in Figure 3.10 are observed to possess a texture along their growth direction (linescans along the columns appear bumpy), which may be due to the individual molecules. Higher resolution images have also been obtained, such as that

shown in Figure 3.11(a), wherein individual features can be resolved along the column directions. These features are expected to correspond to molecules which stack with their molecular plane perpendicular to the substrate in a face-to-face manner forming columns. Since these measurements were performed at room temperature the molecules appear blurred due to thermal motion, whilst it is likely that the molecular positions are affected by the field of the STM tip and so determining their exact positions is difficult. On average, the molecules are observed to be slightly tilted with respect to their stacking direction, in an analogous manner to that observed in the bulk phases, although low temperature studies would be required to confirm this. The average centre-to-centre column spacing is measured to be 1.7 ± 0.1 nm, in agreement with that obtained from Figure 3.9, whilst an average separation of the molecular features along the column direction is measured to be 0.8 ± 0.1 nm, as shown in Figure 3.11(b).

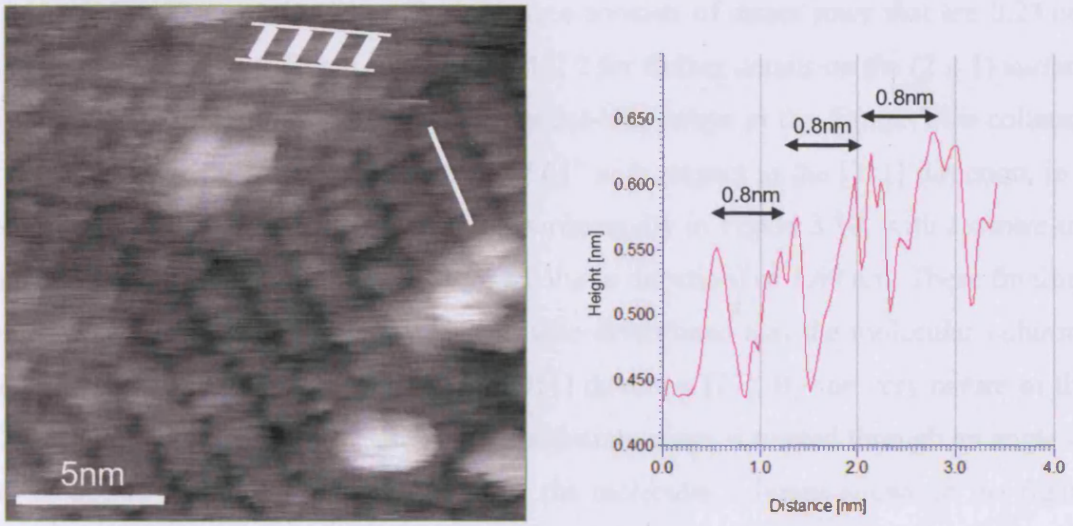

Figure 3.11. *(a) A more detailed STM image in which individual molecular features can be resolved within the columns on Si(100):NH_3 (-2.80V, 0.100 nA, 0.49 ML). (b) A linescan along a molecular column showing ~0.8 nm feature spacing (the position from which the linescan was taken is indicated by the single white line in (a)).*

The molecular features observed in Figure 3.11(a) appear relatively uniform throughout their length. This suggests that the molecules are aligned such that two neighbouring benzene rings are in contact with the surface, in a two-legged arrangement. In contrast, a different appearance would be expected if the molecules were rotated by 90° so that they stood on one benzene ring. For such an orientation a bright dot would be expected through their centres since the current would be greater if passing directly through the Cu atom and benzene rings, in addition to the increased variation in height and absolute width of the molecule if orientated in this manner.

3.2.4 Proposed Model and comparisons with bulk films

The measured column separations and angles between different domains have led to the construction of a model for their alignment with respect to the underlying substrate. This is presented in Figure 3.12. The silicon surface consists of dimer rows that are 0.23 nm wide and separated by 0.76 nm (see Section 1.2.2 for further details on the (2 x 1) surface reconstruction), and these are represented by dot-like arrays in the figure. Two columns have been constructed that form an angle of 64° with respect to the [011] direction, in a similar manner to the columns observed experimentally in Figure 3.10, with a centre-to-centre distance (measured orthogonal to the column direction) of 1.69 nm. These findings are in contrast to those of Nakamura *et al.* who determined that the molecular columns form an angle of ±17° with respect to the [011] direction [77]. By the very nature of the (2 x 1) Si(100) surface reconstruction, if the substrate plane is rotated through an angle of 90°, as occurs when step edges are crossed, the molecular columns shown in the figure will still neatly fit within the rotated dimer arrangement. This allows the molecular rows and island branches to cross step edges without a change in direction, as has been observed experimentally.

In addition to the measured molecular column directions, the molecular positions have also been tentatively included in Figure 3.12. As has already been noted, it is not possible to know these positions with a high degree of certainty since their precise positions and orientations may have been locally influenced by the STM tip. However,

these are observed to readily fit to the two dimensional lattice created by the Si dimer rows to give a separation of 0.76 nm along the column length which is in agreement with the measured value of 0.8 ± 0.1 nm. It is anticipated that the molecules lie parallel to the [011] direction, as shown in the figure, which is in agreement with the presence of a tilt with respect to the stacking direction of the features observed in Figure 3.11(a).

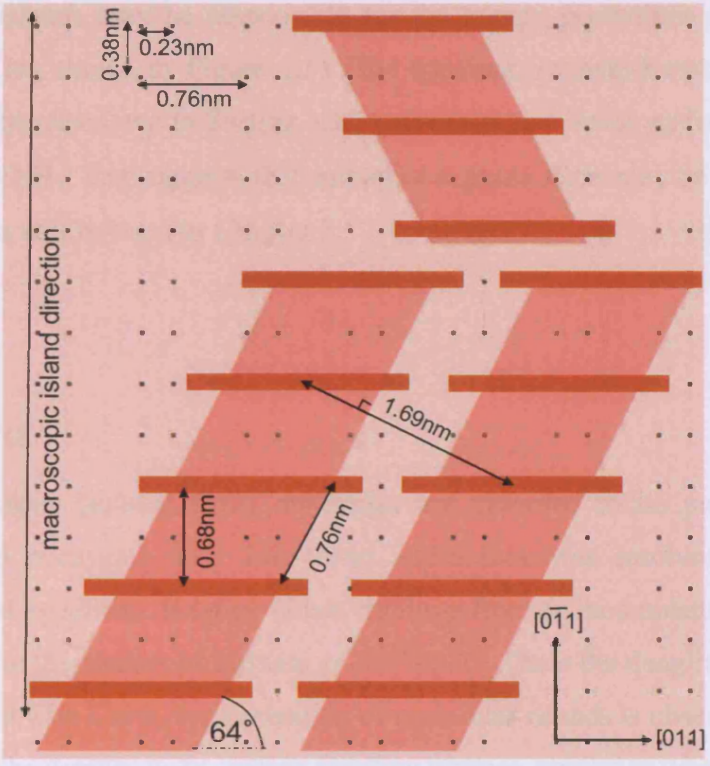

Figure 3.12. *A proposed model for the alignment of CuPc columns (pink) and molecules (red) on the passivated Si(100) surface (dots represent Si dimer rows).*

In the model, the angle between the columns and molecular plane is 64°, which is very close to those of 63.5° and 65.1° predicted by the Ashida and Hoshino models respectively for the tilt angle in the bulk α-phase [27, 28], as depicted in Figure 1.2. As outlined in Section 1.2.1, this is the anticipated phase for thin MPc films deposited onto substrates held at room temperature, as was the case here. In addition, the STM images

and model suggest a molecular separation of ~0.76 nm in a direction taken parallel to the columns, whilst that of the *b*-axis of bulk α-phase is known to be 0.375–0.381 nm (Table 1.1). This is approximately half of the measured distance, and suggests that the features observed in Figure 3.11(a) may each correspond to two molecules. Again, further high resolution studies at low temperature would be required to confirm that this is correct. The similarities between the observations described here and the bulk α-phase suggest that the molecular islands may be responsible for the bumpy crystallites observed for thicker CuPc films (as shown in Figure 1.5). The apparent Stranski-Krastanov growth mode on Si(100):H (as discussed in Section 3.1.3) gives rise to a lower surface roughness than that on Si(100):NH_3; this suggests that smoother α-phase films may be formed on a Si(100):H surface, as will be used in Chapter 5.

3.3. CONCLUSIONS

At very low coverages, isolated CuPc molecules are observed to lie parallel to the substrate, where on occasions their four-lobed appearance was resolved. Here, the molecules are pinned by silicon dangling bonds resulting from an incomplete passivation, in a similar manner to the studies of Hersam *et al.* [79, 80]. Once the dangling bond sites have been terminated with CuPc, the nucleation of molecular islands is observed wherein the molecules align themselves in an upright standing manner, similar to what is observed for thicker films of CuPc on Si(100):H [68]. This suggests that the interactions between the molecules and the substrate are weaker than the π-π and van der Waals interactions between neighbouring molecules. The CuPc molecules are not observed to template to the Bi nanolines on the Si(100):NH_3/Bi, with a morphology similar to that formed upon Si(100):NH_3 found in the vicinity of and away from the Bi nanostructures. On all surfaces, the islands formed are observed to have a preferential long-range directionality along the [011] Si directions.

Larger, more isolated islands are formed on the Si(100):NH_3 surface, whereas those formed on Si(100):H are smaller and more fragmented, suggesting a higher

molecular mobility on the former surface. Furthermore, the nucleation of second layer island growth occurs much earlier on the Si(100)NH_3 surface, suggesting different growth modes on the two surfaces. These differences are attributed to a slightly repulsive interaction between the nitrogen lone pairs (formed by the dissociation of NH_3 molecules at the surface into an NH_2 group and H) and the electronegative Pc ligand, which increases the molecular mobility on the Si(100):NH_3 surface, whereas hydrogen termination produces a more inert surface.

More detailed images show that the islands comprise molecular columns which are responsible for the kinked outlines of the islands. Only two column directions were observed for each branch of the islands; studies on the Si(100):NH_3/Bi surface show that these form an angle of $64 \pm 1°$ to the [011] directions of the underlying silicon surface. In some images, individual features are observed wherein the molecules are stacked in a face-to-face manner. These images have led to the construction of a model of how the molecules align with respect to the Si(2 x 1) surface. It has been noted that in this model the same molecular tilt angle with respect to the stacking direction is observed as for the bulk α-phase, whilst the separation between molecular features is measured to be double that of an α-phase arrangement. This suggests that each feature may represent a CuPc dimer and that this is the first study of the onset of formation of this crystallographic phase.

Chapter Four: Spin Coupling in CuPc Films

The structure and spin-mediated interactions within CuPc films have been studied using EPR, XRD, electronic absorption and AFM. A selection of CuPc film variants have been grown for these analyses. Single layer and templated films (wherein CuPc is deposited onto a PTCDA layer) comprise CuPc arrays wherein the molecules lie upright and flat with respect to the substrate respectively, with both types of film displaying similarities to the bulk α-phase. Co-deposition of CuPc and H_2Pc leads to randomly mixed crystalline films, as evidenced by the appearance of hyperfine structure in the EPR spectra; this suggests that the crystal phases of α-phase CuPc and H_2Pc are similar. The structural alignment of each film has been verified by the EPR studies and permitted analyses of the intra- and inter-column coupling for each type of CuPc film. Specifically, stronger interactions are observed along the molecular stacking directions than between neighbouring columns. These results are promising both for the use of CuPc films in spintronic applications and of EPR as a structural characterisation tool for such systems.

CuPc is a stable, readily available and cheap molecule that absorbs light in the visible region and which forms ordered thin films when sublimed under vacuum conditions (as discussed in Section 1.2 and observed in Chapter 3). Importantly, CuPc films are semiconducting; as described in Section 1.1, they have already been studied for a range of organic electronics applications and so many of their electronic properties are well understood. In addition, CuPc contains an unpaired spin that is mostly located on the $d_{x^2-y^2}$ orbital [220, 221]; this has led to the study of the spin interactions between CuPc molecules by EPR for α- and β-phase crystallites (as discussed in Section 1.3.2). Furthermore, CuPc films have been shown to exhibit a magnetic signature which is

dependent on their polymorph [37]. Here, the aim will be to investigate whether these semiconducting and magnetic properties can be combined for spintronic applications.

EPR is a very useful tool in learning how spins interact for a given sample. Thin CuPc films on amorphous substrates (as will be used in this chapter) are known to comprise columns of molecules stacked such that their molecular planes are perpendicular to the substrate [50, 65]. This is in a similar manner to the STM observations presented in Chapter 3 (for example, as shown in Figure 3.11). One of the aims of this chapter is to understand how spin is transported within thin films, namely to determine whether the CuPc molecules preferentially interact along their stacking direction or between neighbouring columns. Such studies are not possible using bulk crystallites because in these many crystallographic directions exist. Since within films the molecules preferentially align with respect to the substrate, their inter-column and intra-column interactions can be selectively measured via the orientation of the film with respect to the magnetic field. This will provide information about whether or not spin information will be conserved as it transfers through a potential MPc film device; it is already known that charge carriers preferentially migrate along the intra-column directions [222, 223]. In addition, as noted in Section 1.2.1, there is still some debate as to the crystallographic structure of α-phase CuPc [27, 28]. EPR should be a useful tool to learn more about the structure of CuPc thin films.

As has already been noted in Section 1.3.2, it is necessary to dilute CuPc in a H_2Pc matrix to reduce dipolar interactions and so perform a detailed study of the Cu-Cu interactions. This has already been achieved for crystallites [139–142, 144, 145], whilst STM studies of co-deposited CuPc and CoPc to form flat-lying monolayers show a random CuPc:CoPc distribution [55, 56] (it should be noted that in the latter case molecule-substrate interactions dominate, whereas molecule-molecule interactions will be of much greater importance in the films described here). However, it is important to establish whether phase segregation occurs for magnetically diluted CuPc films. This will also provide further insight into whether or not CuPc and H_2Pc are isomorphous.

The approach taken here has been to grow a selection of 100 nm – 200 nm thick CuPc films by OMBD onto amorphous substrates (it should be noted that all substrates

were at room temperature during deposition and so the α-phase polymorph is anticipated). Such a thickness was chosen to allow a reasonable signal-to-noise ratio for the characterisation techniques used. Both 100% CuPc and co-deposited CuPc:H_2Pc mixed films were grown, the molecular arrangements anticipated for these films are shown in Figures 4.1(a)-(c). As seen in Figure 1.5(a), CuPc films comprise many crystallites; although each is a single crystallographic domain, the stacking (*b*-) axis can assume any direction parallel to the substrate. This lack of azimuthal preferential orientation prevents the selection of the inter-column directions via sample positioning in the magnetic field.

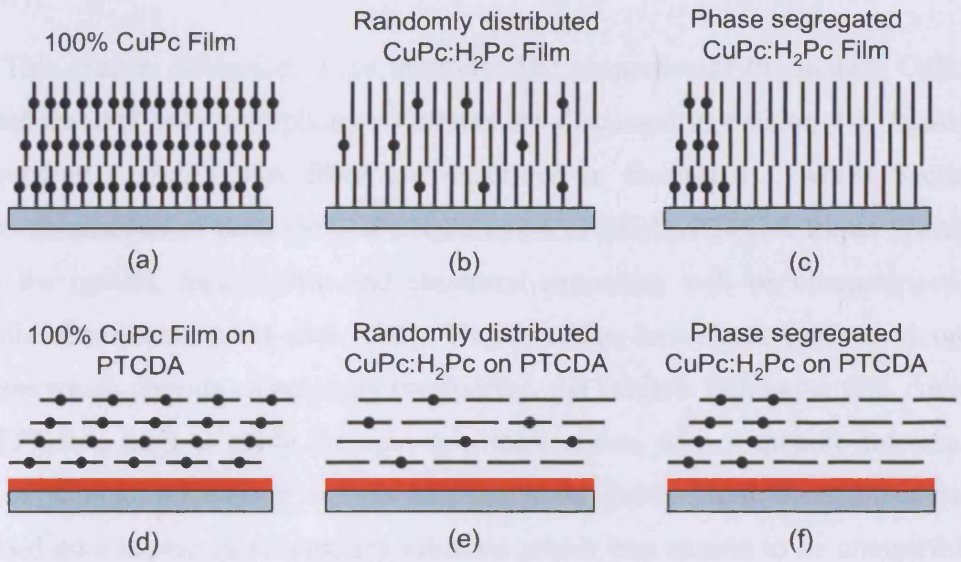

Figure 4.1. *Schematic drawings of the anticipated molecular arrangements of the CuPc thin films studied in this chapter. The Pc molecules are represented by black lines (they are viewed side-on in all images), with Cu atoms as black spheres and the PTCDA layer shown in red where appropriate. (a) and (d) represent 100% CuPc films without and with a PTCDA layer respectively, whilst (b)-(c) and (e)-(f) show possible molecular arrangements of co-deposited CuPc/H_2Pc films without and with a PTCDA layer.*

Instead, it is desirable to form structures wherein the CuPc molecules lie parallel to the substrate, since then the molecular orientation will match that of the substrate in the magnetic field. The deposition of H_2Pc or CuPc onto a thin layer of 3,4,9,10-perylenetetracarboxylic dianhydride (PTCDA) forces the Pc molecules to lie parallel to the substrate [224–226] (PTCDA molecules are known to lie approximately flat on amorphous substrates [227, 228]). This change in Pc orientation has been attributed to a templating effect due to strong π-π interactions between the PTCDA and Pc layers, whilst the induced ordering can be maintained for Pc layer thicknesses of up to 380 nm or more [224]. In the work described in this chapter, 200 nm thick CuPc and CuPc:H_2Pc films were deposited onto 20 nm PTCDA films. These will be referred to as CuPc/PTCDA and CuPc:H_2Pc/PTCDA films respectively (their anticipated structures are shown in Figures 4.1(d)-(f)).

This chapter comprises three sections. The properties of (undiluted) CuPc films deposited directly onto amorphous substrates are discussed in Section 4.1, those of the corresponding CuPc/PTCDA films are described in Section 4.2, whilst Section 4.3 contains an analysis of both the CuPc:H_2Pc and CuPc:H_2Pc/PTCDA films. Within each section the optical, topographic and structural properties will be characterised using electronic absorption, AFM and XRD. These studies have been performed on glass substrates which provide an optically transparent, flat surface. Following this, continuous wave EPR was used to study the spin-spin interactions, with a specific interest in the effect of sample orientation within the magnetic field. These measurements were performed on a kapton (a polyimide) substrate which was chosen to be compatible with future applications in flexible electronics, and since multiple samples can be stacked to fit into the small sample space (to enhance the signal-to-noise ratio). EPR experiments were performed at low temperatures (10-15 K) whilst the other analyses were carried out a room temperature.

4.1. COPPER PHTHALOCYANINE THIN FILMS

This section will comprise an overview of the properties of thin films of CuPc. Specifically, 100 nm thick films on glass and kapton will be characterised by electronic absorption spectroscopy (Section 4.1.1), AFM (Section 4.1.2) and XRD (Section 4.1.3). Following this, their continuous wave (CW) EPR spectra will be discussed in Section 4.1.4, with a particular focus on varying the film orientation with respect to the magnetic field.

4.1.1 Electronic Absorption Spectroscopy

Figure 4.2 compares the electronic absorption spectra of CuPc in solution (in 1-chloronapthalene) and of a 100 nm thick film on a glass substrate. The two spectra are seen to be very different. In the case of the solution spectrum, a sharp peak is observed at 678 nm; as described in Section 1.2.1, this can be attributed to Q-band absorption [30, 38]. Lower intensity vibrational peaks are observed at 610 nm and ~647 nm (shoulder). In comparison, the film spectrum (black line) is broadened whilst the Q-band is split into two main peaks. As described in Section 1.2.1, the broadening arises from phonon scattering , whilst several mechanisms have been proposed to explain the Q-band splitting [33, 41, 44, 45]. The two peaks are centred at 695 nm and 621 nm (a small shoulder is also seen at lower wavelengths) and this spectrum can therefore be attributed to the α-phase, as expected from the growth conditions. The tail observed at low wavelengths is due to absorption from the ground state to the second excited state [1, 30, 45]. Spectra were obtained from multiple locations on the films and were observed to show little (if any) variation in intensity, whilst to the naked eye the films appeared uniform; the films are therefore deemed to be homogeneous.

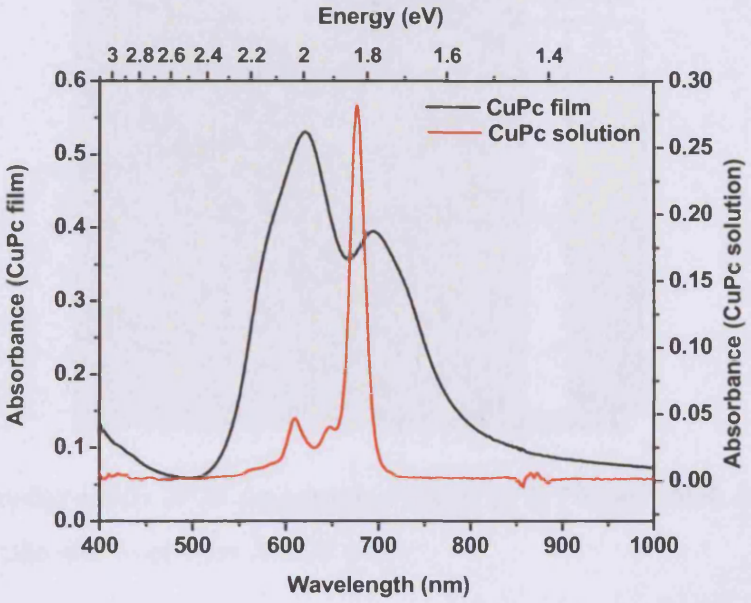

Figure 4.2. *Electronic absorption spectrum of a 100 nm CuPc film on glass (black, left axis) and a 1.5 μM CuPc solution in 1-chloronapthalene (red, right axis).*

4.1.2 Atomic Force Microscopy

Tapping mode AFM has been used to study the topography of 100 nm CuPc films. Figure 4.3 shows a typical image obtained, wherein a series of spherical features are observed. As was discussed in Section 1.2.1, the topography of the CuPc phase is known to be dependent on the molecular crystal phase since the relative stabilities of the crystal phases are dependent on crystallite size [29]. Therefore, bulk α-phase films are observed to consist of small crystallites, typically of spherical appearance, whilst β-phase crystallites are more needle-like in appearance [32, 34]. The CuPc film measured here has the characteristic structure of the α-phase (Figure 1.5(a)), which is consistent with the electronic absorption measurements of Figure 4.2.

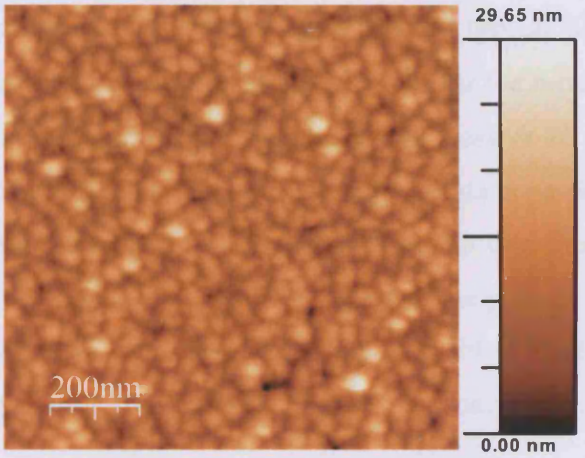

Figure 4.3. *Tapping mode AFM topographic image of a 100 nm thick CuPc film on a glass substrate (the rms roughness is 3.22 nm).*

Each spherical region represents a single crystallographic α-phase domain. Within each domain the CuPc molecules stack in a standing manner with respect to the plane of the substrate forming columns, similarly to what was described in Chapter 3 (the molecular alignment will be confirmed in Section 4.1.3). However, unlike the case of ultra-thin layers of CuPc on passivated Si(100), no preferential in-plane orientations of the molecular columns within the domains are expected here since the glass substrate is amorphous. From Figure 4.3, the crystallites are seen to be typically 25–45 nm in diameter, with a root mean squared (rms) roughness of 3.22 nm. The domain size and roughness of α-phase Pc films prepared by OMBD onto substrates at room temperature are known to increase as a function of film thickness (although this is not claimed to be a linear relationship), with the values obtained here in agreement with those typically observed for a 100 nm thick α-phase film [229].

4.1.3 X-ray Diffraction

X-ray diffraction has been used in order to confirm the phase and unit cell orientation with respect to the substrate of the 100 nm CuPc films. A typical XRD spectrum is shown in Figure 4.4. A sharp peak is observed at $2\theta \sim 6.8°$ whilst the broad peak at $2\theta = 20–35°$ is from the glass substrate. Upon closer inspection, the peak at $2\theta \sim 6.8°$ appears slightly asymmetric, with a shoulder towards higher 2θ values (this is particularly apparent in the inset). Lorentzian fitting has been performed from which two peaks are resolved; these are centred at $2\theta = 6.83°$ and $2\theta = 7.36°$ ($R^2 = 0.996$). The peak at $2\theta = 6.83°$ is far more intense, as shown by the ratio of their fitted areas of 49:1. This peak will be used to identify the polymorph of the film and corresponds to a spacing of $d = 12.93$ Å.

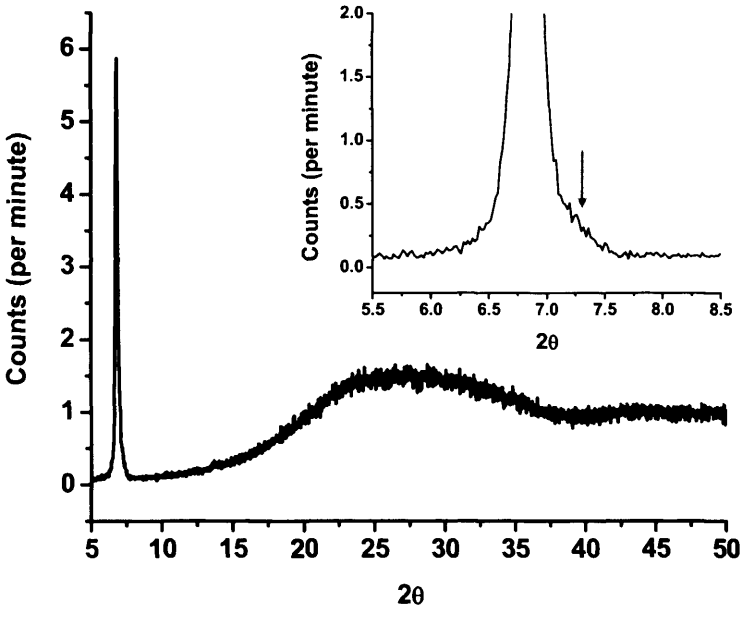

Figure 4.4. An x-*ray diffraction spectrum of a 100 nm thick CuPc film on a glass substrate. The inset contains a detailed plot of the 2θ ~ 6.8° peak, and the asymmetry is highlighted with a red arrow.*

As was discussed in Section 1.2.1, the unit cell dimensions of α- and β-phase CuPc are notably different. For β-phase CuPc films, a peak would be expected at $2\theta = 7.07°$ corresponding to a spacing of 12.68 Å [33, 143] however, this is not observed here. Instead, an α-phase arrangement seems more likely, given the electronic absorption and topographic analyses in Sections 4.1.1 and 4.1.2. As discussed in Section 1.2.1, two crystal structure arrangements of α-phase CuPc have been proposed, known as the Ashida [27] and Hoshino [28] models. Their unit cell parameters were compared in Table 1.1, wherein that of the Ashida model is twice as long as that proposed by Hoshino *et al.*. However, the (200) and (100) planes respectively correspond to spacings of 12.96 Å and 12.89 Å, whilst the value obtained experimentally ($d = 12.93$ Å) is mid-way between these. This confirms that the film is in the α-phase, with the *a*-axis aligned perpendicular to the substrate. Such an orientation implies that the vast majority of the molecules are aligned approximately perpendicular to the substrate, as can be seen from Figure 1.2 (for the projection shown the substrate is in the plane of the page). This finding is in agreement with other reports for MPc films on amorphous substrates [50, 65, 66].

Information regarding the average size of the crystallites can also be determined from consideration of the broadening of the Bragg peak due to edge effects of the spherical crystallites. This can be achieved using the Scherrer equation (Equation 4.1) and the full width half maximum (fwhm) of the $2\theta = 6.83°$ peak of 0.194°. Here, θ is the peak position ($\theta = 3.42°$), λ is the wavelength of the x-rays ($\lambda = 1.54$ Å), η is the fwhm (in radians) and K is the Scherrer constant ($K = 0.9$ for phthalocyanine films [230]).

$$L = \frac{K\lambda}{\eta \cos\theta} \qquad [4.1]$$

Using these values, the average size of the crystallites is calculated to be 41 nm. This is in excellent agreement with the AFM measurements which suggest crystal sizes of typically 25-45 nm in diameter, adding further confirmation that the samples are in the α-phase since this would be the most stable form for crystallites of these dimensions [29].

The shoulder observed at $2\theta = 7.36°$ corresponds to a spacing of $d = 12.0$ Å. Inspection of Table 1.1 suggests that this corresponds to the α-phase where the *c*-axis is aligned perpendicular to the substrate (this can be attributed to the (002) and (001) planes of the Ashida and Hoshino models respectively). A more detailed discussion of the presence of this peak and how it affects the crystallinity of the film will be given in Section 4.3.3. Owing to their similar lattice parameters, it has not been possible to distinguish between the Ashida and Hoshino models using the two peaks observed here.

4.1.4 Electron Paramagnetic Resonance

Electron paramagnetic resonance (EPR) has been used to study the interactions between the unpaired electrons of the Cu^{2+} ions within the CuPc film. In particular, it is of interest here to study the interactions as a function of the molecular orientation within the magnetic field. Many studies have been performed on CuPc in solution [145] and polycrystalline systems [30, 138–142, 144, 145]. These exhibit no preferential molecular orientation (the samples are essentially a powder average) and as a result the continuous wave spectra of these samples are well understood. However, few studies address the impact of the magnetic field orientation with respect to the molecular axis [220].

As was outlined in Section 2.8, the energy levels due to the unpaired electron of the CuPc molecule become split in a magnetic field (the Zeeman effect). The absorption of microwaves occurs when the magnitude of the magnetic field is at the resonant position; from this the *g*-factor can be calculated from Equation 2.18. For CuPc, due to the planar nature of the molecule, the *g*-factor is anisotropic, with two different values depending on the orientation of the magnetic field with respect to the molecular plane. These are defined in Figure 4.5(a) with $g_{//}$ parallel to the z-axis of the molecule (out of the plane of the molecule) and $g_{\perp}$ aligned perpendicular to the z-axis (on the x, y plane of the CuPc molecule defined by the Cu-N bonds).

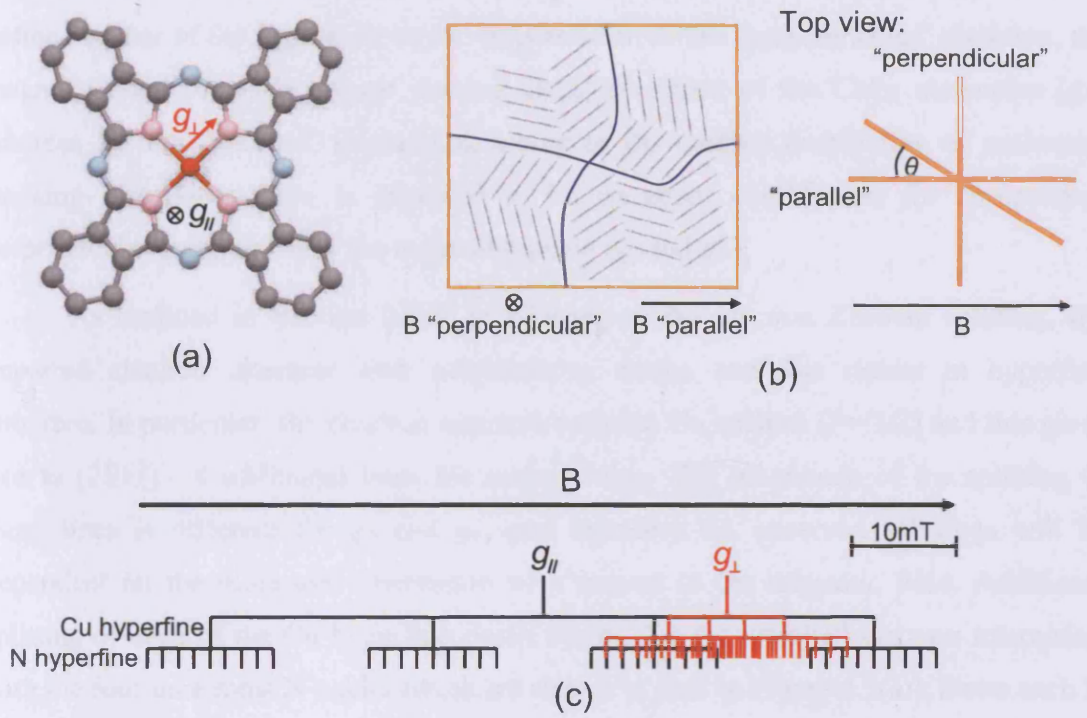

Figure 4.5. *(a) Orientation of $g_{//}$ (black) and $g_\perp$ (red) with respect to a CuPc molecule (Cu = red, N = pink, blue, C = grey, H not shown). (b) Examples of CuPc domains (separated by a blue line, not to scale) in a thin film, along with the definitions of the kapton substrate (orange outline) orientations with respect to the magnetic field that will be used. A top view is also shown in which the angle θ is defined. (c) Position of $g_{//}$ and $g_\perp$ in the magnetic field, along with splittings due to Cu and N hyperfine interactions, drawn approximately to scale using values from [139, 140, 145] (splittings slightly offset in the vertical plane for clarity).*

The results obtained in Sections 4.1.2 and 4.1.3 for CuPc films on glass substrates can be extended to films grown on kapton (another amorphous substrate), which was used here for the EPR studies. Specifically, the film comprises many small single-domain crystallites each containing stacks of upright standing CuPc molecules (the direction of

the in-plane stacking direction is different for each crystallite). This is represented in Figure 4.5(b) wherein four different domain directions are depicted. For the following discussions, the orientation of the sample with respect to the magnetic field will be defined as that of the kapton substrate. In particular, in the "perpendicular" direction, the magnetic field vector is always passing along the plane of the CuPc molecules ($g\perp$) whereas for the "parallel" orientation, owing to the random distribution of molecular stacking directions, there is expected to be an equal contribution for components perpendicular and parallel to the molecular plane ($g_{//}$ and $g\perp$).

As outlined in Section 2.8.2, in addition to the electron Zeeman splitting, the unpaired electron interacts with neighbouring nuclei and this results in hyperfine structure. In particular, the electron interacts with the Cu nucleus ($I = 3/2$) and this gives rise to $(2S+I) = 4$ additional lines for each g-value. The magnitude of the splitting of these lines is different for $g_{//}$ and $g\perp$, and therefore the observed splittings will be dependent on the molecular orientation with respect to the magnetic field. Additional splitting of each of the Cu hyperfine peaks occurs due the unpaired electron interacting with the four innermost N nuclei (these are shown in pink in Figure 4.5(a)). Since each N has a nuclear spin of $I = 1$, this gives rise to $(2 \times 4)\, I + 1 = 9$ lines. Again, anisotropic hyperfine coupling leads to different splittings as a function of magnetic field. It should be noted that there is considerable overlapping of the hyperfine peaks arising from $g\perp$ and so not all of these lines can be individually resolved [138, 139, 144], a point that will be returned to in Section 4.3.5. The spectrum is further complicated since both the Cu^{63} and Cu^{65} isotopes are present and this leads to additional splittings (these have been omitted from Figure 4.5(c)). The Hamiltonian of the system is expressed in Equation 4.2, where $H_{x,y,z}$ and $S_{x,y,z}$ are the components of the magnetic field and spin, β_e is the Bohr magneton, A and B are the Cu hyperfine constants in a similar manner to Equation 2.19 (note that these are of different magnitude), whilst $\vec{A}_n$ and $\vec{I}_n$ are the hyperfine tensor and nuclear spin of the n N atoms.

$$\mathcal{H} = \beta_e\left[g_{//}H_zS_z + g_\perp(H_xS_x + H_yS_y)\right] + AS_zI_z + B(S_xI_x + S_yI_y) + \vec{S}.\sum_n \vec{A}_n.\vec{I}_n \qquad [4.2]$$

In this equation, the first terms (in square brackets) are due to the Zeeman splitting and anisotropic g-factor, the middle two are due to Cu hyperfine interactions, whilst the last term represents the N hyperfine terms (summed over the number of nitrogen atoms, $n = 1, 2, 3, 4$).

Studies have been performed on the CuPc films on kapton at temperatures of 10–15 K, as a function of their orientation in the magnetic field. The orientations were obtained by first aligning the samples by eye, then carefully rotating the sample position until the point of symmetry was found. This position was recorded and the sample was then rotated in equal increments systematically, until it had been rotated through 90°, and the other point of symmetry had been reached. It should be noted that the signal is independent of whether the field passes through the film then the sample, or the sample then film, and so it is only necessary to rotate through 90°; only the molecular orientation with respect to the magnetic field is important.

Figure 4.6 shows the continuous wave (CW) EPR spectra of the CuPc film as a function of film position in the magnetic field. The angle (θ) is defined as the orientation of the film with respect to the magnetic field; when $\theta = 0°$ the film is said to be in the "parallel" orientation whilst for $\theta = 90°$ the sample is defined as being "perpendicular" to the field (as defined in Figure 4.5(b)). A small peak is observed in all spectra, as indicated by the dotted line, and this is due to a free radical in the kapton film (top spectrum). No angle dependence of this peak is observed; this is to be expected since the kapton substrate is amorphous. The sharpest spectrum is observed when the film is aligned perpendicular to the field (90°) (this spectrum is shown in greater detail as the black trace in Figure 4.7); this arises due to the standing arrangement of the CuPc molecules with respect to the substrate and so only the component from $g_\perp$ is seen (see Figure 4.5).

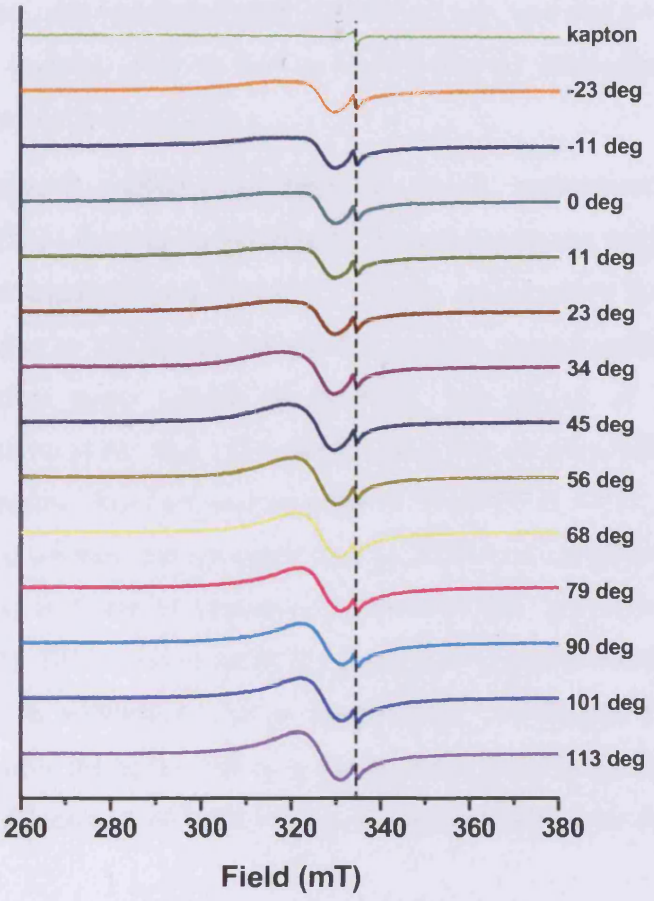

Figure 4.6. *Continuous wave EPR spectra of a 100 nm CuPc film on kapton as a function of film orientation with respect to the magnetic field (as defined in Figure 4.5(b)). Spectra are offset for clarity. A guide to the eye is shown at ~334.3 mT; this corresponds to a signal arising from the kapton substrate which is present in all spectra.*

In order to estimate the value of $g_{\perp}$ from this spectrum, it is necessary to find the magnetic field at which the microwave absorption is a maximum. As shown in Figure 2.9, the CW signal is the first derivative of the absorption spectrum and so this point is where the measured signal crosses zero (i.e. half way between the maximum and minimum of the CW signal). The absorption maximum of the perpendicular ($\theta = 90°$)

spectrum (Figures 4.6 and 4.7) occurs at 327.1 mT. Using Equation 2.18, this gives a value of $g\perp = 2.047$ which is in good agreement with literature values [142, 220]. It is readily apparent that only one broad peak is observed here and that no Cu or N hyperfine structure can be resolved. This is due to Cu-Cu dipolar interactions broadening the spectra, as described in Section 1.3.2.

As the sample is rotated away from the $\theta = 90°$ orientation, a contribution at smaller magnetic fields from $g_{//}$ is introduced, demonstrating the angular dependence of the EPR signals anticipated from Figure 4.5. Again, no hyperfine structure is observed from this g-value due to the dipolar Cu-Cu interactions; these broaden the EPR spectra and so the hyperfine peaks cannot be resolved. The spectra at 79° and 101° are equivalent, as are those at 68° and 113°, emphasising that the perpendicular orientation is at a point of symmetry. Another turning point is observed at $\theta = 0°$, referred to as the parallel orientation, wherein the spectrum has an additional contribution towards lower magnetic fields and is flatter in appearance (note that this spectrum is shown in more detail in Figure 4.7). This is the result of the Cu hyperfine peaks overlapping to form one broad peak for $g_{//}$ in addition to the $g\perp$ contribution (see Figure 4.5). It is therefore difficult to deconvolve the peaks and so it has not been possible to estimate the value of $g_{//}$ from this data (dilution in an H_2Pc matrix is required, as will be discussed in Section 4.3.4).

EPR can provide useful information about the Cu-Cu separations, even for concentrated systems in which the hyperfine structure cannot be resolved. Specifically, the lineshape will vary for different crystallographic phases [30, 142], as outlined in Section 1.3.2. The continuous wave EPR spectra of the α- and β-phase crystallites, which had been crushed to give a true powder average, are shown in Figure 4.7. In this figure, they are compared to the film spectra in the parallel ($\theta = 0°$) and perpendicular ($\theta = 90°$) orientations. Once again, the sharp peak in both of the film spectra centred at ~334.3 mT is from the kapton substrate. The maximum to minimum peak width of the α-phase CuPc crystallites is measured to be 8.5 mT, whilst that of the β-phase is 6.2 mT (the positions of which are indicated by the blue and green dotted lines respectively in Figure 4.7). The narrower absorption peak of the β-phase has been attributed to a greater intermolecular

exchange interaction in this polymorph by Abkowitz *et al.* [142]. However, as is seen in Figure 1.2, the Cu-Cu separations are greater in the β-phase and so a weaker coupling is anticipated (inter-column molecular separations of ~3.8 Å and 4.79 Å are shown for the α- and β-polymorphs respectively). Instead, weaker dipolar interactions would be anticipated for greater Cu-Cu separations (the interaction strength scales as $\sim 1/r^3$, as outlined in Equation 2.20). Therefore, a new interpretation is offered here, wherein the sharper spectrum of the β-phase crystallites is attributed to a reduced broadening (i.e. relative sharpening) due to the increased Cu-Cu distance when compared to the α-phase.

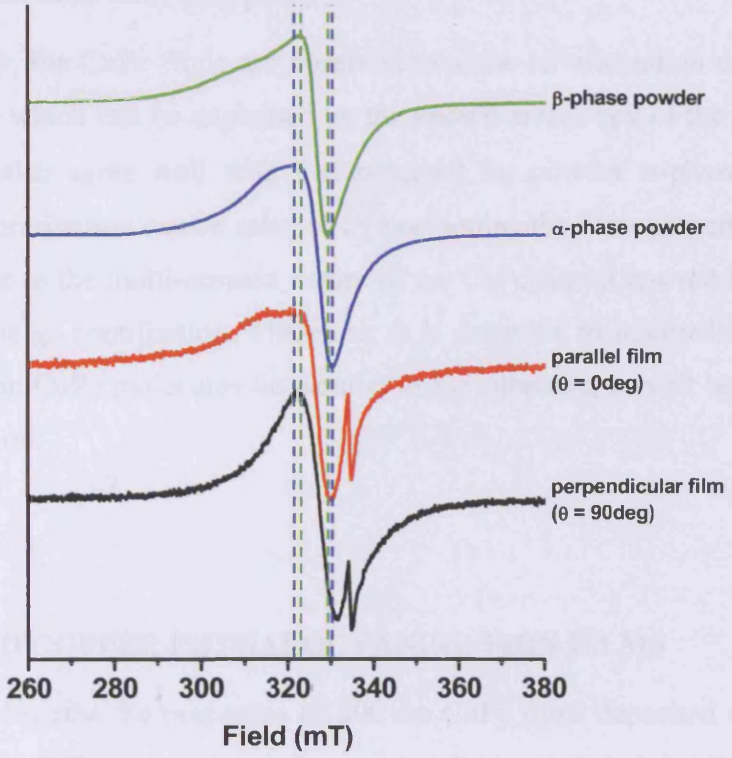

Figure 4.7. *EPR spectra of 100 nm CuPc films aligned parallel (red) or perpendicular (black) to the magnetic field, along with spectra of powder α- (blue) and β-phase (green) crystallites. Blue and green dotted lines show the maximal and minimal field positions of the α- and β-phase powder spectra respectively. Spectra are offset and normalised for clarity.*

Comparison between the film and crystallite spectra should provide further insight into crystallographic phase of the CuPc film (from the previous analyses in this section it is anticipated to be of the α polymorph). In Figure 4.7, a good agreement is observed between the spectra of the parallel film orientation and the α-phase crystallites; this is consistent with Figure 4.5(b) wherein both the $g_{//}$ and $g_{\perp}$ are expected to contribute equally. Any slight discrepancies between the spectra may be a result of the preparation method used for the α-phase crystallites; it is known that if produced from precipitating solutions from H_2SO_4, such as those in Figure 4.7, some H_2SO_4 may remain in the sample. This is known to modify the lineshape of the spectra through interactions with the molecule, as described elsewhere [145].

In summary, the CuPc films are observed to show an orientation dependence to their EPR spectra, which can be explained by the known anisotropy of the *g*-factor. The spectra observed also agree well with that obtained for powder α-phase crystallites. Although the $g_{\perp}$ contribution can be selected by positioning the films perpendicular to the magnetic field, due to the multi-domain nature of the CuPc film it has not been possible to fully analyse the $g_{//}$ contribution. Therefore, it is desirable to manipulate the crystal structure so that the CuPc molecules lie parallel to the substrate, as will be described in the following section.

4.2. TEMPLATED COPPER PHTHALOCYANINE THIN FILMS

This section will describe the properties of 200 nm CuPc films deposited onto a 20 nm PTCDA layer by OMBD. As has already been noted, it is anticipated that the presence of the PTCDA layer will result in a rotation of the crystallographic domains such that the CuPc molecules lie approximately parallel to the substrate. Sections 4.2.1 and 4.2.2 will present the electronic absorption and x-ray diffraction analysis. These will be followed by a discussion of the CW EPR spectra in Section 4.2.3, in which the CuPc/PTCDA film will be compared to the CuPc film described in the previous section.

4.2.1 Electronic Absorption Spectroscopy

The electronic absorption spectrum of a 200 nm thick CuPc film on 20 nm PTCDA is shown in Figure 4.8, where it is compared with those of 55 nm PTCDA and 100 nm CuPc films. The spectrum of the PTCDA film agrees well with that published for its α-phase arrangement [231], with absorption maxima at 482 nm and 557 nm. In general, the absorption spectrum of the CuPc/PTCDA film follows that of the pure CuPc film suggesting that the molecules maintain the crystallographic arrangement of the α-phase, although small shifts occur to the position of the absorption peaks (<0.01 eV). This is in agreement with tapping mode AFM studies of this film (not shown), which demonstrate a similar topography to that described in Section 4.1.2; the surface consists of small spherical crystallites, typical of the α-phase, as has been shown elsewhere [37]. The small additional peak at 482 nm and shoulder at ~557 nm can be attributed to the contributions of the PTCDA layer.

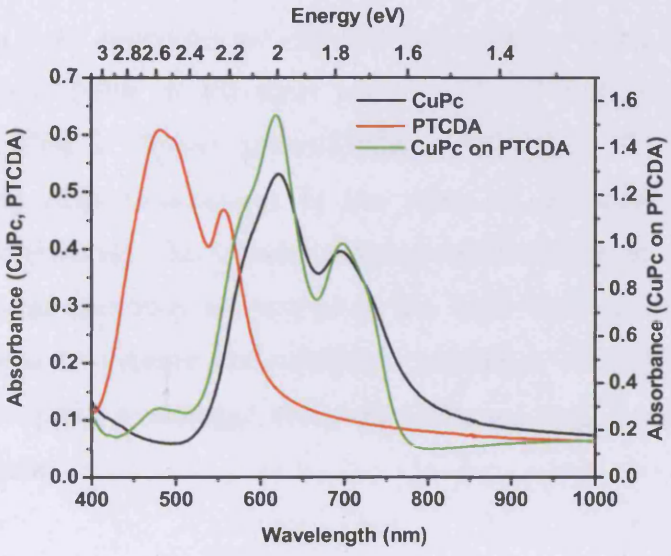

Figure 4.8. *Electronic absorption spectra of PTCDA (55 nm, red), CuPc (100 nm, black) and CuPc (200 nm)/PTCDA (20 nm) (green) films on glass. The axis on the left-hand side represents the absorbance of the pure PTCDA and CuPc films, whilst that of the templated (CuPc/PTCDA) film is given by the right-hand axis.*

The main consequence of depositing CuPc on PTCDA, rather than directly onto amorphous substrates, is a sharpening of the absorption peaks. This is evidenced by the accented dip at ~668 nm between the two main absorption peaks, and the sharper tail at longer wavelengths. The spectrum of the CuPc/PTCDA film also shows a reduction in the relative intensity of the ~695 nm peak with respect to that at ~620 nm. This has been described as a reduction of single molecule behaviour, suggesting enhanced intermolecular interactions within the molecular stacks [225]. Indeed, it can be seen from Figure 4.2 that the monomer absorbs in the region of the high wavelength peaks. As discussed in Section 1.2.1, the peak that at ~620 nm has been attributed to the presence of dimers and higher order aggregates [41, 42].

However, this explanation does not fully account for the differences in lineshape, wherein the minimum at 668 nm is more pronounced for the templated case. In addition, a small shift in the position of the higher wavelength maximum from 695 nm (CuPc only) to 698 nm (CuPc/PTCDA) is observed, a further consequence of peak sharpening. In the templated film, the CuPc molecules are expected to lie parallel to the substrate. Since the electric and magnetic fields of the light wave are perpendicular to the propagation direction, and the film is aligned perpendicular to the beam, this implies a weaker molecular coupling (less broadening) in the plane of the substrate, i.e. between neighbouring CuPc columns. The broader spectrum observed for the single CuPc layer, wherein all molecular directions are probed by the fields (as can be seen from Figure 4.5(b)), suggests that on average the molecular coupling is stronger in this case. This implies that the coupling is stronger along the CuPc stacking direction than between neighbouring columns.

4.2.2 X-ray Diffraction

X-ray diffraction has also been used to verify the CuPc orientation after deposition onto a PTCDA layer, as shown in Figure 4.9. In the case of the 55 nm PTCDA layer on glass, a sharp peak is observed at $2\theta = 27.6°$ (above the broad glass background between 20–35°) corresponding to a spacing of $d = 3.23$ Å. This peak can be attributed to the (102) plane

and shows that the PTCDA molecules lie approximately flat on the glass substrate, in agreement with literature reports [227, 228].

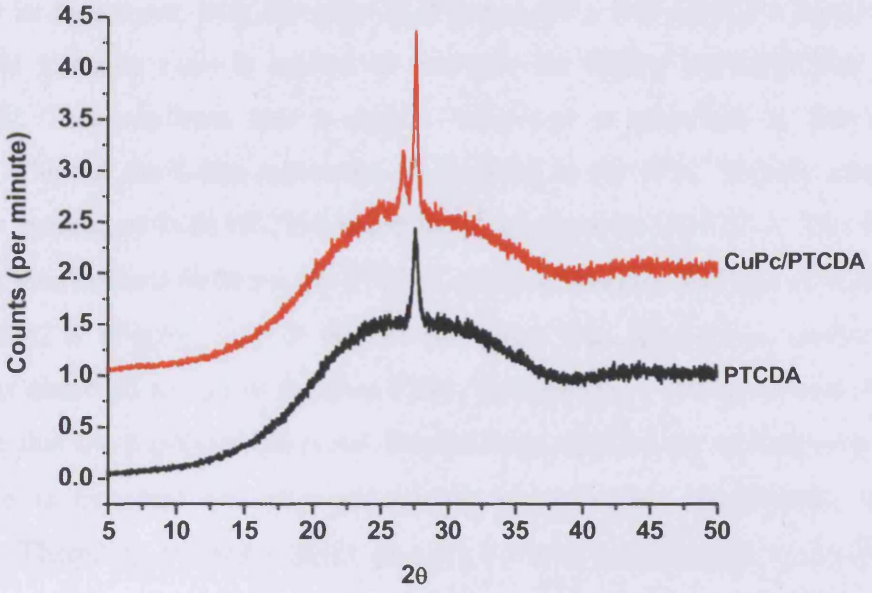

Figure 4.9. *X-ray diffraction spectra of a 55 nm PTCDA film (black) and a CuPc (200 nm) /PTCDA (20 nm) film (red). Both films are on glass substrates, whilst the data has been offset for clarity.*

The most striking feature of the XRD spectra of the CuPc/PTCDA film when compared with that of non-templated CuPc (Figure 4.4) is the absence of a sharp peak at $2\theta = 6.83°$. This demonstrates that the molecules are no longer oriented perpendicular to the substrate. Instead, a double peak is observed between $2\theta = 26–28°$. Lorentzian fitting of these peaks gives peak centres at 26.71° and 27.64° which correspond to spacings of 3.33 Å and 3.22 Å respectively. This finding is in excellent agreement with literature reports [224, 225]. The peak at 27.6° is at the same position as that of the PTCDA film, however it is of greater intensity (a fitted area of 0.803° min^{-1}) than the 55 nm PTCDA film (peak area of 0.628° min^{-1}). This is surprising since for the CuPc/PTCDA film the PTCDA layer is only 20 nm thick, and so the peak intensity does not scale with film

thickness. Instead, this suggests that the CuPc layer is templated by the PTCDA layer, adopting the same lattice spacing. The lower intensity peak observed at 26.7° is not due to the PTCDA layer and is instead attributed to the CuPc film [225, 226].

The ratio of the fitted areas of the 27.6° to 26.7° peaks has been determined to be 1.9. This is in agreement with the ratio of 2 found for a 190 nm H_2Pc layer on 15 nm PTCDA (the intensity ratio is known to decrease for higher H_2Pc:PTCDA thickness ratios) [224]. This confirms that a similar behaviour is observed to that described previously, wherein the CuPc molecules lie parallel to the film, initially adopting the same lattice spacing as bulk PTCDA but relax to a separation of 3.33 Å. The separation of 3.33 Å is intermediate between the PTCDA stacking distance and that of bulk α-phase CuPc of ~3.42 Å (Figure 1.2). It should be noted that although a similar stacking separation is observed to that of β-phase CuPc, the electronic absorption and AFM data demonstrate that the β polymorph is not formed here, and that an arrangement closer to the α-phase is expected (as also anticipated by the room temperature deposition conditions). Therefore, it seems likely that the packing arrangement is similar to that observed in the α-phase, but with a reduced intermolecular (face-to-face) spacing.

4.2.3 Electron Paramgnetic Resonance

As evidenced by the XRD data in the previous section, the deposition of CuPc onto a PTCDA layer results in a rotation of the molecular plane with respect to the substrate. Figure 4.10 shows the molecular orientations with respect to the kapton substrate for a single layer CuPc film (left) and a CuPc film on PTCDA (right), along with examples of the $g_{//}$ and $g_{\perp}$ directions. Table 4.1 summarises the anticipated $g_{//}$ and $g_{\perp}$ contributions for the extreme cases of the sample alignment with respect to the magnetic field at $\theta = 0°$ or $\theta = 90°$ (parallel and perpendicular sample orientations respectively) for both types of film.

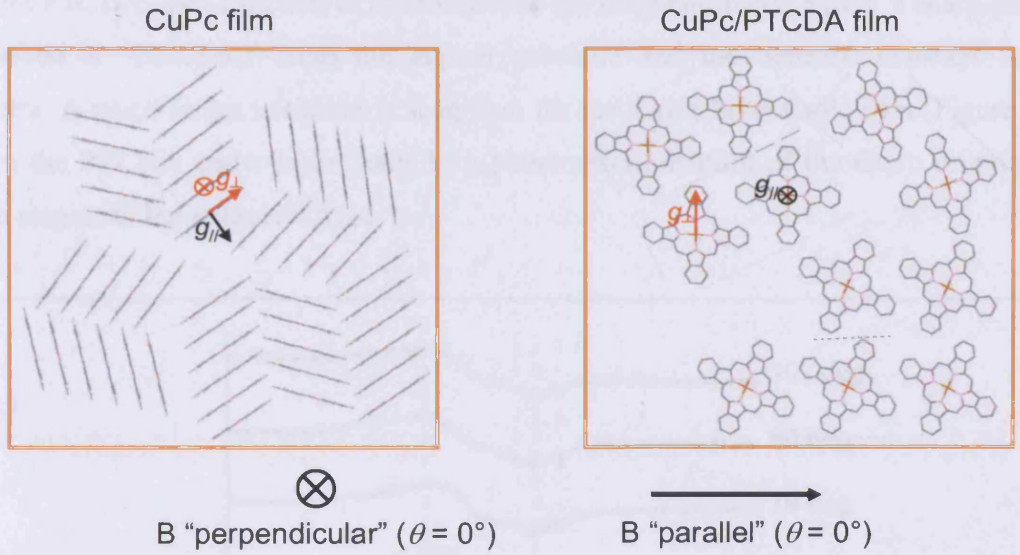

Figure 4.10. *A schematic drawing of the molecular orientation with respect to the substrate for the CuPc (left) and CuPc/PTCDA (right) films. Definitions of the film position with respect to the magnetic field (these are the same as in Section 4.1.4) and the directions of g⊥ and g// are also included. Multiple domains of monolayer arrangements (not to scale and with multilayers omitted for clarity) are shown in both cases.*

Film	B "perpendicular" (θ = 90°)	B "parallel" (θ = 0°)
CuPc single layer	$g_{\perp}$	$g_{//}$ and $g_{\perp}$
CuPc on PTCDA	$g_{//}$	$g_{\perp}$

Table 4.1. *A summary of the g// and g⊥ contributions for the CuPc and CuPc/PTCDA films when aligned perpendicular or parallel to the magnetic field direction.*

Figure 4.11 shows the variation in the CW EPR spectra of a 200 nm CuPc film on 20 nm PTCDA, as a function of orientation in the magnetic field. Again, a sharp peak is observed at ~334.3 mT from the kapton substrate and this remains constant for all spectra. A much larger variation is seen than for the single layer CuPc film (Figure 4.6), since the PTCDA under-layer leads to a better discrimination of the CuPc orientations with respect to the magnetic field.

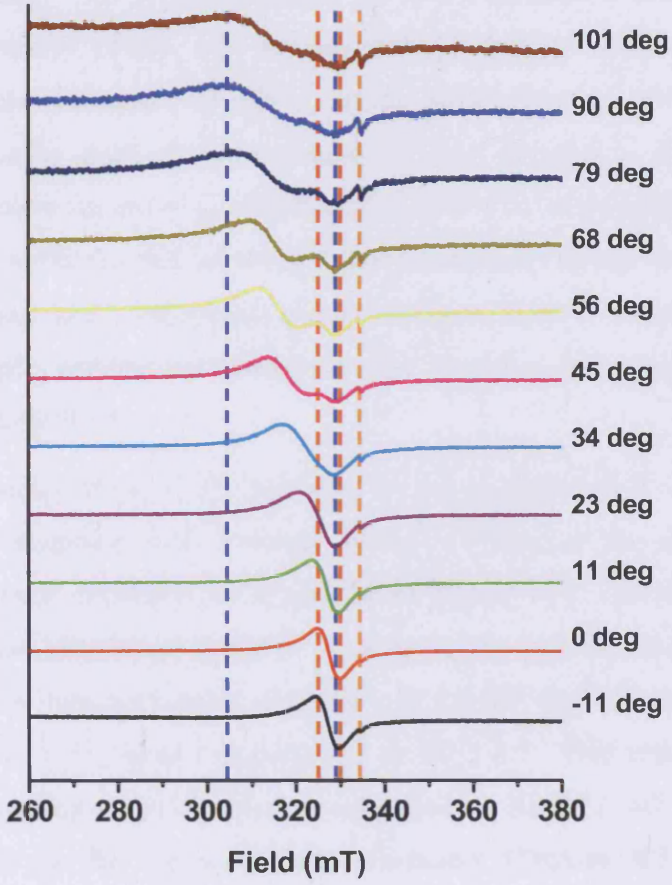

Figure 4.11. *CW EPR spectra of a CuPc/PTCDA film with respect to its orientation in the magnetic field. The blue and red dotted lines represent the maximal and minimal positions of the perpendicular and parallel orientations respectively, whilst the orange dotted line shows the peak due to the kapton substrate. Spectra are offset for clarity.*

From considerations of the molecular positions in the magnetic field, the spectrum at $\theta = 0°$ (in the parallel orientation) is expected to be similar to that of the single layer CuPc film when perpendicular to the magnetic field, as predicted by Table 4.1, with the signal corresponding exclusively to the $g_{\perp}$ contribution in both cases. As the sample is rotated, this absorption peak is observed to broaden and shift towards lower resonant magnetic field values due to the reduction in the size of the field component along $g_{\perp}$ combined with an increase in that along $g_{//}$, in a similar manner to that of Figure 4.6. Once angles between $\theta = 45–79°$ are reached, two distinct peaks can be resolved from the $g_{\perp}$ and $g_{//}$ contributions (these will be discussed in further detail shortly). At the perpendicular sample orientation ($\theta = 90°$), only a trace of the $g_{\perp}$ contribution can be seen, whilst a broader peak at lower magnetic field absorption is observed. This corresponds to the contribution of $g_{//}$, which is expected to be more spread out due to the larger Cu hyperfine splittings and occurs at a lower resonant magnetic field, as suggested in Figure 4.5(c). Once again, the spectra are seen to be symmetric about the parallel and perpendicular sample orientations, demonstrating that the full range of molecular orientations has been probed.

The EPR spectra of the CuPc film on PTCDA at angles of $\theta = 0°$, 45° and 90° with respect to the magnetic field direction, along with those of the single layer CuPc film at its two extreme positions are compared in Figure 4.12. For the CuPc film on PTCDA, the sharpest absorption spectrum is seen for the parallel orientation ($\theta = 0°$), with a maximum to minimum peak separation of 4.9 mT and microwave absorption maximum (when the CW signal crosses zero) at 327.3 mT. This resonant field value corresponds to a $g_{\perp}$ value of 2.045, which is very close to that of 2.047 obtained without the PTCDA layer in the perpendicular orientation (Section 4.1.4). Any slight discrepancies could be due to experimental error, or variations in the molecular position from being precisely perpendicular to (for the 100 nm CuPc film) or parallel to (200 nm CuPc on PTCDA) the substrate, which could lead to small contributions from $g_{//}$. Furthermore, the spectrum of the parallel orientation of the film ($\theta = 0°$) on PTCDA is

sharper than that of the single layer CuPc film when perpendicular to the field (the latter has a maximum peak-to-peak width of 9.2 mT).

The variations in lineshape between these two spectra suggest that there is a weaker Cu-Cu coupling between neighbouring columns in the CuPc/PTCDA film. This is likely to be a result of enhanced intra-column coupling due to the reduction in separation of the molecules along the stacking direction (as evidenced by the XRD data). Such an interpretation would lend support to the Ashida model. As seen in Figure 1.2, the brickstone arrangement of the Hoshino model gives rise to an equivalent side-on molecular separation to that of the CuPc/PTCDA film (the projection shown in the figure is identical to that when looking down upon the substrate, and so it is possible for all molecules within a domain in the Hoshino model to be aligned parallel to the magnetic field). Alternatively, this may suggest that the CuPc/PTCDA film is more textured than its CuPc counterpart. In Section 4.1.3 it was noted that for single layer CuPc films a small contribution from the (002) or (001) planes occur (these planes are for the Ashida and Hoshino models respectively). From Figure 1.2 it is apparent that, due to the molecular tilt, a small component along $g_{//}$ would be present from such a unit cell orientation.

As suggested by Table 4.1, the spectrum of the CuPc film on PTCDA when perpendicular to the magnetic field is largely due to the $g_{//}$ contribution. This spectrum is very broad, mainly due to the large Cu hyperfine splittings from the $g_{//}$ contribution in combination with broadening effects induced by the dipolar interactions (the distance between neighbouring Cu atoms is at its minimum and so the dipole-dipole coupling is relatively large). The maximum and minimum positions of this spectrum occur at 303.4 mT and 329.1 mT respectively (note that the latter may be affected slightly by the presence of a small contribution from $g_{\perp}$), with a peak-to-peak width of 25.7 mT and maximal microwave absorption at 313.9 mT. From Equation 2.18, an estimate for $g_{//}$ of 2.133 is found. Typically, values of $g_{//}$ for CuPc obtained from dilute systems range between 2.157 and 2.159 [139, 141, 142, 144, 220] and that found here is below these literature values. This discrepancy may be due to small contributions from $g_{\perp}$ causing an artificially higher resonant magnetic field, and/or a shifting in the resonant field position by the Cu-Cu dipole-dipole interactions.

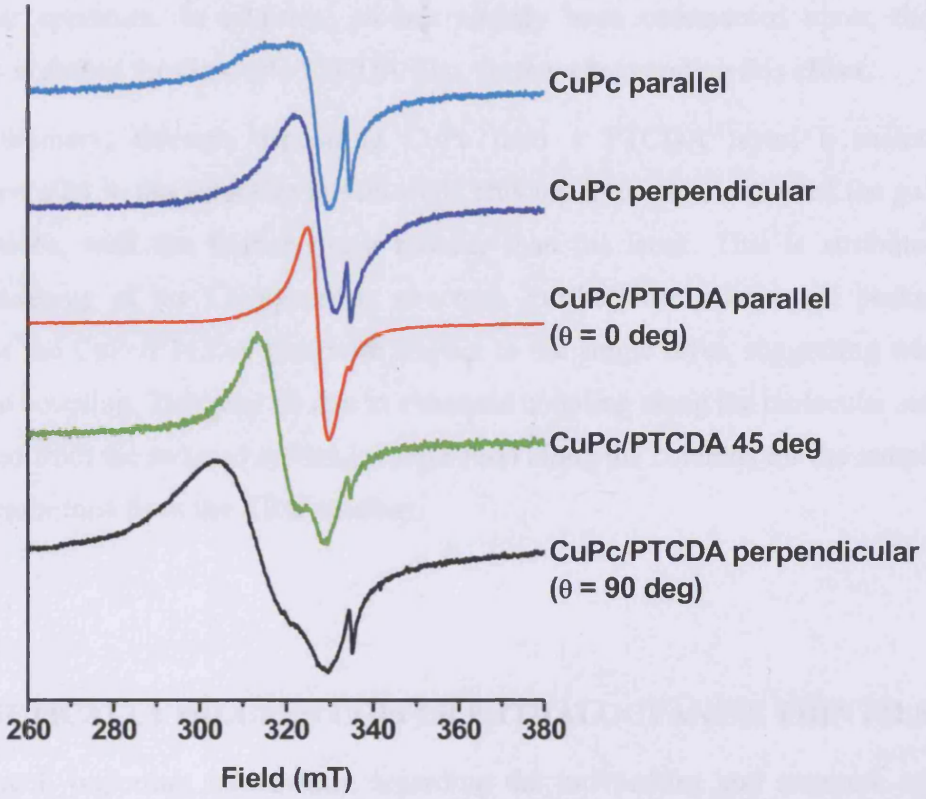

Figure 4.12. *Comparison of the CW EPR spectra of the CuPc and CuPc/PTCDA films at selected orientations with respect to the magnetic field. Data are offset for clarity.*

From consideration of Figure 4.10, at first glance it would seem sensible to expect the spectra of the CuPc/PTCDA film when at 45° to the magnetic field to be similar to that of the CuPc film (without a PTCDA layer) when parallel to the field ($\theta = 0°$), since contributions from $g_{\perp}$ and $g_{//}$ would be expected in both cases. However, from comparison of their lineshapes in Figure 4.12 this is not the case, with more sharply defined peaks for the CuPc/PTCDA film. For the CuPc/PTCDA film aligned at 45° to the magnetic field, contributions arise in the spectrum from $g_{//}$ and $g_{\perp}$ and so this spectrum is a direct superposition of the spectra in the two extreme positions. However, for the CuPc film aligned parallel to the magnetic field, owing to a large number of domain

orientations, this spectrum is the superposition of the spectra of all possible θ values (i.e. from the two extreme positions AND all other orientations in between) and so this results in a broader spectrum. In addition, as has already been commented upon, the $g_{\perp}$ contribution is shaper for the CuPc/PTCDA film, further exaggerating this effect.

In summary, through depositing CuPc onto a PTCDA layer, a molecular orientation parallel to the substrate is achieved. This has allowed analyses of the $g_{\perp}$ and $g_{//}$ contributions, with the former much broader than the latter. This is attributed to dipolar broadening of the Cu hyperfine structure. Furthermore, sharper $g_{\perp}$ peaks are observed for the CuPc/PTCDA film with respect to the single layer, suggesting weaker inter-column coupling. This may be due to enhanced coupling along the molecular stacks, as anticipated from the reduced molecular separation along the columns for the templated phase (as determined from the XRD studies).

4.3. MAGNETICALLY DILUTED COPPER PHTHALOCYANINE THIN FILMS

Although much important information regarding the interactions and structure of the CuPc and CuPc/PTCDA films has already been gained in Sections 4.1 and 4.2, it is anticipated that further insights will be provided by diluting the CuPc molecules in an H_2Pc matrix. In particular, determining whether a randomly diluted system (at the molecular level) or phase segregation occurs will yield important information regarding the structural similarities between the α polymorphs of CuPc and H_2Pc. For a system in which the CuPc molecules are spatially separated, hyperfine structure will be observed in the EPR signal, as shown in Figure 1.10. In turn, it is hoped that this could provide further insight into the mechanisms for spin transport within the Pc films; in particular it is of interest to compare inter-column and intra-column interactions. Furthermore, upon dilution the system will enter the regimes of spin separation relevant for quantum computing (Section 1.3.3), whilst spatial separation of the CuPc molecules could lead to control over their magnetic properties, as has been observed for CoPc:H_2Pc crystallites [232] (anti-ferromagnetism has already been established in pure α-phase CuPc films [37]).

In this section, a detailed characterisation of co-deposited CuPc and H_2Pc films will be presented, both with and without a PTCDA under-layer. A variety of films with different CuPc concentrations were grown (ranging between ~5% and ~85%); the percentage of CuPc present in each calculated from in-situ readings of QCMs positioned near each k-cell. Care was taken to maintain a constant CuPc:H_2Pc ratio throughout the thickness of the films. In all cases the total thickness of the CuPc:H_2Pc layer was 200 nm, with a 20 nm PTCDA layer underneath where appropriate. Their electronic absorption spectra, morphology and x-ray diffraction spectra will be discussed in Sections 4.3.1, 4.3.2 and 4.3.3 respectively. This will be followed by a discussion of the EPR spectra of the most dilute CuPc:H_2Pc and CuPc:H_2Pc/PTCDA films in Section 4.3.4 (since these show the most resolved hyperfine structure, as discussed in Section 1.3.2).

4.3.1 Electronic Absorption

The electronic absorption spectra of single layer 100 nm CuPc and H_2Pc films on glass are shown in Figure 4.13, and compared with those of the co-deposited CuPc:H_2Pc mixtures (each 200 nm thick). The absorption spectra of the pure films are very similar since it is the phthalocyanine ligand that is excited in both cases. Some variations in the absorption profile due to the presence of the central metal are expected, but these are more prominent towards the UV region [45], where unfortunately the glass substrate is also strongly absorbing. However, subtle variations are observed in the visible region (Q-band absorption), namely the presence of a shoulder in the CuPc spectrum towards the shorter wavelength side of the main absorption band, and a greater definition to its main peaks, as reported elsewhere [45, 46]. In addition, slight variations are observed in the positions of the absorption maxima (Figure 4.13(b)), with low-wavelength peak positions at 621 nm and 630 nm for CuPc and H_2Pc respectively, a shift of 0.029 eV that agrees with literature values [45]. Accurate peak-fitting of the spectra is difficult since multiple (at least four) peaks are required to reproduce the line-shape. In addition, it is difficult to determine whether Lorentzian or Gaussian functions should be used; these would model homogenous or inhomogeneous broadening respectively and insufficient information is present to determine which is (or indeed if both are) present [46, 233]. For this reason,

fitting has not been performed on the spectra and instead a qualitative description will be given.

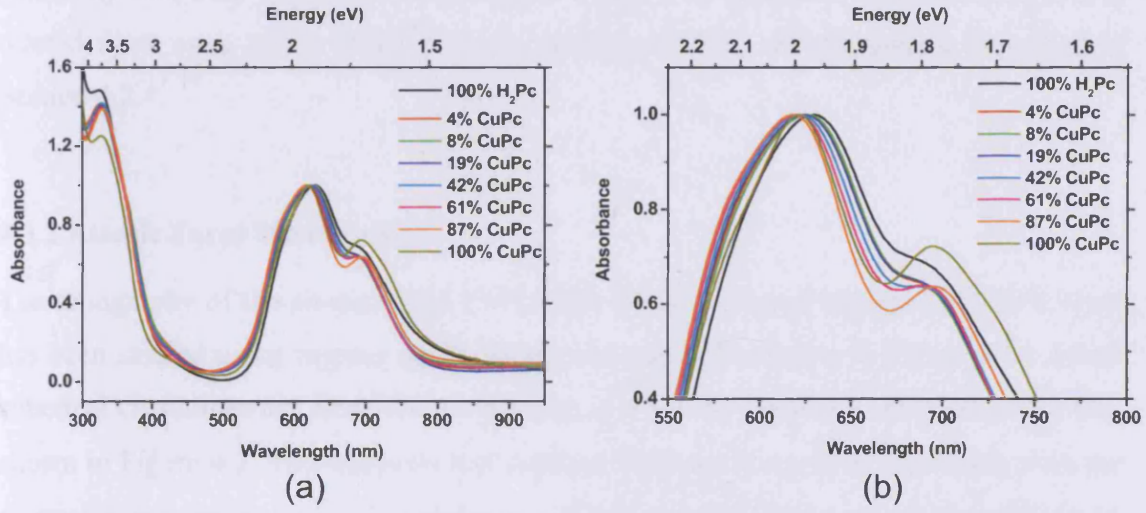

Figure 4.13. *Electronic absorption spectra of 100 nm H_2Pc (100%, black) and 100 nm CuPc (100%, khaki) films, along with a range of co-deposited CuPc/H_2Pc mixtures (percentage CuPc stated in legend, as determined from QCM values during deposition). (a) Full wavelength range of visible region (300 nm to 950 nm), (b) detailed plot centred about the absorption maxima (550 nm to 800 nm).*

As seen from Figure 4.13, the characteristic lineshape of the α-phase (as discussed in Section 4.1.4) is maintained for all compositions and so all films are expected to be crystalline and of the α-phase. However, it is not possible to determine whether the Pc variants are randomly distributed or phase segregated from this technique. The subtle variations in lineshape follow the anticipated trends arising from the differences in the spectra of the pure Pc films, wherein an increase in the magnitude of the ~670 nm dip and the emergence of the high energy shoulder are observed for increasing CuPc concentration. In addition, a general trend of a slight blueshift of the absorption maxima is followed, in agreement with the shift observed between the pure CuPc and H_2Pc films.

The long wavelength tail is broader for the pure materials. This is expected to be due to differences in film thicknesses; as described previously, the domain size will increase with film thickness [229], whilst an increase in relative contribution from the first few layers is observed for thinner films (these may be disordered since glass is an amorphous substrate). It should be noted that analogous trends were observed for the corresponding diluted films on a 20 nm PTCDA layer, accompanied by the sharpening described in Section 4.2.1.

4.3.2 Atomic Force Microscopy

The topography of the co-deposited CuPc:H_2Pc films, with and without a PTCDA layer has been studied using tapping mode AFM, with examples shown in Figure 4.14. Small spherical crystallites are observed in all cases, in a similar manner to the bulk CuPc film shown in Figure 4.3. This suggests that α-phase films are formed, in agreement with the electronic absorption data. All samples are of uniform appearance across the surface, as was seen by multiple analyses performed at different locations on each sample (not shown). It should be noted that when deposited onto substrates at room temperature, PTCDA also forms small spherical crystallites [228] and so for the CuPc:H_2Pc/PTCDA films, the morphology of the PTCDA layer has been preserved. The bulk CuPc and H_2Pc films are of very similar appearance; it is not possible to use AFM to distinguish between CuPc and H_2Pc crystallites. Therefore, Figure 4.14 cannot be used to determine whether the films contain aggregated CuPc and H_2Pc domains (i.e. phase segregation) or a random distribution of the two species at the molecular level.

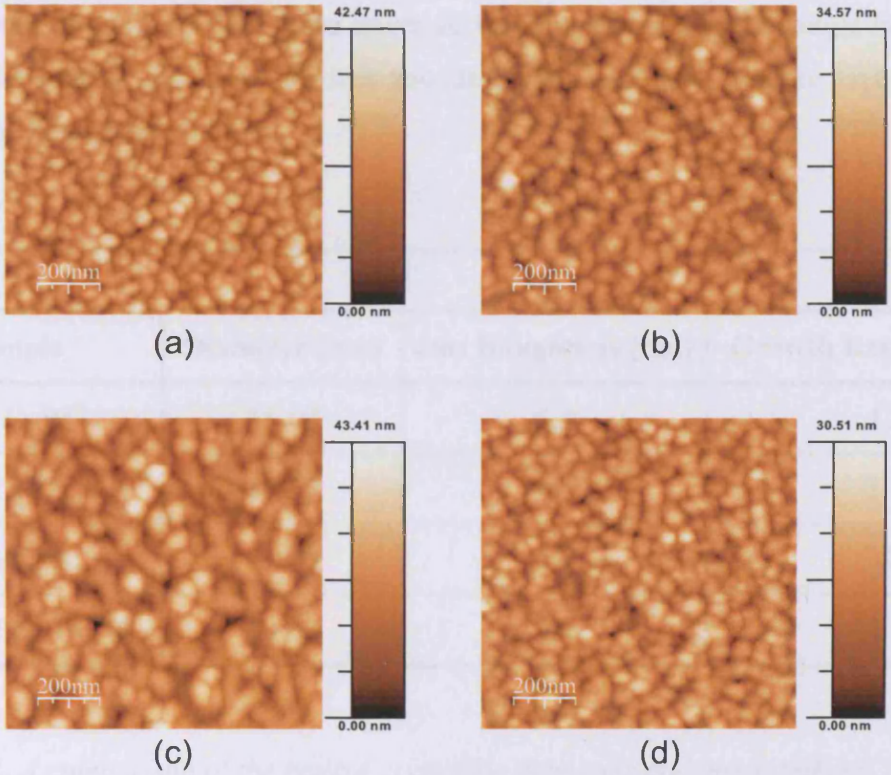

Figure 4.14. *Tapping mode AFM images of (a) 4% CuPc, (b) 5% CuPc/PTCDA, (c) 42% CuPc, (d) 52% CuPc/PTCDA films on glass substrates. Roughness values are given in Table 4.2.*

As seen in Figure 4.14, there are slight variations in the morphology of the four films, with larger crystallites observed for the 42% CuPc film. These differences in domain size can be attributed to variations in the growth rate for each sample. It was important to keep the CuPc and H_2Pc fluxes constant throughout the film deposition, and so faster overall growth rates were used for films requiring low percentages of CuPc (slower total deposition rates would involve a CuPc QCM rate close to the noise level). Table 4.2 compares the average crystallite diameters and rms roughness values with

sample growth rates. The 42% CuPc film was grown at a slower rate and has the largest domain size and surface roughness; for slower growth rates the molecules have more time to migrate across the surface and so form larger crystallographic domains. In addition, the films on PTCDA have lower surface roughness than the single layer CuPc films. This implies that they are less rounded, consistent with a more layer-by-layer growth mechanism on PTCDA.

Sample	Diameter (nm)	rms Roughness (nm)	Growth Rate (nm/min)
4% CuPc	35-60	5.3	13
5% CuPc/PTCDA	35-55	4.3	7.7
42% CuPc	45-70	6.2	2.2
52% CuPc/PTCDA	40-60	4.0	4.3

Table 4.2. *A comparison of the typical crystallite diameters and measured rms roughness values of the AFM images shown in Figure 4.14 with the growth rates of each of the co-deposited CuPc:H_2Pc films.*

4.3.3 X-ray Diffraction

This sub-section will comprise a discussion of the single layer and then templated CuPc:H_2Pc films.

Single layer CuPc:H_2Pc films

X-ray diffraction has been used to asses whether the crystal structure of CuPc is maintained for the diluted films. Firstly though, it is important to consider whether the CuPc and H_2Pc single layer films are isomorphous; if so, a random distribution of Cu^{2+}

ions could be achieved. However, if the crystal structures are vastly different phase segregation might be more favourable. The XRD spectra of 100 nm thick pure H_2Pc and CuPc films are plotted in Figure 4.15(a). Clearly, both are crystalline; since deposition was performed with the substrates at room temperature these are both expected to be of the α-phase, as suggested by the electronic absorption and AFM measurements. As discussed in Section 1.2.1, two models have been proposed for the crystal structure of α-CuPc, referred to here as the Ashida and Hoshino models [27, 28], whilst for H_2Pc it is the model proposed by Brown [36] that is the most commonly cited. The predicted peak positions and lattice spacings of these models are summarised in Table 4.3.

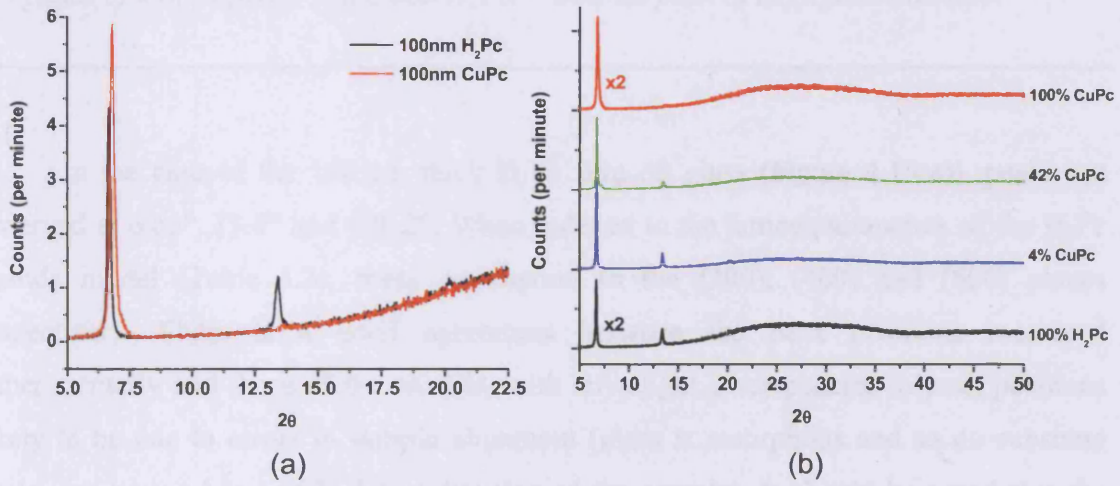

Figure 4.15. *X-ray diffraction spectra of (a) 100 nm CuPc (red) and H_2Pc (black) bulk films and (b) the same spectra compared with 200 nm 4% CuPc (blue) and 42% CuPc (green) mixtures. Note that in (b) the intensities of the pure film spectra have been multiplied by two to compensate for film thickness variations, whilst the data are offset for clarity.*

CuPc (Hoshino model [28])			**CuPc (Ashida model [27])**			**H_2Pc (Brown model [36])**		
2θ (°)	d (Å)	(hkl)	2θ (°)	d (Å)	(hkl)	2θ (°)	d (Å)	(hkl)
6.85	12.9	(100)	6.79	13.0	(200)	6.74	13.1	(200)
7.37	12.0	(001)	7.42	11.9	(002)	7.42	11.9	(002)
13.7 *	6.46 *	(200)	13.7	6.48	(400)	13.5	6.56	(400)

Table 4.3. *A summary of the predicted peak positions and lattice spacings for the first few peaks of bulk α-phase CuPc and H_2Pc. * denotes peak of negligible intensity.*

In the case of the 100 nm thick H_2Pc film on glass (Figure 4.15(a)), peaks are observed at 6.68°, 13.4° and ~20.2°. When indexed to the lattice parameters of the H_2Pc Ashida model (Table 4.3), these correspond to the (200), (400) and (600) planes respectively. There is a good agreement between the peak positions measured experimentally and those of the models, with any slight discrepancies in peak positions likely to be due to errors in sample alignment (glass is amorphous and so no substrate peaks can be used to verify the positioning of the sample). It should be noted that the peak at ~7.4° due to diffraction for the (002) plane is absent; this implies that there are no crystallites with their c-axis perpendicular to the substrate and that the H_2Pc film is very textured.

As discussed in Section 4.1.3, for the 100 nm thick CuPc film only one main peak is observed, the position of which ($2\theta = 6.83°$) occurs at a slightly higher Bragg angle than for the corresponding H_2Pc film. The intensity of the CuPc peak is greater than the corresponding one from H_2Pc; this is to be expected since Cu acts as a strong x-ray scatterer, and so for two equivalently ordered films the peak of CuPc would be of greater intensity. The most striking difference of the spectra in Figure 4.15(a) is the absence of

the peak at $2\theta \sim 13.5°$ for the CuPc film. As a result, comparison of the two models for CuPc from Table 4.3 suggest better agreement with the Hoshino model wherein the (200) plane (the equivalent of the (400) plane in Ashida's model) is of negligible intensity.

However, the absence of the $2\theta \sim 13.5°$ peak could also be explained by a lower degree of ordering in the CuPc film. As discussed in Section 4.1.3, a shoulder is observed at 7.36° and this was attributed to the (001) or (002) planes of the Hoshino and Ashida models respectively. Such a shoulder is not present for the H_2Pc spectrum, implying that the CuPc film is less textured. The influence of disorder on peak intensity increases at higher angles, as described by the Debye-Waller effect [207]. The peak intensity profile $I(\theta)$ as a function of root mean square molecule displacement from the lattice position, $\langle u_s^2 \rangle$ is outlined in Equation 4.3. This is a Gaussian profile in terms of sin θ, where λ is the wavelength of the incident x-rays.

$$I(\theta) \sim \exp\left[\frac{-8\pi^2 \langle u_s^2 \rangle \sin^2\theta}{\lambda^2}\right] \qquad [4.3]$$

Therefore, if the CuPc film is less textured, the intensity of peaks at greater 2θ values may be drastically reduced by the Debye-Waller cut-off, and this may explain why the peak at ~13.5° is not observed.

The XRD spectra of two co-deposited single layer CuPc:H_2Pc films are shown in Figure 4.15(b), where the intensities of the 100 nm CuPc and H_2Pc traces have been doubled to aid comparison (the mixed films are 200 nm thick). All films are crystalline, with peaks observed at ~6.7° and ~13.5° corresponding to the (200) and (400) peaks respectively (note that the unit cell of the Ashida model has been adopted here to simplify the discussion). Table 4.4 summarises the fitted positions of these two peaks and compares their relative intensities ($I_{(400)}/I_{(200)}$). These are seen to decrease for increasing CuPc content, although this does not scale linearly with the percentage of CuPc present in the films. In addition, there is a general trend of shifting (200) peak to smaller 2θ values

as the percentage of CuPc is reduced. This follows the trend expected from the peak positions of the pure CuPc and H_2Pc films, although since this shift is small any variations may also be due to variations in sample alignment.

Film	2θ (°)			Intensity Ratios	
	(200)	(002)	(400)	$I_{(002)}/I_{(200)}$	$I_{(400)}/I_{(200)}$
CuPc	6.83	7.36	n/a	0.020	n/a
42% CuPc	6.73	7.17	13.5	0.013	0.11
4% CuPc	6.70	7.29	13.4	0.0052	0.23
H_2Pc	6.68	n/a	13.4	n/a	0.32

Table 4.4. *A summary of the measured peak positions after Lorentzian fitting (R^2 values of 0.996-0.998 and 0.930-0.989 were found for the ~7° and ~13.5° peaks respectively). The ratios of the integrated areas with respect to the (200) peak are also given. It should be noted that the unit cell assignment of the Ashida model has been followed here.*

As outlined earlier, the variation in the ratio of $I_{(400)}/I_{(200)}$ for pure CuPc and H_2Pc can be attributed to variations in texture of the films. In the case of co-deposited films, phase segregation would lead to the formation of pure CuPc and H_2Pc domains, the relative abundances of which would scale with CuPc content. Therefore, if phase segregation had occurred, the ratio of $I_{(400)}/I_{(200)}$ would follow an approximately linear trend as a function of percentage H_2Pc. This does not appear to be the case here (although more data points would be necessary to confirm this). Furthermore, as has already been commented upon, the (200) peaks of the pure CuPc and H_2Pc films occur at different 2θ values (6.83° and 6.68° respectively). As a result, if this shift is real and if phase segregation has occurred, the 42% film spectrum would be a superposition of these peaks and so would be broader. However, little variation is seen in the width of the peaks; this implies that phase segregation does not occur here.

Alternatively, the disappearance of the peak at ~13.5° upon increased CuPc concentration could be explained by the natural tendency for a reduction in texture of the CuPc films. As was observed for the pure CuPc film, a small shoulder can be seen for the 42% CuPc film at ~7.2°, corresponding to the (002) planes (again the Ashida unit cell is used here). Lorentzian fitting has been performed from which a (002) contribution can be resolved for the 4% and 42% CuPc:H_2Pc films, as summarised in Table 4.4. The ratio of the areas of the (002) to (200) peaks is observed to increase upon increasing CuPc content. Therefore the number of domains wherein the *c*- rather than *a*-axis is aligned perpendicular to the substrate increase with CuPc concentration, thus reducing the texture of the film. For H_2Pc, there is a strong preference for the *a*-axis to align perpendicular to the substrate, but for CuPc crystallites, although this alignment is still preferable, there may be less of an energy penalty for the *c*-axis to align perpendicular to the substrate. The observation of the (002) peak for the CuPc:H_2Pc films suggests that only the presence of CuPc is sufficient to nucleate domains in which the *c*-axis is perpendicular to the substrate.

In summary, pure single layer CuPc films appear less textured than their H_2Pc counterparts, whilst the positions of the (200) peaks are slightly shifted. For the co-deposited films, both the degree of texturing and positions of the (200) peaks follow the trends set out by the pure films. No significant broadening is observed for the 42% film which suggests that phase segregation is not occurring (the EPR studies in Section 4.3.4 should provide further insight into this). If this is the case, the disappearance of the ~13.5° peak and appearance of a (002) plane as a function of increasing CuPc content implies that even small quantities of CuPc (such as are found in the 4% CuPc film) can lead to a reduction in texture.

CuPc:H_2Pc/PTCDA films

The x-ray diffraction spectra of mixed CuPc:H_2Pc films deposited onto a PTCDA layer also suggest crystallinity, with peaks observed between 26–28°, as seen in Figure 4.16. The peak at ~27.5° corresponds to both the (102) plane of the PTCDA and the templated Pc layer, whilst the lower intensity peak at ~26.7° is due to the relaxation of the Pc layer,

in a similar manner to that described for CuPc on PTCDA (Section 4.2.2). It should be noted that the H_2Pc/PTCDA film is only 82.5 nm thick, whilst the other films have a Pc layer of 200 nm (the underlying PTCDA layer is 20 nm thick in all cases). It is apparent from the figure that there is a general increase in intensity of both peaks as a function of increasing CuPc content. This is contrary to the trend observed for the ~13.5° peaks of Figure 4.15(b), and is likely to be due to increased scattering from the Cu atoms (heavier atoms deflect x-rays more efficiently). In addition, the mere presence of these peaks may seem surprising following the aforementioned reduction in intensity of peaks at larger 2θ values, as observed for the non-templated films. This implies that the CuPc/PTCDA films are more ordered (textured) than their single layer counterparts, in agreement with the interpretation of the sharper EPR spectra in Section 4.2.3.

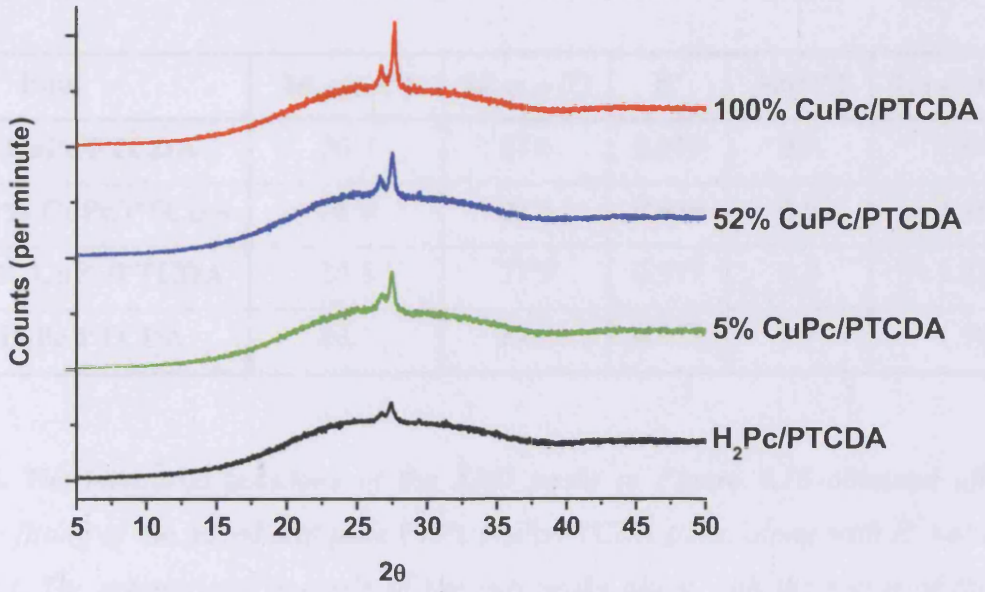

Figure 4.16. *X-ray diffraction spectra of an 81.5 nm H_2Pc layer on 20 nm PTCDA (black) and 200 nm thick (b) 5% CuPc (green), (c) 52% CuPc (blue) and (d) 100% CuPc (red) layers on 20 nm PTCDA. All films are on glass substrates and the spectra are offset for clarity. It should be noted that the H_2Pc/PTCDA film was integrated between 24-31° for longer, to enhance the resolution of its peaks.*

Lorentzian fitting was performed on the two peaks of each spectrum in Figure 4.16, with the positions and ratios of the area of each summarised in Table 4.5. The PTCDA peak at ~27.6° provides a useful maker to correct for errors in sample alignment, and so the separation between the $2\theta \sim 27.6°$ and $2\theta \sim 26.7°$ peaks will be discussed here. As seen in Table 4.5, the separations between these two peaks are seen to increase with increasing CuPc concentration. If the higher 2θ peak is assumed to be due to the PTCDA (102) plane, this increase in separation suggests that the peak at smaller 2θ values of CuPc occurs at a smaller angle than that of H_2Pc. In section 4.2.2, this peak was attributed to the relaxed separation of the Pc molecules (for the uppermost layers of the film). This implies that a greater molecular separation along the column axis is observed for the CuPc films than their H_2Pc counterparts.

Film	$2\theta_{\sim 26.7°}$ (°)	$2\theta_{\sim 27.6°}$ (°)	R^2	$\Delta 2\theta$ (°)	$I_{\sim 27.6°}/ I_{\sim 26.7°}$
200nm CuPc/PTCDA	26.7	27.6	0.977	0.9	1.94
200nm 52% CuPc/PTCDA	26.6	27.5	0.976	0.9	1.46
200nm 5% CuPc/PTCDA	26.8	27.5	0.977	0.8	1.22
82nm H_2Pc/PTCDA	26.7	27.4	0.978	0.7	1.90

Table 4.5. *The measured positions of the XRD peaks in Figure 4.16 obtained after Lorentzian fitting of the mixed and pure CuPc:H_2Pc/PTCDA films, along with R^2 values for each fit. The separations in angle of the two peaks along with the ratios of their integrated areas are also given.*

Comparison of the relative areas of the two peaks again shows a reduction in the peak at $2\theta \sim 26.7°$ as a function of increasing CuPc concentration. It should be noted that although a value of 1.90 is given for the H_2Pc/PTCDA film, this is artificially high due to

the reduced H_2Pc layer thickness (compared to the other films). For the 200 nm thick films, the trend in the $I_{\sim 27.6°}/ I_{\sim 26.7°}$ ratio implies that the thickness of the layer that retains the spacing of the PTCDA (i.e. that corresponding to the $2\theta \sim 27.6°$ peak) is greater for films of higher CuPc concentration. This suggests that the presence of CuPc increases the range at which the PTCDA directly influences the separation between Pc molecules (although the overall flat-lying structure observed, even in the relaxed region, is due to the templating layer). Alternatively, this could be explained by the increase in separation of Pc molecules in the relaxed layers for films of larger CuPc content. It is feasible that the relaxation is more progressive, with the layers of intermediate separation not able to diffract (due to the requirement for multiple layers of the same *d* for Bragg diffraction, as outlined in Section 2.11.2) and so the total thickness of the uppermost (relaxed) layer is reduced.

4.3.4 Electron Paramagnetic Resonance

Continuous wave EPR has been used to study the co-deposited CuPc:H_2Pc films. As described in Section 1.4.2, if the concentration of CuPc is reduced by growing mixed CuPc:H_2Pc crystallites, it should be possible to resolve the Cu and N hyperfine structure shown in Figure 4.5(c). This occurs since the Cu spin centres are separated by the introduction of H_2Pc spacer molecules and so the dipolar interactions are reduced. In this section it is of interest to determine whether this mixing on the molecular scale occurs for the CuPc:H_2Pc films (as opposed to phase segregation). If so, it will be possible to gain further insights into the film structure and Cu-Cu interactions from analysis of the hyperfine structures. For this reason the most dilute (~5% CuPc) films will be used here since they should provide the greatest resolution of the hyperfine structure. It should be noted that H_2Pc does not contain any unpaired electrons and so is essentially invisible in EPR (the measurements were performed in the dark; if this had not been the case signal from the unpaired excited and ground state electrons would have been detectable).

Figure 4.17 shows the variation in spectra of the 4% single layer CuPc:H_2Pc and 5% CuPc:H_2Pc/PTCDA films, as a function of their orientation in the magnetic field (again defined by the position of the kapton substrate with respect to the field in both

cases). Hyperfine structure is observed due to interactions between the unpaired electrons and the Cu and N nuclei, and this replaces the broad spectra of Figures 4.6 and 4.11. Importantly, this demonstrates that the Cu-Cu interactions have been reduced in the films by increasing the spatial separation of the CuPc molecules via H_2Pc spacer molecules, whilst retaining the overall sample crystallinity. This provides unambiguous evidence that the CuPc molecules are randomly distributed within the Pc lattice and that phase segregation has not occurred; concentrated pockets of CuPc would give rise to spectra similar to those of bulk CuPc.

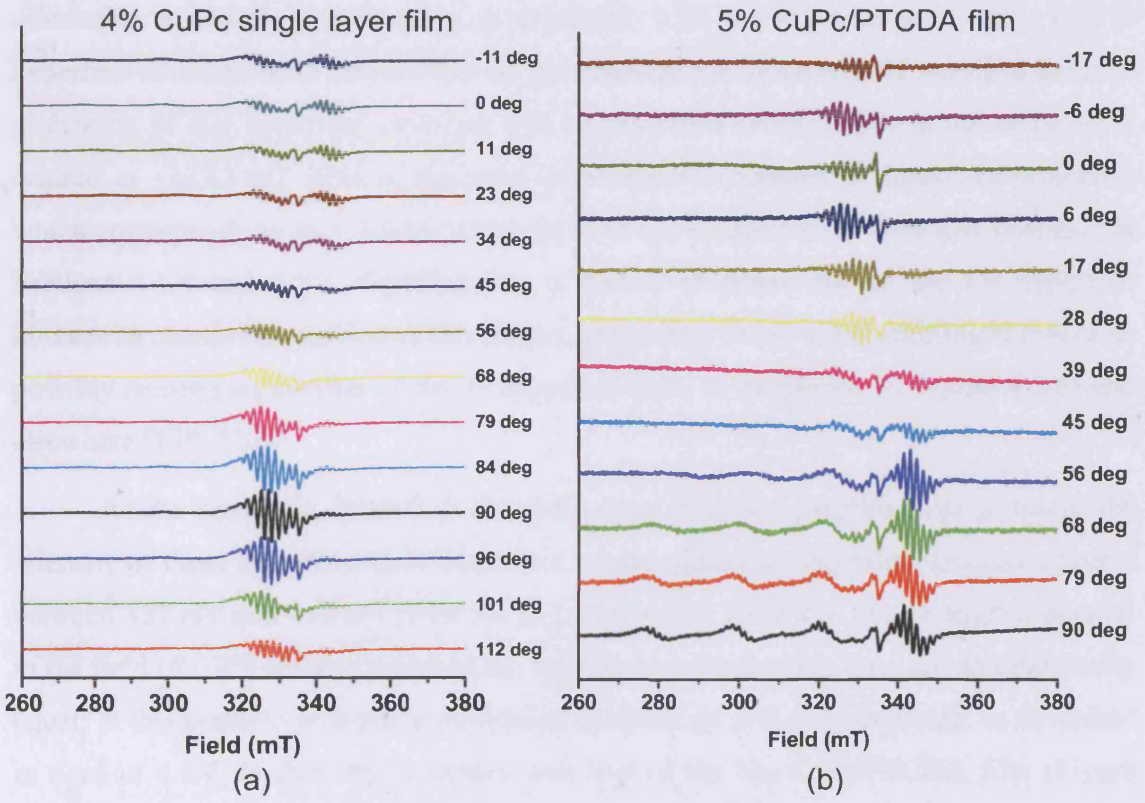

Figure 4.17. *CW EPR spectra of (a) 4% CuPc and (b) 5% CuPc/PTCDA films as a function of position in the magnetic field. Data are offset for clarity.*

In a similar manner to that observed for the 100% CuPc films, points of symmetry are observed when the films are aligned perpendicular ($\theta = 90°$) and parallel ($\theta = 0°$) to the magnetic field. The peak from the kapton substrate is still present and at the same position in all spectra, although it appears larger here since the number of CuPc molecules (and therefore unpaired electrons) has been reduced upon dilution. In the case of the 4% CuPc film (without a PTCDA layer) when aligned perpendicular to the substrate ($\theta = 90°$) a series of sharp lines are concentrated between 320–340 mT. The XRD data has shown that this film is crystalline with the molecules standing perpendicular to the substrate. Therefore, as suggested by Figure 4.5, at this sample orientation a contribution from $g_{\perp}$ is expected, with the multiple sharp lines due to hyperfine structure from interactions of the unpaired electrons with N nuclei (a detailed discussion of this hyperfine structure will be presented shortly). The group of peaks is centred at ~327.1 mT (this is the point of maximum intensity N hyperfine structure) which corresponds to $g_{\perp} = 2.047$, which is in excellent agreement with that obtained in Sections 4.1.4 and 4.2.3. Significantly, a quartet of peaks due to the Cu hyperfine interaction cannot be resolved in this region, suggesting a very small splitting in this case, possibly causing an overlap of the N hyperfine lines, as suggested by Figure 4.5(c) and elsewhere [139, 220].

As the sample is rotated in the field away from the perpendicular position, the intensity of these hyperfine lines decreases, whilst additional hyperfine structure appears between 337 mT and 352 mT from the $g_{//}$ contribution. Once the film is aligned parallel to the field ($\theta = 0°$) the intensities of the two groups of hyperfine lines are approximately equal; at this position an equal contribution from the $g_{\perp}$ and $g_{//}$ is expected, as described in Section 4.1.4. In fact, this spectrum and that of the 5% CuPc/PTCDA film (Figure 4.17(b)) when aligned at $\theta = 45°$ to the magnetic field appear very similar. This is not surprising; in the latter case, equal contributions from the $g_{\perp}$ and $g_{//}$ components are expected due to the reduction in dipolar broadening (compared with that described in Section 4.2.3).

When the CuPc:H_2Pc/PTCDA film is in the parallel orientation ($\theta = 0°$), the magnetic field lines pass parallel to the molecular plane and so only the $g\perp$ component is probed. In a similar manner to that observed from this component in the single layer CuPc:H_2Pc film (i.e. when $\theta = 90°$ in Figure 4.17(a)), this gives rise to a series of sharp peaks from the N hyperfine interactions. These peaks are centred at ~327.0 mT which corresponds to $g\perp = 2.047$, in agreement with the value obtained from the single layer film. However, unlike the spectra in Figure 4.16(a), for the CuPc:H_2Pc/PTCDA film the intensities of these lines are lower when aligned at $\theta = 0°$ than when tilted slightly ($\theta = \pm 6°$). This may be due to the PTCDA and therefore CuPc molecules being slightly tilted with respect to the substrate, as has been reported elsewhere [228].

As this film is rotated in the magnetic field, an additional contribution from $g_{//}$ is observed. At $\theta = 90°$, the N hyperfine splittings from $g\perp$ between 320 mT and 335 mT are no longer seen. Instead, clusters of sharp N hyperfine peaks that are superimposed onto four broader peaks are centred at 279.5 mT, 301.5 mT, 323.0 mT and 343.0 mT. These broader peaks are due to the Cu hyperfine splittings of $g_{//}$, as suggested in Figure 4.5. These four peaks are centred at 311.3 mT, which corresponds to a $g_{//}$ value of 2.151; this value is in closer agreement with literature values (2.156–2.158) [139, 141, 145] than that of 2.133 obtained previously from the 100% CuPc/PTCDA film. The four peaks are separated by 21.2 ± 0.5 mT (the standard error was calculated from the variance in the usual manner) and this corresponds to the Cu hyperfine constant, A as described in Section 2.8.2 (Figure 2.10). The magnitude of A can be derived using Equation 4.4 and values of $g_{//} = 2.151$, $\Delta B = 21.2$ mT and is in excellent agreement with those found in the literature of 0.0216–0.0220 cm^{-1} [139, 141, 145].

$$A = g_{//}\mu_B \Delta B = 0.0219 \pm 0.0005\ \text{cm}^{-1} \qquad [4.4]$$

Detailed information regarding the inter- and intra-column Cu-Cu coupling strengths can be gained from the Cu and N hyperfine structure of the co-deposited films in their parallel and perpendicular orientations with respect to the magnetic field. These

spectra are compared in Figure 4.18. Consideration of the sample and therefore molecular orientations with respect to the magnetic field, as described in Figure 4.10 and Table 4.1 suggests that the group of peaks between 337 mT and 350 mT (the region of vertical grey dashed lines in the figure) correspond to transitions due to $g_{//}$ (with additional peaks of lower intensity at 318 mT–324 mT), whilst those between 320–335 mT (shown as red dashed lines) arise from the $g_{\perp}$ component. The contributions from the Cu hyperfine interactions of the diluted films have been estimated by averaging the sharp N hyperfine peaks as a function of magnetic field, shown as solid black lines in Figure 4.18.

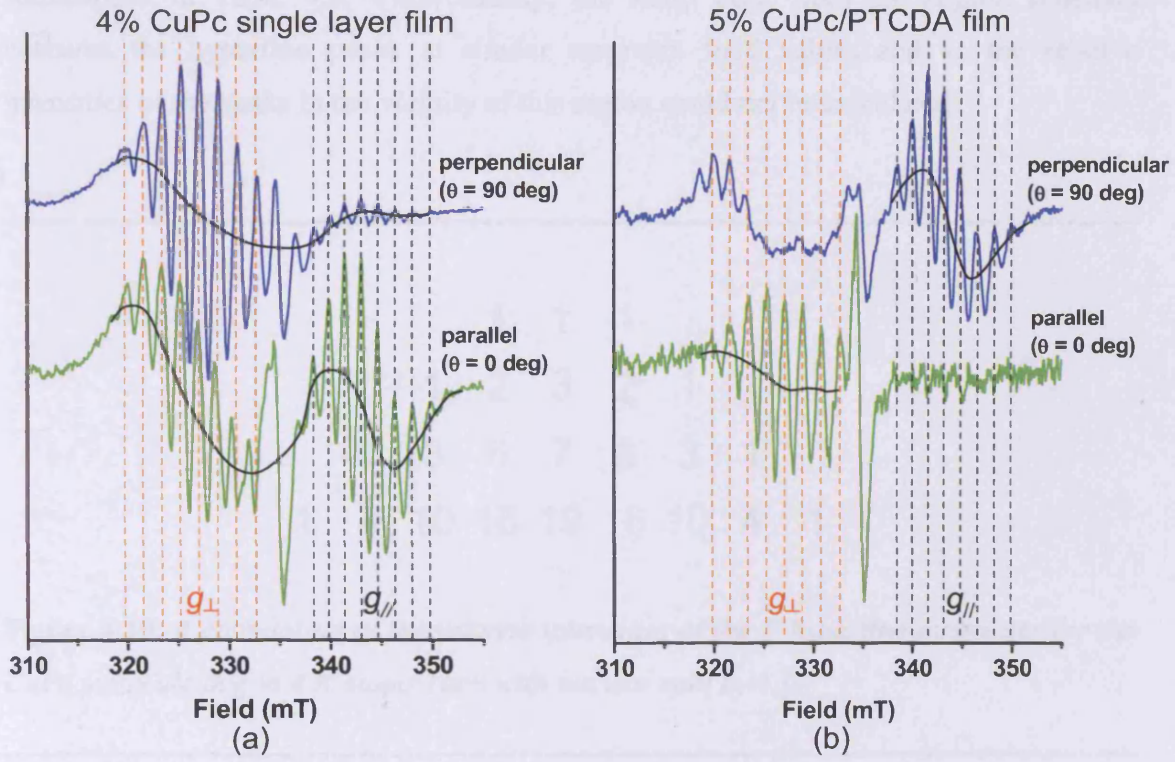

Figure 4.18. *CW EPR spectra of (a) 4% CuPc and (b) 5% CuPc/PTCDA films aligned perpendicular (blue) and parallel (green) to the magnetic field.*

The spectra in Figure 4.18 all exhibit detailed N hyperfine structure. The nuclear spin of N is 1 and so each N atom produces 3 splittings; since there are four N atoms in the vicinity of the unpaired Cu electron this should give rise to 9 lines, as shown in Figure 4.5. The anticipated relative intensities of the N hyperfine peaks can be calculated as outlined in Figure 4.19, which is a variation on Pascal's triangle. In the figure there are four rows (matching the number of contributing N atoms), with the numbers denoting the relative intensities of each peak. The relative intensities are seen to by symmetric, and when scaled so that the largest amplitude has a relative amplitude of 100, give intensity ratios of 5:21:53:84:100:84:53:21:5. The measured relative intensities of the N hyperfine peaks (after subtraction of the Cu hyperfine background from Figure 4.18) are summarised in Table 4.6. Unfortunately, the sharp peak from the kapton substrate obscures the hyperfine peaks at similar magnetic field values and so the relative intensities of the peaks in the vicinity of this region could not be calculated.

---

1 1 1

1 2 3 2 1

1 3 6 7 6 3 1

1 4 10 16 19 16 10 4 1

Figure 4.19. *A calculation of the relative intensities of the N hyperfine intensities for the CuPc molecule due to 4 N atoms each with nuclear spin $I_N = 1$.*

$g_{\perp}$				$g_{//}$ region			
Field (mT)	**H_2Pc:CuPc**		**Pc/PTCDA**	**Field (mT)**	**H_2Pc:CuPc**		**Pc/PTCDA**
	$\theta = 90°$	$\theta = 0°$	$\theta = 0°$		$\theta = 90°$	$\theta = 0°$	$\theta = 90°$
319.8	5.1	18	18	338.4	7.3	24	29
321.6	26	47	47	339.9	6.5	50	46
323.5	51	72	72	341.4	8.5	87	92
325.3	87	100	100	343.0	8.2	100	100
327.1	100	93	93	344.7	6.1	79	83
328.9	98	73	73	346.4	3.3	44	42
330.8	62	40	40	348.1	2.6	28	31
332.7	45	31	31	349.9	-	11	10

Table 4.6. *The calculated relative intensities of the N hyperfine splittings of the spectra shown in Figure 4.18 as a function of resonant magnetic field (these are the average found for each set of peaks). The maximum amplitude of each group of peaks has been scaled to 100. Note that for the $g_{//}$ region of the perpendicularly orientated H_2Pc:CuPc film, the values are scaled to that of the $g_{\perp}$ contribution.*

As shown in Figure 4.18, eight peaks can be resolved for the $g_{//}$ regions of the CuPc spectra ($\theta = 0°$) and CuPc/PTCDA films ($\theta = 90°$). The symmetries of the peaks suggest that an extra peak would be expected at lower magnetic field values, but this is obscured by the kapton peak in both cases. The relative intensities of these peaks are in reasonable agreement with those predicted in Figure 4.19, although higher resolution spectra would be required to confirm this. It should be noted that the films measured here are 200 nm thick, whilst the spectra found in literature are for bulk crystallites wherein a

greater signal-to-noise ratio is more readily achieved. The picture is more complicated for the $g_{\perp}$ component since the Cu hyperfine splittings and therefore N hyperfine peaks overlap. This leads to constructive and destructive interference and so the four sets of nine N hyperfine lines cannot be resolved. At least 15 peaks are measured for the $g_{\perp}$ contribution of the 4% CuPc film, with two more expected in the region masked by the kapton signal (an estimate of two is obtained from the measured separation of 0.85 mT from Table 4.7 that will be discussed shortly). The peaks towards the higher magnetic field region of this group could also arise from $g_{//}$ contributions from Pc molecules aligned slightly off-axis, however this effect appears to be minimal since it cannot account for the relative peaks intensities observed at fields above ~338.4 mT. Instead, it is likely that the $g_{\perp}$ contribution extends into this region, in agreement with reports elsewhere [139, 144].

Only eight peaks are observed for the spectrum of the CuPc/PTCDA film aligned parallel to the field ($\theta = 0°$), although this may be due to a lower signal-to-noise ratio. However, some structure is apparent in this spectrum beyond the kapton region, although it is not possible to determine whether this is from $g_{\perp}$, due to molecular tilt with respect to the substrate, a slight error in sample alignment or an artefact of the noise. The relative intensities of the N hyperfine peaks of the $g_{\perp}$ component are less symmetric than that seen for $g_{//}$, with two neighbouring peaks of almost equal maximal amplitudes at ~327.1 mT. This does not follow the relative amplitudes predicted from a single I = integer species (such as N), and is attributed to the superposition of the N hyperfine peaks caused by the overlapping Cu hyperfine interactions of the $g_{\perp}$ contribution (Figure 4.5).

Comparison of the relative intensities of the Cu and N hyperfine peaks should provide a measure of the degree of Cu-Cu interactions. As seen from Figure 1.10, larger amplitude N hyperfine peaks superimposed on an almost flat Cu hyperfine background are observed for more dilute CuPc:H_2Pc crystallites, whilst more intense (broad) Cu hyperfine peaks, are seen for more concentrated systems. The approximate values of the amplitude and width of the Cu hyperfine contributions for each of the spectra (both are defined by the peak-to-peak values) have been obtained from the fitted black lines in

Figure 4.18, and are summarised in Table 4.7. In addition, the N hyperfine intensities can also be obtained from subtraction of the Cu hyperfine estimates from the raw data, whilst the average peak-to-peak N hyperfine separation can be directly measured. These values are also included in the table. Since the exact number of spins in each sample is not known due to variations in sample size, a direct comparison of the N and Cu amplitudes could be misleading. Instead, by taking the ratio of their amplitudes (A_N/A_{Cu}) any such variations due to sample size are removed and so it is these that will be discussed here. It should be noted that when the 4% CuPc film is aligned parallel to the magnetic field, contributions from $g_{//}$ and $g_{\perp}$ are present. In particular, that from $g_{//}$ at low fields (318–324 mT) will affect the apparent signal of the $g_{\perp}$ component, and so these peaks have not been included in the table.

g-factor	Hyperfine Interaction	4% CuPc		5% CuPc/PTCDA	
		Amplitude	Δ*B* (mT)	Amplitude	Δ*B* (mT)
$g_{\perp}$	Cu	0.261	14.75	~0.1	~12.2
	N	0.872	1.85	0.608	1.84
	A_N/A_{Cu}	3.34	-	~6	-
$g_{//}$	Cu	0.259	5.99	0.406	5.15
	N	0.801	1.62	0.717	1.64
	A_N/A_{Cu}	3.09	-	1.77	-

Table 4.7. *The measured Cu and N hyperfine amplitudes from the spectra in Figure 4.18 (for the case of N this is the maximum value for the group of peaks). The ratio of their amplitudes (A_N/A_{Cu}), along with the widths of the fitted Cu hyperfine peaks and the average separations of the N hyperfine peaks, are included. Note that for the 4% CuPc film the $g_{\perp}$ values were obtained from the perpendicular sample orientation spectrum.*

The ratio of the N to Cu hyperfine amplitudes provides a measure of the Cu-Cu coupling. Literature reports on the effect of dilution of CuPc in H_2Pc to form crystallites (note that no equivalent reports have been found for thin films) suggest that for very dilute systems, such as 5:10,000, only structure from the N hyperfine interaction is observed [141]. Therefore, an increasing N to Cu hyperfine amplitude ratio corresponds to a reduction in Cu-Cu interaction strength. From Table 4.7, a higher A_N/A_{Cu} ratio is observed for the $g\perp$ peaks with respect to those due to $g_{//}$ for each film. Since the $g_{//}$ component is aligned in the z-direction of the CuPc molecule (as shown in Figure 4.5), the lower ratio for $g_{//}$ suggests a stronger Cu-Cu interaction along the molecular stacking direction, whilst that between molecules side-on to each other (between neighbouring columns) is weaker. This seems sensible since not only would the π-π interactions facilitate enhanced intra-column interactions, but also the centre-to-centre intermolecular separation is reduced in this direction and so the Cu-Cu separation is expected to be smaller.

Differences are also observed in Figure 4.18 and Table 4.7 between the CuPc:H_2Pc and CuPc:H_2Pc/PTCDA films. The CuPc:H_2Pc/PTCDA film shows a significantly larger A_N/A_{Cu} ratio for the $g\perp$ orientation, coupled with a smaller $g_{//}$ ratio, suggesting an enhancement of the coupling along the molecular stacking direction compared with the single layer CuPc:H_2Pc film (where less of a difference is observed). This is in agreement with the electronic absorption data (Figure 4.8), and the reduced face-to-face separation measured from the XRD data (Figure 4.16), which would result in a greater intra-column coupling for the 5% CuPc:H_2Pc/PTCDA film with respect to that of the 4% single layer sample. Furthermore, the larger $g\perp$ A_N/A_{Cu} ratio for CuPc:H_2Pc/PTCDA film compared to that of the single Pc layer implies a weaker inter-column interaction. This suggests that the columns of the templated Pc layers are more spatially separated. The known dimensions of the PTCDA unit cell lying parallel to the surface are 11.96 Å x 19.9 Å [234] whilst a separation of ~13 Å is expected for α-phase CuPc:H_2Pc (as given by the *a*-axis in Table 1.1). Since the Pc unit cell is larger than that of the PTCDA layer it is not possible for there to be direct molecular templating (there cannot be one Pc to every PTCDA molecule at the interface). Instead, it is likely that a larger Pc spacing is observed than for the bulk α-phase. This could be confirmed by

molecular resolution AFM studies or grazing incidence x-ray analysis (not performed here).

In summary, upon dilution of CuPc in an H_2Pc matrix, both single layer and templated films display hyperfine features resulting from interactions of the unpaired electrons with neighbouring Cu and N nuclei. This confirms that phase segregation has not occurred. The film spectra are observed to display strong orientation dependence with respect to the magnetic field and this has allowed the calculation of $g_{//} = 2.151$ and $g_{\perp} = 2.047$, both of which agree well with literature reports for bulk crystallites [139, 141, 145]. For the $g_{//}$ orientation, four copper peaks each with up to 8 N peaks are observed; analysis of their intensities and comparison with the number of peaks expected for four $I = 1$ nuclei suggest that 9 N hyperfine peaks should be seen (this discrepancy is likely to be due to a low signal-to-noise ratio and the presence of the kapton signal). In the case of $g_{\perp}$, the Cu hyperfine peaks overlap and this results in more complicated spectra, in particular for the N hyperfine structure. From comparison of the relative intensities of the N and Cu hyperfine peaks, it has been established that stronger interactions occur along, rather than between, columns for both the single layer and templated films. In addition, a greater intra-column interaction was observed for the CuPc:H_2Pc/PTCDA film than for the single layer, verifying the reduced stacking distance measured by the XRD studies. The EPR studies also suggest that the spacing between neighbouring columns of CuPc:H_2Pc/PTCDA films is larger than for bulk α-phase, which is most likely due to the structure of the templating underlayer.

4.4 CONCLUSIONS

For the first time, CW EPR has been used to study CuPc films and to characterise the Cu-Cu interactions therein. In particular, the films display strong orientation dependence with respect to the magnetic field direction. Analysis of the single layer undiluted CuPc films using electronic absorption, XRD and AFM show that they are of the α-phase, with their molecular planes aligned perpendicular to the substrate. Therefore, by aligning the films perpendicular to the field only the intercolumn interactions are probed by EPR; this

is observed as a single contribution from $g_{\perp}$ and the spectrum is significantly sharper than for films aligned parallel (wherein both inter- and intra-column directions are probed). This is because there is a greater CuPc-CuPc separation between neighbouring columns and so less dipolar broadening occurs.

Deposition of CuPc onto a PTCDA layer results in the rotation of the molecular plane such that the CuPc molecules lie parallel to the substrate, as evidenced by the XRD and EPR studies. AFM and electronic absorption suggest that a similar molecular arrangement to the α-phase exists, although a sharpening is observed in the absorption spectrum which implies a stronger intra-column coupling than in the single layer CuPc film. Analysis of the XRD data suggests that for the CuPc/PTCDA film the molecular separation along the stacking direction is reduced from that of bulk α-phase, in agreement with reports elsewhere [224, 225]. For the EPR spectra, the flat-lying molecular arrangement within the CuPc/PTCDA films allows for a greater selectivity of the inter- and intra-column interactions, which permits estimates of $g_{\perp}$ and $g_{//}$ to be deduced.

The co-deposition of CuPc:H_2Pc and CuPc:H_2Pc/PTCDA films results in the appearance of Cu and N hyperfine structure in the EPR spectra. Importantly, this demonstrates that random mixtures on the molecular level are formed and that phase segregation has not occurred. The appearance of the hyperfine peaks demonstrates a reduction in Cu-Cu coupling, suggesting that the interaction strengths between unpaired spins can be controlled upon dilution with H_2Pc. These films are again observed to be crystalline, whilst their electronic absorption and topographic properties resemble those of the α-phase. The formation of such mixtures suggests that the α-polymorphs of CuPc and H_2Pc are structurally similar. The results presented here suggest that the model proposed by Ashida is likely to be correct. However, an in-depth investigation is currently being performed using bulk α-phase crystallites*, the initial results of which favour the Hoshino model. The XRD studies suggest that single layer CuPc films are less textured than H_2Pc films due to the presence of some domains wherein the *c*- rather than *a*-axis is parallel to the substrate in the former case. This reduction in texture is even

* This work is being performed by Soumaya Mauthoor.

observed for the 5% CuPc:H_2Pc films (the degree of texturing reduces upon increasing CuPc content); since the films have been shown to be random mixtures, this implies that only a small presence of CuPc is required to initiate this effect.

From the EPR spectra of the CuPc:H_2Pc and CuPc:H_2Pc/PTCDA films values of $g_{//} = 2.151$, $g_{\perp} = 2.047$ and $A = 0.0219 cm^{-1}$ have been measured, which are in excellent agreement with those obtained from bulk crystallite samples [139, 141, 145]. Careful analysis of the relative Cu and N hyperfine intensities has led to further insights into the molecular structure of the films. A stronger interaction is observed between neighbouring molecules within the columns for both the single layer and templated cases. However, for the CuPc:H_2Pc/PTCDA films, this effect is even more accented, suggesting enhanced coupling within the molecular chains due the reduction in face-to-face Pc separation, whilst the reduced inter-column interactions may suggest a greater column separation than in bulk α-phase.

The work described in this chapter suggests that CuPc thin films, and more generally MPc molecules containing unpaired electron spins, are good candidates for spintronic applications. This is because they readily form crystalline films in which the molecules are aligned in columns; interactions between these columns are weaker than those along the stacks and so spins could be more easily transported and conserved along these stacks. This is in agreement with electrical transport measurements of single layer CuPc films, which show charge mobilities of 4.1×10^{-3} cm^2/Vs and 5×10^{-7} cm^2/Vs parallel to and perpendicular to the substrate respectively [222, 223]. The interactions between the spins can be modified by diluting in metal-free matrix and through the film alignment with respect to the magnetic field. In addition, preliminary pulsed EPR measurements performed on the diluted films suggest spin-spin relaxation times of $T_2 \sim 0.5$ μs, with decoherence due to the interaction between the electron spins and environment leading to lifetimes of $T_1 \sim 250$ μs at low temperatures*. These suggest that the diluted CuPc:H_2Pc films could also be used for quantum computing applications, in a similar approach to that outlined in Section 1.3.3.

* Measurements performed by Marc Warner, Daniel Klose, Gavin Morley and Chris Kay.

Chapter Five: UV-assisted introduction of metal dopants into silicon from phthalocyanine thin films

Thin manganese phthalocyanine films are formed on a Si(100):H surface and subsequently irradiated with 172 nm UV photons. The UV light ruptures the phthalocyanine ligand, releasing the manganese atoms, whilst the organic components are broken into small fragments which desorb from the surface. A manganese and oxide rich surface layer is formed; XPS and XAS measurements suggest that this is MnO. In addition, SIMS and XAS analyses demonstrate that Mn is also incorporated into the bulk Si as an interstitial dopant and that metal clusters are not formed. This process is performed at low temperatures and has the potential to control the three dimensional distribution of metals in silicon, with a wide range of potential applications including in spintronics and quantum computing.

This chapter describes the experimental results so far in the development of a new method for introducing dopants into silicon. As was outlined in Section 1.4.4, traditionally, this is achieved by ion implantation wherein silicon is commonly doped with species such as P, As and B for electronic devices. For spintronic applications, this method has been used for doping silicon with magnetic species such as Mn to create dilute magnetic semiconductors [3, 104] (a Mn in Si system will also be studied here). However, ion implantation introduces damage to the silicon lattice, whilst for certain applications, such as quantum computing, it is highly desirable to have control over the relative spacings between dopants [155] and this cannot be provided by ion implantation. A greater control over the dopant distribution can be achieved by molecular beam epitaxy or chemical vapour deposition, but these are generally only appropriate for the growth of relatively thin dopant-rich layers. Instead, the work presented here outlines a new method for the introduction of metal species into Si that is cheap, versatile and readily scalable for industrial use. Processing is performed at room temperature, with operation at

cryogenic temperature possible, and so this method has the potential to control the positions of a wide variety of dopants in silicon (their diffusional properties are often temperature dependent, as described in Section 1.3.4).

As has already been shown in Chapters 3 and 4, metal phthalocyanines readily form highly ordered films when deposited by vacuum sublimation techniques such as OMBD. Furthermore, control over the molecular orientation with respect to the substrate at the monolayer scale can be gained via the strength of the molecule-substrate interactions, as outlined in Section 1.2.2. In addition, owing to their unpaired electron spin(s), dilute matrices containing transition metal species such as Cu and Mn are of interest for spintronic applications. In this chapter, a new route will be described which introduces transition metal species into silicon from MPc films, building on the experience already gained in Pc film growth. Section 5.1 will provide evidence that post-deposition UV irradiation of the films degrades the organic ligand in a repeatable and systematic manner. Section 5.2 comprises an analysis of the chemical composition of the surface after UV exposure which demonstrates that the majority of the organic matter desorbs from the surface, crucially leaving behind the metal, some of which forms an oxide-rich surface layer. An analysis of the bulk substrate after UV processing is presented in Section 5.3, wherein the metal is observed to have been introduced into Si.

One of the main advantages of this procedure is that it has the potential to permit control over the distribution and spatial separation of a wide range of dopants into silicon. This is desirable for inorganic spintronic applications since clustering has a negative effect on the magnetic properties of dilute magnetic semiconductors [111]. In addition, it is necessary to spatially separate the spin active components for certain applications, including the quantum information processing scheme described in Section 1.3.3 [155]. Figure 5.1 presents a schematic view of how arrays of dopants could be created from MPc monolayers. As described in Section 1.2.2, the order and orientation of MPc molecules on Si can be controlled via the selection of the surface crystal plane, passivation and surface roughness. As a result, upright-standing, flat-lying or randomly distributed monolayers can be formed, as depicted in Figures 5.1(a)-(c).

Such molecular arrays could be used as templates from which to introduce the dopants (the central metal of the MPc) into silicon via UV irradiation, whilst if performed at sufficiently low temperatures to avoid diffusion, the positions of the metals could be retained (Figures 5.1(d)-(f)). For example, for the Si(100):H surface used in this chapter, MPc molecules would be expected to adopt the arrangement shown in Figure 5.1(a) (as observed in Chapter 3), which would lead to linear arrays (Figure 5.1(d)). Evidence that this method leads to the incorporation of metals into Si will be presented in Section 5.3. However, it is not currently known whether the distribution of metal atoms incorporated into the silicon shows spatial ordering corresponding to the original MPc array.

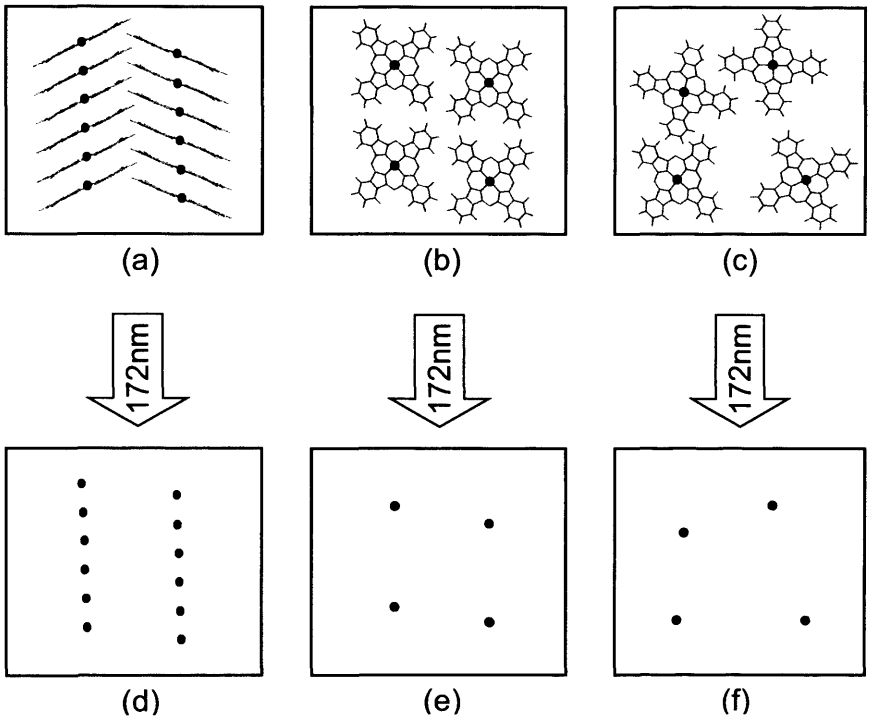

Figure 5.1. *A schematic of the UV induced introduction of metal dopants into silicon from thin MPc films to form arrays of dopants. Three possible arrangements of MPc monolayers on silicon surfaces are shown (a)-(c). After 172 nm UV irradiation the organic fraction is removed, leaving behind the metal species (grey dots) to diffuse just below the silicon surface with their lateral positions pre-determined by the original organic film structure (d)-(f).*

The procedure outlined in Figure 5.1 could be extended by exploiting temperature-dependent diffusion to control the dopant distribution as a function of depth via a post-treatment anneal, possibly with the aid of in-built preferential diffusion paths. It should be noted that, although demonstration of the retention of the order of the initial MPc film within the substrate has not yet been achieved, the results described in this chapter show that this procedure could lead to the creation of ordered arrays of metal dopants in silicon. It could also be readily adapted for the introduction of metallic and non-metallic species into other substrates (for example compound semiconductors) using different organic precursors (and so providing different dopant separations), thus extending the range of potential applications.

5.1. DEGRADATION OF THE PHTHALOCYANINE RING

This section describes experimental results which monitor the effect of 172 nm UV radiation on the MPc films as a function of exposure period. To facilitate measurements and get above the detection limits of the standard analytical techniques to be used, the MPc films were typically 5 nm thick. The aim here is to determine the amount of time required to remove or destroy the organic material and verify the reproducibility of this process. Sections 5.1.1 and 5.1.2 present Raman and electronic absorption measurements performed on MPc films that have been irradiated for a range of times. In each case the amount of molecular material remaining was calculated by referencing to the corresponding integrated peak areas of the initial film. Information about the morphology as a function of irradiation time was provided by tapping-mode AFM measurements and will be described in Section 5.1.3. Multiple measurements and sample preparations were performed to prove the reproducibility of the data.

All MPc thin films were grown by OMBD, as outlined in Section 2.1. Raman and AFM measurements were performed on films grown on Si(100):H (i.e. on Si(100) after an HF dip), whilst glass substrates were used for the electronic absorption studies. The

films were then immediately transferred to a custom built UV chamber (as described in Section 2.2) where they were subjected to 172 nm irradiation and then analysed ex-situ. In the case of the electronic absorption studies, the samples were irradiated for a series of short periods with spectra taken between each irradiation dose. Initial Raman spectroscopy measurements were performed on CuPc films to determine whether the UV was successfully degrading the MPc films and to subsequently establish the optimum experimental conditions. However, owing to its fast diffusion rate in silicon, any copper introduced by the UV treatment would be difficult to detect (Table 1.2). For this reason, the majority of the experimental results presented here are for thin MnPc films, in line with the general theme of this chapter.

5.1.1 Raman Spectroscopy

This section will comprise discussions of the CuPc then MnPc Raman spectra, both as a function of increasing UV exposure. It will be shown that the characteristic MPc signal is reduced as a result of UV irradiation. Following this, possible mechanisms for the rupturing of the MPc ligand will be suggested.

CuPc Films

In order to determine the optimum experimental conditions for the UV-induced degradation of the metal phthalocyanine thin films, initial tests were performed using CuPc films and analysed by Raman spectroscopy. In these experiments, parameters including the sample-lamp distance, ambient atmosphere (pressure and gas species), sample temperature and film thickness were studied. As an example, the effect of varying the initial film thickness (whilst keeping the other parameters at their optimal conditions) is shown in Figure 5.2. Here, the Raman spectra (excitation $\lambda = 514.5$ nm) of CuPc films that were originally 5 nm thick (Figure 5.2(a)) and 10 nm thick (Figure 5.2(b)) after various UV exposure periods are compared.

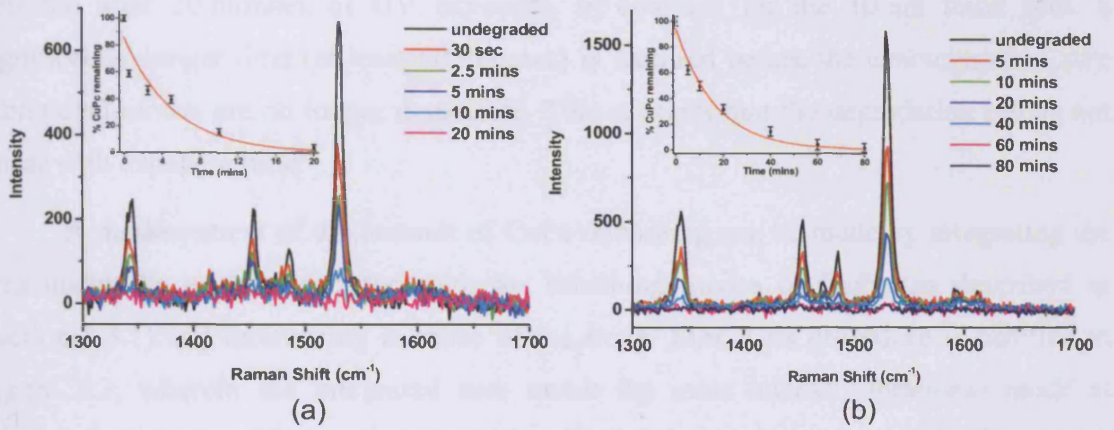

Figure 5.2. *Raman spectra (λ = 514.5 nm) of (a) 5 nm thick and (b) 10 nm thick CuPc films on Si(100):H as a function of UV exposure time (durations stated in the legends). The calculated percentages of CuPc remaining after each exposure time are plotted as insets and fitted to an exponential decay function (red).*

The peak positions and relative intensities of the Raman spectra of the as-deposited 5 nm and 10 nm thick CuPc films in Figure 5.2 (black) agree well with the published spectra (Figure 1.4 [48, 235]), demonstrating that the molecules remain intact once deposited onto the surface. The CuPc thin films give relatively intense Raman signals, permitting a quantitative analysis of the amount of CuPc present. The spectra also present an opportunity to detect and identify any degradation products formed that remain on the surface (these would be seen as additional vibrational bands).

As seen in Figure 5.2, the intensities of the signature CuPc peaks are seen to decrease as a function of UV irradiation time. No additional peaks are detected from the formation of new (modified) species, suggesting that the MPc molecules are removed from the surface (either whole or in fragments). It should be noted that very little variation in peak intensities were observed for measurements performed at different locations on each sample, with that experienced likely due to laser focussing errors in addition to any irregularities in film thickness. As a result, the samples were deemed to

be homogenous. For the 5 nm film, a significant reduction in intensity of the characteristic CuPc peaks is observed after 30 seconds, and only a negligible signal is detected after 20 minutes of UV exposure. In contrast, for the 10 nm thick film, a significantly longer time (at least 80 minutes) is required before the characteristic CuPc vibrational modes are no longer detectable. This suggests that the degradation rate is not linear with exposure time.

A measurement of the amount of CuPc remaining can be made by integrating the area under the peaks associated with the breathing modes of CuPc (as described in Section 1.3.1) and referencing to those of the initial film. This procedure is justified in Figure 5.3, wherein the integrated area under the most intense vibrational mode at 1530 cm^{-1} (between 1513 cm^{-1} and 1556 cm^{-1}) has been plotted as a function of as-deposited CuPc film thickness. The integrated area is linearly proportional to the film thickness, and so this method can be used to perform a quantitative analysis on the fraction of MPc remaining as a function of UV irradiation time. Errors were calculated by performing multiple measurements and calculating the standard deviation and standard error for each sample. Such a treatment combines those due to sample inhomogeneity and laser focussing inconsistencies. As seen in Figure 5.3, these errors are small, further demonstrating the uniformity of the as-deposited thin films.

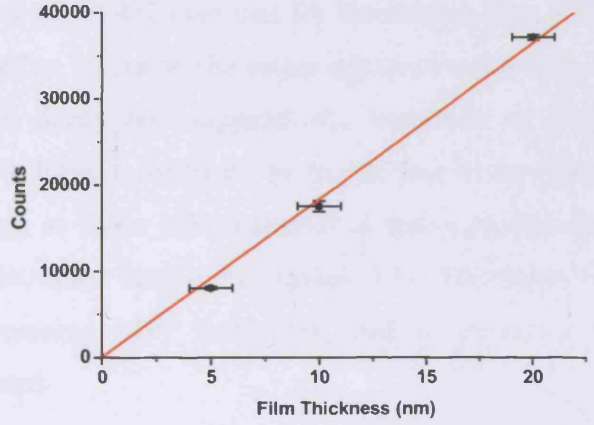

Figure 5.3. *A plot of the integrated area under the 1530 cm^{-1} peak of as-deposited CuPc films as a function of film thickness (as measured during film growth by an in-situ QCM).*

The integrated areas under the 1530 cm^{-1} peak after each UV exposure period have been used to determine the percentage of CuPc remaining as a function of irradiation time, as shown in the insets of Figure 5.2. A non-linear degradation rate with respect to irradiation time is observed, with a faster rate seen for shorter times. The exponential function given in Equation 5.1 was fitted to the data in both insets (i.e. for the two initial film thicknesses), where y is the percentage CuPc remaining and t is the duration of UV exposure.

$$y = Ae^{-t/\tau} \qquad [5.1]$$

This fitting gave values of $A = (85.6 \pm 1.7)\%$, $\tau = (5.21 \pm 0.33)$ min^{-1} ($R^2 = 0.899$) and $A = (94.4 \pm 3.2)\%$, $\tau = (16.6 \pm 1.3)$ min^{-1} ($R^2 = 0.981$) for the 5 nm and 10 nm films respectively. It should be noted that values of $A = 100\%$ would be expected in both cases (since at $t = 0$ the exponential term will have a value of unity and 100% of the film exists at this point). However, this is not obtained since this A and τ were allowed to vary during fitting to the experimental data; although A could have been constrained to a value of 100%, this would have assumed zero error in the quantity of CuPc measured, which is unrealistic. The value of 94.4% obtained for the thicker film is closer to the anticipated value; this is expected to be due to the larger signal-to-noise ratio for the 10 nm film. The apparent exponential decay law suggests the formation of a thin layer that is semi-impervious to the UV light, most likely on the surface of the phthalocyanine film, which increases in thickness as more MPc material is removed (the chemical composition of this layer will be discussed further in Section 5.2). This layer reduces the flux of UV photons on the remaining MPc molecules, and so decreases the rate at which the molecules are degraded.

It is desirable to repeatedly remove all of the MPc starting film over a sensible timescale. Very short exposures (of the order of seconds) would be difficult to control in a repeatable manner using the current set-up, whilst prolonged UV exposure increases the

temperature and this would make the detection of fast diffusers in silicon more difficult. Therefore, exposure durations of the order of a few minutes would be preferable. Furthermore, the molecular layers closest to the silicon interface are of the greatest interest here since these will be more likely to achieve the desired positioning of metal dopants into the Si host matrix; a thinner film will more accurately model a monolayer. However, coverage of a monolayer would be difficult to detect using the techniques employed here. For these reasons, an initial film thickness of 5 nm was chosen for the samples described in the remainder of this chapter.

MnPc Films

The Raman spectra of a 5 nm MnPc film on Si(100):H was measured after a similar range of UV exposure periods as those studied for the 5 nm CuPc film, as shown in Figure 5.4. A similar overall trend was obtained as for the 5 nm CuPc film, wherein the intensity of the Raman signature (most prominently at 1397 cm^{-1}) systematically decreases upon increasing UV exposure. After 20 minutes of irradiation this peak is no longer detectable, suggesting that the MnPc film was removed at a comparable rate to that observed for the CuPc film. A broad, weak peak is observed at ~1455 cm^{-1} after extended UV exposure, as indicated in the figure (this will be returned to shortly).

Although the number of scans and integration time used to obtain the data in Figure 5.4 were increased by factors of 5 and 4 respectively compared to those used for the CuPc spectra (Figure 5.2), a significantly lower intensity and therefore poorer signal-to-noise ratio was observed for the MnPc film. This implies that MnPc is a less Raman active material, suggesting that the delocalised electron density is less easily distorted than for its CuPc counterpart. In addition, the main vibrational peak is shifted to a lower energy than that of CuPc (1397 cm^{-1} versus 1530 cm^{-1}), although it is not possible to deduce whether these are from the same vibrational mode. This is unusual since planar MPcs (for example CuPc and CoPc) have similar Raman signatures, whilst the vibrational peaks of non-planar MPcs such as PbPc are shifted to lower energies [48]. Published Raman spectra of MnPc could not be found and the nature of the differences is not currently understood. Furthermore, the integrity of the MnPc films cannot be

confirmed here using this method. However, the relative shift does suggest that the MnPc molecule is not planar (as has been reported for certain Mn porphyrins, which are structurally similar to the phthalocyanines [236]). Further studies are necessary to determine the true nature of this shift, but are outside the scope of this chapter.

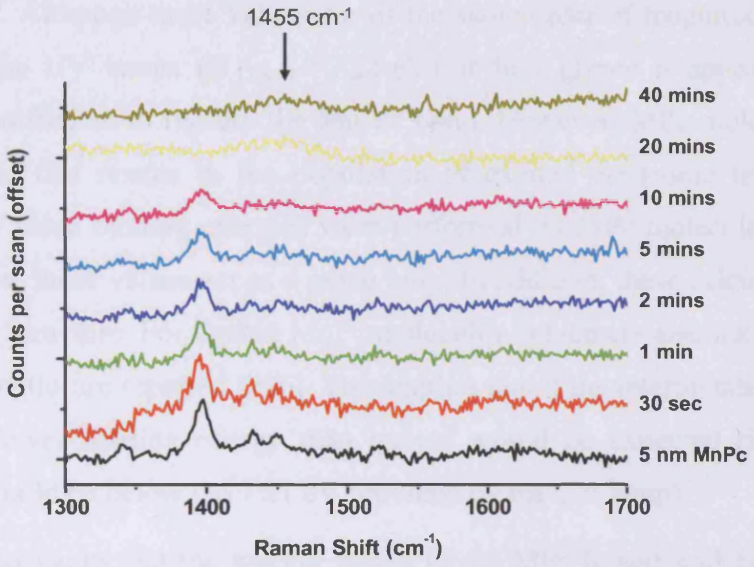

Figure 5.4. *Raman spectra (λ_{exc} = 514.5 nm) of a 5 nm MnPc film on Si(100):H subjected to increasing periods of 172 nm UV exposure. Data are offset for clarity.*

Mechanisms for Rupturing the MPc Ligand

The temperature during UV irradiation was measured by an in-situ thermocouple and observed to remain below 60°C. The MPc molecules are known to be very stable upon heating until temperatures above ~300°C are reached, at which point they sublime. The only known temperature-induced changes to MPc films occur at temperatures just below the sublimation temperature (above ~250°C at ambient pressures, or above ~325°C in high vacuum conditions), where they undergo a phase transition from the α- to β-

polymorph [34, 35]. However, this does not result in a reduction of molecular material. Therefore, the observed changes in the Raman spectra cannot be due to heating effects.

Instead, it is likely that the UV photons cause the MPc molecules to fragment via photo-excitation of the bonding electrons. Calculations of Liao *et al.* suggest that the binding energy of the metal species to the Pc ligand is typically 5–10 eV; for example for CuPc this value is 6.96 eV [237], whilst for MnPc a binding energy of 8.80 eV has been reported [236]. Although these values are of the same order of magnitude as the energy provided by the UV lamps ($E_{172nm} = 7.21$ eV) at first glance it appears that the UV energy is not sufficient to rupture the Mn-Pc bond. However, MPc molecules absorb in this region and this results in the population of excited electronic levels, whilst the calculations of these binding energies were performed on MPc molecules in the ground state. Therefore, these values act as a guide only. In addition, these calculations assumed a planar MnPc structure. For ligated MnPc molecules (which are also non-planar), longer Mn-N bond lengths are reported [236]. This implies that if the interpretation of Figure 5.4 is correct, a lower binding energy than quoted would be expected (it is not known whether this would be below the 7.21 eV provided by the UV lamp).

It is also likely that the weaker bonds in the MPc ligand will be the first to be ruptured by the UV light, and that this would further lower the binding energy of the metal to the organic. Although information on the bond dissociation energies of the Pc ligand could not be found, the C-N and C-C bond dissociation energies of more common aromatic molecules such as pyridine and benzene are known to be 3.55 ± 0.11 eV and 4.41 ± 0.09 eV respectively [238]. These values are comfortably below the energy provided by the UV photons and imply that the C-N bonds of the Pc ligand are the most likely to break first, as suggested by Otha *et al.* [239]. Inspection of the molecular structure of MnPc (which is analogous to that of CuPc shown in Figure 1.1(a)) suggests that it is likely that benzene and pyrrole containing complexes such as isoindoline and carbazole will be formed. The chemical structures of these molecules are shown in Figure 5.5. The broad, weak peak observed in Figure 5.4 at ~1455 cm^{-1} after 20 minutes of UV exposure can be attributed to the formation of carbazole [240]; if formed, this molecule could remain on the surface (it has a sublimation temperature of 82°C [241]), whilst

smaller fragments such as isoindoline would sublime from the surface. A slight reduction in intensity of this peak is observed between 20 mins and 40 mins, suggesting that further UV-induced decomposition of the carbazole molecules occurs to form small volatile fragments which desorb from the surface, as described elsewhere [242].

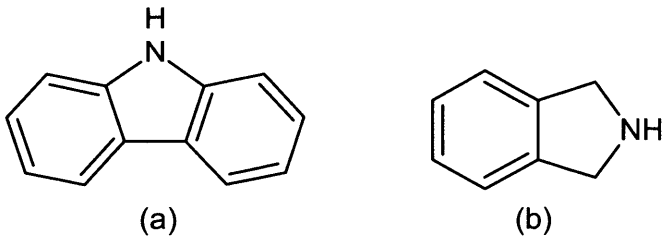

Figure 5.5. *The chemical structures of two possible degradation products after rupturing the Pc ligand; (a) carbazole and (b) isoindoline.*

5.1.2 Electronic Absorption Spectroscopy

Electronic absorption spectroscopy has also been performed on MnPc films (on glass substrates) in order to more accurately quantify the amount of MnPc remaining as a function of UV irradiation time, since this could not be deduced with confidence from Figure 5.4. Figure 5.6(a) shows a plot of the measured electronic absorption of 5 nm MnPc films exposed to 172 nm UV light for the same durations as used for the Raman spectra. These measurements were performed in transmission mode and so any UV-induced modifications to the absorption spectrum of the substrate would affect the measured spectra of the film. For this reason, each film spectrum was referenced to that of a clean glass slide that had been subjected to the same exposure of UV light.

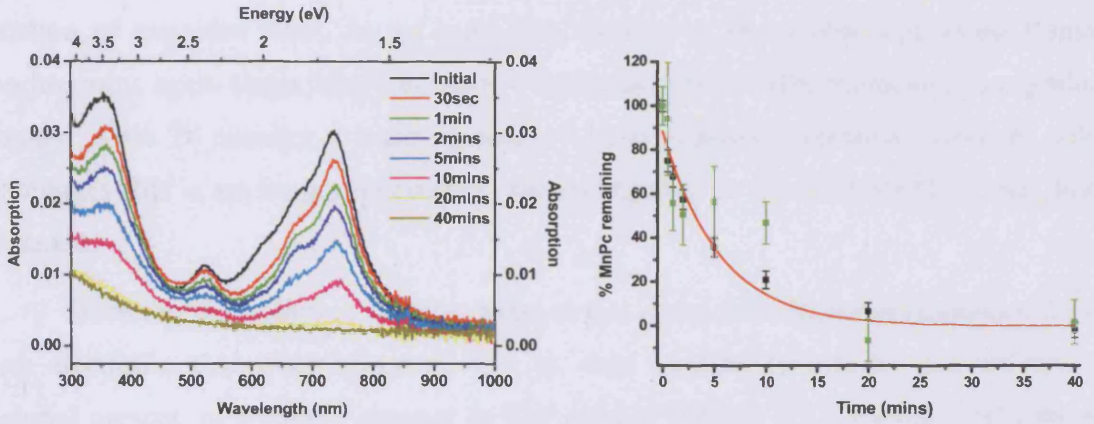

Figure 5.6. *(a) Electronic absorption spectra of a 5 nm MnPc film on glass (black), along with films exposed to 172 nm UV photons for 30 seconds (red), 1 minute (green), 2 minutes (mid-blue), 5 minutes (cyan), 10 minutes (purple), 20 minutes (yellow) and 40 minutes. (b) The calculated percentage of MnPc remaining as a function of UV exposure from the electronic absorption (black) and Raman (green, from Figure 5.4) spectra, with an exponential fit to the values obtained from the electronic absorption data (red).*

MnPc absorbs in the visible region (between 500–850 nm) due to electronic excitation from the ground state to the first excited state (Q-band absorption), in a similar manner to that described in Chapter 4 for CuPc and H_2Pc films. The spectrum of the "as deposited" MnPc film (black) agrees with that published in literature [243, 244] and confirms that the molecules remain intact after film deposition. It should be noted that in general the absorption spectra of MnPc is different to that of most other MPcs; for example, in solution two peaks are observed at ~643 nm and ~660 nm [245] whereas only one main absorption peak is present in the solution spectrum of CuPc (Figure 1.3(b)). The presence of the peak between the Q- and B-bands (at ~523 nm) is intriguing;

similar peaks are only observed for non-planar MPcs such as FePc [45]; such a peak is sonsitent with the interpretation of the Raman spectra (Section 5.1.1). Upon UV irradiation, the intensity of the electronic absorption bands are seen to decrease as a function of exposure time, in an analogous manner to those observed using Raman spectroscopy, again suggesting that the UV light ruptures the MPc molecules in a gradual manner. After 20 minutes a trace amount of MnPc signature remains, however, after 40 minutes this is no longer detectable, suggesting that in this case all MnPc has been degraded.

Since the absorption is directly proportional to the film thickness (Equation 2.13), each electronic absorption spectrum can be used to directly monitor the amount of material present, in a similar manner to that used in Section 5.1.1. Figure 5.6(b) shows the percentage of MnPc remaining as a function of UV exposure periods obtained from the spectra in Figure 5.6(a). This was calculated by integrating the area under each absorption profile between 575 nm and 850 nm and referencing this value to the integrated area of the as-deposited spectrum. For comparison, the equivalent values obtained from peak fitting of the Raman spectra of Figure 5.4 are also included and are seen to follow the same trend. The data obtained from the electronic absorption spectra are observed to fit to an exponential curve, as defined by Equation 5.1, with fitted parameters of $A = (88.4 \pm 4.7)\%$, $\tau = (5.52 \pm 0.91)\ \text{min}^{-1}$ ($R^2 = 0.965$). Again, the exponential decay suggests the formation of a surface layer that either partially absorbs the incident photons and/or hinders desorption. The fitted parameters agree well with those found for the 5 nm CuPc film in Section 5.1.1 ($A = (85.6 \pm 1.7)\%$, $\tau = (5.21 \pm 0.33)\ \text{min}^{-1}$), further demonstrating the reproducibility of this process for different MPc metals.

This agreement suggests a similar degradation mechanism for the two molecular species. As discussed in Section 5.3.1, the MnPc films would not be expected to be degraded in an identical way as CuPc if only the M-Pc bonds were ruptured, since their bond dissociation energies are lower than the 7.21 eV provided by the UV lamp (assuming that these values are appropriate for the MPc films under the conditions used here, as has already been debated). Instead, their similar behaviour upon exposure to UV light implies that other bonds (most likely the C-N) rupture first. If the latter were true,

the metal could still be released from the organic since the fragmentation may destabilise the Mn-N bond; this seems plausible since the delocalised bonding between the Mn and Pc ligand (as described in Section 1.1) would be disrupted.

After prolonged irradiation, the films become increasingly absorbing at lower wavelengths, as seen by the broad tail below ~450 nm. This could be explained by the formation of manganese oxide(s) since these are known to absorb in this region [246]. The formation of manganese oxides would be in agreement with other reports of UV-induced degradation of metal-organic thin films [239, 247], as will be discussed in Section 5.2.

5.1.3 Atomic Force Microscopy

The topography of the films as a function of UV exposure has been studied by tapping mode AFM. Here it is also of interest to determine whether the uniformity on the millimetre scale (shown by the Raman and electronic absorption measurements) is maintained on the nanoscale. Figure 5.7(a) shows a typical AFM image of a 5 nm thick MnPc film on Si. The film has been verified to be uniform by imaging at several different locations across the Si wafer. The surface is seen to comprise many small features of on average 20-30 nm in diameter. Since the substrate was at room temperature during film deposition, it seems likely that the molecules would adopt the arrangement of the bulk α-phase, in an analogous manner to that of the CuPc films on Si(100):H described in Chapter 3 and the thicker films in Chapter 4. Indeed, the 5 nm MnPc film is of similar appearance to the CuPc films of Figures 1.5 and 4.3, suggesting that each grain corresponds to individual crystallographic α-phase domains. The domains of the 5 nm MnPc film are larger than those of 9.7 ± 1.2 nm and 7.3 ± 0.9 nm obtained in Chapter 3 for monolayers on the Si(100):NH_3 and Si(100):H surfaces respectively. In addition, these MnPc features are notably smaller than those observed for the 100 nm thick CuPc film in Figure 4.3 (approximately 40–60 nm). These measurements are in agreement with literature and previous results since the domain sizes of α-phase films are known to increase with increasing film thicknesses [229], and are dependent on growth conditions, as observed in Section 4.3.2.

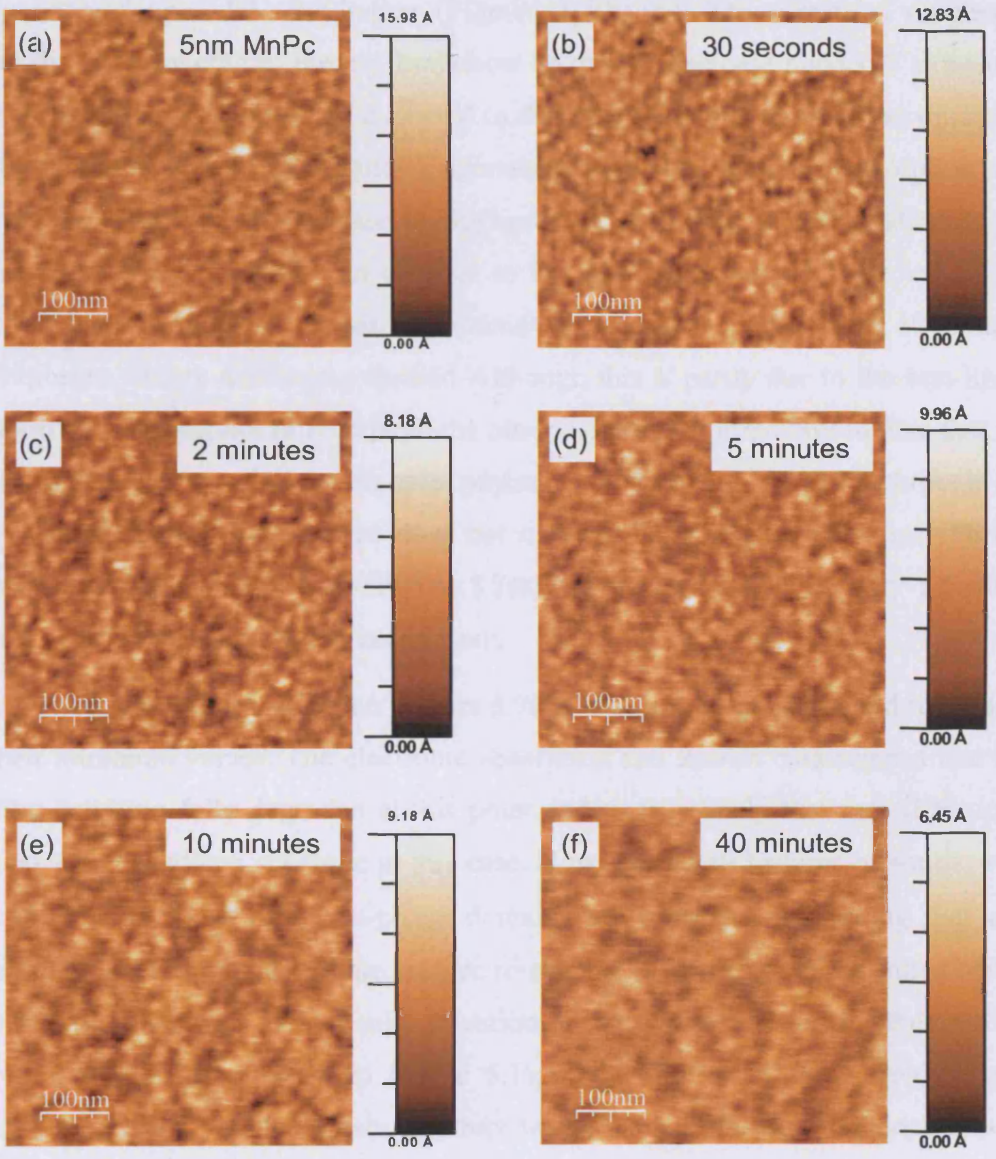

Figure 5.7. *Tapping mode AFM images of (a) the initial 5 nm MnPc film on Si(100) (rms = 0.16 nm) and after UV irradiation periods of (b) 30 seconds (rms = 0.14 nm), (c) 2 minutes (rms = 0.10 nm), (d) 5 minutes (rms = 0.11 nm), (e) 10 minutes (rms = 0.11 nm) and (f) 40 minutes (rms = 0.066 nm).*

The characteristic bumpy appearance of the α-phase film observed in Figure 5.7(a) is retained upon UV irradiation (Figures 5.7(b)-(f)). The measured roughness values of the films (quoted in the caption) show an overall decrease upon UV exposure. In general, the roughness would be expected to decrease upon reduction of the thickness of the films and so this is in a general agreement with the electronic absorption and Raman spectra. However, the decrease in roughness and measured height variation do not follow an exponential decay (i.e. in contrast to Figure 5.6(b)); instead these values are observed to initially decrease, remain approximately constant between 2 and 10 minutes of UV exposure, before decreasing further. Although this is partly due to the non-linear degradation rate, this cannot fully explain the observed trend. It important to note that the AFM tip only interacts with the sample *surface* – it does not penetrate through the organic layer to the substrate and so does not measure the true film thickness. This is observed for the initial MnPc film (Figure 5.7(a)), in which a height of only 1.6 nm is measured, instead of the true thickness of 5 nm.

After 40 minutes of irradiation (Figure 5.7(f)), both the height scale and roughness are at their minimum values. The electronic absorption and Raman data suggest that the MnPc film has been fully degraded at this point and so it is likely that the AFM tip is interacting with the silicon substrate in this case. However, small features of similar size and distribution to those of the α-phase domains are observed, suggesting that any degradation product remaining on the surface retains the morphology of the initial MnPc film. This is promising for the potential retention of the spatial ordering for the creation of arrays in silicon (as outlined in Figure 5.1); if the film were to amorphise upon irradiation, it is likely that the domain structure would be lost (this does not appear to be the case here).

In summary, the analyses described in this section demonstrate that the initial MPc films are uniform and that exposure to UV light results in their degradation. Furthermore, MnPc and CuPc films of the same thickness were observed to respond in an analogous manner upon UV exposure. It is likely that the degradation occurs through the rupturing of the Pc ligand, most probably via the C-N bonds (these were deemed to be the weakest), resulting in the formation of small aromatic fragments. Published M-Pc binding

energies suggest that Cu could be released from an intact CuPc molecule, whereas the energy provided by the UV lamp is insufficient to rupture the Mn-Pc bonds. However, the MnPc molecules are suspected to be non-planar and so the calculated MnPc binding energy (performed on planar molecules) may not be applicable to this system. At this stage it is not known whether the metal is released from the organic ring (this will be discussed in the following section), although it is feasible that rupturing the C-N bonds would destabilise the M-N bonds. The AFM studies suggest that after 40 minutes of UV exposure, the film has been reduced in thickness. This implies that much of the organic material has been removed, supporting the claim that small fragments are formed by rupturing the C-N bonds; many of the aromatic fragments would sublime from the surface (and so be undetectable by Raman spectroscopy), reducing the amount of material present. However, the morphology of the initial MPc film is retained, suggesting that any degradation products maintain the general morphology of the initial α-phase film. A more detailed characterisation of the surface after UV exposure will be presented in the following section.

5.2. CHARACTERISATION OF THE SURFACE AFTER UV TREATMENT

The studies outlined in Section 5.1 show that the MnPc film is being degraded as a result of the UV exposure, however, using these techniques it has not been possible to detect whether the Mn atoms remain after UV treatment. Demonstrating that the metal is released from the organic ring is critical to this procedure, not least because the known Mn-Pc binding energy suggests that the energy of the UV photons is insufficient to release the Mn from an intact MPc molecule. The aim of this section is to investigate the chemical nature of the surface of the MnPc film after UV treatment. This will be achieved by using the more surface sensitive techniques of SIMS, XPS and XAS, as will be used in Sections 5.2.1, 5.2.2 and 5.2.3 respectively. Using these techniques, the composition of the 5 nm MnPc film on Si(100):H before and after 40 minutes of UV exposure (i.e. the point at which the Raman and electronic absorption measurements suggest all of the MnPc films are fully degraded) will be analysed.

5.2.1 Secondary Ion Mass Spectrometry

Secondary ion mass spectrometry is a highly surface sensitive technique that permits the analysis of the chemical composition of a sample as a function of depth. Firstly though, in order to determine which species to trace in SIMS depth profiles, mass spectra of 5 nm thick MnPc and CuPc films, along with that of the initial silicon substrate were measured. These are compared in Figure 5.8. The mass spectra were obtained using a nitrogen profiling beam, with the species collected as positive ions.

In general, the mass spectra of the CuPc and MnPc films are similar. A significant yield of C^+ is observed at 12 amu that is not detected in the silicon spectrum. This peak is attributed to originating from the phthalocyanine ligand, whilst the peak observed at 13 amu for the MPc films is likely to correspond to CH^+ fragments (again from the Pc). The intense peak observed at 55 amu for the MnPc spectrum is due to Mn^+. Any interference with an organic fragment (e.g. $C_4H_2^+$) can be excluded, as no peak at 55 amu is observed in the CuPc film. Importantly, Mn was not detected from the silicon wafer (neither was Cu) and so any Mn detected in the Si wafer after UV exposure must have been introduced from the MnPc film. A peak is observed in all spectra at 28 amu (an order of magnitude more intense for the Si wafer) which could be attributed to Si^+, CO^+ or N_2^+. Since it is accompanied by peaks at 29 amu and 30 amu, which correspond to the known isotopes of Si with the relative intensities of all three peaks in good agreement with their known natural isotopic abundances (92.2% Si^{28}, 4.7% Si^{29} and 3.1% Si^{30}), these peaks can be confidently attributed to the presence of Si. Na^+, K^+, Ca^+ and Fe^+ are also observed, although their presence is not surprising since these are commonly observed positive impurities in SIMS [190]. However, species such as O^+ are less likely to be detected, even though O may be present in the samples; O^- ions would be expected to have a far greater yield (i.e. if the spectra had been collected as negative ions). For this reason, the polarities of the species collected in the following depth profiles were chosen according to their individual preferential formation of cations or anions; C and O were collected as negative species whilst positive ions of Mn and Si were detected.

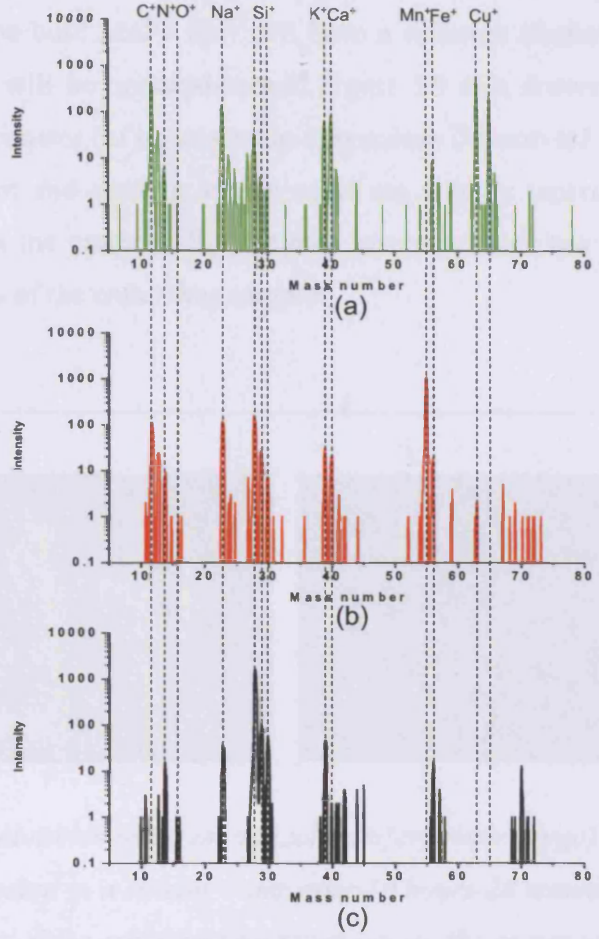

Figure 5.8. *Mass spectra collected as positive ions of (a) a 5 nm CuPc film on Si (green), (b) a 5 nm MnPc film on Si (red), and (c) a Si(100) wafer (black). The mass numbers of key species are identified.*

It was necessary to calibrate the depth scale in order to permit a full characterisation of the depth profiles. This was performed by creating a crater after sputtering a Si wafer for 16 hours and 28 minutes and measuring its depth. The sputtering conditions used here were the same as used for the remainder of this chapter, namely a 1.25 keV Ar^+ beam at grazing incidence (see Section 2.5 for more details). The crater formed is shown in Figure 5.9 and was found to be 2.35 μm deep, from which a sputtering rate of 2.38 nm/min was calculated. It should be noted that this sputtering rate

has been used throughout all depth profiles shown and is not correct for materials other than bulk silicon; the bulk MnPc film will have a different (faster) etch rate and so its measured thickness will be underestimated. Figure 5.9 also shows that the crater has a regularly shaped perimeter (of approximate dimensions 0.5 mm x 1 mm), that the base of the crater is uniform and that the crater walls are slightly tapered. In order to avoid collecting data from the crater walls, the data presented here has been gated such that only the central 50% of the crater was sampled.

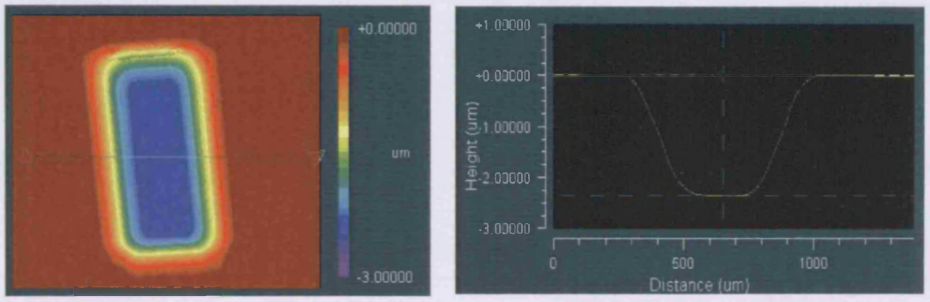

Figure 5.9. *Images obtained using an optical interferometer (Zygo) to measure the depth of a SIMS crater created in a silicon wafer after 16 hours 28 minutes of sputtering. (a) A 3-dimensional image, (b) a cross section taken across the crater width (the location the cross section was taken from is indicated by the horizontal line in (a)).*

SIMS has been used to analyse a 5 nm MnPc film on silicon, before and after UV treatment. For these studies C^-, O^-, Si^+ and Mn^+ yields were traced as a function of depth. A typical SIMS depth profile of a 5 nm MnPc film on silicon (i.e. before UV exposure) is shown in Figure 5.10(a). Regions of this profile can be attributed to the MnPc film and Si substrate, as indicated in the figure. Within the organic film, a relatively constant Mn signal is observed, as would be expected from the MnPc layer. This is accompanied by a high carbon presence, which is mainly due to the Pc rings. However, the C content is not uniform in this region, with a high C signal observed at the film surface. This is likely to

be due to both surface contamination and the fact that equilibrium between the incident beam and sputtered yields had not yet been established (as discussed in Section 2.5.3). Higher yields of O and Si are observed at the film surface for the same reasons, whilst the yields of these species also rise as the interface is approached; the latter effect is a result of beam induced mixing, as will be discussed shortly.

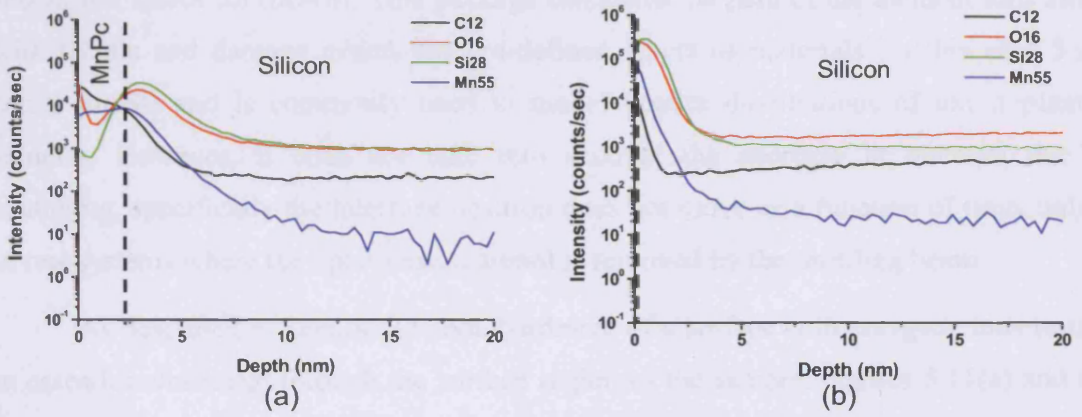

Figure 5.10. *SIMS depth profiles obtained using a 1.25 keV Ar^+ profiling beam of a 5 nm MnPc film on Si (a) before and (b) after UV exposure. Carbon (black), oxygen (red), silicon (green) and manganese (blue) are traced in each case as a function of depth. Dotted lines indicate the film-substrate boundaries.*

The interface with the substrate is reached after 2 minutes 13 seconds (as depicted by the dotted line in Figure 5.10(a)), the position of which has been defined as the maximum of the first derivative of the silicon trace. At the interface, a high oxygen signal is observed. This is most likely due to a native SiO_2 layer reforming during the time between film growth and measurement (this analysis was performed several days after film deposition). As was explained in Section 2.5, the increased presence of oxygen artificially enhances the yield of silicon [191], and this leads to a peak in the silicon trace that mimics that of oxygen. The oxygen (and therefore silicon) signals then decay, reaching a constant value beyond the oxide layer and within the bulk Si. At this point, the

O signal is likely to be due to the residual chamber vacuum and is not expected to originate from the sample.

From the depth profile, it is apparent that Mn and C are driven beyond the interface and into the substrate by the profiling beam. In order to investigate this further, Monte-Carlo simulations have been performed (using the SRIM package) to model the effect of the Ar^+ beam on the MnPc-Si system. The results of these calculations are shown in Figures 5.11(a)-(d). This package calculates the path of the incident ions along with recoils and damage events for pre-defined layers of materials (in this case 5 nm MnPc on Si) and is commonly used to model dopant distributions of ion implanted samples. However, it does not take into account the decrease in material due to sputtering, specifically the interface position does not move as a function of time, unlike in real systems where the uppermost material is removed by the profiling beam.

As described in Section 2.5, bombardment of a surface with energetic ions results in cascades which run through the surface region of the sample. Figures 5.11(a) and (b) contain plots of the number of C and Mn atoms that are displaced by the cascades as a function of depth. Here it can be seen that even for the initial MnPc film, the distribution of C and Mn species is influenced by the beam throughout the layer (significantly more than the uppermost layer is affected). Surprisingly, the cascades also penetrate the film and displace the Si atoms near the interface, as shown in Figure 5.11(c). This is displayed pictorially in Figure 5.11(d) wherein the distributions of all displaced species are plotted in terms of sample depth and horizontal co-ordinates. From this it is apparent that the beam interacts with the species throughout the film and through to the uppermost ~5 nm of the Si substrate. It has the effect of mixing the species in this region; this is known as the mixing layer. The fact that this mixing layer penetrates the film, even at the onset of profiling (where the film is at its thickest) results in Si atoms being detected in the "MnPc film" region of Figure 5.10(a) and so the film-substrate interface becomes blurred.

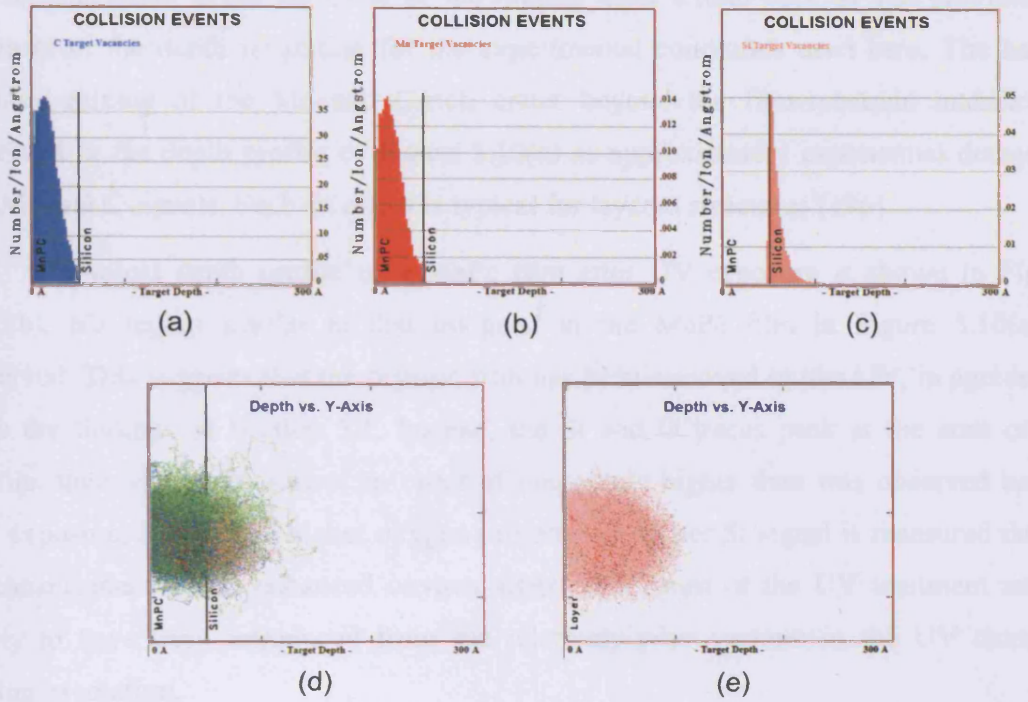

Figure 5.11. *Monte-Carlo simulations (from SRIM) of (a-d) a 5 nm MnPc film on Si and (e) bulk Si. All simulations were performed using a 1.25 kev Ar^+ beam (tilt angle of 45°) to match the experimental conditions. In all cases hydrogen (green), carbon (blue), manganese (red), nitrogen (orange) and silicon (pale pink) are traced. (a)-(c) The density of collision events as a function of depth for C, Mn and Si respectively for the MnPc film on Si (the film-silicon interface is marked by a vertical line). Lateral distributions after bombardment as a function of depth for (d) MnPc on Si and (e) bulk Si.*

Another important consequence of the relatively large mixing layer occurs just beyond the film-substrate interface. At the interface, significant quantities of Mn and C are present in the near-surface region of the crater. These become mixed with Si and so are effectively driven beyond the original interface by the profiling beam. The thickness of the mixing layer in this region is modelled in Figure 5.11(e) where the sputtering of

bulk Si is simulated (it should be noted that this assumes the majority species beyond the interface to be Si). This figure shows that the beam influences the uppermost ~9 nm of the Si; this value is the thickness of the mixing layer within bulk Si and provides an estimate of the depth resolution for the experimental conditions used here. The beam-induced mixing of the Mn and C-rich crater beyond the film-substrate interface is observed in the depth profile of Figure 5.10(a) as approximately exponential decays of the Mn and C signals. Such an effect is typical for layered structures [196].

A typical depth profile of a MnPc film after UV exposure is shown in Figure 5.10(b). No region similar to that assigned to the MnPc film in Figure 5.10(a) is observed. This suggests that the organic film has been removed by the UV, in agreement with the findings of Section 5.1. Instead, the Si and O traces peak at the start of the profile; their yields are almost an order of magnitude higher than was observed before UV exposure, implying a higher oxygen presence (a higher Si signal is measured due to O enhancement). This enhanced oxygen signal is a result of the UV treatment and is likely to have been introduced from the relatively poor vacuum in the UV chamber during irradiation.

Significantly, a much greater Mn yield is observed at the interface, in combination with a lower C yield (some of the C is likely to be due to surface contamination during sample storage prior to measurement). This demonstrates that the metal is left behind after UV treatment and than a Mn-rich surface layer is formed. It should be noted that the signal at 55 amu cannot be due to a $C_4H_2^+$ interference since its yield would be expected to scale with the amount of C^- detected (the C^- yield would also be the greater of the two). Unfortunately, it is not possible to quantify the amount of Mn present at the interface owing to both the non-equilibrium sputtering conditions, the enhanced oxygen presence and the anticipated difference in sputtering yield between the bulk MnPc film and wafer. The reduction in C^- yield demonstrates that much of the C has been removed. This suggests that the rupturing of the Pc ring (as evidenced in Section 5.1) results in the creation of some small fragments that desorb from the surface. However, it is not possible to determine how much of the organic material remains due to the presence of surface contaminants, in addition to the aforementioned difficulties described for Mn.

Once within the bulk substrate, the C and Mn traces decrease in a similar manner to that described for Figure 5.10(a) due to beam induced mixing, with a similar yield of C reached as for the untreated MnPc film. However, after its exponential decay due to the mixing layer, the Mn yield is seen to plateau at a constant value (approximately 30 counts/s). This is in contrast to the untreated MnPc film which continued to decay reaching a value of ~7 counts/s after 20 nm, implying that some Mn has been introduced to the silicon wafer by the UV process. This possibility will be addressed in Section 5.3.

5.2.2 X-ray Photoelectron Spectroscopy

XPS has been used to gain more information about the chemical composition of the surface after UV exposure. Although the SIMS data suggests a high presence of Mn, O and Si at the sample surface, with a reduced C content (compared to that of the MnPc film), it does not provide information on the oxidation states of the species and their local bonding environment. In XPS, charging effects can lead to shifts in the measured electron energies and therefore binding energies [190]; in order to correct for these it is standard procedure to shift the spectra such that the binding energies match a known reference (typically the C 1s peak or substrate peaks are used). Here, the spectrum of the 5 nm MnPc film was shifted such that the C 1s peak, which was assumed to be from the Pc ligand (the molecule has already been shown to remain intact after deposition in Section 5.1.2), matched the published value of 284.8 eV attributed to the Pc benzene rings [248–250]. The post-UV spectra were then re-scaled to the carbon peak at 284.8 eV, as determined experimentally from that of the initial 5 nm MnPc film.

The XPS spectra obtained of the initial 5 nm MnPc film (which had been transferred to the XPS chamber within 15 minutes of its preparation) and that after 40 minutes of UV exposure are compared in Figure 5.12. The peaks have been assigned as shown in the figure, with Mn, O, N, C and Si present in both cases. The relative yields of these species are seen to vary significantly between the two spectra, most notably in the increased O and reduced C and N presence after UV processing. The relative abundances of each element were calculated from the integrated areas of each species after Gaussian fitting (during which care was taken to ensure consistent Gaussian peak

widths) and correcting for the different sensitivity factors [206], as outlined in Section 2.10. The relative abundances for the MnPc film before and after UV exposure are compared in Table 5.1. Errors were calculated from comparison of the raw data and Gaussian fit.

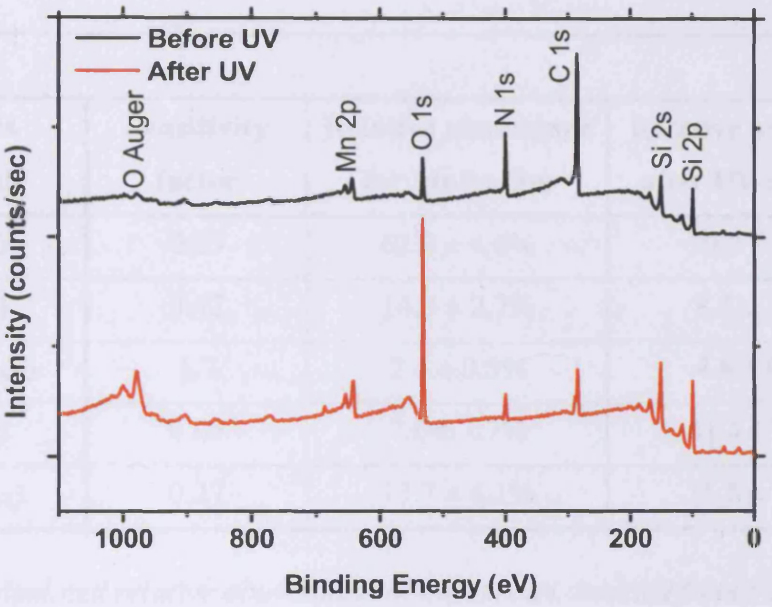

Figure 5.12. *XPS survey data for a 5 nm MnPc film before (black) and after 40 minutes of 172 nm irradiation (red). The species responsible for the main peaks are labelled accordingly, whilst the data are offset for clarity.*

As expected, carbon is the most abundant species observed for the as-deposited MnPc film. A C:N:Mn ratio of 26:6:1 is found, in reasonable agreement with that obtained from the empirical formula of 32:8:1. After UV exposure, the C and N signals decrease drastically, whilst that of Mn remains of similar intensity. This is consistent with the SIMS data which suggested the UV photons remove the organic material, leaving behind the metal. Since the data in Figure 5.12 were collected on different days, slight variations in absolute intensities would be anticipated due to variations in experimental

set-up, however, these general trends are expected to be real. In addition, there is a significant increase in oxygen content after UV treatment, as suggested by the SIMS profile in Figure 5.10(a). The relative abundance of O rises from 7.5 ± 1.7% to 41.4 ± 1.6% and suggests the formation of a surface oxide. As has been noted, oxygen is likely to have been introduced by impurities in the nitrogen gas and/or from the relatively poor vacuum of the UV chamber.

Species (orbital)	Sensitivity factor	Relative abundance for MnPc film	Relative abundance after UV exposure
C (1s)	0.25	62.0 ± 4.6%	30.2 ± 6.5%
N (1s)	0.42	14.3 ± 2.7%	8.1 ± 3.8%
Mn ($2p_{3/2}$)	1.7	2.4 ± 0.5%	4.8 ± 0.7%
O (1s)	0.66	7.6 ± 1.7%	41.4 ± 1.6%
Si ($2p_{3/2}$)	0.27	13.7 ± 4.1%	15.5 ± 1.5%

Table 5.1. *Calculated relative abundances of the species detected from a 5 nm MnPc film before and after UV processing after correcting for empirical sensitivity factors relative to F (1 s) (from [206]). Errors were calculated from the Gaussian fitting.*

High resolution XPS spectra of the C 1s, N 1s, O 1s, Mn 2p and Si 2p orbitals were collected in order to learn more about the local chemical environment of the species before and after UV treatment. These are shown in Figure 5.13. The extracted peak binding energies and corresponding relative abundances (after Gaussian fitting) are summarised in Table 5.2. Three peaks are seen in the C 1s spectra of the 5 nm MnPc film. As was mentioned previously, the most intense of these was normalised to a binding energy of 284.8 eV and is attributed to the benzene rings of the phthalocyanine ligand. A second intense peak is detected at 286.3 eV which can readily be assigned to the carbon

atoms bound to nitrogen [249, 250]. The ratio of the intensities of these fitted peaks is 74.8:25.2, which is in excellent agreement with the expected ratio of 75:25 obtained from the molecular structure, further justifying the choice of reference peak. The small peak at 288.0 eV is a satellite peak of C 1s, as has been reported elsewhere [250]. Studies of the nitrogen spectra also agree well with literature [249], with a dominant peak at 399.1 eV and a satellite peak at 400.5 eV; the latter has a comparable shift to the main N 1s peak of +1.5 eV that has been reported for more widely studied MPc's [250]. Four peaks are observed for the manganese spectra, as is expected for transition metal species, namely those due to the $2p_{1/2}$ (653.9 eV) and $2p_{3/2}$ (642.6 eV) orbitals, along with their corresponding lower intensity satellite peaks. Again, their positions agree with published work [249]. This agreement between the measured XPS spectra and that expected for MnPc further demonstrates the integrity of the molecular film.

Table 5.1 shows that a relatively low presence of oxygen is observed in the freshly prepared MnPc film; that detected may be a result of exposing to air for short periods whilst transferring between chambers, or due to the HF etch not being completely successful. It should be noted that during the preparation of this sample, difficulties arose in evacuating the OMBD chamber prior to growth. Although the chamber was situated in a nitrogen glovebox (and so the passivated silicon substrate was not exposed directly to air during this additional period), it is anticipated that the measured oxygen content of this film serves as an upper limit to that present in other films transferred to the UV chamber directly after MnPc growth. Studies of a MnPc film as a function of time after its preparation (not shown here) demonstrate a significantly increased relative oxygen concentration after two weeks of 29%, which remains relatively constant after the longer times studied (up to two months). The peak centred at 531.1 eV (from Table 5.2) can be assigned to the presence of a small amount of oxygen within the organic film [249], whilst that at 532.5 eV is due to SiO_2 formation [251]. The presence of SiO_2 is also observed in the silicon spectrum where, in addition to the expected $Si_{1/2}$ and $Si_{3/2}$ features observed at 99.7 eV and 99.1 eV respectively, a third peak is present at 102.9 eV which can be attributed to silicon oxide formation [252].

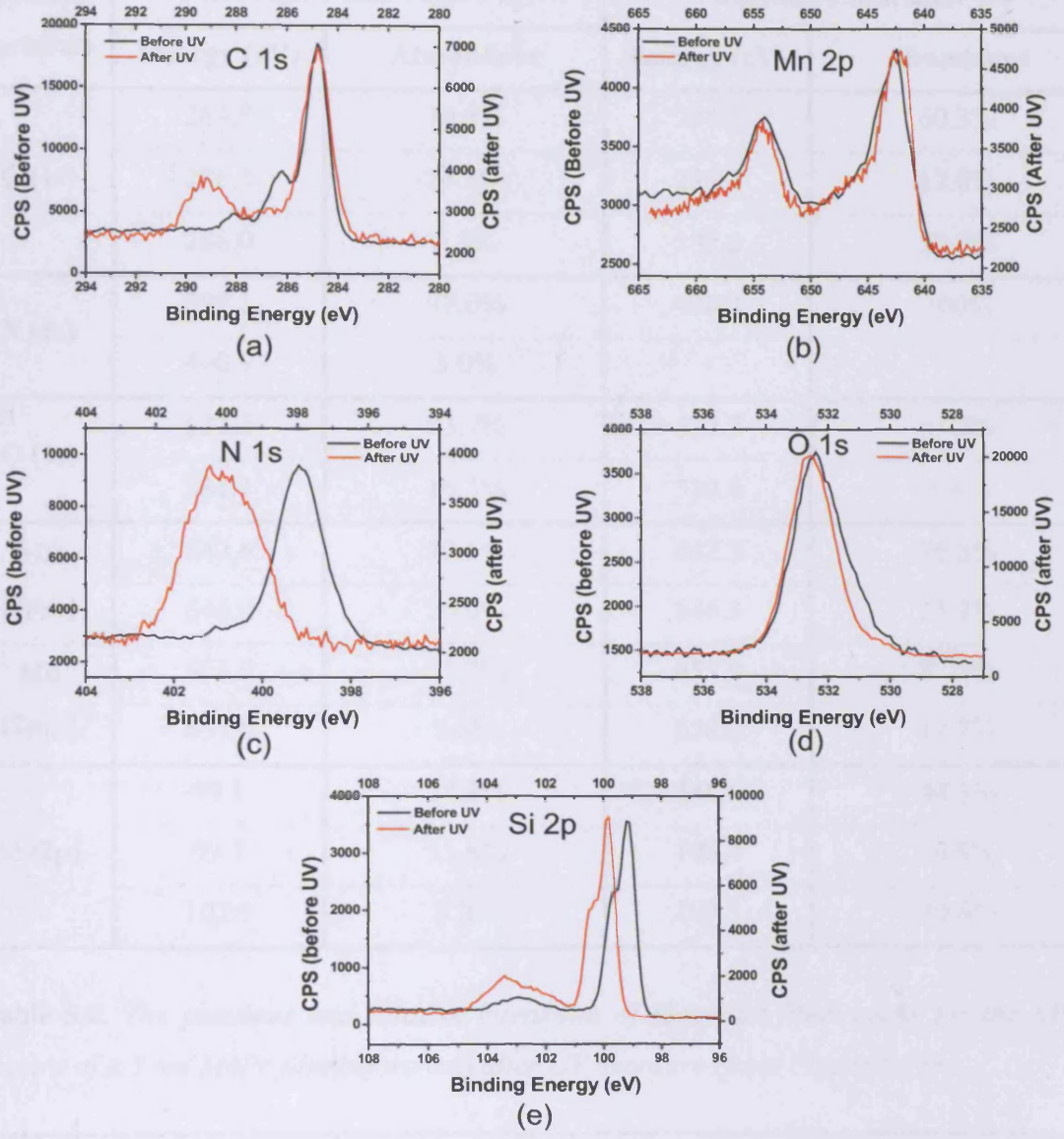

Figure 5.13. *High resolution XPS profiles of the (a) C 1s, (b) Mn 2p, (c) N 1s, (d) O 1s and (e) Si 2p peaks. In each case the spectrum of the initial MnPc film (before UV exposure) is shown in black (counts per second scale, on left-hand axis), whilst that of a MnPc film after 40 minutes of UV exposure is shown in red (scale on right-hand axis).*

Species (orbital)	5 nm MnPc film before UV		5 nm MnPc film after UV	
	Energy (eV)	**Abundance**	**Energy (eV)**	**Abundance**
C (1s)	284.8	70.5%	284.8	60.3%
	286.3	23.8%	286.7	12.8%
	288.0	5.8%	289.2	26.8%
N (1s)	399.1	97.0%	400.2	100%
	400.9	3.0%	-	-
O (1s)	532.5	83.7%	532.5	95.2%
	531.1	16.3%	530.6	4.8%
Mn ($2p_{3/2}$)	642.6	79.1%	642.3	76.8%
	646.0	20.9%	646.3	23.2%
Mn ($2p_{1/2}$)	653.9	91.2%	653.9	82.3%
	657.6	8.8%	658.2	17.7%
Si (2p)	99.1	58.3%	99.8	44.3%
	99.7	33.8%	100.4	24.9%
	102.9	8.0%	103.1	30.8%

Table 5.2. *The positions and relative intensities of Gaussian fitted peaks for the XPS spectra of a 5 nm MnPc film before and after UV exposure (from Figure 5.13).*

After UV irradiation, drastic changes to the high resolution XPS spectra of all species can be seen in Figure 5.13. A notable variation in line-shape of the carbon signal with respect to the original MnPc film is observed, demonstrating that significant changes to the organic ligand have occurred (the quantity of C has also been reduced, as described previously). The most intense peak at 284.8 eV can be attributed to small benzene

containing fragments created by the destruction of the organic framework, whereas that at 286.7 eV is most likely due to C-N fragments. It should be noted that the ratio of these two peaks is now 82.5:17.5 and no longer matches that found for the original film. Furthermore, a significant peak is observed at 289.2 eV and this can be attributed to the formation of carbonyl groups [253] (which are not present in the molecular structure of MnPc). Carbonyl groups were not detected in the Raman spectra, suggesting that these may be a result of surface contamination; carbazole structures were detected in Section 5.1.1, but these would be expected to contribute to the benzene and C-N peaks at 284.8 eV and 286.7 eV. However, it is clear that the organic ligand is being broken by the UV photons. Since the largest quantity of carbon remaining is in the form of aromatic groups, it seems likely that the bonds between the carbon and nitrogen atoms of the MPc are those that are most readily ruptured, which is consistent with the discussion presented in Section 5.1. In addition, the post-UV sample was exposed to air prior to measurement for much longer times than the freshly grown films, and so some carbon-rich surface contamination by residual dust from the air is expected.

Significantly, a shift of 0.7eV is observed in the Si 2p peaks shown in Figure 5.13. It should be noted that the dopant concentration of the two substrates was identical and so this suggests that a change to the electronic properties of the Si wafer has occurred (the introduction of Mn into the substrate will be discussed in Section 5.3). This shift is accompanied by an increase in the relative intensity of the SiO_2 peak with respect to the main Si 2p peaks. However, this increase is most likely due to the re-growth of the native oxide layer, and is not large enough to explain the dramatic increase in oxygen content that occurs as a result of the UV treatment. Instead, it is apparent that other oxide compounds are formed. Figure 5.12 demonstrates that a significant quantity of Mn remains at the surface after UV exposure, whilst Figure 5.13(b) shows notable changes in the Mn line-shape after UV treatment, suggesting a change in chemical environment of this species. In addition, as described in Section 5.1.2, a broad tail at low wavelengths was observed in the electronic absorption spectra after UV irradiation, which could be attributed to the formation of manganese oxide(s).

Owing to the aforementioned enhanced oxygen presence, it is likely that MnO has been formed. After UV treatment, the Mn $2p_{3/2}$ peak of Figure 5.13(b) appears truncated

with a width of ~1.0 eV; this, along with the relatively low intensities of the satellite peaks, is in good agreement with the experimentally determined line-shape of MnO published elsewhere [254]. A selection of Mn 2p binding energies (ranging between 639.0-641.4 eV for Mn $2p_{3/2}$) have been reported for manganese oxides [255–257], and that it is preferable to use the lower intensity Mn 3s peak for the determination of the oxide species [258]. Unfortunately, owing to the dilute nature of this sample, it was not possible to obtain sufficient resolution for the Mn 3s peak. Table 5.3 summarises variations of binding energies for a range of Mn oxides, from which it is not possible to identify the presence of a manganese oxide. In summary, from the XPS measurements, it appears that a manganese oxide has been formed, most likely MnO, but this result is not conclusive and needs to be confirmed by other techniques.

Compound	Mn $2p_{3/2}$ (eV)	Mn $2p_{3/2}$ (eV)	O 1s (eV)
MnO_2	641.9	653.6	529.2
Mn_3O_4	641.3	652.9	529.1
MnO	641.4	653.1	529.8
Mn_2O_3	641.7	653.4	529.8
Mn	638.6	649.7	-
Experimental data	642.3	653.9	530.6

Table 5.3. *Binding energies of the Mn $2p_{3/2}$, Mn $2p_{3/2}$ and O 1s peaks of manganese oxides and manganese metal (from [257]). The experimentally obtained value for the post-UV sample, from Table 5.2, is also included to aid comparison.*

5.2.3 X-ray Absorption Spectroscopy

X-ray absorption spectra are very sensitive to the local chemical environment of the absorbing species. For this reason, near-edge XAS has been used to gain further insight into the Mn oxidation state, both in the initial MnPc film and after UV exposure. The x-ray absorption profiles of a Mn foil, MnPc (in powder and thin film forms) and a MnPc film that had been subjected to irradiation, after normalisation and background subtraction (performed using the Athena software [259]) are compared in Figure 5.14(a). The corresponding positions of the x-ray absorption edges are summarised in Table 5.4; these were defined as the maxima of the first derivative of each profile.

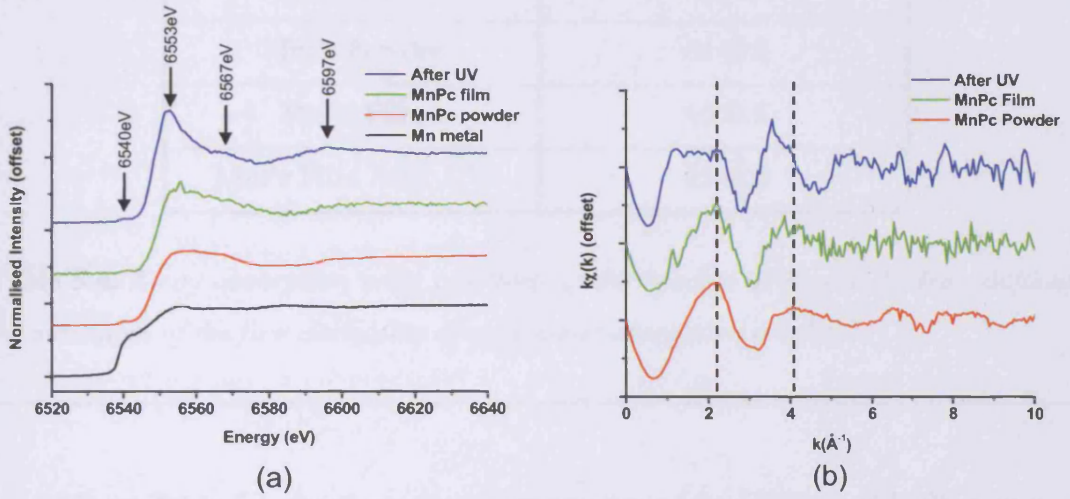

Figure 5.14. *(a) XANES and (b) EXAFS oscillations of a Mn foil (black), MnPc powder (red), and a 5 nm MnPc film before (green) and after (blue) UV exposure. Data are offset for clarity in both cases.*

As was described in Section 2.9.4, the x-ray absorption edge position becomes shifted to higher energies with respect to that of the metal upon increasing oxidation state (a greater shift is observed for higher oxidation states). The edge position of the Mn foil, in which Mn is in a neutral oxidation state, occurs at a lower energy (a difference of ~10 eV) than for the other spectra, suggesting a higher oxidation state in the latter cases.

The features of near-edge spectra are unique to individual compounds; since the theory behind this is not sufficiently understood, in order to model materials *ab initio*, in general the XANES is compared to model compounds. Similar features are observed between the MnPc film and powder reference, further demonstrating the integrity of the organic film. This agreement is further emphasised in Figure 5.14(b) in which the EXAFS oscillations are compared; the maximal positions of the MnPc powder oscillations are marked by dotted lines and these are seen to coincide with the oscillations of the film.

Sample	Edge Position (eV)
Mn foil	6538.6
MnPc Powder	6548.0
MnPc Film	6550.5
MnPc Film After UV	6548.0

Table 5.4. *X-ray absorption edge positions of the spectra of Figure 5.14(a), defined as the maximum of the first derivative of each x-ray absorption profile.*

From Table 5.4, the absorption edge position of the UV-treated MnPc film is seen to be very similar to that of MnPc. Since, the metal is in the 2+ oxidation state within the phthalocyanine molecule, this implies that Mn^{2+} remains after processing. However, the line-shape of the spectra beyond the absorption edge, particularly as seen in the EXAFS oscillations, does not resemble that of MnPc. This suggests that the local environment of the Mn ion has changed as a result of UV exposure, i.e. that the Mn is no longer bound to the Pc ligand. This is agreement with the aforementioned Raman and electronic absorption measurements, in which the molecular signature was no longer present after this duration of UV exposure. Furthermore, the SIMS data in Section 5.2.1 demonstrated a high O presence, whilst the XPS analysis suggested that MnO was formed. The implied presence of Mn^{2+} after UV treatment, as judged from the x-ray absorption edge position

(Table 5.4), is therefore consistent with these observations. Published XANES spectra of a range of Mn oxides were shown in Figure 2.12. MnO shows a pre-edge at ~6540 eV and peaks at ~6554 eV, ~6568 eV and ~6598 eV (these values are approximate since they have been read from experimental plots) [203, 204]. Features at similar positions are observed in the XANES spectrum of Figure 5.14(a), again suggesting the formation of MnO.

In order to gain further insight into the chemical nature of the surface after UV exposure, the data has been fitted using the Excurv98 software package (from SRS, Daresbury). Owing to the low signal to noise ratio, only the first shell was fitted over the first two EXAFS oscillations. A comparison between the modelled and experimental data is shown in Figure 5.15. The best fit yielded a Mn-O bond distance of 2.23 Å and co-ordination number of ~6. Table 5.5 summarises the known bond distances between Mn and its nearest O and Mn neighbours of a range of Mn oxides (along with that of Mn metal). Comparison of the bond distance obtained by simulation of the EXAFS data with those shown in the table suggests that MnO is formed, in agreement with the XPS data.

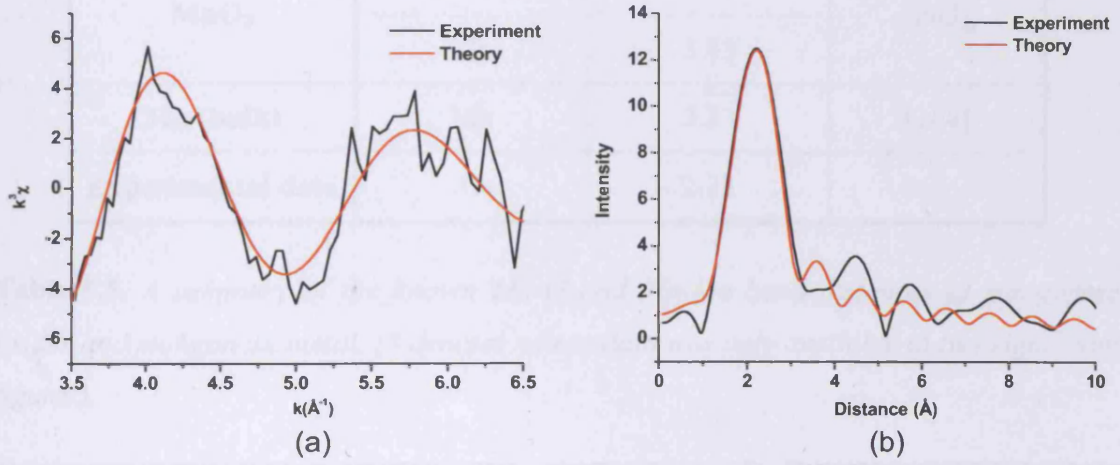

Figure 5.15. *A comparison between the (a) EXAFS oscillations and (b) Fourier Transform of the experimental (black) and simulated (red) data of a 5 nm MnPc film after UV exposure.*

Compound	Neighbour	Distance (Å)	Reference
MnO	O	2.22	[260]
	Mn	3.14	
Mn_3O_4	O	2.04	[261]
	Mn	4.34	
	O	1.93	
	O	2.28	
	Mn	3.12	
	Mn	3.43	
Mn_2O_3	O	2.0*	[262]
	Mn	3.1*	
MnO_2	O	1.89	[263]
	Mn	3.43	
Mn (bulk)	Mn	2.73	[264]
Experimental data	O	2.23	

Table 5.5. *A summary of the known Mn-O and Mn-Mn bond distances of manganese oxides and manganese metal. (* denotes where data was only available to two significant figures).*

In summary, the UV exposure of the thin MnPc films results in the formation of a surface MnO film. Since the initial MnPc film comprises regular domains of crystallites, this processing procedure could be used to form nanosized MnO clusters, which would be of interest for their magnetic, electronic and catalytic properties [265]. In addition, this

film could be reduced by bombardment with low energy electrons, which is also being investigated as an alternative method for the introduction of Mn into Si in our group*. However, the SIMS profile of Figure 5.10(b) suggests that, in addition to the formation of MnO, Mn may also be introduced directly into the Si wafer by UV exposure (the aim of this chapter). This will be investigated in the following section.

5.3. EXAMINATION OF THE BULK SUBSTRATE AFTER UV EXPOSURE: METAL IMPLANTATION

It was established in Section 5.2 that a MnO layer is formed at the surface as a result of the UV treatment. In this section, it is of interest to determine whether Mn has also been introduced into the Si substrate. In order to achieve this, it is necessary to remove the MnO layer since this layer has been seen to dominate the Mn signal of the surface sensitive techniques used here. Sputtering techniques such as Ar^+ bombardment would be likely to drive any surface Mn into the substrate (as described in the aforementioned SIMS analysis), and so instead a chemical clean has been used to etch the samples after UV treatment. Briefly, the samples were immersed in a 2:1 ratio of H_2SO_4 and H_2O_2, a standard technique known as a Piranha clean that is commonly used for the removal of surface metal contamination of silicon wafers. The samples were then analysed with a specific focus on any Mn present in the silicon substrate resulting from the UV treatment. This was mainly achieved through SIMS and XAS measurements, as will be described in Sections 5.3.2 and 5.3.3 respectively. Calculations on the concentration and diffusion of the Mn detected, as determined from the experimental SIMS data, are also included in Section 5.3.2, along with a discussion on possible incorporation mechanisms (Section 5.3.4).

5.3.1 X-ray Photoemission Spectroscopy

Before analysis of the bulk Si could be performed, it is important to determine whether the chemical cleaning process had successfully removed the MnO layer. Owing to its

* Experiments are being conducted by David Humphreys and Geoff Thornton.

high surface sensitivity, XPS has been used to verify this. An XPS spectrum of a UV irradiated MnPc film after chemically cleaning the surface is shown in Figure 5.16. As expected, a dominant Si signal is observed from the bulk wafer. This is accompanied by low C and O signals, which display abundances consistent with those expected from surface contamination after cleaning or from inside of the vacuum chamber. In addition, a small peak at 686.4 eV is seen and this is due to F attaching to the clean Si(100) surface during the HF dip. Most significantly though, no Mn was detected after cleaning, in contrast to the spectra shown in Figure 5.12. Since XPS only probes the uppermost surface (it has a depth range of typically 10 nm) this suggests that the MnO rich surface has been successfully removed and that the concentration of any Mn within the silicon in the region sampled, if present, is low.

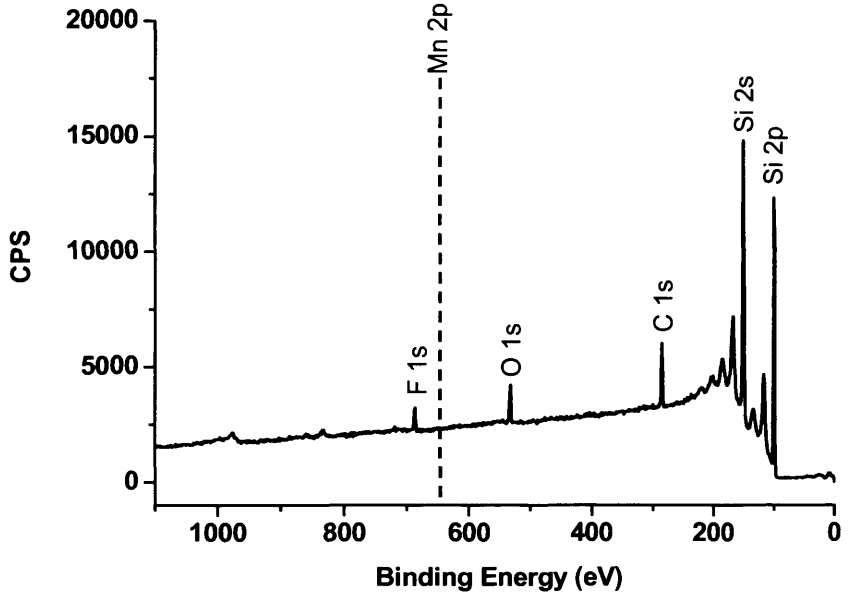

Figure 5.16. *An XPS survey of a MnPc film on silicon after UV irradiation and a subsequent chemical clean. The dotted vertical line represents the binding energy of a Mn $2p_{3/2}$ peak. The absence of Mn demonstrates that the clean has been successful.*

5.3.2 Secondary Ion Mass Spectrometry

SIMS offers an enhanced elemental sensitivity over XPS and so it is anticipated that it will be more successful in the detection of dilute species. Representative SIMS depth profiles of a MnPc film on silicon after UV exposure and chemical cleaning are shown in Figures 5.17(a)-(c). Here, C^- O^-, Si^+ and Mn^+ ions are traced under the same conditions as used for the depth profiles of Figure 5.10. The most striking difference when compared with the profile of the initial silicon wafer (Figure 5.17(d)) is the significant presence of Mn within the substrate in all three cases. A sharp peak is not observed in the Mn trace at the surface of these profiles (confirming the XPS observation that the surface Mn oxide-rich layer has been removed), whilst the Mn yield remains relatively constant as a function of depth into the substrate. This indicates that Mn is not being driven in from the surface, in contrast to the cases shown in Figure 5.10, and instead that a relatively uniform Mn presence exists within the silicon in the regions measured. In order to determine whether the UV or the chemical clean were responsible for this Mn signal, multiple profiles of chemically cleaned MnPc films (not subjected to UV irradiation) were analysed. No Mn trace was detected for any such samples, with the depth profiles obtained of similar appearance to that of the initial Si wafer. This confirms that the UV light plays a crucial role in the introduction of Mn into Si.

The Mn concentration is found to be inhomogeneous as a function of lateral sample position, with the profiles of Figures 5.17(a) and (b) taken approximately 1 mm apart and showing varying Mn yields. In addition, it should be noted that a Mn presence was not observed in all regions, with some depth profiles appearing similar to that of the blank silicon wafer (any Mn present was below the limits of detection). After a statistical analysis of the regions sampled across a range of samples (prepared in separate batches) approximately 20-30% of the sample regions were estimated to be Mn-rich, with that shown in Figure 5.17(a) at the upper limit of the Mn/Si ratio. The non-uniformity of the Mn may be due to either the sample preparation steps, or a property of Mn in silicon as a result of the UV processing conditions, as will be discussed in more detail in Section 5.3.4.

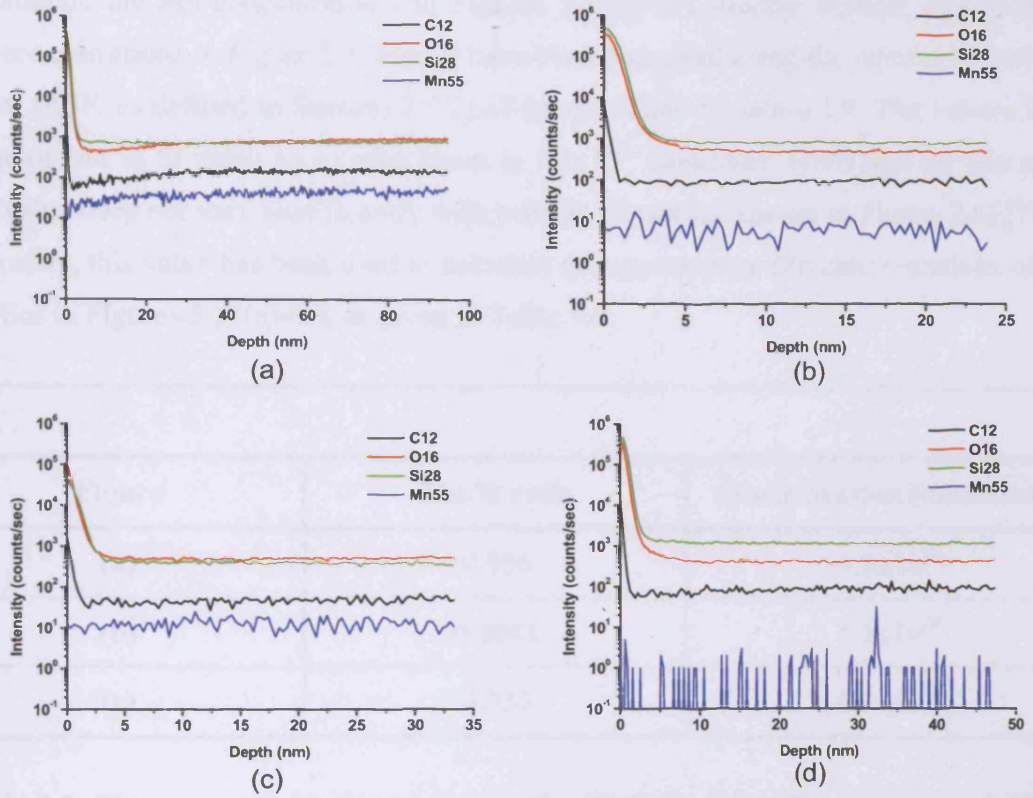

Figure 5.17. *SIMS depth profiles of (a)-(c) a MnPc film on Si after UV treatment and a chemical surface clean and (d) the initial untreated silicon wafer. Profiles (a) and (b) were obtained 25 hours after UV irradiation, 1 mm apart. Profile (c) was performed inside the crater of (a), 53 hours after sample preparation (note that the size of this crater was reduced by 80% so that only the bottom of the original crater was measured).*

Calculation of the average Mn concentration

As outlined in Section 2.5, dynamic SIMS can be used to perform a quantitative analysis of the concentrations of dilute species. SIMS profiling of a dilute Mn in Si reference sample (produced by ion implantation) of average concentration ~4 x 10^{18} atoms/cm^3 within the uppermost 300 nm was performed, but the concentration of Mn was insufficient for detection. (It should be noted that this value provides an estimate of the

detection limit of the experimental conditions used here.) Therefore, it was not possible to calibrate the Mn concentrations in Figures 5.17(a)-(c) directly. Instead, approximate Mn concentrations in Figure 5.17(a)-(c) have been estimated using the relative sensitivity factor (RSF, as defined in Section 2.5.2) of Mn in Si and Equation 2.9. The known RSF value of Mn in Si using an oxygen beam is $1.3x10^{22}$ atoms/cm^3 [194] and for Mn in Si this value does not vary significantly with profiling beam (as shown in Figure 2.6) [193]. Therefore, this value has been used to calculate the approximate Mn concentrations of the profiles in Figures 5.17(a)-(c), as given in Table 5.6.

Figure	Mn/Si ratio	Concentration (atoms/cm^3)
(a)	0.056	$7.3x10^{20}$
(b)	0.0081	$1.1x10^{20}$
(c)	0.033	$4.3x10^{20}$

Table 5.6. *The measured Mn/Si yields from the SIMS depth profiles of Figures 5.17(a)-(c), and their corresponding estimated concentrations.*

The profiles shown in Figures 5.17(a) and (b) were obtained from regions separated by 1 mm and were taken back-to-back (they can be approximated as being taken at the same time, rendering time-dependent diffusion effects negligible). These profiles can be used to estimate the Mn distribution in the "patch" from which they were obtained. Here, the concentration of (a) is assumed to be the maximum for the patch (C_{max}), with the concentration profile assumed to be radially symmetric and to linearly decrease as a function of increasing distance from (a), as shown in Figure 5.18. The concentration is constant as a function of depth (for the range probed in Figure 5.17) for any given distance from the centre. Therefore, the patch is approximated as a cylinder with the lateral concentration gradient as defined by Figure 5.18.

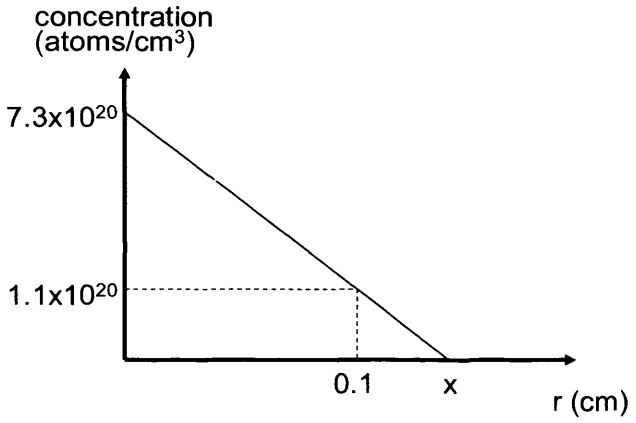

Figure 5.18. *The anticipated radial Mn concentration profile of the Mn-rich patch measured in Figure 5.17 used to estimate the number of Mn atoms present in the patch.*

The value of x, the radius of the cylindrical patch, can be readily calculated using trigonometry, as outlined in Equation 5.2.

$$\frac{x}{7.3\times10^{20}} = \frac{0.1}{7.3\times10^{20} - 1.1\times10^{20}}$$

$$\Rightarrow x = 0.12\ cm \qquad [5.2]$$

The concentration, $C(r)$ shown in Figure 5.18 can therefore be expressed as shown in Equation 5.3.

$$C(r) = C_{max}\left[1 - \frac{r}{0.12}\right] \qquad [5.3]$$

The Mn traces in the depth profiles of Figure 5.17 appear constant in all cases, with the deepest depth sampled being 95 nm. This value is therefore the minimum depth of this Mn-rich region and can be used as the length of the cylinder to obtain an approximate value of the number of Mn atoms present in the patch (N_{patch}), as outlined in Equation 5.4. However, it should be noted that this assumption introduces a large error in the calculation since the true depth of this patch is expected to be greater than 95 nm, and so the calculations will provide a lower limit to the Mn concentration.

$$N_{patch} = \int_0^{2\pi} d\theta \int_0^{95\times10^{-7}} dz \int_0^{0.12} r dr C_{\max}\left[1-\frac{r}{0.12}\right] \qquad [5.4]$$

$$N_{patch} = 2\pi \times 95\times10^{-7} C_{\max}\left[\frac{r^2}{2}-\frac{r^3}{3\times0.12}\right]_0^{0.12}$$

$$N_{patch} = 1.0\times10^{14}\ atoms$$

The concentration of Mn atoms in a MnPc film can be approximated by assuming that the unit cell of MnPc is similar to that of α-phase CuPc, with dimensions a = 25.9 Å, b = 3.8 Å, c = 23.9 Å and β = 90.4° (with four metal atoms per unit cell) [27]. This concentration (C_{MnPc}) is calculated in Equation 5.5, where V_{uc} is the volume of the unit cell (in cm^3).

$$C_{MnPc} = \frac{4}{V_{uc}} = \frac{4}{abc\sin\beta} = 1.7\times10^{21}\ atoms/cm^3 \qquad [5.5]$$

The number of Mn atoms in a 1 cm x 1 cm surface region of a MnPc film of thickness d_{film} (in cm, in this case 5 nm thick) is given by Equation 5.6.

$$N_{Mn} = C_{MnPc} d_{film} = 8.5 \times 10^{14}\ atoms / cm^2 \qquad [5.6]$$

In a circle of radius 0.12 cm (i.e. the exposed surface area of the patch), the number of Mn atoms (N_{circle}) is given by Equation 5.7.

$$N_{circle} = N_{Mn} \pi x^2 = 3.7 \times 10^{13}\ atoms \qquad [5.7]$$

This is a factor of 2.7 times less than the number of Mn in the patch (N_{patch}) and implies that Mn has migrated laterally to the region sampled in Figure 5.17(a). However, these patches are isolated and Mn is not detected for approximately 70-80% of the total sample, as determined from over 30 analyses over a range of sample preparation runs. This implies that 69 ± 14% of the Mn from the MnPc film is introduced into the sample. It should be noted that this value provides a rough guide only, with errors likely to be due to the assumed depth of the crater, the choice of a radial distribution function, the use of published RSF values (not experimentally calibrated for our system), along with the limited statistics on patch distribution and concentrations. However, it appears to be of the right order of magnitude and is very encouraging for the further development of this technique.

Calculation of diffusion

In addition to the total concentration, information can be gained from the SIMS profiles regarding the diffusion of Mn within the Si wafers as a function of time. The profiles in Figure 5.17(a) and (c) were taken at the same location; that of (a) was performed 25 hours after UV irradiation, whilst that of (c) was obtained 53 hours after sample preparation (i.e. 28 hours after that of (a)). As outlined in Section 1.3.4, for a system where a thin dopant film is deposited onto a surface and allowed to diffuse (at a given temperature), the concentration profile as a function of time (t) and depth (z) is given by

the Gaussian distribution presented in Equation 1.9 (the choice of using the interstitial diffusion coefficient will be verified shortly).

Here, it is of interest to use the concentrations calculated for profiles (a) and (c) to determine the diffusion coefficient of Mn in this system. As seen in Figure 5.17, these profiles appear constant over the depths studied. However, it is difficult to determine whether this is real or if the profiling beam is artificially increasing the Mn yield detected at greater depths due to beam-induced mixing (as described in Section 5.2.1). For this reason, the values of the two concentrations from Table 5.6 will be used to approximate the concentration profile at the start of each sputtering sequence, i.e. at 0 nm and 95 nm for (a) and (c) respectively. Theoretical expressions for the concentrations of the profiles (a) and (c) are given in Equations 5.8 and 5.9, where S is the surface concentration (the same in both cases) and D_{exp} is the experimentally determined interstitial diffusion coefficient of Mn in Si.

$$C(0\,nm, 25\,h) = \frac{S}{\sqrt{\pi D_{\exp} 25 \times 60^2}} \qquad [5.8]$$

$$C(95\,nm, 53\,h) = \frac{S}{\sqrt{\pi D_{\exp} 53 \times 60^2}} \exp\left[\frac{-(95 \times 10^{-7})^2}{4 D_{\exp} 53 \times 60^2}\right] \qquad [5.9]$$

It should be noted that the surface concentration value is likely to be subject to a large error since it is dependent on the use of the RSF values (these only give an approximation of the concentration). However, by taking the ratio of the concentrations, such an error can be cancelled out (the initial surface concentration was the same for both profiles). From Table 5.6, the ratio of C(0 nm, 25 h) to C(95 nm, 53 h) is 1.70. Therefore, by taking the ratio of Equations 5.8 to 5.9, a value of D_{exp} can be calculated, as outlined in Equation 5.10.

$$D_{exp} = \frac{(95\times10^{-7})^2}{4\times53\times60^2 \ln\left[1.70\times\sqrt{\frac{25}{53}}\right]} = 7.6\times10^{-16}\ cm^2/s \qquad [5.10]$$

This value is in good agreement with that found in literature of 2.8 x 10^{-15} cm^2/s for interstitial Mn in Si at room temperature [175], especially given that diffusion coefficients generally vary over many orders of magnitude, as seen from Table 1.2. This suggests that Mn is introduced as an interstitial dopant; substitutional dopants and stable silicide patches would show negligible diffusion over this time period [266]. Furthermore, it is energetically favourable to form interstitial rather than substitutional Mn in Si (these require an energy of 2.47 eV and 3.00 eV respectively [267]), and so the observations are consistent with the preferential occupation of interstitial sites reported under equilibrium epitaxial growth conditions [267]. Any discrepancies between the experimental and literature values may arise from the non-equilibrium conditions during UV irradiation (as will be discussed in Section 5.3.4), from energy imparted by the SIMS profiling beam during sputtering, or from experimental errors.

It is also important to verify whether the apparently constant Mn profiles seen in Figure 5.17 can be explained from the theoretical diffusional model of interstitial Mn in Si. In the case of Figure 5.17(a), this can be achieved by taking the ratios of the concentrations at z = 0 nm and z = 95 nm after 25 hours (this assumes negligible diffusion during the time taken to obtain this depth profile). The concentration profiles of C(0 nm, 25 h) and C(95 nm, 25 h) are given in Equations 5.8 and 5.11 respectively, whilst their ratio is expressed in Equation 5.12.

$$C(95\,nm, 25\,h) = \frac{S}{\sqrt{\pi D 25\times60^2}} \exp\left[\frac{-(95\times10^{-7})^2}{4D25\times60^2}\right] \qquad [5.11]$$

$$\frac{C(95\,nm, 25\,h)}{C(0\,nm, 25\,h)} = \exp\left[-\frac{(95\times10^{-7})^2}{4D\times25\times60^2}\right] \qquad [5.12]$$

Substitution of the values of D_{exp} and D_{lit} = 2.8×10^{-15} cm^2/s [175] into Equation 5.12 suggest that the Mn concentration of profile (a) would be expected to fall by 72% and 91% respectively over the first 95 nm, both of which would be difficult to see on a logarithmic scale (as used in Figure 5.17). Therefore, since the profiling beam may also be driving some Mn into Si, the apparently constant yield detected is consistent with that expected for interstitial Mn in Si at the times and depths measured.

5.3.3 X-ray Absorption Spectroscopy

XAS was used to learn more about the local environment of the implanted manganese. For this, the Mn *K*-edge absorption XANES profile of the UV-treated MnPc film after chemical cleaning to remove any surface metal oxide was measured. Comparison of the magnitude of the absorption edge before normalisation of the data with that of Mn foil (assuming similar x-ray penetration and escape depths in both cases) gives an approximate Mn concentration of $\sim 5 \times 10^{20}$ atoms/cm^3 for the region measured here. This value is in good agreement with that obtained from the SIMS data (Table 5.6), further justifying the use of the RSF values in the determination of Mn concentrations in Section 5.3.2.

The spectral features of the UV treated MnPc film after normalisation are compared with those obtained for MnPc, Mn bulk metal and MnSi in Figure 5.19(a). This spectrum is vastly different to that of the MnPc film; the x-ray absorption edge of the UV-treated film occurs at a lower energy than that of MnPc (indicative of a different oxidation state) and has no clear pre-edge. This demonstrates that the metal is no longer bound to the organic ligand. Comparison with the XANES profile of bulk manganese suggests a similar edge position, implying that after UV processing the Mn is in a neutral oxidation state (as is also the case for the Mn silicide reference), and rules out the possibility that the metal species introduced into the bulk Si are in the form of an oxide (if this were the case a positive oxidation state would be expected, as shown in Figure 2.12). Commonly, small Mn clusters can form in Si [268], however, the edge features seen in Figure 5.19(a) are vastly different to the bulk metal case, suggesting that UV

processing does not lead to the formation of small metal clusters. Instead, the features are similar to those of the manganese silicide reference, suggesting that the Mn atoms have been incorporated into the bulk silicon. Comparison of the spectrum with experimental XANES spectra of implanted Mn in Si reported by Wolska *et al.* [269] also shows good agreement. Furthermore, the absence of a sharp peak at ~6542 eV demonstrates that the Mn is not a substitutional dopant (as predicted by theoretical simulations performed by these authors). The low signal to noise ratio in Figure 5.19(a) means that it is not possible to resolve the fine structure expected for interstitial Mn in Si, however this seems the most likely type of dopant, especially given the observed diffusional characteristics described in Section 5.3.2.

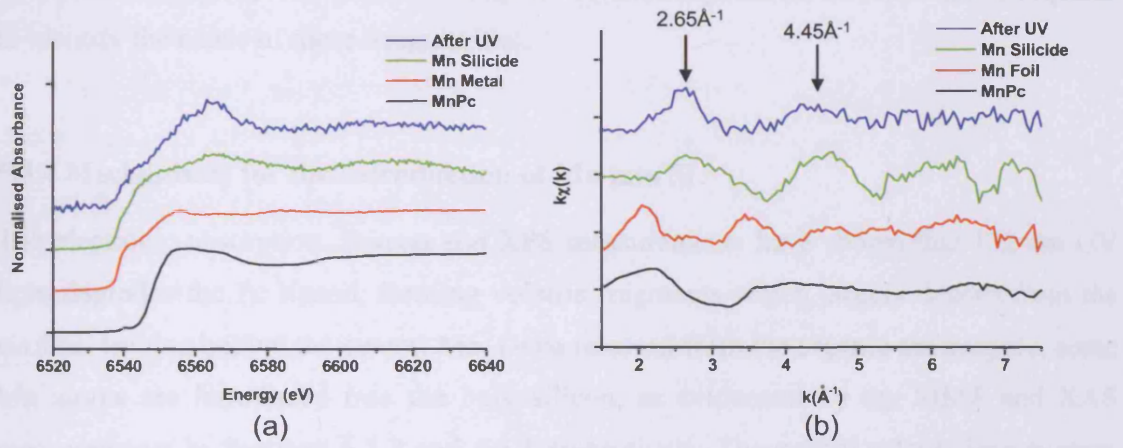

Figure 5.19. *(a) XANES and (b) EXAFS oscillations of MnPc (black), Mn foil (red), Mn silicide (green) and a MnPc film after UV exposure and cleaning (blue). Data are offset for clarity in both cases.*

Although the signal-to-noise ratio was also too low to permit the simulation of the Mn-Si bond distance and co-ordination number, a direct comparison of the EXAFS oscillations is shown in Figure 5.19(b). Once again, the spectrum of the UV-treated MnPc film (after chemically cleaning) is different from that of the starting material (MnPc) and the bulk Mn foil. Instead, the closest agreement is seen between the data with that of the silicide reference, although slight variations are seen, suggesting a difference in the Mn-

Si distance and/or co-ordination number. A very good agreement is found between the positions of the EXAFS oscillations of the experimental data and those reported for ion-implanted Mn in Si, which occur at ~2.7 $Å^{-1}$ and ~4.5 $Å^{-1}$ (these values were read from a graph) [269], further justifying the claim that Mn has been introduced into the silicon lattice.

In summary, the SIMS and XAS measurements demonstrate that Mn is introduced into Si. The closest agreement of the XANES and EXAFS spectra are observed between the post-UV sample and silicide reference. This suggests that the Mn is surrounded by Si and that metal clusters are not formed. Furthermore, analyses of the SIMS profiles show that the Mn atoms occupy interstitial lattice sites, as judged by their diffusional behaviour. However, at present the samples are inhomogeneous; further work is required to identify the cause of these irregularities.

5.3.4 Mechanisms for the Introduction of Mn into Si

The electronic absorption, Raman and XPS measurements have shown that 172 nm UV light degrades the Pc ligand, forming volatile fragments which largely desorb from the surface, leaving behind the central Mn. Once released from the organic macrocycle, some Mn atoms are introduced into the bulk silicon, as evidenced by the SIMS and XAS measurements in Sections 5.3.2 and 5.3.3 respectively. Theoretical calculations suggest that an energy of 2.47 eV (in equilibrium systems) is required to introduce interstitial Mn into clean Si(100) whilst 3.2 eV is needed in the case of Si(100):H [267]. Even though during UV irradiation the system is not in equilibrium, the energy provided by the 172 nm (7.2 eV) UV photons exceeds the required value for effective diffusion of the Mn into Si, regardless of whether the Si-H bonds remain intact. In addition, the UV photons create electron-hole pairs inside the Si lattice which release energy upon recombination. If they recombine near the surface, the energy produced could assist the introduction of Mn into Si, in a process known as recombination enhanced diffusion [159]. Defects in the silicon substrate may also provide pathways that aid Mn incorporation. Once beyond the silicon surface, the large concentration gradient coupled with a high diffusivity of Mn in Si is expected to drive the Mn atoms into the bulk wafer; they would only return to the

surface for temperatures higher than 770°C [270] (far milder conditions were used in this work).

Although care was taken to minimise the time between both HF passivation and transfer to the vacuum deposition chamber, and the subsequent transfer to the UV chamber, it is feasible that a thin native oxide layer may have re-grown. Any oxide layer may hinder diffusion, although a native SiO_2 layer is not expected to be impenetrable (Mn has been observed to diffuse through such a layer [271]). The degree to which Mn diffusion is suppressed is dependent on the diffusion coefficient of Mn in SiO_2 and the segregation coefficient [98]. It is possible that the formation of an inhomogeneous oxide layer may lead to the observed variation in the lateral distribution of Mn in the samples. This non-uniformity may be introduced during surface preparation (for example, grease on the silicon wafer before or after the HF dip), as a result of variations in oxygen migration through the organic film, or due to differences in SiO_2 growth during UV processing (other energetic processes such as thermal annealing are known to result in gaps in the SiO_2 layer that are of the order of tens of microns in diameter [272–274]). The initial MnPc layer has been proven to be of uniform thickness through the electronic absorption and Raman studies, whilst the UV intensity has also been verified to be uniform across the entire sample stage region, and so these are not expected to be responsible for the observed inhomogeneities.

Alternatively, when thin layers of Mn are deposited onto clean silicon surfaces, they can form silicide regions that are up to hundreds of microns in diameter, and are often up to hundreds of nanometers thick [271, 275, 276] (these dimensions could be further enhanced by the energy provided by the UV photons). The highest concentration of Mn obtained from the SIMS depth profiles yields a ratio of Mn:Si of 1:68 (calculated from the known Si unit cell density of 2.33 g/cm^3 [264] giving a silicon concentration of 4.99×10^{22} atoms/cm^3), which is significantly lower than that of stable manganese silicides such as MnSi and $MnSi_{1.7}$. Therefore, the formation of silicides in this case is unlikely. Alternatively, small Mn clusters are often formed in Si [268], however, the presence of such metal-rich clusters has been ruled out by the XAS measurements of Section 5.3.3.

5.4 CONCLUSIONS

Raman and electronic absorption measurements demonstrate that thin MPc films can be degraded in a uniform and highly repeatable way through exposure to 172 nm UV light from an excimer lamp. The quantity of MPc remaining follows an exponential decay which is dependent on the initial film thickness, suggesting the formation of a surface layer. However, this decay was found to be the same for the different MPc species studied (namely MnPc and CuPc) suggesting a similar degradation mechanism for all MPc molecules. Post UV-treatment surface analysis verifies that the majority of the organic material is removed (as evidenced by a drastic reduction in carbon content). This demonstrates that the Pc is ruptured and forms small, volatile fragments that desorb from the surface. This is accompanied with the formation of a MnO surface layer, which proves that the metal is separated from the organic by the UV photons. It is likely that the C-N bonds of the Pc ligand are ruptured first and that the resulting fragmentation destabilises the M-N bond.

Owing to the textured nature of the original MnPc film it is anticipated that after UV irradiation the surface comprises nanosized MnO clusters (as evidenced by the AFM studies). These are likely to be of interest for catalysis or their magnetic properties [265]. In addition, their existence shows that the morphology of the MnPc film is retained; this is encouraging for the use of molecular films as precursors from which to form metallic arrays in Si. Analyses of the silicon wafer after UV treatment and once the MnO surface layer has been removed demonstrate that Mn is also introduced into silicon. SIMS analysis suggests that $69 \pm 14\%$ of the original atoms Mn from the MPc film are incorporated into the Si, whilst time-dependent measurements show that the Mn atoms occupy interstitial lattice sites (as judged by their diffusional behaviour). Furthermore, XAS measurements show that the Mn atoms are diluted in the silicon lattice and do not form metal clusters.

Further optimisation of the processing steps is necessary since the samples are observed to be laterally inhomogeneous. This is likely to be due to irregularities introduced during sample preparation, which may lead to the formation of an irregular

SiO_2 layer, although the inhomogeneity may be assisted by the low solubility of Mn in Si. However, on the whole, the introduction of Mn into Si from an organic layer is very encouraging and validates this new method. It is anticipated that other dopants could be introduced into silicon (or indeed III-V semiconductors) in this manner, and that after further optimisation, arrays of metals containing unpaired electron spins could be created which would be of high significance for spintronic and quantum computing applications (as described in Section 1.4).

Chapter Six: Conclusions

Detailed conclusions have already been given at the ends of Chapters 3, 4 and 5. For this reason, the discussions in this chapter will focus more on the implications of the results obtained towards spintronic applications. These are divided into two paths, as outlined in Section 1.1, namely an all-organic route and a Pc-assisted inorganic route. Conclusions that can be drawn related to the all-organic route, wherein the unpaired spins of intact CuPc molecules are studied, will be given in Section 6.1. The key results for the UV-induced introduction of transition metal dopants into Si from MPc films (as described in Chapter 5) will be summarised in Section 6.2. In addition, a discussion of possible future implications of the work as a whole will be offered in Section 6.3.

6.1. APPLICATIONS OF METAL PHTHALOCYANINE FILMS FOR ORGANIC SPINTRONICS

As seen from Chapters 3 and 4, CuPc readily self-assembles to form highly ordered films when sublimed under vacuum conditions. Studies have shown that the (single-layer) films formed here comprise stacks of molecules with their planes perpendicular to the substrate, forming columns, and that these are of the α-polymorph. One of the most important achievements of this work has been to use continuous wave EPR to characterise the structures of the CuPc films. Furthermore, this technique has been used to study the interactions of unpaired electron spins within the films, specifically to compare those along and between neighbouring columns. Previous work has mainly focussed on powder samples, which does not allow preferential selection of the inter- and intra-column directions, since many domains of different directions are randomly present in any one sample. The Pc film studies presented here address this problem, as preferential directions can be probed in a form that can be directly used for devices.

However, further work is required (and is currently being undertaken*) to unambiguously establish the crystal structure of α-phase CuPc, and to understand the mechanism behind the reduced texture of CuPc films, compared to their H_2Pc counterparts, seen here for the first time.

From these studies it can be deduced that the intra-column interactions are stronger than those between neighbouring columns. This is highly compatible with studies on the electrical conduction in MPc films, which show enhanced conductivity along the stacking directions [222, 223], most likely mediated through π-π interactions [221]. For use in spintronics, it is necessary to combine the electronic and magnetic properties. The CuPc polymorph studied here, namely the α-phase, is known to possess a magnetic signature at low temperatures [37]. Furthermore, the EPR measurements described in Chapter 4 allowed the measurement of *g*-factor of CuPc; this was found to be anisotropic with values of $g_{//} = 2.151$ and $g_{\perp} = 2.047$. The larger *g*-factor in the direction of molecular stacking ($g_{//}$) corresponds to a larger magnetic moment along this direction, as expressed in Equation 6.1 (where μ is the magnetic moment, μ_B is the Bohr magneton, S is the spin of ($S = 1/2$) and $\hbar$ is Planck's constant).

$$\mu = \mu_B g\left(\frac{S}{\hbar}\right) \qquad [6.1]$$

The stronger magnetic moment of CuPc along the column direction is likely to aid retention of the electron spin polarization as the charges flow through the film. This renders CuPc films, and more generally MPc films containing unpaired electron spins, excellent candidates for spintronic applications.

The ability to co-deposit magnetic and non-magnetic Pc molecules to form crystalline films is also of significance. By diluting CuPc molecules in a H_2Pc matrix their spatial separation enters the regime desired for quantum computing applications,

* A detailed analysis of the crystal structure based on diffraction is being undertaken by Soumaya Mauthoor and Dr. Sandrine Heutz.

wherein the Cu spins could act as qubits. The average spacings could be tailored through control of the relative deposition rates of CuPc and H_2Pc, whilst the randomness of such a system is advantageous for the model proposed by Stoneham *et al.* [155]. As mentioned in Section 4.4, initial measurements on the lifetimes of the Cu spins in the 5% CuPc:H_2Pc films suggest that they are sufficiently long-lived to perform quantum algorithms. Furthermore, co-deposition could be used to adapt the magnetic properties of the films. For example, as discussed in Section 1.3.2, the dilution of antiferromagnetic CoPc:H_2Pc crystallites is known to reduce the Neel temperature [232], whilst doping with group I species is also known to induce changes to MPc magnetism [135, 136].

The work described in Chapter 4 could be directly applied to ultra-thin systems of CuPc on passivated Si surfaces since, even at the monolayer scale, an arrangement similar to the α-phase is observed, as described in Chapter 3. The STM studies highlighted that on these surfaces, CuPc islands are formed with a preferential alignment along the [110] directions of the Si lattice. Preferential domain directionality is advantageous for device applications due to the existence of in-built spin transport directions (the direction of conductance along the columns would be known with respect to the substrate directions). Furthermore, larger domains would enhance the efficiency of spin coherence, since losses are likely to occur at domain boundaries. In Section 3.1, larger domains were observed on Si(100):NH_3 rather than Si(100):H, and this was attributed to a repulsive interaction between the NH_3 surface (specifically the N lone pair) and the Pc ligand, increasing the mobility of CuPc on this surface. Therefore, by tailoring the chemical interactions between CuPc and the passivating species, it may be possible to grow even larger domains.

As shown in Section 4.2, deposition of CuPc onto PTCDA results in the formation of flat-lying molecular arrays. Unlike for the single-layer films, wherein the column length is limited by molecular mobility on the substrate and the presence of other domains, longer stacking chains are possible for CuPc/PTCDA systems since their growth is unrestricted and so can increase as a function of film thickness. Again, this is important for device applications since such a morphology offers potential for longer spin pathlengths within the film. Furthermore, it was observed that the face-to-face molecular

separation for these films is less than for the bulk α-phase, whilst the EPR investigations suggest that the molecular columns are more separated. This implies that spin conservation along the columns for the CuPc/PTCDA films is likely to be more efficient than in the single layer films. It would be possible to capitalise on this feature by designing multilayered spintronics devices, as will be discussed in Section 6.3.

6.2. APPLICATIONS OF METAL PHTHALOCYANINE FILMS AS PRECURSORS FOR INORGANIC SPINTRONICS

A new route for the introduction of spin-containing metallic elements into silicon was described in Chapter 5. Here, transition metal Pc films were grown on Si substrates and subsequently exposed to UV irradiation, which degraded the MPc molecules. This process was shown to occur for both CuPc and MnPc films, demonstrating its versatility (different dopant species could be introduced, which is important for potential applications, as will be described in Section 6.3). Comparisons of the bond dissociation energies within the MPc molecules suggest that the C-N bonds are the most likely to be broken first. This is expected to destabilise the metal-N bond such that its binding energy is lower than the 7.21 eV provided by the 172 nm photons, and so the metal can be released from the organic.

For the specific example of MnPc, it was shown that the metal atoms released from the MPc film either form a metal oxide surface layer, or diffuse into the Si substrate. The former case was demonstrated by the presence of MnO (as evidenced by XPS and XAS studies). Although this is not the desired product for the applications in mind here, it is anticipated that the small MnO clusters formed could have a range of interesting magnetic and catalytic applications [265]. It is feasible that performing these experiments in-situ in a UHV environment would lead to a lower yield of metal oxide (less oxygen would be present). However, the studies described in Section 5.3 showed that this layer can be easily removed by a simple cleaning procedure, and so its formation is not detrimental to the production of the metal-doped silicon wafers.

Analyses of the substrates after UV treatment have demonstrated that the metal species are incorporated into Si. XAS measurements have shown that, at least for the particular example of Mn studied in Chapter 5, metal clusters are not formed and that the Mn atoms are isolated within the Si lattice. This alone is an important result for applications such as quantum computing wherein the dopants would act as qubits; these must be spatially separated in order for their interactions to be controlled. The observed diffusional behaviour of the Mn atoms suggests that they occupy interstitial lattice sites. As mentioned in Section 1.4.1, interstitial Mn gives rise to magnetic ordering [110] and so could be used for inorganic spintronic applications. Analysis of the SIMS data suggests that an approximate yield from the original MPc layer of ~55-83% is currently achieved. It is anticipated that a higher yield could be obtained from monolayer films. Furthermore, the concentration of dopants could be controlled by varying the initial film thickness or density (via co-deposition with H_2Pc, as described in Section 4.3, or by using a different metallorganic precursor).

Currently, the metal distribution is laterally inhomogenous. It is anticipated that this is due to irregularities introduced during sample preparation. Studies have not yet been performed to investigate whether the original order of the MPc film is retained within the silicon (future experiments will be discussed in Section 6.3), although it is anticipated that the conditions used in Chapter 5 would lead to linear arrays. However, the work described here is very promising for the development of this technique as a low temperature, low cost method for the introduction of dopants into Si, and so even in its current state is likely to be of high interest to the inorganic spintronics community.

6.3. IMPLICATIONS FOR FUTURE WORK

This section will comprise two sub-sections. A brief overview of future experiments (some of which are currently being performed) that could provide further insights into the use of MPc films for spintronic applications will be given in Section 6.3.1. This will be followed in Section 6.3.2 by new ideas for the creation of MRAM devices from MPc films, based on the findings of Chapters 3, 4 and 5.

6.3.1 Future Work

Although it has been found that MPc films are very promising for spintronic applications, much work is still required to create actual devices. Preliminary studies have shown that multilayered structures of CuPc and H_2Pc can be grown, and that it would be possible to produce successive magnetic and paramagnetic Pc layers. Such systems could be used as MPc-based spin transistors. On a more fundamental level, it would be of interest to build on the knowledge gained in the magnetic properties of such films by studying more MPc systems with different spin states. For example, we have already established that α-phase CuPc films are antiferromagnetic, whilst β-phase MnPc films are ferromagnetic. It therefore seems likely that other transition metal Pc films may also couple magnetically. As has been shown in Chapter 4, co-deposition of CuPc and H_2Pc leads to the formation of randomly mixed films. It is anticipated that such a dilution could lead to control over the magnetic properties of MPc films (such an investigation is currently underway). Also of interest is the optical excitation of MPc films; occupation of the LUMO level is likely to modify the magnetic properties of MPc systems (the magnetic coupling is known to be due to orbital overlap [37]), whilst the creation of triplet states from the Pc ligand is expected to affect the electrical conductance and magnetic properties.

As outlined in Chapter 5, the use of UV irradiation to introduce metal dopants into silicon is very promising for a wide range of potential applications. Although it has been demonstrated that this procedure does lead to the inclusion of Mn in Si, further work is required to improve the homogeneity of the samples. In addition, for some applications it is of interest to form arrays of metals in Si. Current methods involve manipulating Mn atoms with an STM tip on semiconductor surfaces [97], however, such an approach is not readily scalable for device applications. Although retention of order from the MPc film has not yet been demonstrated, encouragingly, AFM measurements have shown that the general domain structure is maintained. Grazing incidence x-ray measurements are planned to determine whether ordered metal arrays are present after introduction into the Si lattice. In addition, modification of the current experimental set-up for low temperature operation would be required to study arrays of fast diffusing species such as Mn, whilst

in-situ experiments would allow for a greater control over conditions. It is also of interest to demonstrate the introduction of other metal species into Si, and from other metalorganic species; it is anticipated that these could lead to a new routes for the fabrication of silicon-based dilute magnetic semiconductors.

6.3.2 MPc routes to MRAM devices

This section will outline a potential route for capitalising on the potential of MPc thin films for spintronic applications. As described in Section 1.3.1, MRAM devices would be advantageous since they would allow the writing and re-writing of data with faster read-out times than current ROM devices. Phthalocyanine films have the potential (either directly or indirectly) to create devices comprising regions of different magnetic properties. For example, this could be achieved via MPc deposition through a mask (in a similar route to that followed for depositing photoresists in current silicon manufacturing) to create patches of MPc films with different coercive fields. It has already been shown that β-phase MnPc films are ferromagnetic [37] and so it is feasible that other ferromagnetic MPc film regions could be created, as will be discussed shortly. Alternatively, through the creation of patches of different MPc species on Si and subsequently irradiating with UV photons, regions of dilute magnetic semiconductors each with different magnetic properties could be produced [104, 277–279].

The ability to generate domains with different magnetic properties and with high spatial resolution allows the design of complex and potentially very powerful MRAM assemblies. A proposed general approach to such an MPc based MRAM device, inspired by the results obtained in this work, is outlined in Figure 6.1. The figure shows three patches (blue, pink and green squares), each representing well-defined regions of different coercive fields, separated by ferromagnetic contacts (which are all of the same magnetisation direction). A current is injected through the first ferromagnetic layer (A) and this creates a spin polarised current that passes across the device. In a similar method to the spin valve (Figure 1.9), the current can only flow across each domain if it is aligned parallel to the magnetisation direction of A. If the magnitudes of the coercive fields of each patch are ordered such that $H_{C1} > H_{C2} > H_{C3}$, then applications of small

magnetic fields downwards in the plane of the device would act to selectively rotate one, two or all three of the magnetic domains. This could be read out by measuring the current flow at the contacts B, C and D. Such a model could be extended to a two dimensional array.

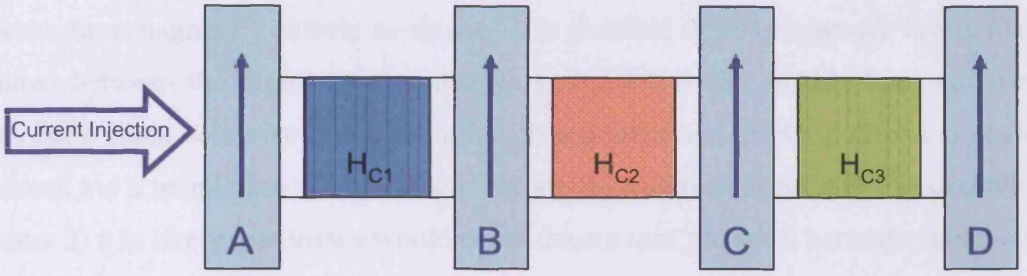

Figure 6.1. *A possible MRAM device. Domains of different coercive fields created either directly or indirectly from MPc films (H_{C1}, H_{C2} and H_{C3}) are separated by ferromagnetic contacts (A-D). Current is injected from the left, as shown. Through the application of a small in-plane magnetic field, the domain directions of the successive regions could be manipulated, thus changing the charge transfer across the device. Spacer layers (white) may be necessary to prevent the ferromagnetic contacts from magnetising the low coercivity regions.*

All-organic Route

It has already been commented upon that our discovery of switchable and structure dependent magnetic interactions in CuPc and MnPc films is very promising for the potential of MPc films in spintronic applications, whilst a theoretical understanding of the magnetic ordering in these systems is already in place (as demonstrated for α- and β-phase CuPc) [37]. The EPR measurements in Section 4.3 showed that randomly mixed CuPc:H_2Pc films can be easily grown by OMBD. Furthermore, it is possible to modify the magnetic ordering of MPc arrays through dilution in an H_2Pc matrix [232], whilst

doping of CuPc crystallites with Na leads to ferromagnetism with Curie temperatures greater than 77 K [135]. Therefore, it is plausible that through a combination of theoretical and experimental effort it would be possible to identify and produce MPc films with different magnetic properties, specifically ferromagnetic films with different coercive fields.

One approach could be to create devices in a similar manner to that proposed in Figure 6.1. Here, masking could be used to selectively deposit different MPc regions between ferromagnetic contacts as shown (it is possible that H_2Pc spacer layers may be required between the regions and contacts). However, as has already been commented upon, MPc films comprise domains; although a preferential stacking direction could by produced via a templating effect to the substrate (in a similar manner to that described in Chapter 3) it is likely that losses would occur during spin transport between neighbouring domains and this would lower the efficiency of the device. Perhaps a more appealing approach would be to build a layered device, capitalising on the molecular templating effect described in Chapter 4 for MPc/PTCDA films, to create vertical molecular columns. Successive MPc layers of different coercivity, each sandwiched between ferromagnetic conducting layers, would benefit from the enhanced intra-column spin transport anticipated for these systems (compared to the single layer α-phase films). For such a layer-by-layer device growth method, alkali metal dopants such as Li or Na could be introduced during deposition to also modify the magnetic properties of each layer (as discussed in Section 1.3.2) [135, 136]. However, care would need to be taken to ensure that dopant diffusion was minimised (this might be controlled using the aforementioned ferromagnetic metal layers).

Inorganic Route

As demonstrated in Chapter 5, irradiation of MPc films with UV light can be used to introduce dopants into silicon. Isolated MPc film regions on silicon comprising different metallic species could be formed, either by masking, or adding chemical substituents to the Pc ligand to enforce phase segregation. Subsequent UV irradiation at low temperature could then be used to introduce the metal species into the substrate whilst retaining the

segregation of the domains (this would not be possible for fast diffusing species using techniques that require annealing). Application of a magnetic field could then be used to control the relative magnetization directions of each region, since each of these would have a different coercive field [104, 277–279], in a similar manner to that described previously. Apart from being readily compatible with existing silicon technologies, this method would also capitalise on the large coherent spin diffusion lengths within Si [3].

Interestingly, the formation of metal oxides by UV irradiation of MPc films (as described in Section 5.2) could also be used in a similar device structure. Metal oxides, particularly when doped with transition metals, are of high interest as dilute magnetic semiconductors [280–284]. These generally display strong magnetic signatures, even at room temperature, and a wide variety of such systems have already been identified. Therefore, the creation of regions of different magnetic oxides by the irradiation of MPc films in an oxygen rich environment could lead to the production of MRAM devices (in a similar method to that outlined in Figure 6.1). Such a system might be easier to study than the others suggested here since measurements could be performed at room temperature (for example, these could be analysed by magnetic force microscopy).

References

[1] N. B. McKeown, *Phthalocyanine Materials; synthesis, structure and function*, Cambridge University Press, Cambridge (1998).

[2] S. A. 83, D. D. Awschalom, R. A. Buhrman, J. M. Daughton, S. von Molnar, M. L. Roukes, A. Y. Chtchelkanova, D. M. Treger, *Science* **294** (2001) 1488.

[3] I. Zutic, J. Fabian, S. Das Sarma, *Rev. Mod. Phys.* **76** (2004) 323.

[4] C. Reese, Z. N. Bao, *Mater. Today* **10** (2007) 20 .

[5] Q. Tang, H. Li, M. He, W. Hu, C. Liu, K. Chen, C. Wang, Y. Liu, D. Zhu, *Adv. Mater.* **18** (2006) 65.

[6] J. Xue, S. Uchida, B. P. Rand, S. R. Forrest, *Appl. Phys. Lett.* **84** (2004) 3013.

[7] F. Garnier, R. Hajlaoui, A. Yassar, P. Srivastava, *Science* **265** (1994) 1684.

[8] S. R. Forrest, *Nature* **428** (2004) 911.

[9] G. E. Moore, *Electronics* **38** (1965).

[10] S. Sanvito, *J. Mater. Chem.* **17** (2007) 4455.

[11] W. J. M. Naber, S. Faez, W. G. van der Wiel, *J. Phys. D: Appl. Phys.* **40** (2007) R205.

[12] A. Braun, J. Tcherniac, *Ber. Dtsch. Chem. Ges.* **40** (1907) 2709.

[13] H. de Diesbach, E. von der Weid, *Helvetica Chimica Acta* **10** (1927) 886.

[14] G. Dufour, C. Poncey, F. Rochet, H. Roulet, S. Iacobucci, M. Sacchi, F. Yubero, N. Motta, M. N. Piancastelli, A. Sgarlata, M. De Crescenzi, *J. Elect. Spect. Rel. Phen.* **76** (1995) 219.

[15] M. Calvete, M. Hanack, *Eur. J. Org. Chem.* (2003) 2080.

[16] A. Lyubimtsev, S. Vagin, S. Syrbu, M. Hanack, *Eur. J. Org. Chem.* (2007) 2000.

[17] S. Makarov, C. Litwinski, E. A. Ermilov, O. Suvorova, B. Roder, D. Wohrle, *Chem. Eur. J.* **12** (2006) 1468.

[18] D. Voss, *Nature* **407** (2000) 442.

[19] C. J. Liu, J. J. Shih, Y. H. Ju, *Sens. Actuators B* **99** (2004) 344.

[20] Y. Lee, C. Sheu, R. Hsiao, *Sens. Actuators B* **99** (2004) 344.

[21] M. Bouvet, G. Guillaud, A. Leroy, A. Maillard, S. Spirkvitch, F. Tournilhac, *Sens. Actuators B* **73** (2001) 63.

[22] A. Altindal, Z. Z. Ozturk, S. Dabak, O. Bekaroglu, *Sens. Actuators B* **77** (2001) 389.

[23] M. Bora, D. Schut, M. A. Baldo, *Anal. Chem.* **79** (2007) 3298.

[24] J. Xue, B. P. Rand, S. Uchida, S. R. Forrest, *Adv. Mater.* **17** (2005) 66.

[25] C-H. Liao, M-T. Lee, C-H. Tsai, C. H. Chen, *Appl. Phys. Lett.* **86** (2005) 203507.

[26] S. A. Van Slyke, C. H. Chen, C. W. Tang, *Appl. Phys. Lett.* **69** (1996) 2160.

[27] M. Ashida, N. Uyeda, E. Suito, *Bull. Chem. Soc. Jpn.* **39** (1966) 2616.

[28] A. Hoshino, Y. Takenaka, H. Miyaji, *Acta. Cryst.* **B59** (2003) 393.

[29] F. Iwatsu, *J. Phys. Chem.* **92** (1988) 1678.

[30] J. H. Sharp, M. Abkowitz, *J. Phys. Chem.* **77** (1973) 477.

[31] M. K. Debe, K. K. Kam, *Thin Solid Films* **186** (1990) 289.

[32] S. M. Bayliss, S. Heutz, G. Rumbles, T. S. Jones, *Phys. Chem. Chem. Phys.* **1** (1999) 3673.

[33] O. Berger, W-J. Fischer, B. Adolphi, S. Tierbach, V. Melev, J. Schreiber, *J. Mater. Sci.: Mater. Electron.* **11** (2000) 331.

[34] S. Heutz, S. M. Bayliss, R. L. Middleton, G. Rumbles, T. S. Jones, *J. Phys. Chem. B* **104** (2000) 7124.

[35] L. Fenenko, C. Adachi, *Thin Solid Films* **515** (2007) 4812.

[36] C. J. Brown, *J. Chem. Soc. A* (1968) 2488.

[37] S. Heutz, C. Mitra, W. Wu, A. J. Fisher, A. Kerridge, A. M. Stoneham, T. H. Harker, J. Gardener, H-H. Tseng, T. S. Jones, C. Renner, G. Aeppli, *Adv. Mater.* **19** (2007) 3618.

[38] L. Edwards, M. Gouterman, *J. Mol. Spectr.* **33** (1970) 292.

[39] P. S. Vincett, E. M. Voigt, K. E. Rieckhoff, *J. Chem. Phys.* **55** (1971) 4131.

[40] Y. Sakakibara, R. N. Bera, T. Mizutani, K. Ishida, M. Tokumoto, T. Tani, *J. Phys. Chem. B* **105** (2001) 1547.

[41] B. P. Rand, J. Xue, S. Uchida, S. R. Forrest, *J. Appl. Phys.* **98** (2005) 124902.

[42] T. Gunaratne, V. O. Kennedy, M. E. Kenney, M. A. J. Rodgers, *J. Phys. Chem. A* **108** (2004) 2576.

[43] J. D. Wright, *Molecular Crystals*, 2nd Edition, Cambridge University Press, Cambridge, (1995).

[44] A. A. M. Farag, *Opt. Laser Technol.* **39** (2007) 728.

[45] A. T. Davidson, *J. Chem. Phys.*, **77** (1982) 168.

[46] B. R. Hollebone, M. J. Stillman, *J. Chem. Soc. Faraday Trans. II*, **74** (1978) 2107.

[47] D. Li, Z. Peng, L. Deng, Y. Shen and Y. Zhou, *Vibrational Spectroscopy* **39** (2005) 191.

[48] D. R. Tackley, G. Dent, W. E. Smith, *Phys. Chem. Chem. Phys.* **3** (2001) 1419.

[49] W. Y. Tong, A. B. Djurisic, M. H. Xie, A. C. M. Ng, K. Y. Cheung, W. K. Chan, Y. H. Leung, H. W. Lin, S. Gwo, *J. Phys. Chem. B* **110** (2006) 17206.

[50] H. Peisert, T. Schweiger, J. M. Auerhammer, M. Knupfer, M. S. Golden, J. Fink, P. R. Bressler, M. Mast, *J. Appl. Phys.* **90** (2001) 466.

[51] L. Ottaviano, L. Lozzi, S. Santucci, S. Di Nardo, M. Passacantando, *Surf. Sci.* **392** (1997) 52.

[52] Y. Maeda, T. Matsumoto, M. Kasaya, T. Kawai, *Jpn. J. Appl. Phys.* **35** (1996) L405.

[53] M. Kanai, T. Kawai, K. Motai, X. D. Wang, T. Hashizume, T. Sakura, *Surf. Sci.* **329** (1995) L619.

[54] I. Chizhov, G. Scoles, A. Kahn, *Langmuir* **16** (2000) 4358.

[55] X. Lu, K. W. Hipps, X. D. Wang, U. Mazur, *J. Am. Chem. Soc.* **118** (1996) 7197.

[56] K. W. Hipps, X. Lu, X. D. Wang, U. Mazur, *J. Phys. Chem.* **100** (1996) 11207.

[57] P. H. Lippel, R. J. Wilson, M. D. Miller, C. Woll, S. Chiang, *Phys. Rev. Lett.* **62** (1989) 171.

[58] S. Yim, T. S. Jones, *J. Phys.: Condens. Matter* **15** (2003) S2631.

[59] C. Ludwig, R. Strohmaier, J. Petersen, B. Gompt, W. Eisenmenger, *J. Vac. Sci. Technol. B* **12** (1994) 1963.

[60] S. D. Wang, X. Dong, C. S. Lee, S. T. Lee, *J. Phys. Chem. B* **108** (2004) 1529.

[61] A. C. Brieva, T. E. Jenkins, D. G. Jones, F. Strossner, D. A. Evans, G. F. Clark, *J. Appl. Phys.* **99** (2006) 073504.

[62] E. Bauer, *Zeit. Krist.* **110** (1958) 372.

[63] M. Kasaya, H. Tabata, T. Kawai, *Surf. Sci.* **406** (1998) 302.

[64] L. Wang, D. Qi, L. Liu, S. Chen, X. Gao, A. T. S. Wee *J. Phys. Chem. C.* **111** (2007) 3454.

[65] M. Komiyama, Y. Sakakibara, H. Hirai, *Thin Solid Films* **151** (1987) L109.

[66] A. K. Hassan, R. D. Gould, *Phys. Stat. Sol. A* **132** (1992) 91.

[67] M. D. Upward, P. H. Beton, P. Moriarty, *Surf. Sci.* **441** (1999) 21.

[68] N. Nakamura, Y. Morita, Y. Mori, A. Ishitani, H. Tokumoto, *J. Vac. Sci. Technol. B* **14** (1996) 1109.

[69] M. Gorgoi, W. Michaelis, T. U. Kampen, D. Schlettwein, D. R. T. Zhan, *Appl. Surf. Sci.* **234** (2004) 138.

[70] Y. Suzuki, M. Hietschold, D. R. T. Zahn, *Appl. Surf. Sci.* **252** (2006) 5449.

[71] D. P. Woodruff, T. A. Dechar, *Modern Techniques of Surface Science*, 2nd Edition, Cambridge University Press, Cambridge (1994).

[72] J. Gardener, J. H. G. Owen, K. Miki, S. Heutz, *Surf. Sci.* **602** (2008) 843.

[73] http://www.chem.qmul.ac.uk/surfaces/scc/scat1_6a.htm

[74] L. Lozzi, L. Ottaviano, F. Rispoli, P. Picozzi, S. Santucci, *Surf. Sci.* **433-435** (1999) 157.

[75] T. Nonaka, Y. Nakagawa, Y. Mori, M. Hirai, T. Matsunobe, M. Nakamura, T. Takahagi, A. Ishitani, H. Lin, K. Koumoto, *Thin Solid Films* **256** (1995) 262.

[76] M. Nakamura, H. Tokumoto, *Surf. Sci.* **377-379** (1997) 85.

[77] M. Nakamura, H. Tokumoto, *Surf. Sci.* **398** (1998) 143.

[78] G. P. Lopinski, D. D. M. Wayner, R. A. Wolkow, *Nature* **406** (2000) 48.

[79] M. C. Hersam, N. P. Guisinger, J. W. Lyding, *Nanotechnology* **11** (2000) 70.

[80] M. C. Hersam, N. P. Guisinger, J. W. Lyding, *J. Vac. Sci. Technol. A* **18** (2000) 1349.

[81] P. S. Peercy, *Nature* **406** (2000) 1023.

[82] D. D. Awschalom, M. E. Flatte, *Nature Phys.* **3** (2007) 153.

[83] S. A. 83, A. Y. Chtchelkanova, D. M. Treger, *J. Res. & Dev.* **50** (2006) 101.

[84] C. Chappert, A. Fert, F. van Dau *Nature Mater.* **6** (2007) 813.

[85] M. Biabich, J. Broto, A. Fert, F. v. Dau, F. Petroff, P. Etienne, G. Greuzet, A. Friederich, J. Chazelas, *Phys. Rev. Lett.* **61** (1988) 2472.

[86] G. Binash, P. Grunberg, F. Saurenbach, W. Zinn, *Phys. Rev. B* **39** (1989) 4828.

[87] J. S. Moodera, L. R. Kinder, T. M. Wong, R. Meservey, *Phys. Rev. Lett.* **74** (1995) 3273.

[88] T. Miyazaki, N, Tezuka, *J. Magn. Magn. Mater.* **139** (1995) L231.

[89] S. S. P. Parkin, C. Kaiser, A. Panchula, P. M. Rice, B. Hughes, M. Samant, S-H. Yang, *Nature Mater.* **3** (2004) 862.

[90] J. M. Daughton, *J. Appl. Phys.* **81** (1997) 3758.

[91] H. J. Zhu, M. Ramsteiner, H. Kostial, M. Wassermeier, H. P. Schonherr, K. H. Ploog, *Phys. Rev. Lett.* **87** (2001) 016601.

[92] X. Lou, C. Adelmann, S. A. Crooker, E. S. Garlid, J. Zhang, K. S. M. Reddy, S. D. Flexner, C. J. Palmstrom, P. A. Crowell, *Nature Phys.* **3** (2007) 542.

[93] V. F. Motsnyi, J. De Boeck, J. Das, W. Van Roy, G. Borghs, E. Goovaerts, V. I. Safarov *Appl. Phys. Lett.* **81** (2002) 265.

[94] R. Fiederling, M. Kleim, G. Reuscher, W. Ossau, G. Schmidt, A. Waag, L. W. Molenhamp, *Nature* **402** (1999) 787.

[95] B. T. Jonker, Y. D. Park, B. R. Bennett, H. D. Cheong, G. Kioseoglou, A. Petrou, *Phys. Rev. B* **62** (2000) 8180.

[96] F. Matsukura, H. Ohno, A. Shen, Y. Sugawara, *Phys. Rev. B* **57** (1998) R2037.

[97] D. Kitchen, A. Richardella, J-M. Tang, M. E. Flatte, A. Yazdani, *Nature* **442** (2006) 436.

[98] S. M. Sze, *Semiconductor Devices Physics and Technology*, John Wiley & Sons,, New Jersey (1985).

[99] G. Schmidt, D. Ferrand, L. W. Molenhamp, A. T. Filip, B. J. van Wees, *Phys. Rev. B* **62** (2000) R4790.

[100] I. Applebaum, B. Huang, D. J. Monsma, *Nature* **227** (2007) 295.

[101] A. Fert, H. Jaffres, *Phys. Rev. B* **64** (2002) 184420.

[102] B-C-Min, K. Motohashi, C. Lodder, R. Jansen, *Nature Mater.* **5** (2006) 817.

[103] B. T. Jonker, G. Kioseoglou, A. T. Hanbicki, C. H. Li, P. E. Thompson, *Nature Phys.* **3** (2007) 542.

[104] M. Bolduc, C. Awo-Affouda, A. Stollenwerk, M. B. Huang, F. G. Ramos, G. Agnello, V. P. LaBella, *Phys. Rev. B* **71** (2005) 033302.

[105] Y. H. Kwon, T. W. Kang, H. Y. Cho, T. W. Kim, *Sol. State Comm.* **136** (2005) 257.

[106] I. T. Yoon, C. J. Park, T. W. Kang, *J. Magn. Magn. Mater.* **311** (2007) 693.

[107] T. Dietl, H. Ohno, F. Matsukura, *Phys. Rev. B* **63** (2001) 195205.

[108] S. C. Erwin, A. G. Petukhov, *Phys. Rev. Lett.* **89** (2002) 227201.

[109] G. M. Dalpian, A. J. R. da Silva, A. Fazzio, *Phys. Rev. B* **68** (2003) 113310.

[110] H. Wu, P. Kratzer, M. Scheffler, *Phys. Rev. Lett.* **98** (2007) 117202.

[111] C. Awo-Affouda, M. Bolduc, V. P. LaBella, *J. Vac. Sci. Technol. A* **25** (2007) 976.

[112] S. Sanvito *Nature Mater.* **6** (2007) 803.

[113] L. Bogani, W. Wernsdorfer *Nature Mater.* **7** (2008) 179.

[114] O. Mermer, G. Veeraraghavan, T. L. Francis, Y. Sheng, D. T. Nguyen, M. Wohlgenannt, A. Kohler, M. K. Al-Suti, M. S. Kahn, *Phys. Rev. B* **72** (2005) 205202.

[115] O. Mermer, G. Veeraraghavan, T. L. Francis, M. Wohlgenannt, *Solid. State Commun.* **134** (2005) 631.

[116] N. Tombros, C. Jozsa, M. Popinciuc, H. T. Jonkman, B. J. van Wees, Nature 448 (2007) 571.

[117] V. Dediu, M. Murgia, F. C. Matacotta, C. Taliani, S. Barbanera, *Solid State Commun.* **122** (2002) 181.

[118] Z. H. Xiong, D. Wu, Z. V. Vardeny, J. Shi, *Nature* **427** (2004) 821.

[119] M. Ouyang, D. D. Awschalom, *Science* **301** (2003) 1074.

[120] J. R. Petta, S. K. Slater, D. C. Ralph, *Phys. Rev. Lett.* **93** (2004) 136601.

[121] A. R. Rocha, V. M. Garcia-Suarez, S. W. Bailey, C. J. Lambert, J. Ferrer, S. Sanvito, *Nature Mater.* **4** (2005) 335.

[122] S. Majumdar, R. Laiho, P. Laukkanen, I. J. Vayrynrn, H. R. Majumdar, R. Osterbacka, *Appl. Phys. Lett.* **89** (2006) 122114.

[123] L. E. Heuso, I. Bergenti, A. Riminucci, Y. Zhan, V. Dediu, *Adv. Mater.* **19** (2007) 2639.

[124] T. S. Santos, J. S. Lee, P. Migdal, I. C. Lekshmi, B. Satpati, J. S. Moodera, *Phys. Rev. Lett.* **98** (2007) 016601.

[125] J. S. Jiang, J. E. Pearson, S. D. Bader, *Phys. Rev. B* **77** (2008) 035303.

[126] R. Liu, S-H. Ke, H. U. Baranger, W. Yang, *Nano Lett.* **5** (2005) 1959.

[127] N. E. Chakov, S-C Lee, A. G. Harter, P. L. Kuhns, A. P. Reyes, S. O. Hill, N. S. Dalal, W. Wernsdorfer, K. A. Abboud, G. Christou, *J. Am. Chem. Soc.* **128** (2006) 6975.

[128] C. J. Milios, A. Vinslava, W. Wernsforfer, S. Moggach, S. Parsons, S. P. Perlepes, G. Christou, E. K. Brechin, *J. Am. Chem. Soc.* **129** (2007) 2754.

[129] A. N. Pasupathy, R. C. Bialczak, J. Martinek, J. E. Grose, L. A. K. Donev, P. L. McEuen, D. C. Ralph, *Science* **306** (2004) 86.

[130] C. Timm, F. Elste, *Phys. Rev. B* **73** (2006) 235304.

[131] H. Wende, M. Bernien, J. Luo, C. Sorg, N. Ponpandian, J. Kurde, J. Miguel, M. Piantek, X. Xu, P. H. Eckhold, W. Kuch, K. Baberschke, P. M. Panchmatia, B. Sanyal, P. M. Oppeneer, O. Eriksson, *Nature Mater.* **6** (2007) 516.

[132] A. Scheybal, T. Ramsvik, R. Bertschinger, M. Putero, F. Nolting, T. A. Jung, *Chem. Phys. Lett.* **411** (2005) 214.

[133] D. Gatteschi, *Nature Mater.* **6** (2007) 471.

[134] P. Liljeroth, J. Repp, G. Meyer, *Science* **317** (2007) 1203.

[135] E. G. Sharoyan, A. S. Manukyan, *J. Porphyrins Phthalocyanines* **9** (2005) 846.

[136] Y. Taguchi, T. Miyake, S. Margadonna, K. Kato, K. Prassides, Y. Iwasa, *J. Am. Chem. Soc.* **128** (2006) 3313.

[137] M. F. Craciun, S. Rogge, A. F. Morpurgo *J. Am. Chem. Soc.* **127** (2005) 12210.

[138] R. Neiman, D. Kivelson *J. Chem. Phys.* **35** (1961) 156.

[139] I. Chen, M. Abkowitz, J. H. Sharp, *J. Chem. Phys.* **50** (1969) 2237.

[140] C. M. Guzy, J. B. Raynor, M. C. R. Symons, *J. Chem. Soc. A* (1969) 2299.

[141] M. Abkowitz, I. Chen, J. H. Sharp, *J. Chem. Phys.* **48** (1968) 4561.

[142] M. Abkowitz, I. Chen, *J. Chem. Phys.* 54 (1971) 811.

[143] J. M. Assour, *J. Phys. Chem.* **69** (1965) 2295.

[144] S. P. Greiner, D. L. Rowlands, R. W. Krellek, *J. Phys. Chem.* **96** (1992) 9132.

[145] C. Finazzo, C. Calle, S. Stoll, S. van Doorslaer, A. Schweiger, *Phys. Chem. Chem. Phys.* **8** (2006) 1942.

[146] D. P. DiVicenzo, *IBM* (2000) arXic:quant-ph/000207v3.

[147] D. Leibfried, E. Knill, S. Seidelin, J. Britton, R. B. Blakestad, J. Chiaverini, D. B. Hume, W. M. Hano, J. D. Jost, C. Langer, R. Ozeri, R. Reichle, D. J. Wineland, *Nature* **438** (2005) 639.

[148] M. Steffen, M. Ansmann, R. C. Bialczak, N. Katz, E. Lucero, R. McDermott, M. Neeley, E. M. Weig, A. N. Cleand, J. M. Martinis, *Science* **313** (2006) 1423.

[149] A. O. Niskanen, K. Harrabi, F. Yoshihara, Y. Nakamura, S. Lloyd, J. S. Tsai, *Science* **316** (2007) 723.

[150] J. Majer, J. M. Chow. J. M. Gambetta, J. Koch, B. R. Johnson, J. A. Schreier, L. Frunzio, D. I. Schuster, A. A. Houck, A. Wallraff, A. Blais, M. H. Devoret, S. M. Girvin, R. J. Schoelkopf, *Nature* **449** (2007) 443.

[151] X. Li, T. H. Stievater, D. G. Steel, D. Gammon, D. S. Katzer, D. Park, C. Piermarocchi, L. Sham, *Science* **301** (2003) 809.

[152] P. M. Platzman, M. I. Dykman, *Science* **284** (1999) 1967.

[153] S. C. Benjamin, A. Ardavan, G. A. D. Briggs, D. A. Britz, D. Gunlycke, J. Jefferdon, M. A. G. Jones, D. F. Leigh, M. W. Lovett, A. N. Khlobystov, A. A. Lyon, J. J. L. Morton, K. Porfyrakis, M. R. Sambrook, A. M. Tyryshkin, *J. Phys. Cond. Matter* **18** (2006) S867.

[154] W. Harneit, *Phys. Rev. A* **65** (2002) 032322.

[155] A. M. Stoneham, A. J. Fisher, P. T. Greenland, *J. Phys. Cond. Matter* **15** (2003) L447.

[156] H. Ennen, G. Pomrenke, A. Axmann, K. Eisele, W. Haydl, J. Schneider, *Appl. Phys. Lett.* **46** (1985) 381.

[157] A. J. Kenyon, *Prog. Quant. Electr.* **26** (2002) 225.

[158] E. Bustarret, C. Marcenat, P. Achatz, J. Kacmarcik, F. Levy, A. Huxley, L. Ortega, E. Bourgeous, X. Blasé, D. Debarre, J. Boulmer, *Nature* **444** (2006) 465.

[159] N. Itoh, A. M. Stoneham *Materials Modification by Electronic Excitation*, Cambridge University Press, Cambridge (2001).

[160] V. Privitera, *Curr. Opin. Solid State Mater. Sci.* **6** (2002) 55.

[161] S. Xiong, J. Bokor, *IEEE Trans. Electron Devices* **51** (2004) 228.

[162] J. C. Bean, *J. Electron. Mater.* **19** (1990) 1055.

[163] V. G. Schengurov, S. P. Sveltov, V. Y. Chalkov, D. V. Shengurov, S. A. Denisov *Semiconductors* **40** (2006) 183.

[164] J. C. Bean, *Appl. Phys. Lett.* **33** (1978) 654.

[165] G. E. Becker, J. C. Bean, *J. Appl. Phys.* **48** (1977) 3395.

[166] P. Rai-Choudhury, E. I. Salkovitz, *J. Cryst. Growth* **7** (1970) 361.

[167] M. K. Sanganeria, K. E. Violetta, M. C. Ozturk, *J. Electrochem. Soc.* **142** (1995) 285.

[168] J. Bloem, *J. Cryst. Growth* **13/14** (1972) 302.

[169] W. H. Shepherd, *J. Electrochem. Soc.* **115** (1968) 541.

[170] R. Reif, *J. Electrochem. Soc.* **129** (1982) 1122.

[171] J. Kemmer, F. Wiest, A. Pahlke, O. Boslau, P. Goldstrass, T. Eggert, M. Schindler, I. Eisele, *Nucl. Instr. Meth. Phys. Res. A* **544** (2005) 612.

[172] J. C. Ho, R. Yerushalmi, Z. A. Jacobson, Z. Fan, R. L. Alley, A. Javey *Nature Mater.* **7** (2008) 62.

[173] A. Fick, *Ann. Phys. Leipzig* **170** (1855) 59.

[174] A. Zamouche, T. Heiser, A. Mesli, *Appl. Phys. Lett.* **96** (1995) 1440.

[175] H. Nakashima, K. Hashimoto, *J. Appl. Phys.* **69** (1991) 1440.

[176] B. Henderson, *Defects in Crystalline Solids*, 1st Edition, Edward Arnold, London (1972).

[177] R. J. Borg, G. J. Dienes, *An Introduction to Solid State Diffusion*, 1st Edition, Academic Press Inc., Boston (1988).

[178] J. H. G. Owen, D. R. Bowler, K. Miki, *J. Mater. Sci.* **41** (2006) 4568.

[179] M. Grundner, H. Jacob, *Appl. Phys. A* **39** (1986) 73.

[180] G. S. Higashi, Y. J. Chabal, G. W. Trucks, K. Raghavachari, *Appl. Phys. Lett.* **56** (1990) 656.

[181] V. A. Burrows, Y. J. Chabal, G. S. Higashi, K. Raghavachari, S. B. Christman *Appl. Phys. Lett.* **53** (1988) 998.

[182] I. W. Boyd, J. Y. Zhang, *Nucl. Instr. Meth. Phys. Res. B* **121** (1997) 349.

[183] E. A. Sosnin, T. Oppenlander, V. F. Tarasenko, *J. Photochem. Photobiol. C: Photochem. Rev.* **7** (2006) 145.

[184] J-Y. Zhang, G. Windall, I. W. Boyd, *Appl. Surf. Sci.* **186** (2002) 568.

[185] V-M Graubner, R. Jordan, O. Nuyken, B. Schnyder, T. Lippert, R. Kotz, A. Wokaun, *Macromolecules*, **37** (2004) 5936.

[186] K. Yamaguchi, Y. Uematsu, Y. Ikoma, F. Watanabe, T. Motooka, T. Igarashi, *J. Vac. Sci. Technol. B* **15** (1997) 277.

[187] T. Ikematsu, N. Hayashi, S. Ihara, S. Sato, C. Yamabe, *Vacuum*, **73** (2004) 579.

[188] H. J. Guntherodt, R. Wiesendanger, *Scanning Tunneling Microscopy I*, 2nd Edition, Springer-Verlag, New York (1994).

[189] R. Wiesendanger, *Scanning Probe Microscopy and Spectroscopy Methods and Applications,* Cambridge University Press, Cambridge (1998).

[190] J. C. Vickerman, *Surface Analysis The Principle Techniques*, John Wiley & Sons Ltd., New York (1997).

[191] K. Wittmaack, *Surf. Sci.* **112** (1981) 168.

[192] H. A. Storms, K. F. Brown, J. D. Stein, *Anal. Chem.* **49** (1977) 2023.

[193] S. W. Novak, R. G. Wilson, *J. Appl. Phys.* **69** (1991) 463.

[194] R. G. Wilson, S. W. Novak, *J. Appl. Phys.* **69** (1991) 466.

[195] D. P. Woodruff, T. A. Delchar, *Modern Techniques of Surface Science*, 2nd Edition, Cambridge University Press, Cambridge (1994).

[196] M. H. Yang, G. Mount, I. Mowat *J. Vac. Sci. Technol. B* **24** (2006) 428.

[197] G. D. Christian, J. E. O'Reilly, *Instrumental Analysis*, 2nd Edition, Allyn and Bacon Inc., Boston (1986).

[198] C. K. Mann, T. J. Vickers, W. M. Gulick, *Instrumental Analysis*, Harper & Row, New York (1974).

[199] N. M. Atherton, *Principles of Electron Spin Resonance*, Prentice Hall, New York (1993).

[200] J. I. Goldstein, D. E. Newbury, P. Echlin, D. C. Joy, A. D. Romig, C. E. Lyman, C. Fiori, E. Lifshin, *Scanning Electron Microscopy and X-ray Microanalysis*, 2nd Edition, Plenum Press, New York (1992).

[201] B. K. Teo, *EXAFS: Basic Principles and Data Analaysis,* Springer-Verlag, New York (1986).

[202] M. Newville *Fundamentals of XAFS,* Chicago (2004).

[203] F. Fagres, *Phys. Rev. B* **71** (2005) 155109.

[204] F. H. B. Lima, M. L. Calegero, E. A. Ticianelli *J. Electroanal. Chem.* **590** (2006) 152.

[205] J. H. Schofield, *J. Elect. Spectrosc. Rel. Phenom.* **8** (1976) 129.

[206] C. D. Wagner, L. E. Davis, M. V. Zeller, J. A. Taylor, R. H. Raymond, L. H. Gale, *Surf. Interface Anal.* **3** (1981) 211.

[207] B. E. Warren *X-ray Diffraction*, 2nd Edition, Dover Publishing Ltd., New York (1990).

[208] J. C. Buchholz, G. A. Somorhai, *J. Chem. Phys.* **66** (1997) 573.

[209] J. M. Auerhammer, M. Knupfer, H. Peirsert, J. Fink, *Surf. Sci.* **506** (2002) 333.

[210] G-M. Riganese, A. Pasquarello, *Appl. Phys. Lett.* **76** (2000) 553.

[211] J. H. G. Owen, D. R. Bowler, S. Kusano, K. Miki, *Phys. Rev. B* **72** (2005) 113304.

[212] J. H. G. Owen, K. Miki, *Surf. Sci.* **600** (2006) 2943.

[213] J. H. G. Owen, K. Miki, *Nanotechnology* **17** (2006) 430.

[214] S. Nakamura, S. Kashirajima, Y. Johdai, Y. Yoshiwa, M. Naitoh, S. Nishigaki, Y. Shimizu, T. Ikari, F. Shoji, *Surf. Rev. Lett.* **5** (2007) 957.

[215] K. Miki, J. H. G. Owen, D. R. Bowler, G. A. D. Briggs, K. Sakamoto, *Surf. Sci.* **421** (1999) 397.

[216] R. Ruiz, B. Nickel, N. Koch, L. C. Feldman, R. F. Hagland, A. Kahn, G. Scholes, *Phys. Rev. B* **67** (2003) 125406.

[217] J. Hoogboom, P. M. L. Garcia, M. B. J. Otten, J. A. A. W. Elemans, J. Sly, S. V. Lazarenko, T. Rasing, A. E. Rowan, R. J. M. Nolte, *J. Am. Chem. Soc.* **127** (2005) 11047.

[218] R. L. Schwoebel, E. J. Shipsey, *J. Appl. Phys.* **37** (1966) 3682.

[219] S. M. Bayliss, S. Heutz, R. Cloots, R. L. Middleton, G. Rumbles, T. S. Jones *Adv. Mater.* **12** (2000) 202.

[220] S. E. Harrison, J. M. Assour, *J. Chem. Phys.* **40** (1964) 365.

[221] L. Guo, E. Ellis, K. C. Mundim, B. M. Hoffman *J. Porphyrins Phthalocyanines* **3** (1999) 196.

[222] K. Xiao, Y. Q. Liu, G. Yu, D. B. Zhu, *Synth. Met.* **137** (2003) 991.

[223] R. D. Gould, *Thin Solid Films* **125** (1985) 63.

[224] S. Heutz, R. Cloots, T. S. Jones *Appl. Phys. Lett.* **77** (2000) 3938.

[225] P. Sullivan, T. S. Jones, A. J. Ferguson, S. Heutz, *Appl. Phys. Lett.* **91** (2007) 233114.

[226] W. Chen, H. Huang, S. Chen, X. Y. Gao, A. T. S. Wee, *J. Phys. Chem. C* **112** (2008) 5036.

[227] N. Mobus, N. Karl, *J. Cryst. Growth* **116** (1992) 495.

[228] A. J. Lovinger, S. R. Forrrest, M. L. Kaplan, P. H. Schmidt, T. Venkatesan, *J. Appl. Phys.* **55** (1984) 476.

[229] S. Yim, T. S. Jones, *Phys. Rev. B* **73** (2006) 161305.

[230] F. Iwatsu, T. Kobayashi, N. Uyeda, *J. Phys. Chem.* **84** (1980) 3223.

[231] A. J. Ferguson, T. S. Jones, *J. Phys. Chem. B* **110** (2006) 6891.

[232] A. R. Harutyunyan, A. A. Kuznetsov, O. A. Kuznetsov, O. L. Kaliya, *J. Mag. Mag. Mater.* **194** (1999) 16.

[233] Z. T. Liu, H. S. Kwok, A. B. Djurisic, *J. Phys. D: Appl. Phys.* **37** (2004) 678.

[234] J. B. Gustafsson, H. M. Zhang, L. S. O. Johansson, *Phys. Rev. B* **75** (2007) 155414.

[235] J. Dowdy, J. J. Hoogland, K. W. Hipps, *J. Phys. Chem.*, **95** (1991) 3751.

[236] M.-S. Liao, J. D. Watts, M.-J. Huang, *Inorg. Chem.* **44** (2005) 1941.

[237] M.-S. Liao, S. Scheiner *J. Chem. Phys.* **114** (2001) 9780.

[238] D. F. McMillen, D. M. Golden, *Ann. Rev. Phys. Chem.* **33** (1982) 493.

[239] N. Ohta, M. Gomi, *Jpn. J. Appl. Phys.* **39** (2000) 4195.

[240] M. Tamada, H. Koshikawa, H. Omichi, *Thin Solid Films* **293** (1997) 113.

[241] J. S. Chickos, W. A. Acree, *J. Phys. Chem. Ref. Data* **31** (2002) 537.

[242] Q-R Li, C-Z Gu, Y. Di, H. Yin, J-Y Zhang, *J. Hazard. Mater. B* **113** (2006) 68.

[243] K. R. Rajesh, C. S. Menon, *Mater. Lett.* **51** (2001) 266.

[244] A. Yamamoto, L. J. Phillips, M. Calvin, *Inorg. Chem.* **7** (1968) 847

[245] G. Engelsma, A. Yamamoto, E. Markham, M. Calvin *J. Phys. Chem.* **66** (1962) 2517.

[246] A. A. Dakhel, *Thin Solid Films* **296** (2006) 353.

[247] S. Trudel, G. Li, X. Zhang, R. H. Hill, *J. Photopolym. Sci. Technol.* **19** (2006) 467.

[248] M. A. T. Gilmartin, R. J. Ewen, J. P. Hart, *Journal of Electroanalytical Chemistry* **401** (1996) 127.

[249] R. J. Ewen, C. L. Honeybourne, *J. Phys.: Condens. Matter* **3** (1991) S303.

[250] Y. Niwa, H. Kobayashi, T. Tsuchiya, *J. Chem. Phys.*, **60** (1974) 799.

[251] Nefedov V. I., Salyn Y. V., Leonhardt G., Scheibe R., *J. Electron. Spectrosc., Relat. Phenom.*, **10** (1977) 121.

[252] Aarnink W. A. M., Weishaupt A., van Silfhout A., *Appl. Surf. Sci.*, **45** (1990) 37.

[253] J. L. Jordan, P. N. Sana, J. F. Morar, C. A. Kovac, F. J. Himpsel, R. A. Pollack, *J. Vac. Sci. Technol. A* **4** (1986) 1046.

[254] F. Parmigiani, L. Sangaletti, *J. Electron. Spectrosc. Res. Phenom.* **98-99** (1999) 287.

[255] V. DiCastro, G. Polzonetti *J. Electron. Spectrosc., Relat. Phenom.*, **48** (1989) 117.

[256] M. Oku, K. Hirokawa, S. Ikeda *J. Electron. Spectrosc., Relat. Phenom.*, **7** (1975) 465.

[257] B. J. Tan, K. J. Klabunde, P. M. A. Sherwood *J. Am. Chem. Soc.* **113** (1991) 855.

[258] M. Chigane, M. Ishikawa, *J. Electrochem. Soc.* **147** (2000) 2246.

[259] http://cars9.uchicago.edu/~ravel/software/Welcome.html

[260] S. Sasaki, K. Fujino, Y. Takeuchi, R. Sadanaga, *Acta Crystallographica A*, **36** (1980) 904.

[261] D. Jarosch, *Journal of Physics and Chemistry of Solids*, **23** (1962) 711.

[262] S. Geller, *Acta Crystallographica B*, **27** (1971) 821.

[263] A. A. Bolzan, C. Fong, B. J. Kennedy, C. J. Howard, *Australian Journal of Chemistry*, **46** (1993) 939.

[264] http://webelements.com

[265] M. J. Han, T. Ozaki, J. Yu, *J. Chem. Phys.*, **123** (2005) 034306.

[266] D. Giles, W. Bergholz, W. Schroter, *J. Appl. Phys.* **59** (1986) 3590.

[267] G. M. Dalpian, A. J. R. da Silva, A. Fazzio *Phys. Rev. B* **68** (2003) 113310.

[268] J. Martin, J. Wedekind, H. Vollmer, R. Labusch *Phys. Rev. B* **61** (2000) 1918.

[269] A. Wolska, K. Lawniczak-Joblonska, M. Klepka, M. S. Walczak, A. Misiuk *Phys. Rev. B* **75** (2007) 113201.